THE UNIVERSITY OF HULL

Wave-induced ripple development in mixed clay-sand substrates

being a Thesis submitted for the Degree of Doctor of Philosophy in the University of Hull

by

Xuxu Wu, M.Sc.

October 2017

Abstract

Wave-induced ripples are significant tools in reconstructing a range of paleo-environments and in establishing predictors of sediment transport in modern estuarine, marine and coastal environments. Previous studies, however, have focused on the dynamics of bedforms composed primarily of well-sorted, non-cohesive, sand. This restriction to one sediment type is far from being a realistic representation of natural sediment size distributions. This thesis reports on a flume experiments and aligned field investigations of rippled formed in mixed (cohesive and non-cohesive) sediments substrates under combined flows. The flume experiments were conducted in the Total Environment Simulator at the University of Hull and comprised of 6 separate runs, in which 5 runs were conducted under identical sets of regular (monochromatic) waves with period of 2.48 s. A control experiment, with a pure non-cohesive sand bed, proceeded runs where the bed clay content was systematically varied in its composition ranging from a bed comprising 4.2% clay through to 7.4%. A series of state-of-the-art measurements were employed to quantify interactions of near-bed hydrodynamics, sediment transport, and turbulence over rippled beds formed by wave action. The experimental results demonstrate the significant influence of cohesive clay materials in the substrate on ripple evolution under waves. Most importantly, addition of clay in the bed remarkably slows the rate of ripple development and ripple evolution. Both equilibrium time of wave ripple length and height exponentially increased with increases in clay content, from 40 minutes to 200 minutes for ripple wavelength and from 30 minutes to 120 minutes for ripple height. The slower ripple growth rates with higher cohesive substrate fractions is shown to alter the critical shear stress and reduce clay winnowing rates. However, the results also highlight that the equilibrium size of ripples is independent of increasing substrate clay fraction, with equilibrium length and height standing around 140 mm and 20 mm, respectively. Laser granulometry of cores from the final substrates verified that ripple crests were composed of pure sand layers and that substrates within the ripple troughs remained mixtures, reflecting a relatively higher winnowing efficiency at wave ripple crest. The winnowing process, and its efficiency, is shown to be inexorably linked to wave ripple development and evolution. Furthermore, the remaining clay was able to stabilize the rippled bed, ripple migration rate decreasing from 0.06 mms^{-1} to 0.02 mms^{-1} and bed sediment flux falling from 0.43

mm^2s^{-1} to 0.22 mm^2s^{-1} from the non-cohesive run to the run with the highest initial concentrations of clay. Finally, the results also highlight the influence of clay concentrations on damping of turbulence, which is related to the stratification of suspended sediments.

In concert with the flume experiments, a series of field surveys were conducted at Red Cliff sand bar in the upper Humber estuary NE England. The fieldwork aims were to study bedform dynamics under combined current-wave flows. Field surveys were conducted in a matrix of periods covering spring and neap tides and during periods of high and quiescent wind conditions. Field surveys were also conducted across both winter and summer periods to investigate the influence of biological cohesive Extracellular polymeric substances (EPS) on ripple size. The results identified that two-dimensional current-induced ripples dominated under low wave forcing calm conditions. While the bed morphology under high wind conditions with significant wave forcing on the bed resulted in a morphology dominated by plane bed and 2D wash-out ripples. Finally, although the EPS content increased from 0.003% in winter to 0.013% in summer survey periods, its influence on the size of the ripple size was very negligible. However, the ripple symmetry index (RSI) does show a distinctive seasonal trend, with ripples forming in winter being more asymmetrical than those in the summer. Further work is needed to tease out the complex interactions of biological factors and combined flows in estuarine settings. However, these results here highlight a complex interplay, which has significant implications for paleoenvironmental reconstructions.

Stealing 8 hours

Acknowledgements

My deepest gratitude first and foremost to Prof. Daniel R. Parsons, my supervisor, for offering me the great opportunity studying in the United Kingdom and for his constant encouragement and guidance in my academic research. Without his consistent and illuminating instruction, this thesis could not have reached its present form. I also must express my heartfelt gratitude to Dr. Jaco H. Baas who provided great help on my PhD research and guided me to be involved flume experimental work with the COHWAV project. Moreover, I am honoured to work in the great project and thank to the outstanding research teammates including Dr. Dominique Mouazé, Dr. Stuart McLelland, Dr. Laurent Amoudry, Dr. Jorris Eggenhuisen, Dr. Matthieu Cartigny, and Prof. Gerben Ruessink.

In particular, my acknowledgements would go to the China Scholarship Council (CSC) and the University of Hull for a joint scholarship supporting my study and living in the U.K. In addition, I am much obliged to Dr. Steve Simmons for his help on data processing for my thesis. I also thank to the technician team of the Department of Geography including Mike Dennett, Kim Rosewell, and Mark Anderson. Without their assistance, my field work would have not been completed. Besides that, I would like to thank Dr. Leiping Ye, Hao Hu, Rita Santos and Dr. Chris Unsworth for their help on my study.

Additionally, my great thanks to my colleagues and friends for wonderful memories with them living in Hull. Lastly, my thanks would go to my beloved parents for their loving and unfailing support in my living in the U.K.

Contents

Figures

Tables

Nomenclature

α_m	sum of sound attenuation by water and suspended sediment
α_{w}	sound attenuation by water
α_{s}	sound attenuation by suspended sediment
φ	angle between wave move direction and current direction
$\mathcal{K}$	von Karman's constant (0.4)
η	ripple height (mm)
η_e	equilibrium ripple height (mm)
η_t	ripple height at time t (mm)
k_s	scattering properties of suspended sediment
k_t	parameter of the ABS measurement system
λ	ripple length (mm)
λ_0	initial ripple length (mm)
λ_e	equilibrium ripple length (mm)
λ_s	length of ripple stoss side (mm)
λ_t	ripple length at time t (mm)
λ_l	length of ripple lee side (mm)
μ	dynamic viscosities ($kgm^{-1}s^{-1}$)
v	kinematic viscosity coefficient (m^2s^{-1})
θ'_{c}	current mobility parameter
$\theta'_{\mathrm{c,cr}}$	critical current mobility parameter
θ'_{w}	wave mobility parameter
$\theta'_{\mathrm{w,cr}}$	critical wave mobility parameter
ρ	fluid density (kgm^{-3})
ρ_{s}	sediment density (kgm^{-3})
τ_{b}	combined flow induced bed shear stress ($kgm^{-1}s^{-2}$)
τ_{bm}	mean combined flow induced bed shear stress ($kgm^{-1}s^{-2}$)
τ_{bmax}	maximum combined flow induced bed shear stress ($kgm^{-1}s^{-2}$)
τ_{cr}	critical threshold of bed-shear stress for sediment transport ($kgm^{-1}s^{-2}$)
τ_0	total bed shear stress ($kgm^{-1}s^{-2}$)

τ_{0f}	form drag ($kgm^{-1}s^{-2}$)
τ_{0s}	skin friction ($kgm^{-1}s^{-2}$)
τ_{0t}	sediment transport shear stress ($kgm^{-1}s^{-2}$)
τ_{w}	wave-induced bed shear stress ($kgm^{-1}s^{-2}$)
χ	Yalin number
ψ	departure from spherical spreading within the ABS transducer nearfield
A	semi-orbital excursion (m)
c_m	ripple migration rate (mms^{-1})
C	Chézy coefficient
C'	Chézy drag coefficient related to grain roughness
C_D	drag coefficient
d_o	wave orbital diameter (m)
D_{50}	median grain size (m)
D_*	particle diameter parameter
f	Darcy-Weisbach resistance coefficient
f_w	wave friction factor
g	gravity acceleration (ms^{-2})
h	water depth (m)
H_s	significant wave height
k_s	Nikuradse roughness
L	distance between upstream and downstream fixed URS probes (mm)
L_w	parameter to acquire wave friction factor
n	Manning coefficient
p	bed porosity (p=0.35)
q_b	bed sediment flux per unit width (mm^2s^{-1})
r	relative roughness
r_d	range from ABS transducer
r_λ	ripple length growth rate ($mmmin^{-1}$)
r_η	ripple height growth rate ($mmmin^{-1}$)
R	correlation coeeficient

Re_p	non-dimensional particle size
Re_w	wave Reynolds number
t_f	delay time for ripples appearance on bed (min)
T	wave period (s)
T	transport stage parameter
T_η	equilibrium time for ripple height (min)
T_λ	equilibrium time for ripple length (min)
$T_{\lambda d}$	ripple length development time (min)
$T_{\eta d}$	ripple height development time (min)
$\mathrm{T_z}$	mean zero upcrossing period (s)
u	streamwise fluid velocity (ms^{-1})
$\bar{u}$	mean streamwise fluid velocity (ms^{-1})
u'	horizontal turbulent fluctuation (ms^{-1})
$\tilde{u}$	periodic velocity (ms^{-1})
$\langle u \rangle$	phase-averaged velocity (ms^{-1})
$u_{*,\mathrm{c}}$	current-related shear velocity (ms^{-1})
$u_{*\mathrm{w}}$	wave-related shear velocity (ms^{-1})
$\mathrm{U_{max}}$	maximum bottom orbital velocity (ms^{-1})
$\mathrm{U_{rms}}$	root-mean-square wave velocity (ms^{-1})
U_u	unidirectional velocity (ms^{-1})
$\mathrm{U_w}$	wave bottom orbital velocity (ms^{-1})
U_∞	free stream velocity (ms^{-1})
V_{rms}	voltage recorded by ABS probes
z	height above the bed (m)
z_0	bed roughness length (m)

CHAPTER1-Introduction

1.1 Background

The coastal zone, with complex interactions between land and sea, is one of the most productive zones in terms of ecosystem services and in supporting human populations globally. Indeed, over half of all inhabitants on Earth live within 100 km of the coastline (Crossland et al., 2005). However, such systems are under significant pressure. Human actions, including industrial and agricultural activities, are increasingly altering sediment input at river mouths, which is also affecting the release of both nutrients and harmful pollutants (e.g. Jordan et al., 1996; Boesch, 2002; Xu and Milliman, 2009; Dugan et al., 2010; Yang et al., 2011). Moreover, global warming is likely to induce a higher frequency of extreme weather systems (e.g. Meehl and Tebaldi, 2004; Goswamin et al., 2006; Meinshausen et al., 2009; Couou and Rahmstorf, 2012) and sea level rise (e.g., Meehl et al., 2005; Nicholls and Cazenave, 2010), which will also impart significant stress on existing balances among hydrodynamics, sediment dynamics and bed morphology in these interface zones.

Fully understanding of the interactions between fluid flow, sediment transport and bed morphology within these zones (SFD, Perillo, 2013) is crucial for improved predictive capacity. Such productive capacity is vital for civil engineering project design and in steering responses to the challenges from climate and environmental change. SFD in coastal waters is related to a broad spectrum of environmental sciences ranging from the physical and chemical, to the biological and ecological. Understanding linkages between these system components is challenging and of great practical importance (Frostick and McCave, 1979; Black et al., 2002; Soulsby and Whitehouse, 2005; Jorgensen et al., 2007). A key process operating within these environments is bedform dynamics, and a comprehensive understanding of entrainment, transport and deposition of sediment is needed in order to provide insight into their impact on the coastal system as a whole. Wave-induced small scale bedforms (ripples with lengths smaller than 60 cm) are ubiquitous in coastal depositional environments and of interest to coastal engineers and geologists. The formation of ripples from flat beds increases bed roughness and near-bed hydrodynamics, which affect sediment transport (e.g., Grant and Madsen, 1986; Mathisen and Madsen, 1996). In terms of sedimentology, sedimentary structures recorded in the rocks is a vital tool in interpreting ancient depositional environments, not only on Earth but also on Mars and Titan (e.g., Clifton and Dingler, 1984; Baas et al., 2015; Grotzinger et al., 2005; Southard and Tosca, 2012; Lapotre et al., 2017).

1.2 Rationale

A range of large-scale flume studies concerning the dynamics of bedforms composed of well-sorted pure sands under oscillatory waves have been performed over the two last decades, highlighting a range of complex sediment-flow processed (e.g., Williams et al., 2000; Williams et al., 2004; Maddux et al., 2007; Schretlen et al., 2009). However, this single bed sediment composition is far from being a realistic representation of natural coastal sediment size distributions, where fine cohesive bed materials are commonplace (Figure 1-1, Healy et al., 2002). Recent studies have begun to pay attention to bedform dynamics in substrate mixtures of cohensionless sands and cohesive clay under unidirectional flows (Baas et al., 2013; Schindler et al., 2015; Ye, 2016). The results have shown some significant differences compared with bedform evolution within pure sands. However, investigations of bedform development within mixtures of sand-clay under combined wave and current flows are lacking. This shortcoming is transposed to the derived predictive bedform model, which commonly assumes that sediment consists of a single grain size despite the predominance of mixtures of sand, silt and clay in most coastal environments. Cohesive clay within the bed substrate significantly changes bedform dynamics, in turn influences near bed turbulence intensity and sediment dynamics within models (Baas et al., 2013). Accurate bedform models require models for near-bed boundary conditions that properly represent hydrodynamics, sediment dynamics, and turbulent process. However, our existing predictive ability is seriously impeded by an almost complete lack of knowledge of modelling bedform and near-bed turbulence behaviour in mixed sand-clay sediments.

There is therefore a clear need for detailed process measurements of the near bed interactions across the triad of hydrodynamics, sediment dynamics, and bedform within mixed sand-clay bed under oscillatory and combined flow conditions, which focus on resolving both near bed wave generated turbulence and sediment transport.

The interaction between waves and currents, one of characteristics of coastal area such as estuarine zones, undoubtedly complicates depositional environments and bedforms evolution. For example, storms enhance maximum orbital velocity and will affect bedform evolution and sediment transport. Although flume experiments conducted under combined flow have provided excellent information of bedform dynamics (Yokokawa, 1995; Sekiguchi and Yokokawa, 2008; Dumas et al., 2005; Perillo, 2014), the related knowledge is still far from understanding bedform dynamics in natural estuarine environments where biologically active fine grained sediments are ubiquitous. In particular, micro-organisms are pervasive in natural environment and their products of extracellular polymeric substances (EPS) is characterised by biological cohesion (Wotton, 2004). Akin to cohesive clay, EPS has been show to play a significant role in retarding bedform development in the laboratory (Malarkey et al., 2015; Ye, 2016).

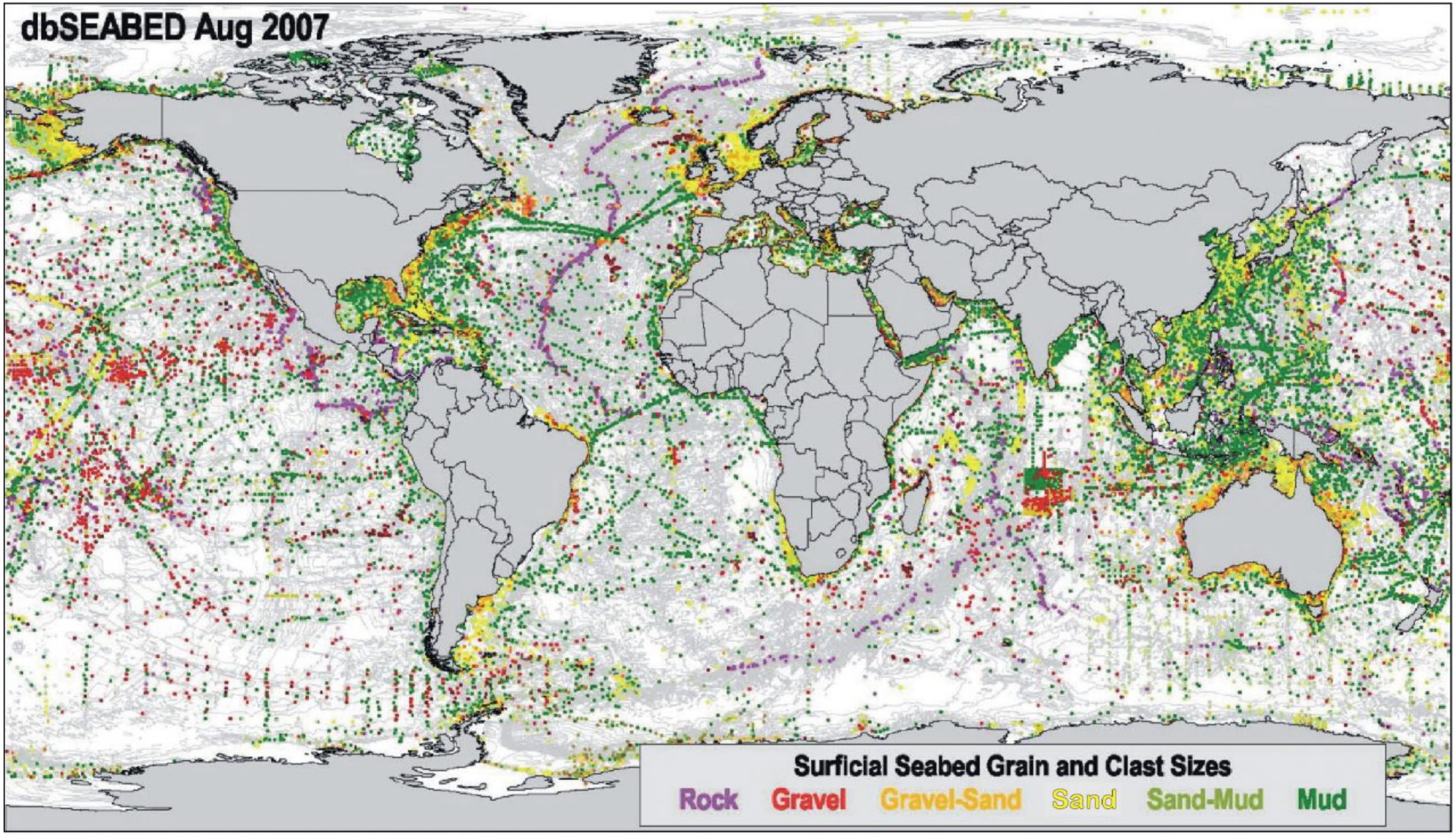

Figure 1-1. The broad distribution of surficial seabed with cohesive clay in the wolrd. Source: http://instaar.colorado.edu/~jenkinsc/dbseabed.

1.3 Aims and research questions

1.3.1 Flume experiment study

The modelling shortcomings outlined above concern the general representation of near-bed turbulence and sediment transport process over mixed-sediment beds (e.g., Amoudry and Souza, 2011). The principal aim of the present investigation is therefore fully quantify near-bed turbulence and sediment transport interactions over rippled beds of clay-sand mixtures under waves and combined flows. Such cohesive mixtures are hypothesised to have a yield strength that affects the timing of first appearance of bedforms from a flat bed, and likely subjected to winnowing processes, which will in turn affect the rate of bedform development (Baas et al., 2013). This presumably alters the equilibrium size and shape of the bedforms and quantifying these process rates is as the heart of the aims of this work.

Herein, the following set of research questions are needed to answer:

1) How does mixed-sediment substrate, compared with a pure sand bed, affect i) the first appearance of wave-induced ripples, and ii) the bedform development rate.

2) Does a relationship exist between initial bed fraction and equilibrium wave ripples lengths and heights?

3) What is the rate of winnowing and how does winnowing influence wave ripples development?

4) How does near-bed turbulence intensity and suspended sediment concentration change during wave ripple evolution?

5) How does the dynamics system including cohesive bed, near-bed turbulence and sediment transport work?

1.3.2 Field survey

The lack of field observation to record accurate ripple size formed under combined flows restricts applicability of many flume experiments (e.g., Dumas et al., 2005; Perillo et al., 2014). The primary aim of the field work conducted herein is to investigate ripple morphology with combined flow induced hydrodynamics. Additionally, the field observations also aim to quantify the influence of biological cohesion (EPS) on ripple evolution by comparing ripples formed in winter months to those in the warmer summer months, respectively.

Hence, the field survey addresses these additional research questions:

1) Does wave-induced bottom orbital motion and combined flows significantly change bedform morphology compared with calmer, low-wave height conditions?

2) Does the quantity of EPS alter bedform morphology?

1.4 Approach

To meet the above-mentioned aims and address the research questions, a series of large flume experiments were conducted in Total Environment Simulator (TES), University of Hull. These experiments were augmented with a set of field surveys in the upper Humber estuary.

In terms of flume experiment, there were five runs with constant wave velocities and wave heights, water depth and salinity, with initial bed clay content systematically altered between the experiments. A suite of state-of-the-art instruments were mounted above the bed to measure the interaction of near-bed hydrodynamics, turbulence and bedform dynamics. The three measured variables are: i) sediment surface elevation and evolution, ii) near-bed velocity and turbulence, and iii) near-bed sediment concentration. A bespoke ultrasonic ranging system (URS) was used to record ripples development with interval high temporal resolution and near-bed hydrodynamics was measured by Acoustic Doppler Velocity (ADV). Near-bed sediment concentration was measured by dedicated acoustic (Acoustic Backscatter Sensor, ABS), optical techniques (Optical Backscatter Sensors, OBS) and Laser In-Situ Scattering and Transmissometry, LISST.

As far as field survey is concerned, a set of field surveys of ripples on large sand bar were conducted under clam (current alone) and windy (combined wave and current) conditions. Furthermore, additional field observations were held in summer in order to investigate the role of EPS on ripple geometry. Each field work was conducted during low water of either spring or neap tide, therefore the sand bar is accessible. Individual ripple cross-section geometry was recorded by high-resolution FARO 3D scanner, which provides information of ripple height and length. In addition, both current and wave conditions were recorded by MIDAS WTR Wave and Tide Recorder. Substrate sediment samples were collected as well to EPS test and grain size test.

1.5 Thesis structure

The thesis is comprised of the following chapters:

Chapter 2 is literature review of boundary layers for unidirectional, oscillatory and combined flows. The chapter also briefly reviews bedforms and the background literature on the controls on bedform development.

Chapter 3 concentrates on bedform dynamics with varying initial bed clay fraction under oscillatory flows and reveals the role of cohesive clay on the ripples development. At the beginning of this chapter, there is a detailed introduction of experiment set-up, methodologies and procedures.

Chapter 4 focuses on the evolution of near bed turbulence intensity and suspended sediment concentration as the bed developed from initial conditions. The chapter also explores the process interactions during the experiments as winnowing, near-bed turbulence and sediment dynamics altering in concert with the evolution rippled bed.

Chapter 5 reports the results of a set of field surveys at Red Cliff sand bar located at upper Humber estuary. The chapter provides detailed information on ripples size under calm and windy conditions (i.e. current only and combined wave-current flows), respectively. The chapter also examines the applicability of existing phase diagrams. In addition, this chapter discuss the role of biological cohesion (EPS) on bedform morphology.

Chapter 6 discusses near-bed interacting traid of hydrodynamics, sediment dynamics, and bedforms in mixed sand-mud conditions.

Chapter 7 is the conclusion of the principal outcomes of the thesis and provides an outlook for future study.

CHAPTER 2 –Literature Review

2.1 Fluid flow

2.1.1 Introduction

In coastal zone, tidal currents and waves interact with seabed topography, forming a complex and dynamic system (Leeder, 2011). For each unit area of bed, the fluid forces are driven by these processes, and are acted by shear stress on the bed. The interaction between flow and the bed generates a thin zone near the bed, called the boundary layer. Turbulence is mainly generated in the boundary layer and the bed shear stress imparted by hydrodynamics results in sediment entrainment, and sediment transportation, bedform formation and migration (Bagnold, 1966; van Rijn, 1984; Nielsen, 1992; Best, 1993; Nielsen, 2002). In turn, formation of bedforms, such as ripples and dunes, changes near-bed flow velocity field, altering the near bed turbulence distribution (Tunstall and Inman, 1975; Leeder, 1983; Nelson et al., 1995; Bennett and Best, 1995; Admiraal et al., 2006). Understanding this complex process trinity is at the heart of process sedimentology and understanding coastal morphodynamics.

When flow velocity is low, viscous forces dominate and prevent flow deformation, leading to fluid flows in parallel layers without lateral mixing. This is called laminar flow. With higher velocity, enhanced inertial forces contribute to intense turbulent motions between fluid layers, which generates turbulent flow. In nature, almost all water flows are turbulent and these turbulent flows dominate sediment transport processes. The following review therefore focuses on boundary layers in turbulent flows and the importance of theses processes on coastal zone morphodynamcis.

2.1.2 Unidirectional flows

2.1.2.1 Unidirectional turbulent boundary layer

The vertical structure of a boundary layer induced by unidirectional flow is traditionally subdivided into viscous sublayer, transition layer, and turbulent logarithmic layer (Figure 2-1).

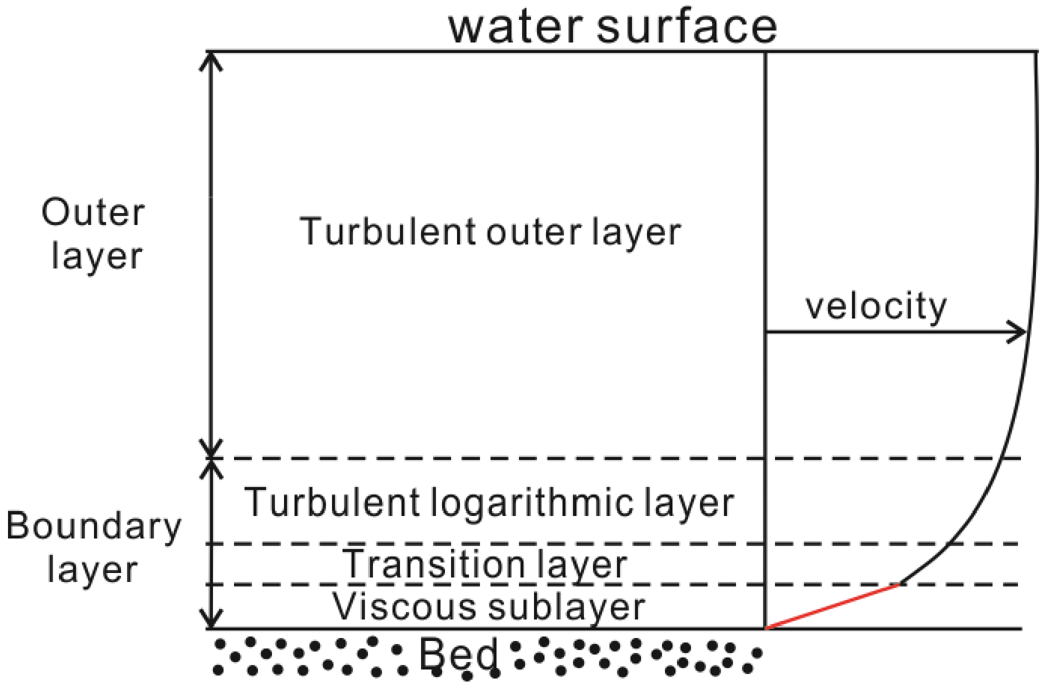

Figure 2-1. Boundary layer and velocity distribution in unidirectional flow. The red line denotes a linear increase of velocity with height above the bed in the viscous sublayer (modified after van Rijn, 1993).

The viscous sublayer (δ_v) is an extremely thin zone very close to the bed. In this zone, flow turbulence is absent and velocity linearly decreases towards to the bed. The flow velocity can be described by:

$$\frac{u}{u_{*,c}} = \frac{u_{*,c}z}{v} \quad \text{(after van Rijn, 1993)} \qquad 2\text{- }1$$

where z is the height above the bed, v is the kinematic viscosity coefficient, $u_{*,c}$ is the current-related shear velocity.

A bed can be covered by a large grain sizes of sediments, which is known as a hydraulically rough bed. Under this condition, sediment grains are able to generate the same order size of eddies, which modifies near bed velocity distribution. As a result, the viscous sublayer is disturbed (Grass, 1971). Van Rijn (1993) proposed criteria to distinguish different hydraulic regimes as shown following:

$$\frac{u_{*,c}\mathrm{k_s}}{v} \leq 5 \text{ (Hydraulically smooth)} \qquad 2\text{- }2$$

For hydraulically smooth flow, the roughness elements are totally enclosed in the viscous sublayer, therefore little affecting the near-bed velocity.

$$\frac{u_{*,c}\mathrm{k_s}}{v} \geq 70 \text{ (Hydraulically rough)} \qquad 2\text{- }3$$

$$5 < \frac{u_{*,c}\mathrm{k_s}}{v} \leq 70 \text{ (Hydraulically trasitional)} \qquad 2\text{- }4$$

where $\mathrm{k_s}$, the Nikuradse roughness, is proportional with grain size and widely computed by:

$$\mathrm{k_s} = 2.5\mathrm{D}_{50} \text{ (Soulsby, 1997)} \qquad 2\text{- }5$$

When the flow is hydraulically transitional, near-bed velocity is influenced by both viscous force and roughness elements.

Above the viscous sublayer, there is the transition layer. The viscous force and turbulent force are comparable in this zone. Above this the turbulent logarithmic layer extends to the top of boundary layer. In this layer turbulence is fully developed. Velocity in this zone can be expressed by a logarithmic velocity profile.

$$u = \frac{u_{*,c}}{\mathcal{K}} \ln\left(\frac{z}{z_0}\right) \text{ (von Karḿán, 1930)} \qquad 2\text{- }6$$

where $\mathcal{K}$ is the von Karman's constant (0.4), z_0 is the bed roughness length.

For the hydraulically smooth flow ($u_{*,c}\mathrm{k_s}/v \leq 5$)

$$z_0 = v/9u_{*,c} \qquad 2\text{- }7$$

For the hydraulically rough flow ($\frac{u_{*,c}\mathrm{k_s}}{v} \geq 70$)

$$z_0 = \mathrm{k_s}/30 \qquad 2\text{- }8$$

2.1.2.2 Bed shear stress

Current-induced bed shear stress exerts a frictional force on unit area of bed. The total shear stress exerted on bed contains three parts. The first one is called the skin friction ($\tau_{0\mathrm{s}}$) that frictional force acting on sediments. It is regarded as a significant quantity for sediments initial motion and transportation. If there are ripples or dunes, different pressure over the bedform induces a net force that is the form drag ($\tau_{0\mathrm{f}}$). Under high flow velocities, close to sheet flow, sediment transport shear stress ($\tau_{0\mathrm{t}}$) is produced by momentum extracted by the current to move sediments. The total bed shear stress (τ_0) is related to the drag coefficient (C_D)

$$\tau_0 = \rho C_\mathrm{D}\overline{\mathrm{U}}^2 \qquad 2\text{- }9$$

where ρ is flow density, $\overline{\mathrm{U}}$ is the depth-averaged current speed, C_{D} is mathematically determined by

$$C_{\mathrm{D}} = \frac{f}{8} = \frac{\mathrm{g}}{C^2} = \frac{\mathrm{g}n^2}{h^{1/3}} \qquad 2\text{- }10$$

where f is the Darcy-Weisbach resistance coefficient, C is the Chézy coefficient, g is the gravity acceleration, *n* is the Manning coefficient, and *h* is the water depth.

2.1.2.3 Unidirectional flow structure over rippled beds

The presence of bedforms alters the flow structure compared to flat bed scenarios (Vanoni and Hwang, 1967; Mclean and Smith, 1986; Vincent et al., 1991; Bennett and Best, 1995; Sandbach et al., 2012). Over the last several decades, researchers have improved the knowledge of flow structure over two-dimensional bedforms (Mclean and Smith, 1979; Nelson and Smith, 1989; Mclean, 1990; Mclean, 1999; Bridge, 2009). Best (2005) summarized earlier works and subdivided flow over river dunes into five zones (Figure 2-2). This classification is applicable to flow over the smaller-size ripples as well (Mclean and Smith, 1986; Nelson and Smith, 1989; Leeder, 2011). The flow structure over ripples is characterised by a separation zone and a recirculating zone of lee side flow, due to the asymmetrical cross-section profile and the sharp crest break. Between the separation zone and the free flow zone, there is a shear layer which comprises large-scale turbulence known as Kelvin-Helmholtz instabilities. From ripple crest downstream, the point that shear layer contacts with bed is called reattachment point, the distance between ripple crest and the reattachment point is smaller or close to 4.5 times of ripple heights (Nelson and Smith, 1989). A weak zone develops from the reattachment point due to shear expansion from the shear layer, in which there is a new internal boundary layers within logarithmic velocity profile. Downstream the weak region, there is an expanding flow zone.

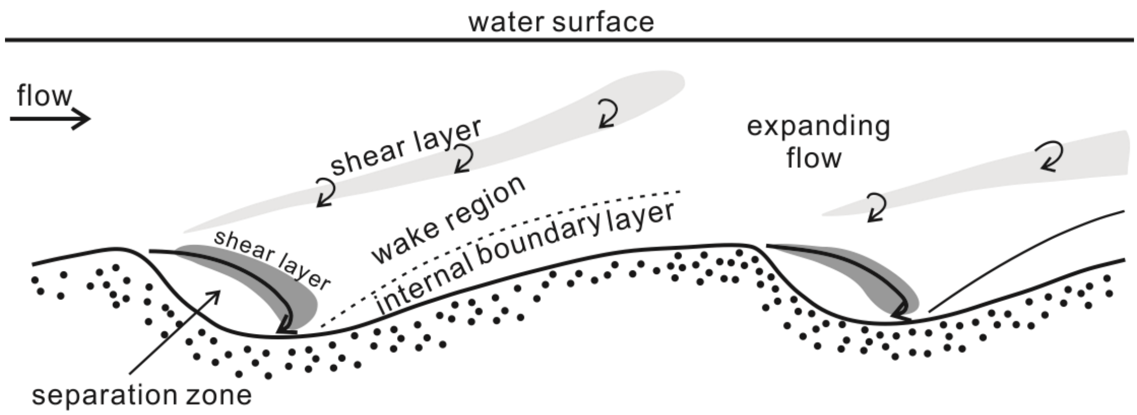

Figure 2-2. Schematic diagram depicting the principal zones of flow over asymmetrical two-dimensional bedform (from Best, 2005).

2.1.2.4 Turbulence modulation in clay-laden current flow

A phenomenon of drag reduction near bed is observed with high suspended clay particles in the flow (Gust, 1976; Gust and Walger, 1976; Best and Leeder, 1993; Wang et al., 1998; Li and Gust 2000). It greatly affects boundary layer flow structure and bed shear stress (Dyer, 1986; Mehta and Dyer, 1990; Baas and Best, 2002; Baas et al, 2011; Baas et al, 2013; Baas et al., 2016). Li and Gust (2000) found that drag reduction is proportional with suspended clay concentration from 4 to 8 gL^{-1}, which they linked to a thickening of the viscous sublayer. The reason for the drag reduction was linked to clay particle flocculation and induced turbulence damping (Gust, 1976; Baas et al, 2009). Suspended clay particles in the flow is featured by cohesive behaviour because van der Waals forces and electrostatic force promote particles attracting each other (Van Olphen, 1977, Pye, 1994; Righetti and Lucarelli, 2007; Grabowski et al., 2011). The electro-chemical charges on the clay particle surface is strongly related to mineralogy and layer structure which heavily control the degree of cohesion (Gillott, 1987; Ravisangar et al., 2005). Once the distance between two clay particles smaller than 10 µm, they aggregate to form floc (Krone, 1963; Winterwerp and van Kesteren, 2004; Leeder, 2006). As long as enough clay concentration exists in the flow, floc size grows until gelling structure that a particle bond with volume-filling network is formed. Then this kind of particle bond gradually pervades in flow and results in a viscous fluid, which leads to significant turbulence suppression (Baas et al, 2009). The above mentioned process of floc or gel bond formation can be prevented with strong flow turbulence, therefore inducing a balance between cohesive forces and turbulence forces (Winterwerp and van Kesteren, 2004; Baas et al, 2009).

Detailed flume experiments of Baas and his colleagues (Baas and Best, 2002; Baas and Best, 2008; Baas et al., 2009) have investigated turbulence modulation in the transitional flow within increasing clay concentration. Baas and Best (2008) study the influence of raised cohesive forces on turbulence dynamics over the rippled bed. The results show four classes of flow structure generated on ripple lee side, which are i) turbulent flow, ii) turbulent-enhanced transitional flow, iii) turbulence-attenuated transitional flow, and iv) laminar plug flow (Figure 2-3). At low suspended clay concentration (<1%), like clay free flow, classic flow separation zone presents including shear layer, reattachment point, and wake zone. With suspended clay concentration exceeding 2%, turbulence in the separation layer is not supressed by increasing cohesive forces. Conversely, turbulence intensity is enhanced since turbulence generation at internal shear layer (Phase 1 in Figure 2-3). In the phase 2 and 3 of transitional flow, cohesive force is dominated in the separation zone in which vortices tend to be gentle. The length of separation zone is progressively shorten from phase 2 to phase 3. In the upper free stream, cohesive particle bonds are pervasive and herein turbulence is completely suppressed, forming plug flow. With condition of the highest suspended clay concentration over 10%, stagnant flow zone is observed at ripple lee side. Up towards from crest, flow is fully transformed to be laminar (Phase 4 in Figure 2-3).

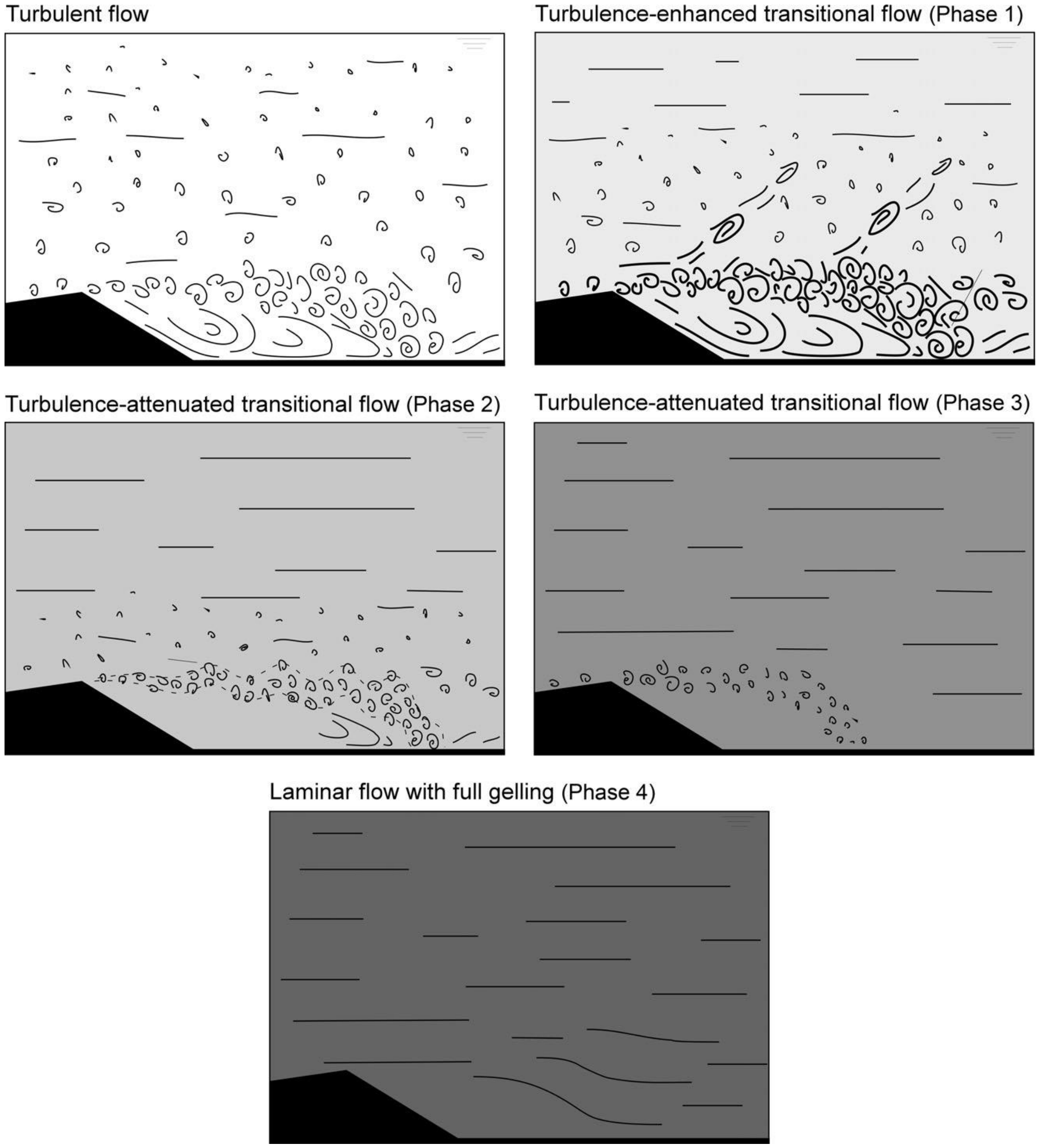

Figure 2-3. Conceptual model reflecting lee side flow stracuture chage with raised suspended clay concentration (from Baas et al., 2011).

2.1.2 Oscillatory flows

Oscillatory flows (wave) passing along the surface of the water set the water molecules within the water column into an orbital motion whose diameter increases with increasing wave size and decreases with water depth. As shown in Figure 2-4, in deep water, depth (h) is larger than a quarter length (L) of wave, sinusoidal waves induced water particle orbital motion are essentially circular. In shallow water, the orbital water motions transformed into ellipses, gradual becoming flatter and smaller with depth. Under this circumstance, at the bottom wave-induced to-and-fro motion interacts with the bed, resulting in bedload and suspended sediment transport and finally formation of ripples (Clifton and Dingler, 1984).

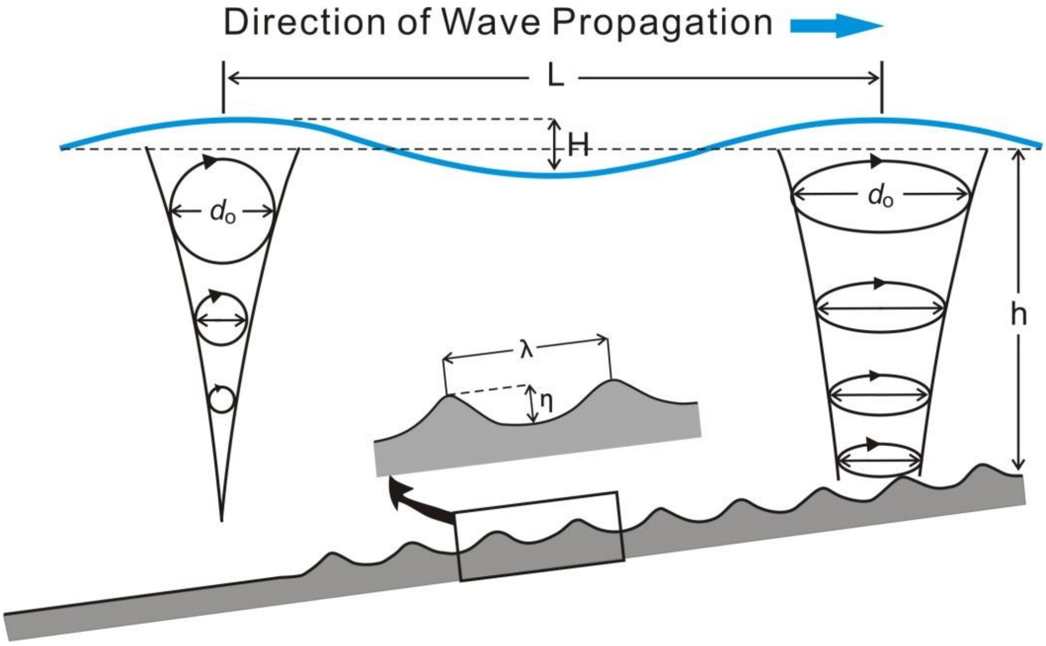

Figure 2-4. Diagram of wave-induced water molecules orbital motion. Orbital diameter (d_o) is the maximum horizontal distance of excursion of water particles as a wave passes; and the maximum orbital velocity (U_w) is the maximum horizontal velocity in the direction of wave passage (from Clifton and Dingler, 1984).

2.1.2.1 Oscillatory turbulent boundary layer

In contrast to current-induced boundary layers, wave-induced boundary layer over a flat bed is thinner, ranging from 0.01 to 0.1 m since flow reversal prevents boundary layer development (Nielsen, 1992; van Rijn, 1993; Davies and Villaret, 1997; Soulsby, 1997). Jonsson (1980) defined the boundary layer (δ_{w}), varying with different wave phase, from the bed to the height that velocity equals to free stream velocity just below the overshooting zone (Figure 2-5). Nielsen (1992) argued that velocity defect damped wave by adding from free stream velocity, resulted in formation of the velocity overshoot. Furthermore, previous work (e.g., Jonsson and Carlsen, 1976; Jensen et al., 1989; Sawamoto, 1991) indicated that phase-averaged horizontal velocity increases logarithmically from bed to outside of the boundary layer (Figure 2-5). A wide acceptable expression, to describe velocity profile, is similar to the unidirectional current discussed above (Equation 2-6, Fredsoe, 1984; Block, 1994). Jonsson (1980) emphasized the thickness of boundary layer could be expended to $2\delta_w$, considering die-out shear stress at this level.

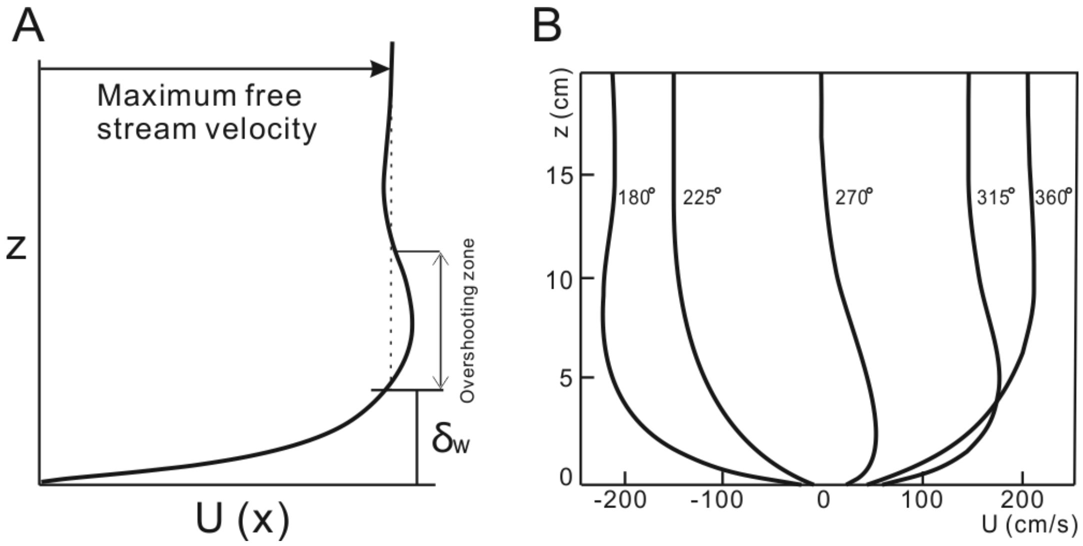

Figure 2-5. A) Wave-induced boundary layer. B) The thickness of wave boundaty layer chages with wave phase (from Jonsson, 1980).

Sleath (1987) investigated temporal and spatial distribution of turbulence intensity over a rough flat bed ($D_{50} = 1.63$ mm). In such research, root-mean-square (RMS) values of the fluctuations in velocity were used to approximate turbulence intensity. Figure 2-6 depicts both horizontal and vertical turbulence intensity, in the boundary layer, are much stronger than that in the free stream, periodical fluctuating with phase in wave cycle. Moreover phase lag of turbulence identity peaks gradually increases as the turbulence transports from bottom out upwards to the free stream.

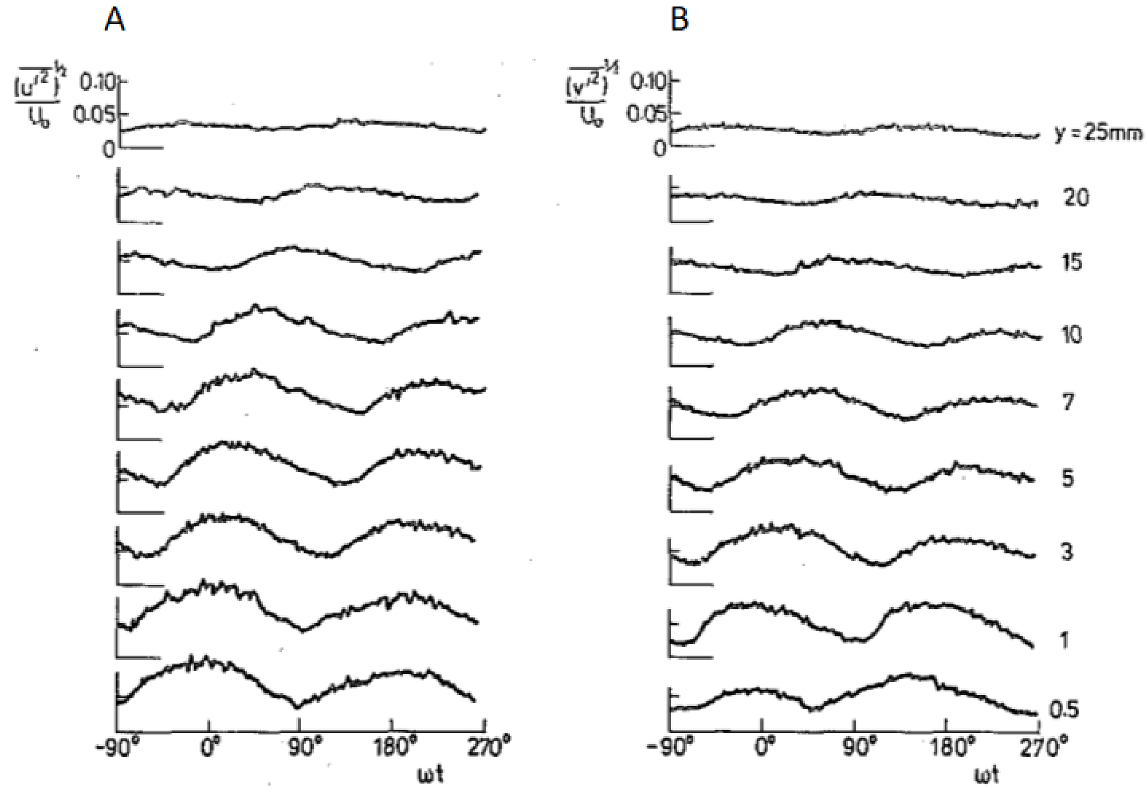

Figure 2-6. Horizonal (A) and vertical (B) turbulence intensity fluctuate in wave cycle and gradually tend to be gentle with height (from Sleath, 1987).

2.1.2.2 Wave-induced bed shear stress

As mentioned above, wave boundary layer is thin compared with current boundary layers. Herein, velocity shear in the wave-induced boundary layer is much larger than that in boundary produced by comparable magnitude current. In turn, wave-induced bed shear stress (τ_{w}) should be many times larger than current-induced bed shear stress (Soulsby, 1997). It could be computed from waves bottom orbital velocity ($\mathrm{U_w}$) and the wave friction factor (f_{w}).

$$\tau_{\mathrm{w}} = 0.5\rho f_{\mathrm{w}}\mathrm{U_w} \qquad 2\text{-}11$$

Earlier studies, indicated the wave friction factor, show this is closely related to wave hydraulic regimes (Myrhaug, 1989; Nielsen, 1992; Soulsby, 1997; Pedocchi and García, 2009a).

$$f_{\mathrm{w}} = \mathrm{f}\,(r, Re_{\mathrm{w}}) \qquad 2\text{-}12$$

where *r* ($\frac{A}{k_s}$) is relative roughness and *A* ($\frac{\mathrm{U_w T}}{2\pi}$) is semi-orbital excursion. Re_{w} ($\frac{\mathrm{U_w A}}{v}$) is the wave Reynolds number. The mathematical expressions to acquire the wave friction factor can be derived (e.g. Swart, 1974; Nielsen, 1992; Soulsby, 1997). Pedocchi and García (2009a) proposed a revised expression to estimate the wave friction factor for rough turbulent flow ($r > 30$; $Re_{\mathrm{w}} > 6.6 \cdot 10^4$), which is suitable for both laboratory and field conditions.

$$\frac{1}{\sqrt{f_{\mathrm{w}}}} = 1.9\ln\left(\frac{1}{1.5} r \sqrt{\frac{f_{\mathrm{w}}}{2}} L_{\mathrm{w}}\right) \qquad 2\text{- }13$$

where L_{w} is a parameter used in iterative loop

$$L_{\mathrm{w}}\left(\frac{u_{*\mathrm{w}}k_s}{v}\right) = \left\{\frac{1}{7.5}\left[1 - \exp\left(-\left[\frac{1}{90}\frac{u_{*\mathrm{w}}k_s}{v}\right]^2\right)\right] + \frac{1}{2.1}\frac{v}{u_{*\mathrm{w}_*}k_s}\right\}^{-1} \qquad 2\text{-}14$$

2.1.2.3 Vortex dynamics over rippled bed

Over the rippled bed of 1-2 ripple heights, instead of random turbulent mixing over flat bed, the spatially and temporally generated vortex at ripple lee side dominates sediment transport (Horikawa and Watanabe, 1970; Sleath, 1984; Ranasoma and Sleath, 1992; Ikeda et al., 1992). Many have examined the characteristics of the vortex over the past 40 years (e.g. Nakato et al., 1977; Toit and Sleath, 1981; Davies and Villaret, 1997; Voropayev et al., 1999; Admiraal et al., 2006; van der Werf et al., 2006; Li and Brian, 2007). With the passage of time the experimental instruments developed have progressively developed from hot-wire anemometer (Nakato et al., 1977; Sato et al., 1984) to laser Doppler anemometer (Horikawa abd Mizutani, 1992; Belorgey et al., 1993) to particle image velocimetry (van der Werf et al., 2006), increasingly precise measurement of near-bed velocity allow study of the detailed vortex formation and movement.

When the oscillatory flow moves onshore flow, vortex with anti-clock circulation is originated at the separation zone of lee side. In order to clearly show vortices trajectories, three vortices are numbered as shown in Figure 2-7. They are gradually strengthened in the first half wave cycle (Figure 2-7 1 and 2). Detailed experiments show the vortex is ejected just before flow reversal (e.g., Admiraal et al., 2006; van der Werf et al., 2006). After flow reversal to offshore, vortices are ejected upwards and tend to move along flow direction. Meanwhile new clock circulation vortices are formed cross the lee side as shown in grey (Figure 2-7 4 and 5). At the end of the second half of wave cycle, vortex 2 and 3 travel around one ripple length, approaching adjacent ripples (Figure 2-7 6). Significant controversy concerns the vortex travel distance. Based on the experiment with artificial ripples Earnshaw and Greated (1998) argued that the vortex is able to be advected as far as two or more wavelengths. However, Admiraal et al. (2006) disagreed and suggested the travel distance of a vortex should be smaller than two wavelengths. In the experiment of van der Werf et al. (2006), vortices moving around two ripple lengths were observed, but this may due to the asymmetrical wave velocity in this particular experiment. Before flow reversal from offshore to onshore, the newly formed vortices are ejected and repeated above mentioned vortex movement (Figure 2-7 from 6 to 3).

2.1.2.4 Turbulence modulation in clay-laden oscillatory flow

Studies that have investigated suspended clay influence in oscillatory flow and modulating turbulence are rare (Lamb et al., 2004; Lamb and Parsons, 2005). In the experiment of Lamb et al. (2004), the bed was dominated by silt-sized sediments, with clay and sand fraction reaching to 10% and 20%, respectively. Thus during experiments, high suspended sediment concentration was observed varying from 17-80 gL^{-1}, which contributes to stratification of suspended sediments. Lamb et al. (2004) highlighted that stratification is a limiting factor in vertical mixing of momentum leading to a significant reduction in boundary layer thickness. But, in contrast to studies that explore stratification effects on damping turbulence under unidirectional flow (e.g. Sheng and Villaret, 1989; Winterwerp, 2001), Lamb et al. (2004) argued stratification did not lead to turbulence suppression under wave forcing, instead resulting in an upward transport of turbulence, which leads to high suspended sediment concentration at relatively higher water column.

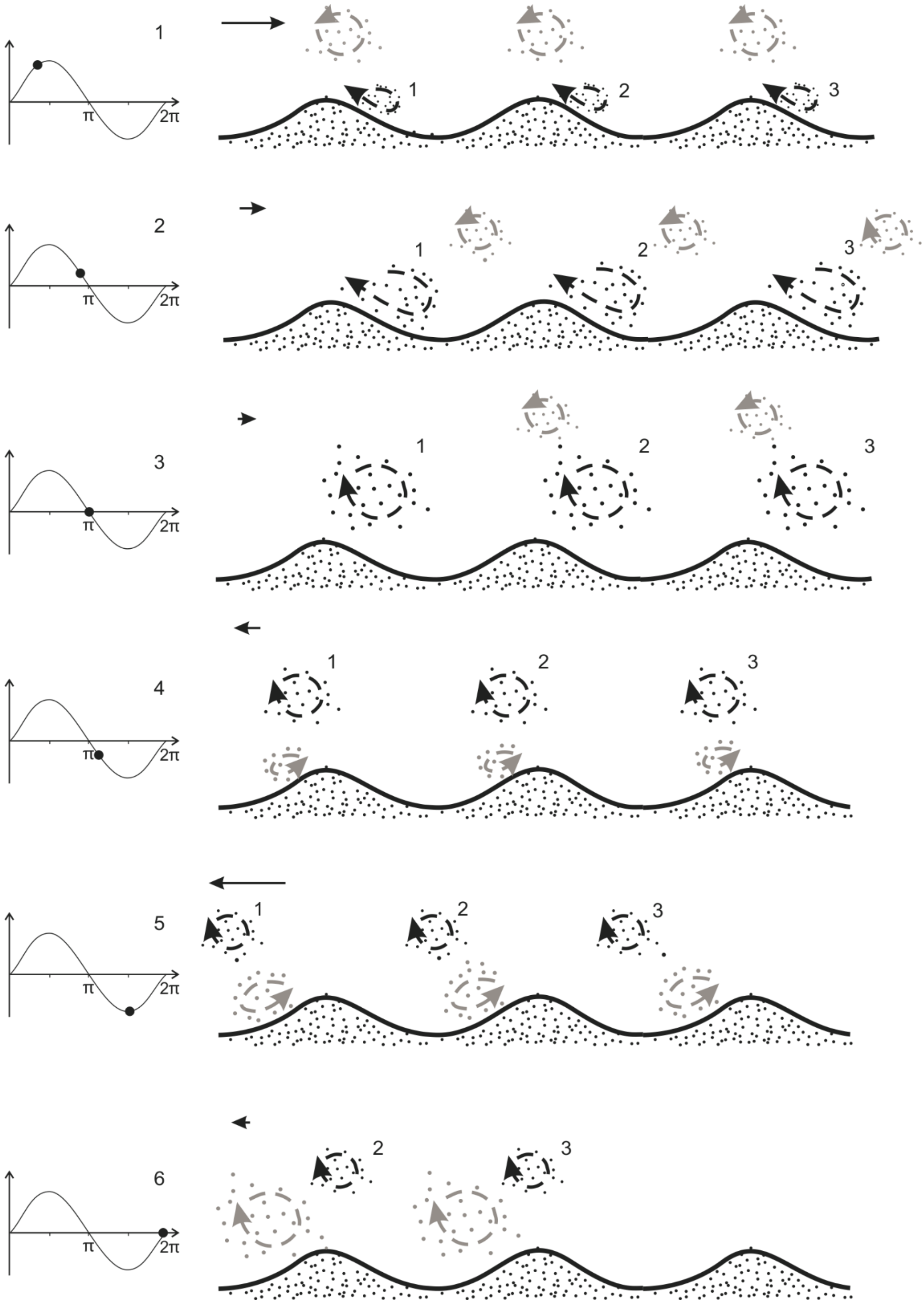

Figure 2-7. Diagram of vortex formation and transportation. The vortices with black dash lines are generated by onshore flow, while that are generated by offshore flow are represented by grey dash lines (based on Admiraal et al., 2006).

2.1.3 Combined flow

Combined flow concerns the two flow types discussed above, including oscillatory flow (wave) and unidirectional flow (current). In general, there are wave-dominated and current-dominated combined flows, which could be identified by comparing maximum shear stress at flow reversal (τ_{bmax}) with critical shear stress (τ_{cr}) for sediment entrainment (Perillo, 2014b). Wave-dominated flow is defined as τ_{bmax} is larger than τ_{cr}, otherwise, the combined flow is current-dominated flow.

2.1.3.1 Combined flow induced vortex over rippled bed

Compared with wave or current only flow, the interaction between waves and currents lead to a complex near-bed hydrodynamics system, which affect not only velocity profile and boundary layer, but also turbulent intensity (Bakker and van Doorn, 1978; Kemp and Simons, 1982; Grant and Madsen, 1979; Nap and van Kampen, 1988; Sleath, 1991; Ranasoma, 1993; Soulsby et al., 1993). Very close to the bed, there is a zone called inner region that waves and currents non-linearly interact (Ranasoma, 1993). Furthermore, Perillo (2013) concluded that the inner layer could be subdivided in to near-bed wave-dominated layer and a logarithmic layer. Above the inner layer, there is a current-induced boundary layer in which the influence of wave is tiny (Ranasoma, 1993).

The experiment of Kemp and Simons (1982) found that significant increase of turbulent intensity with ripples forming from flat bed, akin to pure wave flow, is dominated by periodical ejection of vortices. However, in contrast to symmetrical vortices generated across both ripple side, asymmetrical vortices are formed around the time of flow reversal since current superimposed within waves (Villaret and Perrier, 1992; Ranasoma, 1993; Fredsoe et al., 1999; Leeder, 2006; Li and O'Connor, 2007, Ojha and Mazumder, 2010). As shown in Figure 2-8, in the first half circle, wave is following with current direction, resulting formation of a large vortex with strong circulation at lee side. As a result, vortex carrying more suspended sediments is ejected when wave-induced flow reverse. While, during the second half, an opposite direction between wave and current generates a relatively smaller vortex.

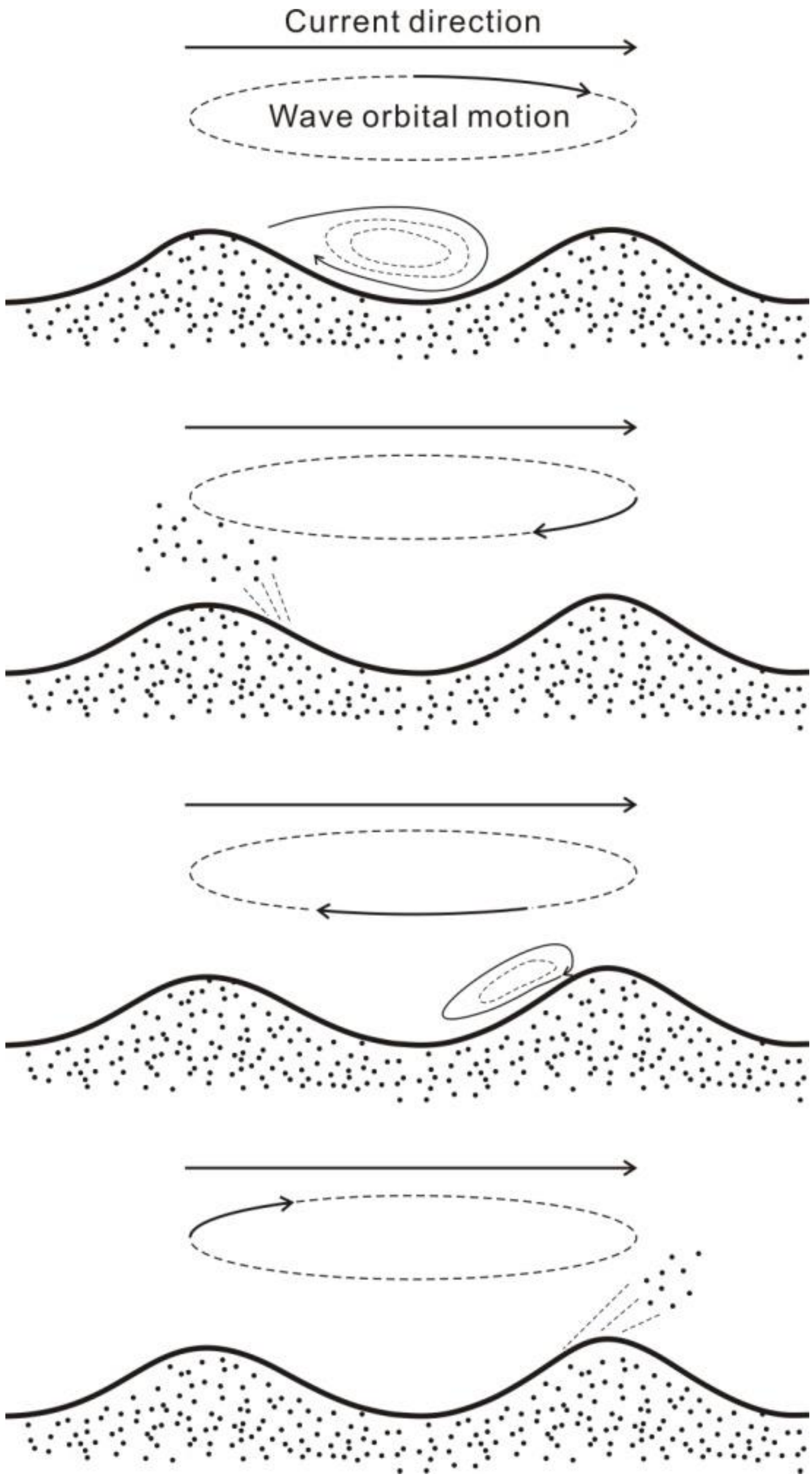

Figure 2-8. Assymmetric vortex generated under the combined flow (from Leeder, 2011).

2.1.3.2 Bed shear stress

Because of a non-linear interaction between waves and currents in the boundary layer, the combined flow induced bed shear stress could not be linearly added by the wave-induced and current-induced bed shear stress (Soulsby et al., 1993). A series of numerical models were proposed in order to approximate the mean and maximum near-bed shear stress (Bijker, 1967, Grant and Madsen, 1979; Christoffersen and Jonsson, 1985; Davies et al., 1988; Myrhaug and Slaattelid, 1990; Huynh-Thanh and Temperville, 1991). However, Soulsby (1995) examined the existing models using data set including 61 experimental data and 71 field data and indicated that all of models were poor to agree with collective data. Thus, Soulsby (1995) established a new model which is enable to fit data very well and a relationship between combined flow induced bed shear stress (τ_{b}) and wave alone induced bed shear stress (τ_{w}) and current alone induced bed shear stress (τ_{c}).

$$\tau_{\mathrm{bm}} = \tau_{\mathrm{c}}[1 + 1.2\left(\frac{\tau_{\mathrm{w}}}{\tau_{\mathrm{c}}+\tau_{\mathrm{w}}}\right)^{3.2}] \qquad 2\text{- }15$$

$$\tau_{\mathrm{bmax}} = [(\tau_{\mathrm{bm}} + \tau_{\mathrm{w}}\cos\varphi)^2 + (\tau_{\mathrm{w}}\sin\varphi)^2]^{0.5} \qquad 2\text{- }16$$

where τ_{bm} and τ_{bmax} are the mean and the maximum bed shear stress, respectively. φ is the angle between wave move direction and current direction.

2.2 Bed morphology

2.2.1 Introduction

Bedforms are topographic features that develop on sedimentary beds during periods when fluid force enables sediments to move. Bedform dynamics, sediment transport and turbulent flow constitute a dynamic system in the natural environment (Leeder, 2011). Bedforms are often characteristic to the forming flow parameters (Guy et al., 1966; Southard, 1991; Leeder, 2011), therefore being indicative of formative modern and ancient depositional environments (Schwartz, 1982; Clifton and Dingler, 1984; Schindler et al., 2015).

The origin of bedforms under unidirectional flow within pure sand and flat bed is controversial, but two models including defect initiation and instantaneous initiation are widely accepted (e.g. Raudkivi, 1963; Venditti, 2005). The defect initiation is found to occur under low flow velocity, leading to sporadic sediment transport (Simons and Richardson, 1961). The origin of defects are regarded as being related to turbulent sweeps, which are part of the turbulence bursting process (Best, 1992). Then small mounds of sediment are generated and finally bedforms are developed (Venditti et al., 2005). Under high flow velocity, the flume experiment of Venditti et al. (2005) observed another process of the initiation of bedforms. At beginning, a cross-patch pattern is formed once reaching threshold of initial motion of sediments, which results in developing chevron-shaped form that is an early form of ripple crest line. Finally, ripple crest lines evolve to two-dimensional structures and meantime bedform size develops as well. The whole process lasts only in seconds therefore defining as the instantaneous initiation.

The above mentioned two models of bedform initiation are also applicable for the bedforms origin under oscillatory flows (Perillo, 2013), although related studies are rare (Lofquist, 1978).

2.2.2 Bed morphology under unidirectional flow

2.2.2.1 Bedform phase diagrams

The bedforms with similar size and cross-section geometry constitute the *bed configuration* under flow condition in a given time. The ensemble of *bed configurations* generated under prescribed conditions of flow and sediment is the *bed state*. Bedform phases are used to identify different kind of bed states forming under a variety of flow velocities and grain sizes. Therefore, bedform phase diagrams are construct in order to predict bed states with known flow and sediments conditions (e.g. van den Berg and van Gelder, 1993). In addition, the phase diagrams are also helpful to reconstruct ancient depositional environments from known sedimentary structure persevered in rocks (Reineck and Singh, 2012).

In 1990s, seminal studies, such as Southard, van Rijn, van den Berg and van Gelder, constructed widely used phase diagrams for non-cohesive sediment. Southard (1991) collected a large number of flume experimental studies and established a classic phase diagram using dimensional variables of flow velocity and median grain size (Figure 2-9). The author emphasized the influence of water temperature change on the experimental results, therefore standardizing the dimensional variables to an arbitrary water temperature of 10°C. The arithmetic of standardization are shown as:

$$h_{10} = h(\mu_{10}/\mu)^{2/3} \qquad 2\text{-}17$$

$$U_{10} = U(\mu_{10}/\mu)^{1/3} \qquad 2\text{-}18$$

$$D_{10} = D(\mu_{10}/\mu)^{2/3} \qquad 2\text{-}19$$

where μ is the dynamic viscosities, h is water depth and symbols with the subscribe 10 denotes standardized parameters.

Phase diagrams with dimensionless parameters were constructed in order to reduce the overlap between bedform phases (e.g. van Rijn 1993; van den Berg and van Gelder, 1993). The phase diagram of van Rijn (1993) contained transport stage parameter (T) and particle diameter parameter (D_*).

$$T = (\tau_{0\mathrm{s}} - \tau_{cr})/\tau_{cr} \qquad 2\text{-}20$$

where $\tau_{0\mathrm{s}}$ is grain-induced bed-shear stress, τ_{cr} is the critical threshold of bed-shear stress for sediment transport.

$$\mathrm{D}_* = \mathrm{D}_{50}[(\rho_\mathrm{s}/\rho - 1)\mathrm{g}/v^2]^{1/3} \qquad 2\text{-}21$$

in which D_{50} is the median grain size of sediment, ρ_s and ρ are sediment and water density, respectively, g is gravity acceleration, and v is the kinematic viscosity of water.

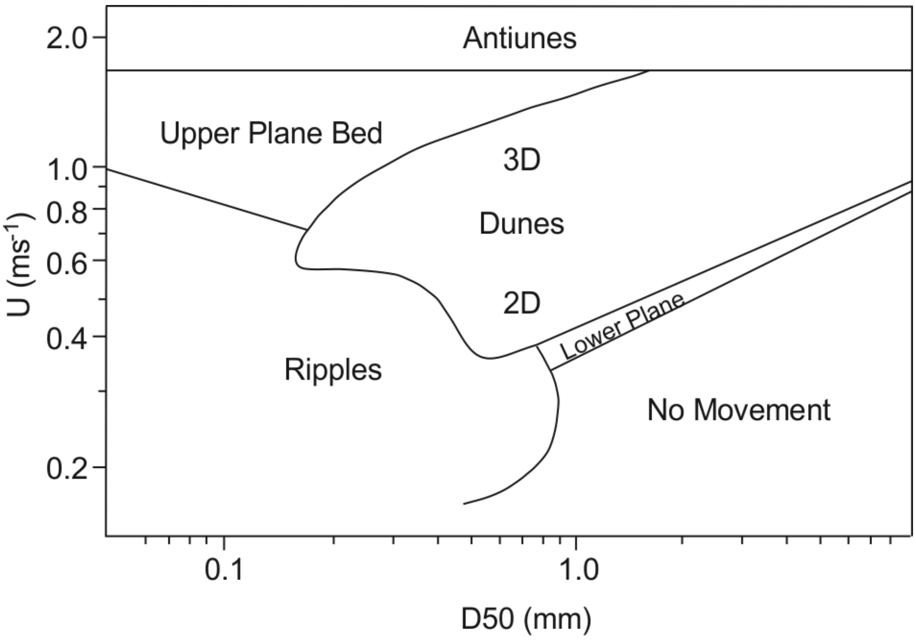

Figure 2-9. Unidirectional bedform phase diagram with dimesional variables that velocity against median grain size for flow depth between 0.25m-0.40m (Southard, 1991). It should be noted that the variables are standardized to water temperature of 10 Celsius degree.

Berg and van Gelder (1993) improved the earlier existing phase diagrams which were restricted to grain sizes larger than 100 μm (e.g. Allen, 2012) by introducing a new dimensionless current mobility parameter (θ'_{c}) linked to the grain roughness (Figure 2-10). In this phase diagram particle diameter parameter (D_{*}) is the same with van Rijn (1993) and the mobility parameter (θ'_{c}) is used to quantify flow strength and is calculated via the following equation.

$$\theta'_{c} = \rho\bar{u}^{2}/[(\rho_{s} - \rho)(C'^{2})D_{50}] \qquad 2\text{- }22$$

where $\bar{u}$ is the water-depth averaged flow velocity and C' is the Chézy drag coefficient related to grain roughness.

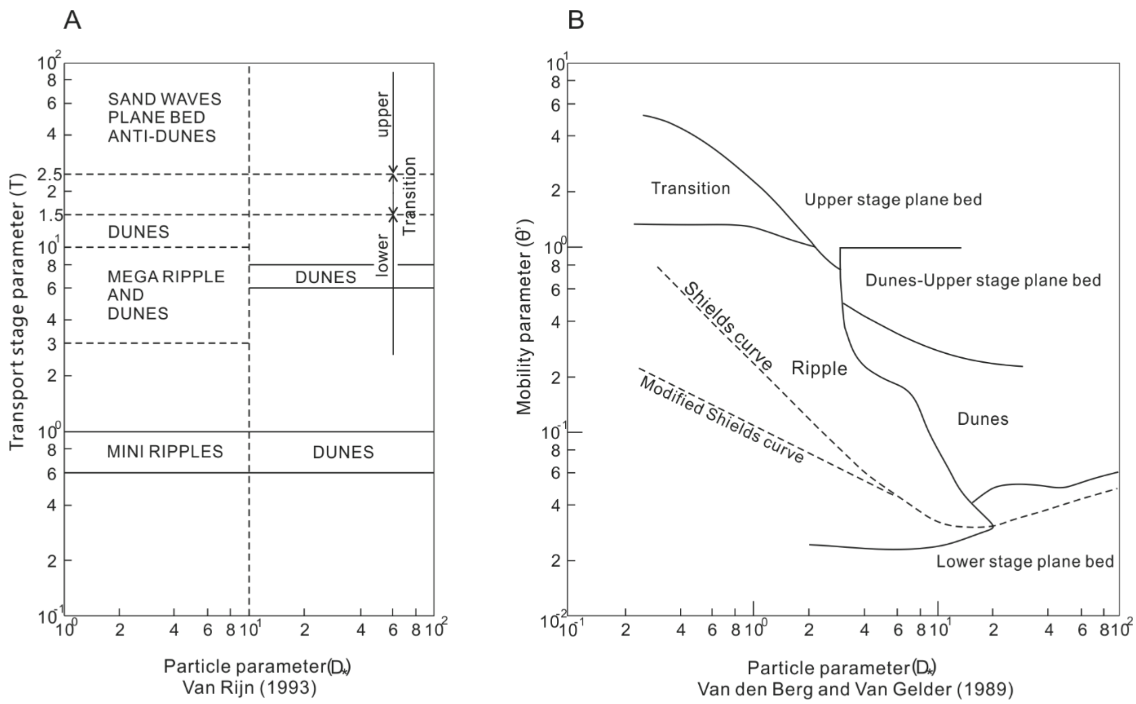

Figure 2-10. Phase diagram with the dimensionless parameters, A: Transport stage parameter (T) versus Particle parametr (D_*) by van Rijn (1993); B: Mobility parameter (θ'_c) versus Particle parametr (D_*) by Berg and van Gelder (1993).

2.2.2.2 Current ripples

Current ripples are one of the principal bedform types. They are rarely generated with coarse sand that median grain size exceeding 700 μm and at relatively high flow velocity (Figure 2-9). In contrast to larger-size bedforms, called dunes, ripple s tend to have dimensions of length (λ) and height (η) universally less than 0.5 m and 0.04 m, respectively (Leeder, 2011). Lapotre et al. (2017) introduced a new dimensionless parameter (Yalin number, χ) to discriminate ripples from dunes.

$$\chi = \frac{u_{*c}\mathrm{D}^{0.5}}{v\sqrt{\left(\frac{\rho_S}{\rho}-1\right)\mathrm{g}}} \qquad 2\text{-}23$$

The results show that ripples are commonly with $\chi < 4$ which is consistent with $\lambda = 60\ \mathrm{cm}$. Importantly, Yalin number reflects different physical development process between ripples and dunes (Lapotre et al., 2017). Conventionally, there is no relationship between ripple size and flow depth (e.g. Ashely, 1990; Leeder, 2011), however the latest study by Bartholdy et al. (2015) found that ripple height scales with flow depth. But a strong relationship between ripple size and grain size was revealed by the previous studies (e.g. Yalin, 1985; Baas, 1993). Baas (1993) improved function of Yalin (1985) and proposed the functions:

$$\lambda = 75.4 \log(\mathrm{D}_{50}) + 197 \qquad 2\text{- }24$$

$$\eta = 3.4 \log(\mathrm{D}_{50}) + 18 \qquad 2\text{- }25$$

Lapotre et al. (2017) updated the above relation between ripple length and grain size, emphasizing the role of flow properties as well.

$$\lambda = \frac{2504 v^{2/3} D^{1/6}}{[\left(\frac{\rho_s}{\rho} - 1\right) \mathrm{g}]^{1/6} u_*^{1/3}} \qquad 2\text{- }26$$

Current ripples could be either two-dimensional (2D) with straight and sinuous crest lines or three dimensional (3D) with curved linguoid crest lines (Figure 2-11). Additionally, current ripples could be described by cross-section geometry. Ripple index (RI), ripple symmetry index (RSI), and ripple roundness index (RRI) are frequently used dimensionless parameters.

$$\mathrm{RI} = \lambda/\eta \qquad 2\text{- }27$$

$$\mathrm{RSI} = \lambda_s/\lambda_l \qquad 2\text{- }28$$

$$\mathrm{RRI} = \lambda_{0.5s}/\lambda_s \qquad 2\text{- }29$$

where λ_s and λ_l are the length of ripple stoss side and lee side, respectively, $\lambda_{0.5s}$ is the distance between half height point to stoss side point, which is parallel with sedimentary bed (Figure 2-12). For the current ripples, typical RI ranges from 10 to 40 (Leeder, 2011), RSI is larger than 3 (Tanner, 1967), indicating an asymmetrical cross-section with a gentle stoss side and a steep lee side (30°- 35°), and RRI approximates 0.5 (Perillo, 2013).

Another kind of current ripples could be generated once the flow velocity is high enough but did not reach the threshold velocity for upper plane bed (Figure 2-10B, Southard and Harms 1972; Harms 1979; Joplin and Forbes, 1979; Bridge, 1981; Baas, 1994; Baas and De Koning, 1995). They are transitional ripples which are named as washout ripples as well, because the formation process is closely related to be washed out (Southard and Harms 1972). Washout ripples trains are sinuous and flat in plan-view since same ripple lengths as ripples forming under lower velocities and smaller ripple heights (Figure 2-11; Harms, 1979; Baas and de Koning, 1995). In profile, symmetrical washout ripples are significantly different from 2D ripples or linguiod ripples, with round crest and low lee side slope angle (Harms, 1979; Joplin and Forbes, 1979), which results from a spatial shift of maximum sediment flux from the ripple crest to the downstream wake region (Baas and de Koning, 1995). Furthermore, the high suspended sediment concentration was observed experiments under relatively higher flow velocity during flume (Lowe, 1988; Bridge and Best, 1988; Baas and de Koning, 1995). It directly contributes to increase flow viscosity, therefore supressing vertical turbulence and preventing height of washout ripple growth (Allen and leeder, 1980; Baas and de Koning, 1995).

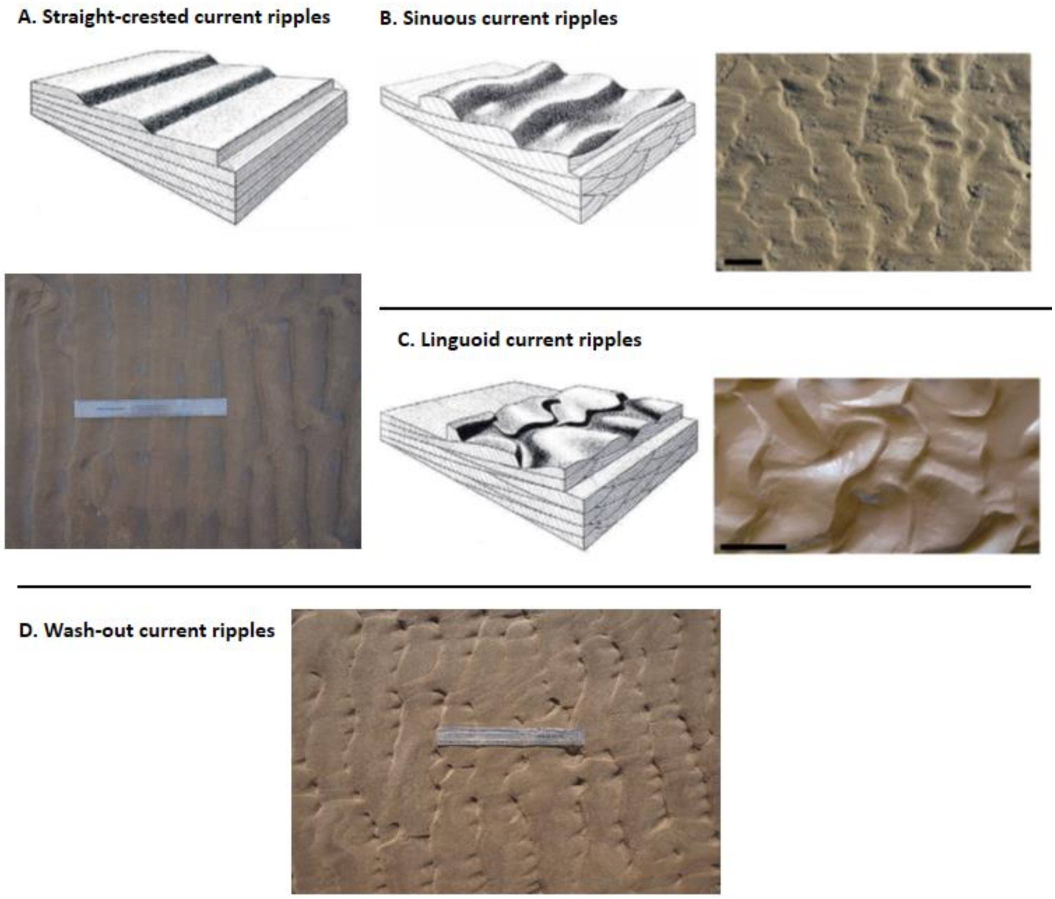

Figure 2-11. Schematic drawings (from Baas et al., 2015) and examples of ripples foming with cohesionless sands under current flows. A. Straight-crested current ripples; the field example is from the Red Cliff sand bar located in the upper Humber estuary, NE England. B. Sinuous current ripples. C. Linguoid current ripples. The details of examples of sinous and linguiod ripples see Figure 3 of Baas et al. (2015). D. Wash-out current ripples. The example is from the Red Cliff sand bar as well.

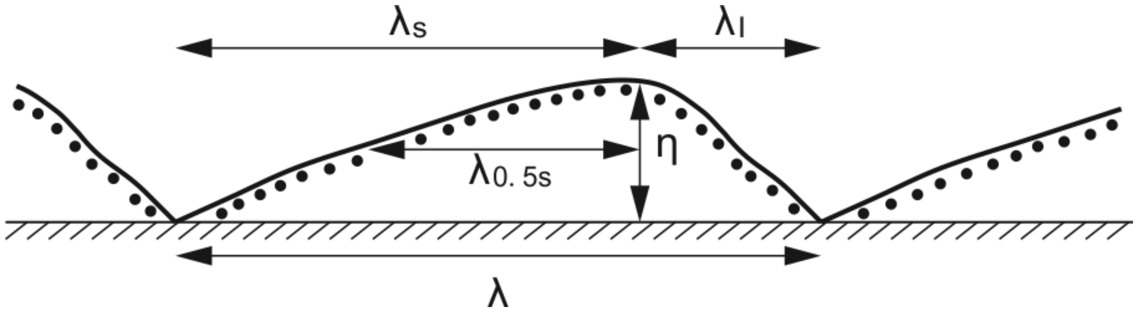

Figure 2-12. Current ripple cross-esction geometry

2.2.2.3 Current ripples evolution over noncohesive sands

Seminal work of Baas (1993, 1994, and 1999) focused on ripple evolution from the non-cohesive flat bed to reaching equilibrium, providing detailed information to fully understanding ripple dynamics. This process, that is independent with flow velocity, begins when the sediments are eroded and transported at very start of the experiment, forming the small incipient ripples (Stage 1, Figure 2-13). The incipient ripples progressively expand and grow up to two-dimensional ripples trains covering the whole flume with straight and sinuous crestlines (Stage 2, Figure 2-13). In the next stage, two-dimensional ripples transform to linguiod three-dimensional ripples, with significant increasing of ripples size (Stage 3, Figure 2-13). Finally, the linguiod ripples attain equilibrium without increase of ripple lengths and heights (Stage 4, Figure 2-13). Based on the above mentioned progress of ripples development, Baas (1994) developed classical equations to acquire equilibrium time and equilibrium size.

$$\frac{\eta_t}{\eta_e} = 1 - (0.01)^{t/T_\eta} \qquad \text{2- 30}$$

$$\frac{\lambda_t - \lambda_0}{\lambda_e - \lambda_0} = 1 - (0.01)^{t/T_\lambda} \qquad \text{2- 31}$$

where η_t and λ_t are the ripple height and length at time t, η_e (equilibrium height), λ_e (equilibrium length), T_η (equilibrium time for height), T_λ (equilibrium time for length), and λ_0 (initial ripple length) could be computed by using the nonlinear fitting. 0.01 means 99% of ripples reach equilibrium and sometimes 90% (0.1) of the ripples reaching equilibrium is acceptable according to experimental duration (Baas et al., 2013).

Moreover, Baas (1994) revealed that the inverse relation between the equilibrium time and the flow velocity.

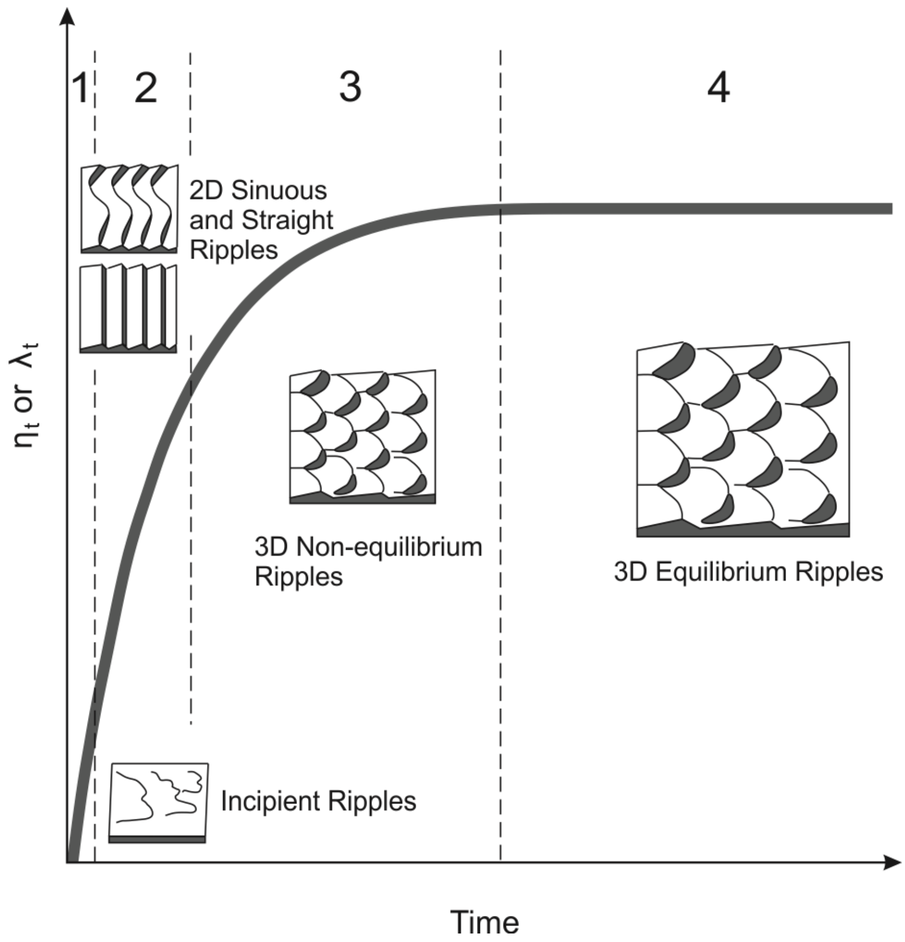

Figure 2-13. Conceptual model of four stages of ripple development under unidirectional flow. The dash lines denote bondaries between stages (modified after Baas, 1999).

2.2.2.4 Current ripples with sand-clay mixture

Rather than pure sand ripples, a number of studies have been gradually focusing on ripples development within bed mixtures of cohesive clay and cohesionless sand (e.g. Basaniak and Verhoeven, 2008; Baas et al., 2013; Schindler et al., 2015; Ye, 2016). Clay particles, characterised by electrochemical cohesion are able to attract each other by van der Waals forces (Grabowski et al., 2011). Laboratory studies found that adding cohesive clay into the bed substrate is as a key element in increasing the bed yield strength, therefore stabilizing the bed (Grissinger et al., 1981; Whitehouse et al., 2000; van Ledden et al., 2004; Jacobs et al., 2011). However, the threshold of clay content for transition from non-cohesive bed to cohesive bed is controversial, with wide ranging from only 0.18% to extremely high 30% by weight (Dyer, 1986; Nalluri and Alvarez, 1992; Torfs, 1994; Mitchener and Torfs, 1995; Panagiotogoulos et al., 1997; Bartzke et al., 2013). Apart from cohesive nature of clay particles, sedimentary texture is changed by adding fine clay into coarse sands, leading to bed stabilization (Panagiotogoulos et al., 1997; Hir et al., 2008; Hir et al., 2011; Bartzke et al., 2013). Notably, Bartzke et al. (2013) proposed a 'blocked layer' structure in which the small clay particles completely fill the pore space. Therefore this texture enable to prevent flow into sediments and to enhance bed stability.

In terms of the influence of cohesive clay on current ripples, the pioneering flume experiment, with the clay fractions up to 18%, of Baas et al. (2013) quantified the rate of ripples development over clay-sand mixed substrates and furthermore discovered the relationship between ripple dimension and initial bed clay fraction. The remarkable experimental results highlighted that increasing clay fraction significantly delayed the first appearance of current ripples, and importantly ripple size dramatically decreased with clay fraction over 13% (Baas et al, 2013). In addition, a large flume experiment, with 2 m width and 10 m length, was conducted in order to examine availability of existing predictors for bedforms forming from cohesive bed (Schindler et al., 2015; Ye, 2016). Schindler et al. (2015) revealed the prominent inverse relationship between bedform size and initial bed clay fraction (Figure 2-14) and emphasized over-prediction of the present models for cohesive bedform size.

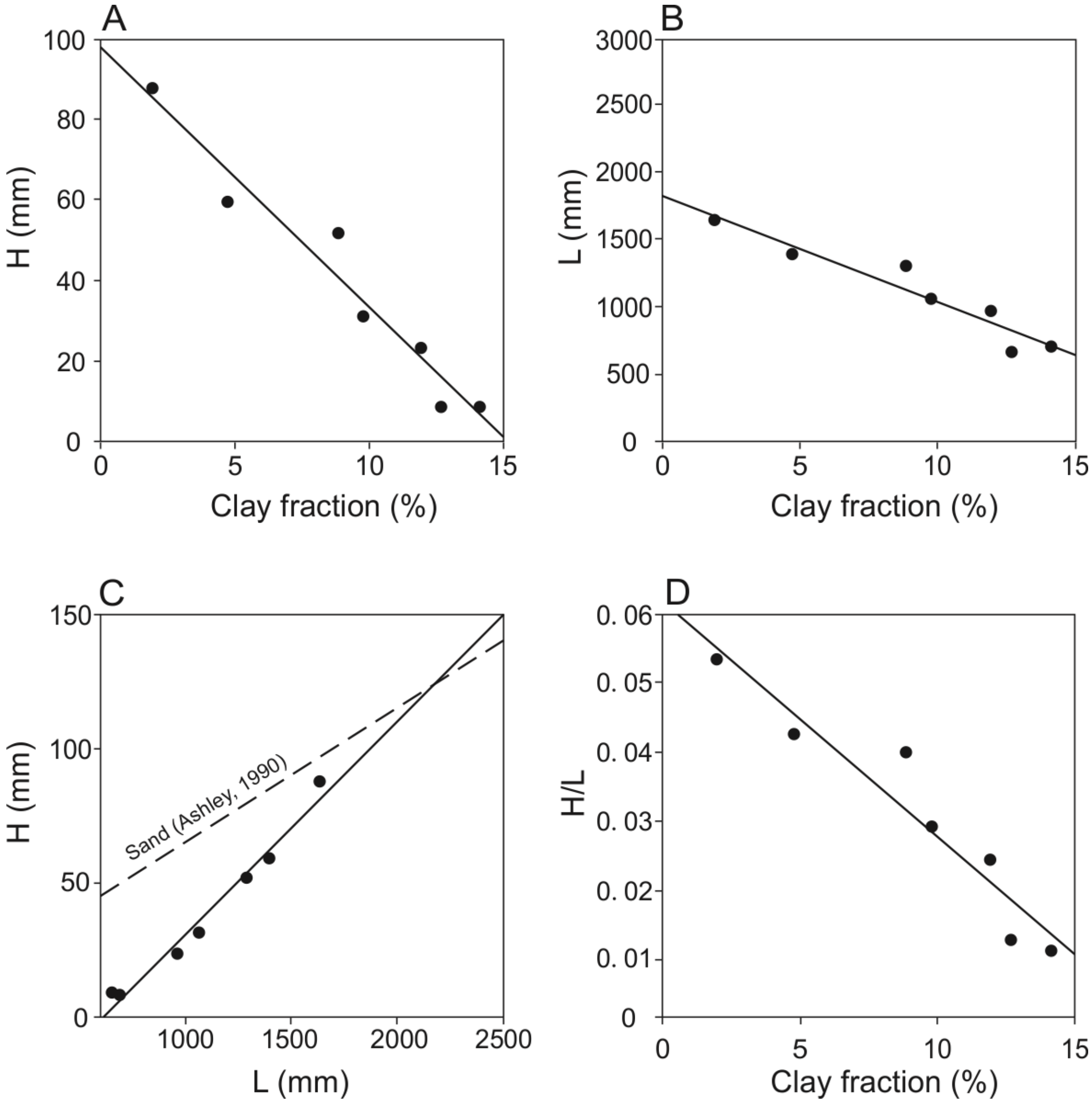

Figure 2-14. Relationship between initial clay fraction and bedform height (A), bedform length (B), and steepness (D), respectively. C: The predicted result for pure sand based on Ashley (1990) is examined by the measured length and height (modified after Schindler et al., 2015).

2.2.3 Bed morphology under oscillatory flow

2.2.3.1 Phase diagram

Akin to the phase diagram of current-induced bedforms, both dimension and non-dimension variables are used. Allen (1984) collected a large number of laboratory and field data and established a classical bedform phase diagram, using maximum orbital velocity and sediment particle diameter. Three bed states are defined in the phase diagram: no movement, wave ripples and upper plane bed. The regime of wave-induced ripples is dominated while large scale bedforms (e.g. dunes) in the current-induced bedforms phase diagram are absent. In specialty, the author highlighted ripple index as a function of these two dimensional variables, wave ripples becoming much more flat with increase of grain size and maximum orbital velocity (Figure 2-15).

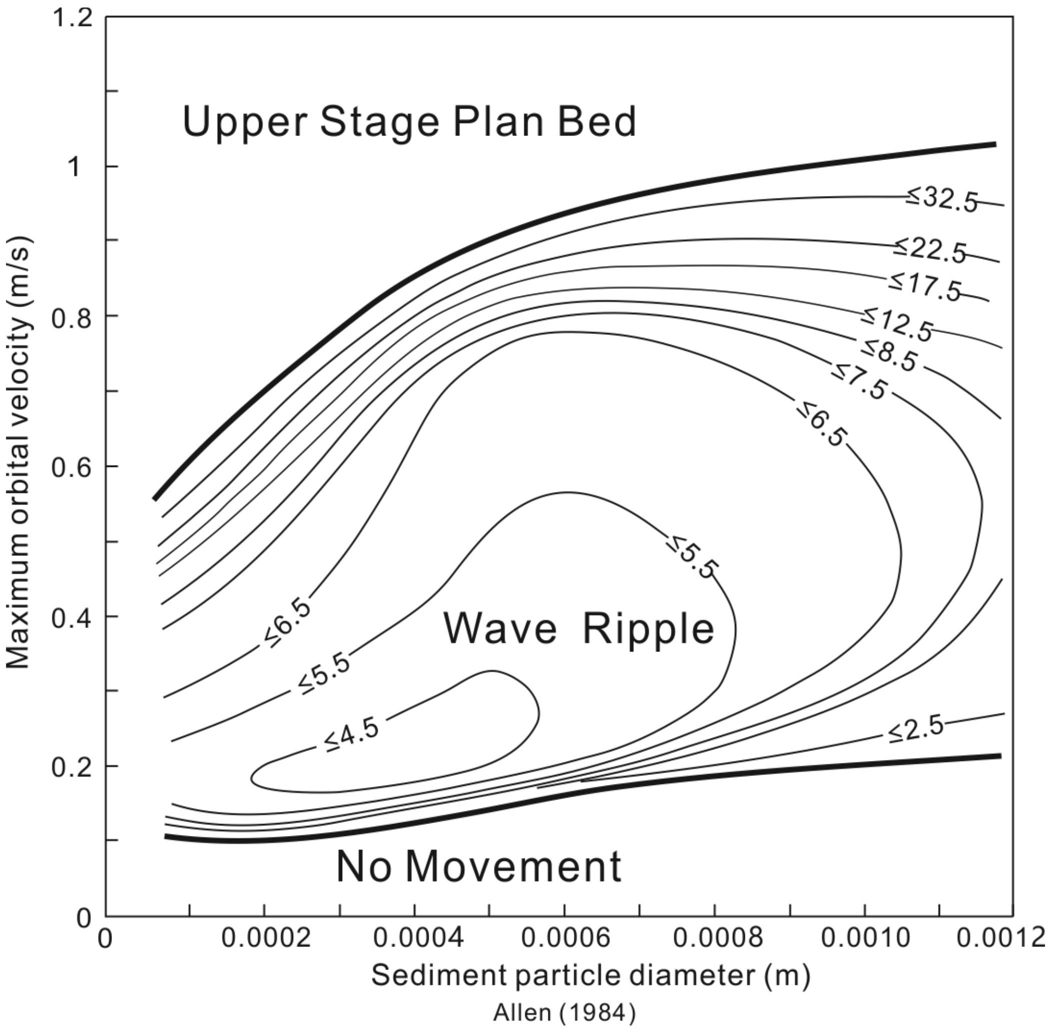

Figure 2-15. Phase diagram for wave-induced bedforms; the contour lines represents ripple index (modified after Allen, 1984).

The bedform phase diagram of Southard (1991) selected maximum orbital velocity on the ordinate and wave period on the abscissa for fine and coarse sediments (Figure 2-16). It is should be noted that the boundary between ripples and no movement is not clear without documented data. For the fine sediment (0.1 mm<D_{50}<0.2 mm), two dimensional ripples gradually transformed to irregular three dimensional ripples which are absent in coarse sediments (Figure 2-16 A). Furthermore, it is obvious that the ripple regime expands towards higher velocity with coarse sands (Figure 2-16). As far as ripple size is concerned, as shown in Figure 2-16 ripple length (dot and dash line) tends to gradually rise with velocity and wave period increase and to scale with wave orbital diameter (dot line).

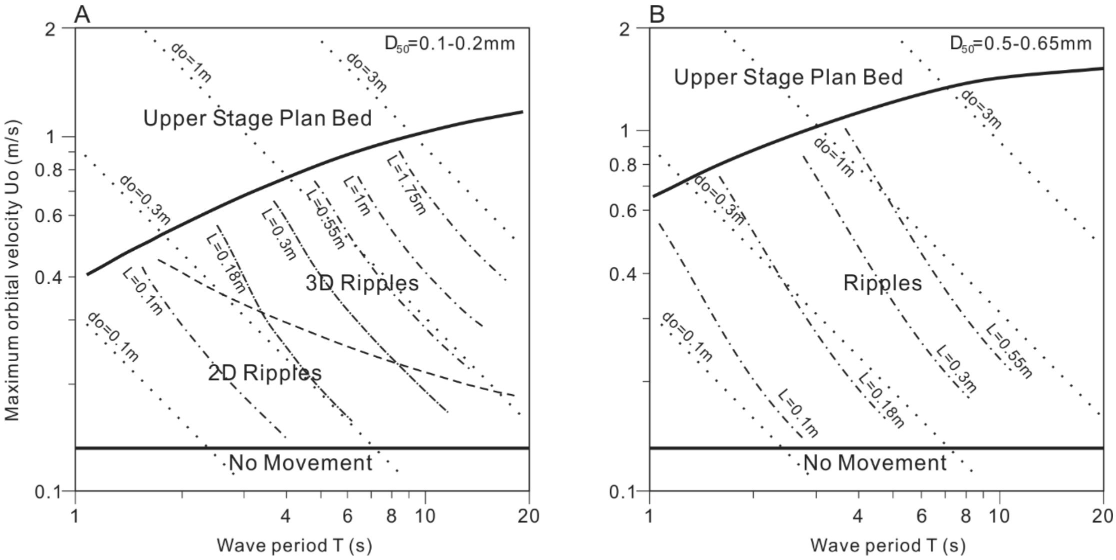

Figure 2-16. Oscillatory bedforms phase diagram with dimesnional variables that maximum orbital velocity (U_0) versus wave period (T). The boudary between ripples and no movement is vaguely defined since lack of data. A: for fine sedments with median grain size (D_{50}) is betwwn 0.1 and 0.2mm; B: for coarse sediment with median grain size (D_{50}) is betwwn 0.5 and 0.65mm. It should be noted that the variables are standardized to water temperature of 10 Celsius degree. The contour dot lines and the contour dot and dash lines denote orbital diameter (d_o) and ripple length, repectiely. The dash line denotes boudary between regimes of 2D ripples and 3D ripples (modified after Southard, 1991).

In contrast to traditional phase diagrams based on laboratory and field datasets, Kleinhans (2005) presented a non-dimensional bedform phase diagram according to bed state predictors. The dimensionless variables are particle diameter parameter (D_*) acquired from equation (Equation 2-21) and wave mobility parameter (θ'_w) that is calculated by using maximum orbital velocity to replace depth-averaged velocity in equation (Equation 2-22). In the phase diagram of Kleinhans (2005), the boundary between no movement and ripples is derived from Zanke model (Zanke, 2003) and the model of Allen-Leeder (Allen and Leeder, 1980) is selected for the transition from ripples to upper stage plan bed (Figure 2-17). Moreover, Kleinhans (2005) highlighted the existence of hummocks that are neglected in Allen's phase diagram.

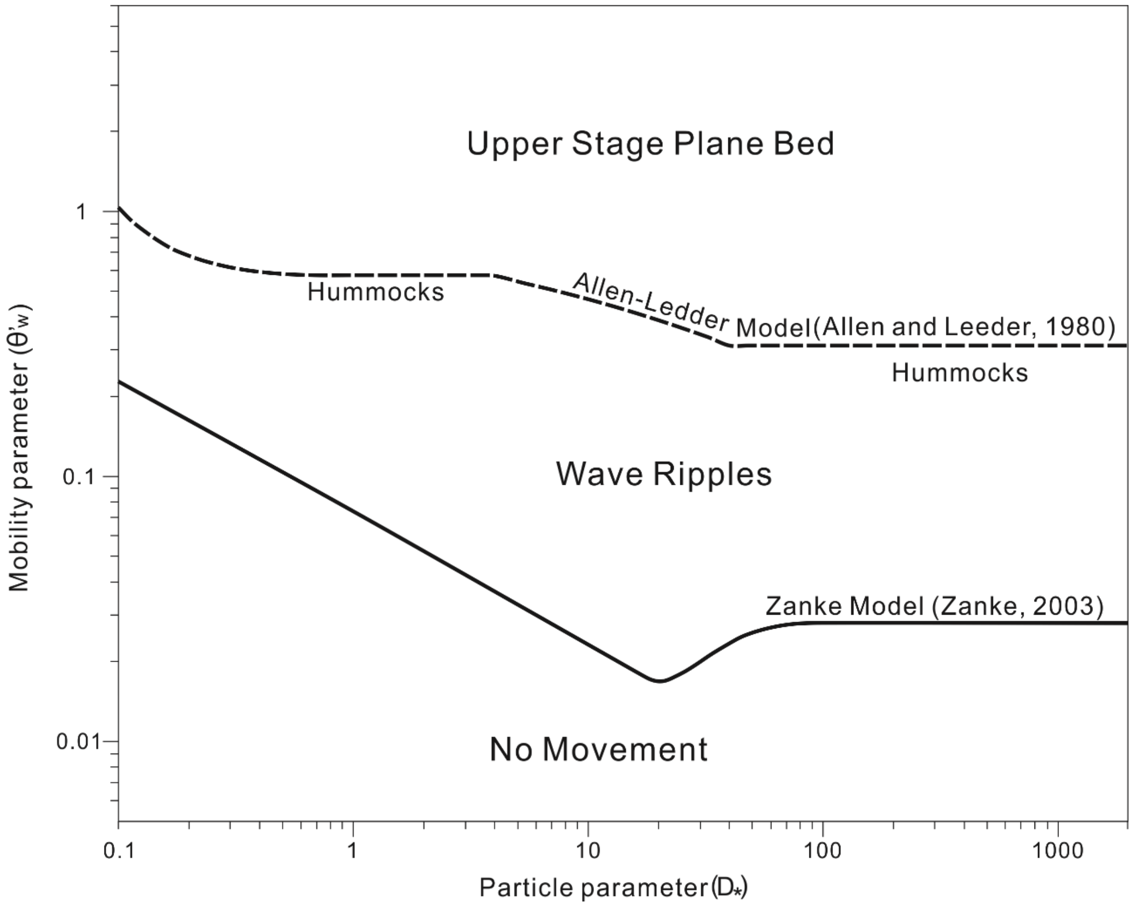

Figure 2-17. Non-demisional wave phase diagram based on bed state predictors. The black line denote incipient motion model of Zanke (2003), and the balck dash line denote model of Allen and Leeder (1980) to predict transifition of upper satge plan bed (modified after Kleinhans, 2005).

2.2.3.2 Wave ripples

Sediments start to move back and forth once wave-induced bed shear stress meet threshold of initial motion, immediately forming small grain ripples on flat bed. Bagnold (1946) firstly observed development of the rolling grain ripples with rolling grains resting in parallel bands. Andersen (2001) argued a 'shadow zone' that is shielded from wave action is formed at lee side of each band. The shadow zone enable more grains to rest at bands and few grains to be entrained, therefore bands growing to ridges that the rolling grain ripples. With increasing size of ridge, the shadow zone develops as well until extends as far as the next rolling grain ripple. As a result, no more grains could be lifted from the larger shallow zone and rolling grains ripples tend to be stable. The cross-section geometry of rolling grain ripple is triangular, with spacing smaller than 1 cm (Andersen, 2001) and height smaller than 20 grain diameters (Leeder, 2011). Andersen

(2001) developed a numerical model in order to quantify the evolution of rolling grain ripples from flat sand bed. This model describes particle motion and accurately characterizes the length of the shadow zone. The results of Andersen (2001)'s model reveal the proportional relationship between rolling grain ripple size and non-dimensional shear stress ($\theta = \tau_{\mathrm{w}}/[\rho(\rho_s - 1)\mathrm{g}\mathrm{D}_{50}]$).

The above mentioned stable state is broken down with higher oscillatory velocities that exceed twice of the threshold velocity for initial motion. Under this circumstance, the lee slope of the ripples gradually become steeper and meantime to-and fro flow contributes to formation of vortex on each ripple side, generating the vortex ripples (Bagnold, 1946). Academically the terminology vortex ripples are widely replaced by orbital ripples (see later section) or wave ripples.

In terms of size of wave ripples, the length of small wave ripple is commonly shorter than 30 cm, while others with length larger than 30 cm are called large wave ripples (Hanes et al., 2001). Similar to the current ripples, wave ripples could be two-dimensional of three-dimensional in plan view. In general, two-dimensional wave ripples have straight or sinuous crest lines. However, compared with 2D ripples forming under current, 2D wave ripples are symmetrical of cross-section geometry with RSI approaching 1 (Clifton and Dingler, 1984). The shapes of three-dimensional wave ripples are irregular, with short crestlines. Sediment size, maximum near-bed orbital velocity and wave orbital diameter are regarded as three vital elements affecting wave ripples geometry (Cummings et al., 2009).

Cummings et al. (2009) suggested sediment grain size is the first-order to control wave ripple shape. Over the fine sands ($D_{50} = 0.12\ \mathrm{mm}$), firstly oscillatory motion generated small wave ripples, evolving to large wave ripples with increasing maximum orbital velocity. But only large wave ripples were observed on the coarse sand bed ($D_{50} = 0.8\ \mathrm{mm}$).

The transition from 2D ripples to 3D ripples seems to be strongly related to finer grain size and longer wave period (Vongvisessomjai, 1984; Southard, 1991; O'Donoghue and Clubb, 2001; O'Donoghue et al., 2006; Pedocchi and García, 2009b). As shown in Figure 2-16, under the conditions of the same wave velocity, 3D ripples are more likely generated with fine sediments under a longer wave period.

2.2.3.3 Wave ripples evolution with noncohesive sands

Wave ripple development from a flat bed to equilibrium has been studied a number of times (Faraci and Foti, 2002; Doucette and O'Donoghue, 2006; Perillo, et al., 2014b). The experiment of Faraci and Foti (2002) revealed two development stages including rolling grain ripples and vortex ripples, which are consistent with previous research (Bagnold, 1946; Andersen, 2001). Doucette and O'Donoghue (2006) found 2D small ripples ($\eta < 10\ \mathrm{mm}, \lambda = 120\ \mathrm{mm}$) were firstly appeared and then evolved to 3D ripples with vortex formation, followed by equilibrium 2D ripples. Perillo et al. (2014b) confirmed that wave ripples experience four stages until they attain equilibrium, including incipient stage, growing stage, stabilizing stage and fully-developed stage. Incipient stage starts from initial sediment movement until the bed is mostly covered by the two-dimensional rolling grain ripples. Then the individual ripple size significantly increases, transforming to three dimensional vortex ripple. Next stage is stabilizing stage in which the growth rate of ripple remarkably declines. Finally, wave ripple acquires equilibrium with ripple length and height slight fluctuating around equilibrium values. Both 2D and 3D ripples are detected in the equilibrium stage, whereas the equilibrium ripples forming under unidirectional flow are only three dimensional.

2.2.3.4 Predicting wave-induced ripple geometry

Several existing planform geometry predictors (e.g., Carstens et al., 1969; Vongvisessomjai, 1984; Sato, 1987), that were constructed only with laboratory datasets, are unable to accurately discriminate between 2D ripples and 3D ripples, especially for the field observations. Pedocchi and García (2009b) collected a large amount of laboratory data and field data and established a new model which indicates ripples tend to be two-dimensional if

$$Re_p > 0.06\sqrt{Re_w} \qquad 2\text{-}32$$

where Re_p is the non-dimensional particle size and Re_w is the wave Reynolds number.

$$Re_p = \sqrt{g(\rho_s - \rho)D_{50}}D_{50}/v \qquad 2\text{-}33$$

$$Re_w = \mathrm{U_{max}}A/v \qquad 2\text{-}34$$

The authors emphasized the criterion is available for the coarse sediments that $Re_p \geq 13$ while it fails to provide clear division with fine sediments ($Re_p < 9$).

Previous studies (e.g. Inman, 1957, Clifton, 1976; Miller and Koman, 1980; Clifton and Dingler, 1984; Wiberg and Harris, 1994; Cummings et al., 2009) also found a strong relationship between wave ripple length (λ) and wave orbital diameter (d_o). Based on the relationship, wave ripples could be categorized into three types.

i) Orbital ripples: length is scaled with wave orbital diameter (Equation 2-35). Clifton and Dingler (1984) indicated the orbital ripples exist if d_o/D ranges between 100 and 3000 (Figure 2-18).

$$\lambda = 0.65 d_o \tag{2- 35}$$

ii) Anorbital ripples: length is independent with wave orbital diameter, but is proportional to grain size (Equation 2-36, Wiberg and Harris, 1994). Such ripples are most likely formed on the fine sandy beds, with d_o/D exceeding 5000 (Figure 2-18).

$$\lambda = 535\mathrm{D} \tag{2- 36}$$

iii) Suborbital ripples: ripple length is inverse of increasing orbital diameter and is dependent with grain size as well. The suborbital ripples are commonly observed in the region that d_o/D transiting from 1000 to 3000 (Figure 2-18).

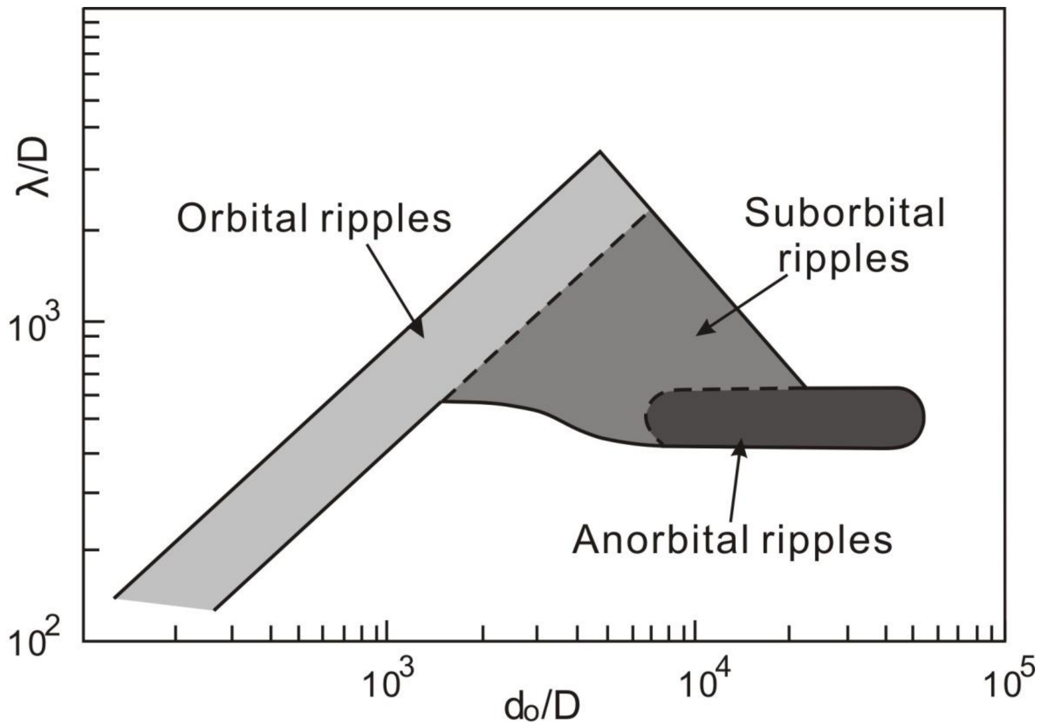

Figure 2-18. Orbital ripples, suborbital ripples and anorbital ripples distribution in the plot of dimenionless d_o/D versus λ/D (from Clifton and Dingler, 1984).

In addition, Wiberg and Harris (1994) confirmed a relation between ripple height (η) and wave orbital diameter and proposed a new criteria to class wave ripple types as following.

$$d_o/\eta < 20 \text{ Orbital ripples} \qquad 2\text{-}37$$

$$20 < d_o/\eta < 100 \text{ Suborbital ripples} \qquad 2\text{-}38$$

$$d_o/\eta > 100 \text{ Anorbital ripples} \qquad 2\text{-}39$$

Predicting equilibrium size of wave-induced ripples has also attracted a range of investigations (Komar, 1974; Nielsen, 1981; Grant and Madsen, 1982; Van Rijn, 1993; Mogridge et al., 1994; Wikramanayake and Madsen, 1994; Styles and Glenn, 2002; Faraci and Foti, 2002; Grasmeijer and Kleinhans, 2004; Soulsby and Whitehouse, 2005; Traykovski, 2007; Pedocchi and García, 2009a; Nelson et al., 2013). The existing models try to precisely predict equilibrium ripple dimensions for known sediments and wave conditions, therefore creating non-dimension parameters according to wave properties and sediment characteristics, such as dimensionless oscillation period ($\mathrm{T}v/D_{50}^2$), Re_p (Equation 2-33), sediment Reynolds number ($Re_d = \mathrm{U_w D_{50}}/v$). Nelson et al. (2013) examined the existing models by database constituted of earlier and relatively new experimental data and field data and revealed these predictors fail to fit database well. For example, models of van Rijn (1993) and Grasmeijer and Kleinhans (2004) are unable to predict lengths of ripples forming under large wave condition. Besides that models of Nielsen (1981), Faraci and Foti (2002) also heavily deviate the data of ripple height when wave force is large. Hence, Nelson et al. (2013) proposed new predictors to establish relation between ripple length and wave orbital amplitude (A) and median grain size (D_{50}) for both regular and irregular waves, which show a great agreement with the new dataset.

For regular waves:

$$\lambda = 6.76A^{0.68}D_{50}^{0.32} \qquad 2\text{-}40$$

For irregular waves:

$$\lambda = 2.22 \times 10^3 \cdot A^{-0.11}D_{50}^{1.11} \qquad 2\text{-}41$$

2.2.4 Bed morphology under combined flow

2.2.4.1 Phase diagram

In the 21st century, there was a paucity of research focusing on bedforms formed under combined flow (Inman and Bowen, 1963; Harms, 1969; Brevik and Aas, 1980; Arnott and Southard, 1990). Arnott and Southard (1990) drew a graph of U_u versus $\mathrm{U_w}$ with single sediment size ($\mathrm{D}_{50} = 0.09\mathrm{mm}$) and wave period (T=9.5s) to reflect relation between bedforms and combined flow. Until recently, an increasing number of studies involved this field and gradually improved our knowledge for combined flow bedform phase diagram (e.g. Yokokawa et al., 1995; Dumas et al., 2005; Kleinhans, 2005; Sekiguchi and Yokokawa, 2008; Perillo et al., 2014). In general, unidirectional velocity (U_u) and maximum orbital velocity ($\mathrm{U_w}$) are the most commonly used dimensional variables combined flow bedforms phase diagram. Dumas et al. (2005) conducted a series of flume experiments to stimulate bedorms generating under storm condition, therefore combined flow bedforms with wave velocity varying from 0 to 120 cms^{-1} and current velocity restricting under 25 cms^{-1} (Figure 2-19). The phase diagram contains four bed states including no movement, combined flow generated ripples (details of classification see below section), hummocks, and upper stage plan bed. Especially reverse large ripples are appeared with median grain size of 0.22 mm and 10.5 s of wave period (Figure 2-19C). Furthermore, the phase diagram shows the influence of wave period and grain size on the bedform phase distribution. The shorter wave period results in bedform phase forming at lower velocities (Figure 2-19 A and B), and the coarser grain size significantly expands ripples regime towards higher oscillatory (Figure 2-19 B and C). Perillo et al. (2014) bridged the gap of knowledge combined flow bedform generating with unidirectional velocity larger than 0.3 ms^{-1} and with intermediate wave periods (2-8s). It should be noted that the terms ''dune'' in the phase diagram is used to describe large ripples (Figure 2-20). Additionally, Figure 2-20 (A, B and C) highlights that three phase diagrams are similar, also indicating the minor influence of small period changes (increases from 4s to 6s) on the bed state. Kleinhans (2005) selected non-dimensional current mobility parameter (θ'_{c}) on the abscissa and non-dimensional wave mobility parameter (θ'_{w}) on the ordinate (Figure 2-21). The region of combined flow induced ripple prevails in the phase diagram with averaged grain size of 0.21 mm. Moreover, the authors use the following two criterions to assess wave or current force intensity on bedforms.

If bedforms are only generated under pure wave conditions then,

$$\theta'_{\mathrm{c}} < 0.2\theta'_{\mathrm{w,cr}} \qquad 2\text{- }42$$

If bedforms are only generated under pure wave conditions then,

$$\theta'_{\mathrm{w}} < 0.2\theta'_{\mathrm{c,cr}} \qquad 2\text{- }43$$

Where $\theta'_{\mathrm{w,cr}}$ and $\theta'_{\mathrm{c,cr}}$ are the critical wave and current mobility parameter derived from the model of Zanke (2003).

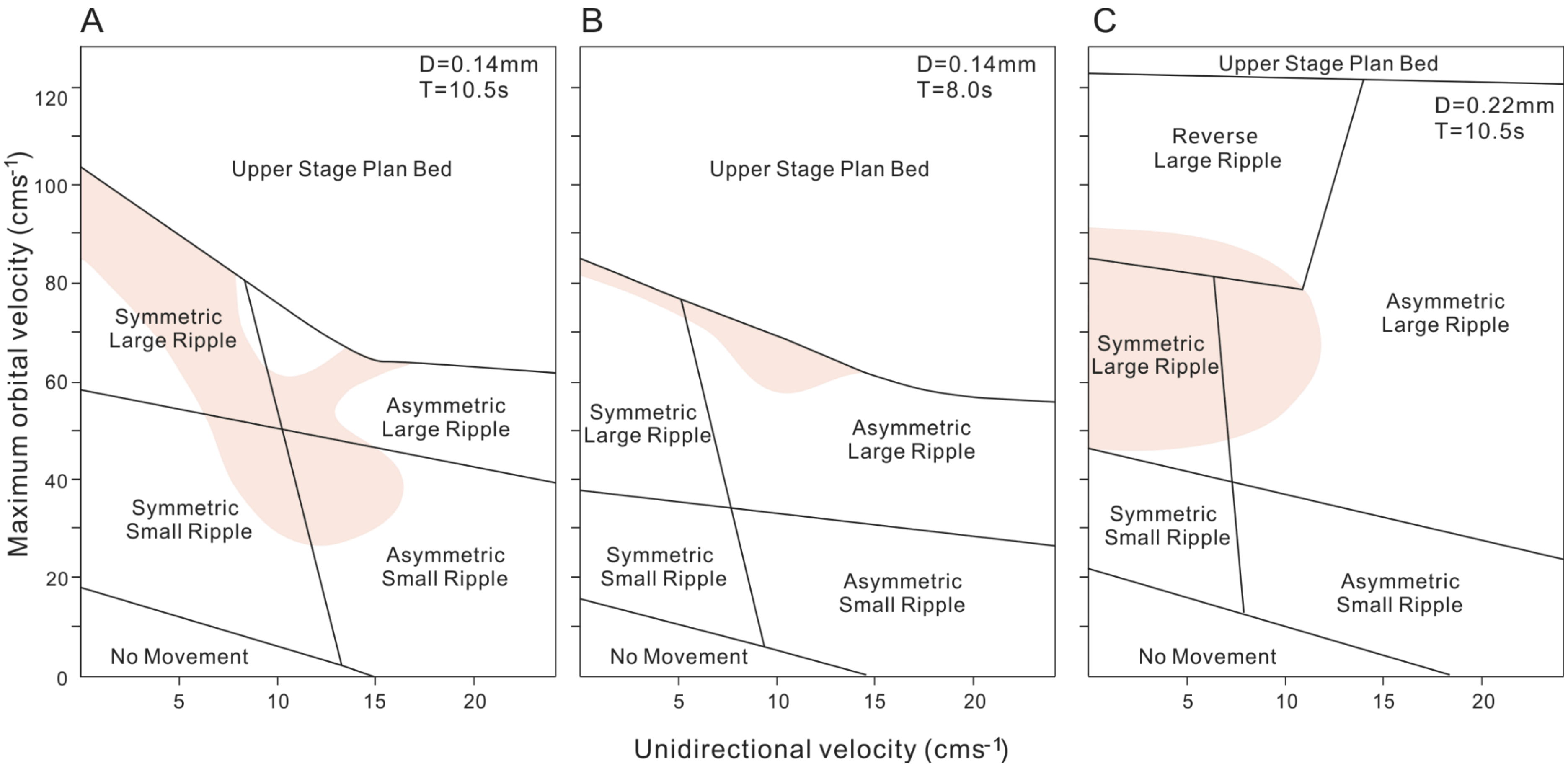

Figure 2-19. Combined flow bedform phase diagram. A) $\boldsymbol{D_{50} = 0.14\ mm, T = 10.5\ s}$***. B)*** $\boldsymbol{D_{50} = 0.14\ mm, T = 8\ s}$***. C)*** $\boldsymbol{D_{50} = 0.22\ mm, T = 10.5\ s}$***. The shded area denotes hummocky bedforms (from Dumas et al., 2005).***

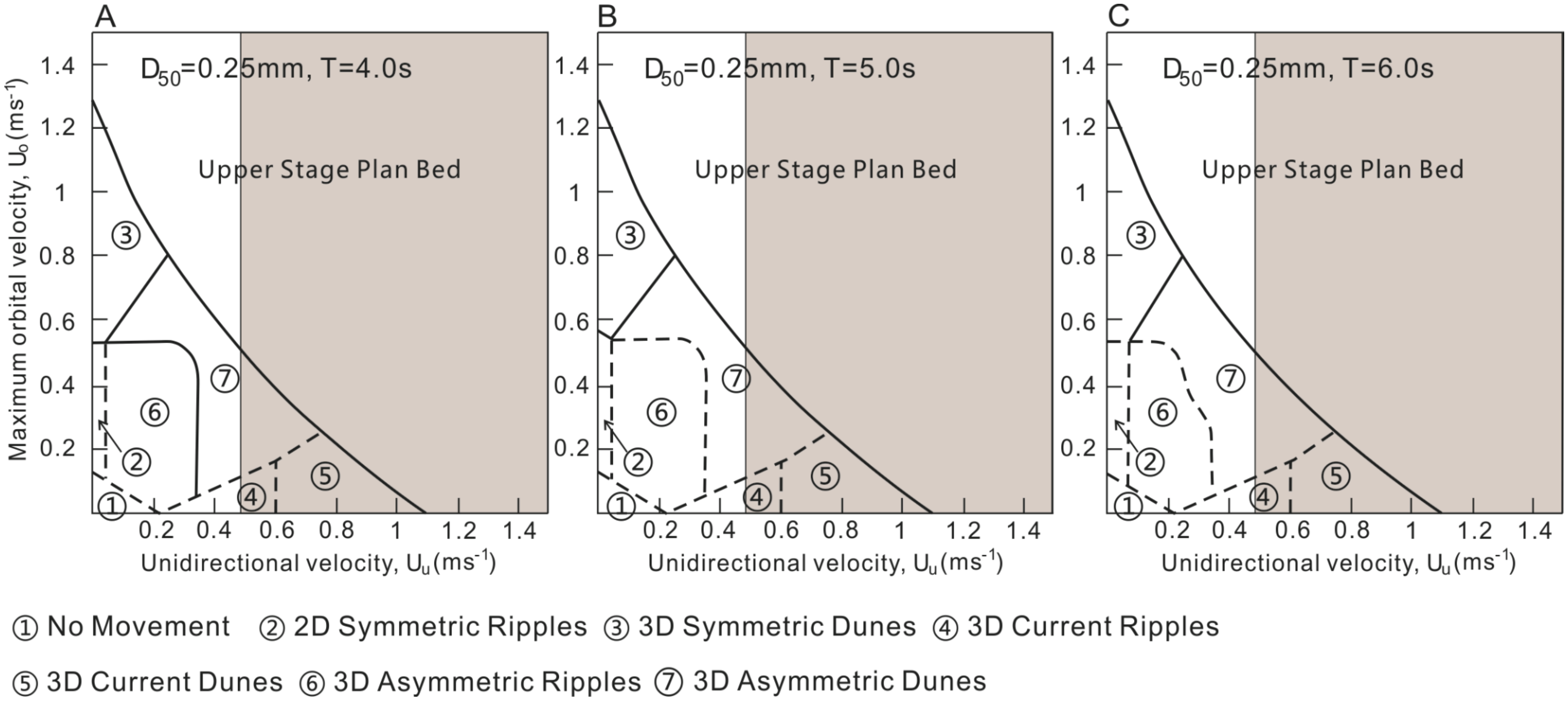

Figure 2-20. Combined flow bedform phase diagram for wave period of 4 s, 5 s and 6 s, repectively. It should be noted that the terms ''dune'' in the phase diagram is used to describe large ripples. The extrapolated regions are gray. Dash lines are gradual transition boundaries between different bedform states, whereas solid lines are sharp transition boundaries (modified after Perillo et al., 2014).

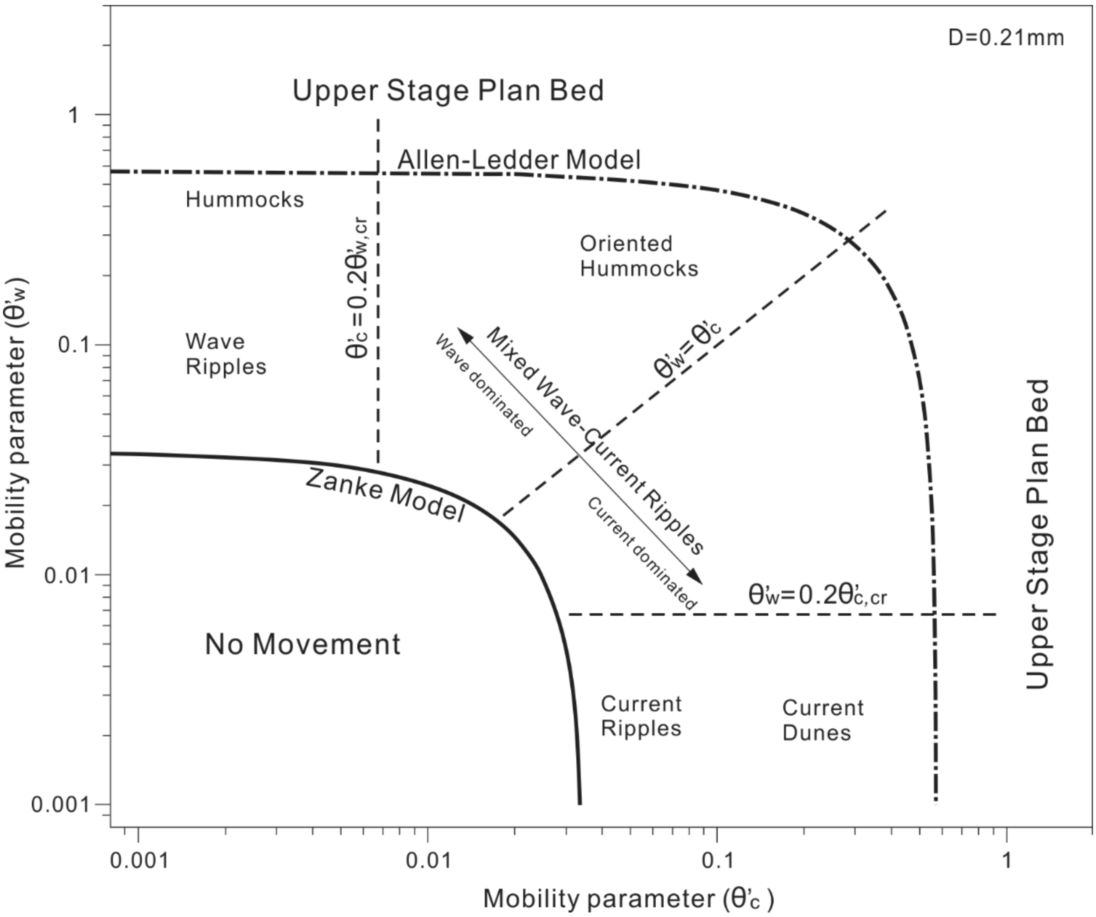

Figure 2-21. Non-demisional combined flow phase diagram with the averaged grain size of 0.21 mm. The black line denotes incipient motion model of Zanke (2003), and the dash dot line denotes mordel of Allen and Leeder (1980) to predict transifition to upper satge plan bed. Dash lines are arbitary boundaries to show wave or current force intensity on bedforms. Bedforms are only generated under pure wave condition if $\theta'_c < 0.2\theta'_{w,cr}$, whereas bedforms are only fomred under current condition if $\theta'_w < 0.2\theta'_{c,cr}$ (modified after Kleinhans, 2005).

2.2.4.2 Combined flow ripples

The region of combined flow generated ripples dominates the space within the phase diagrams, including different types of ripples. Researchers try to use descriptive terminology to classify combined flow ripples from the aspect of ripple geometry. Ripple length is widely used size modifier to identify small (λ<0.3 m) ripples from large (λ>0.5 m) ripples (Dumas et al., 2005; Sekiguchi and Yokokawa, 2008; Perillo et al., 2014). Besides ripple length, ripple symmetry index (RSI, see Figure 2-12) is an important criteria since ripples tend to be progressively asymmetrical with increasing current flow velocity. However there is not clear boundary between symmetric and asymmetric ripples. For example, Dumas et al. (2005) and Sekiguchi and Yokokawa (2008) used symmetry index of 2 in their research, while Perillo et al. (2014) preferred to index of 1.5. Furthermore, Perillo et al. (2014) combined planform geometry (2D, 2.5D and 3D) with cross-section geometry (RSI) to subdivide ripples. The definitions of 2D and 3D ripples are the same as mentioned before in the section of current ripples. 2.5D ripples are transitional stage with either continuous or straight crest lines. Based on the nomenclature of Perillo et al. (2014), the combined flow generated ripples could be described as following:

i) 2D Symmetric Small Ripples (2D SSR). In plan form, they have regular shapes with straight and continuous crest lines perpendicular to the flow direction. In addition they are characterized by a symmetrical cross-section profile with RSI of 1, therefore creating equal angles of leeside and stoss side (20°). Equilibrium ripple length are approximately 230 mm and 37mm, respectively.

ii) 3D Symmetric Small Ripples (3D SSR). The shapes of these ripples are irregular and the crest lines are short and strongly curved, which are significantly different from 2D SSR in terms of plan view geometry. However, individual ripple size and cross-section geometry are quietly similar as the 2D SSR.

iii) 3D Asymmetric Small Ripples (3D ASR). The 3D ASR is characterized by asymmetrical cross-section shape (RSI=1.9) with relative steep stoss side. The angle of stoss side approaches to 21°, whereas lee side angle declines to 11°.

iv) 3D Symmetric Large Ripples (3D SLR). Compared with the 3D SSR, the ripple length and height of the 3D SLR significantly increase, reaching to about 720 mm and 60 mm, respectively. Additionally, bedform geometry of both 3D SLR and 3D SSR are almost the same.

v) 3D Asymmetric Large Ripples (3D ALR). These ripples are formed with gradual increasing unidirectional velocity, with ripple length of 800 mm and height of 74 mm. These ripples have strongly asymmetric cross-section profile, with RSI reaching to 3.1.

2.2.4.3 Combined flow ripples evolution with non-cohesive sands

Akin to the development stages for wave ripples, there are mainly four stages for ripples evolving from flat bed to attaining equilibrium under combined flow conditions (Perillo et al., 2014b).

i) Incipient stage. The incipient bedforms are the rolling grain ripples under wave-dominated combined flow. Under this circumstance, direction of ripple crestlines periodically change from upstream to downstream. Bedforms that similar as incipient ripples under unidirectional flow are observed if the combined flow is current-dominated. The direction ripple crestlines do not change and is always towards downstream.

ii) Growing stage. This stage is characterised by sharp increase of bedform size by combining sediments and amalgamating with nearby bedforms.

iii) Stabilizing stage. Ripples in this stage tend to slowly enlarge, with significant decline of the growth rate.

iv) Fully-developed stage. The majority of combined flow induced ripples reach equilibrium, with equilibrium length and height fluctuating around the equilibrium values. The equilibrium ripples are most likely three dimensional.

2.3 General overview

Interactions among fluid flow, sediment transport and bed morphology constitute a complicated and dynamic system in the nature (Best, 1993; Leeder, 2011; Perillo, 2013). In the first part of the present chapter (Section 2.1), a brief review of boundary layer theory was introduced under unidirectional (current), oscillatory (wave), and combined (wave-current) flows, respectively. Compared with smooth boundary layer, flow structures significantly change when bedforms are present on the bed. For unidirectional flows, flow separation is generated at leeside of bedform, resulting in a relatively complicated set of structures including shear layer, wake region and inter boundary layer. Periodical generation and ejection of vortices is the main feature over rippled bed under oscillatory and combined flow conditions, which dominate near bed turbulence and sediment entrainment. Moreover, suspended clay particles in the current is able to significantly damp turbulence by forming particle bonds of gelling and flocs. However, the literature concerning the mechanisms of cohesive suspended sediment modulation of near-bed turbulence in oscillatory and combined flows is poorly developed (Lamb et al., 2004).

The second part (Section 2.2) of literature review focused on bed morphology, especially ripples, formed under current, wave, and wave-current flows. Baas' work (e.g., Baas, 1993; Baas, 1999) provided excellent information about current ripple evolution from flat bed to 2D ripples, finally reaching equilibrium 3D ripples. Once wave-induced bed-shear stress exceeds the critical shear stress, rolling grains along the bed contribute to formation of rolling grains ripples, then developing to vortex ripples with ripple steepness increasing (Andersen, 2001). Perillo (2013) suggested existence of four stages of ripple development under wave and wave-current flows, including incipient stage, growing stage, stabilizing stage and fully-developed stage. In terms of ripple cross-section geometry, current ripples tend to be asymmetric with a gentle stoss side and a steep lee side (Tanner, 1967), while wave ripples are symmetrical. However, ripple generated under combined flow, the cross-section geometry is strongly linked to relation between wave velocity and current velocity (Dumas et al., 2005; Perillo et al., 2014).

Compared with the significant number of studies on non-cohesive ripples, there is a little attention on how cohesive clay influences ripple development (Baas et al., 2013; Schindler et al., 2015; Ye, 2016). Under unidirectional flow condition, increasing initial clay friction of bed significantly delayed the first appearance of ripples (Baas et al., 2013). Moreover, bedform size tend to be smaller with increasing bed clay fraction (Schindler et al., 2015; Ye, 2016). Therefore, traditional two dimensional bedform phase diagrams (Southard, 1991; Berg and van Gelder, 1993) should be improved by adding the third axis of initial bed clay fraction (Figure 2-22). But, study concerning ripple evolution with cohesive clay mixtures under wave condition remains a significant knowledge gap and will be discussed in the following charters. Additionally, clay particle winnowing processes from the bed during unidirectional experiments have been observed (Baas et al., 2013, Ye, 2016). However the efficiency under oscillatory flows is unknown as is the impact of high suspended clay concentrations on modulating near-bed turbulence. These research questions will be answered in the following two chapters.

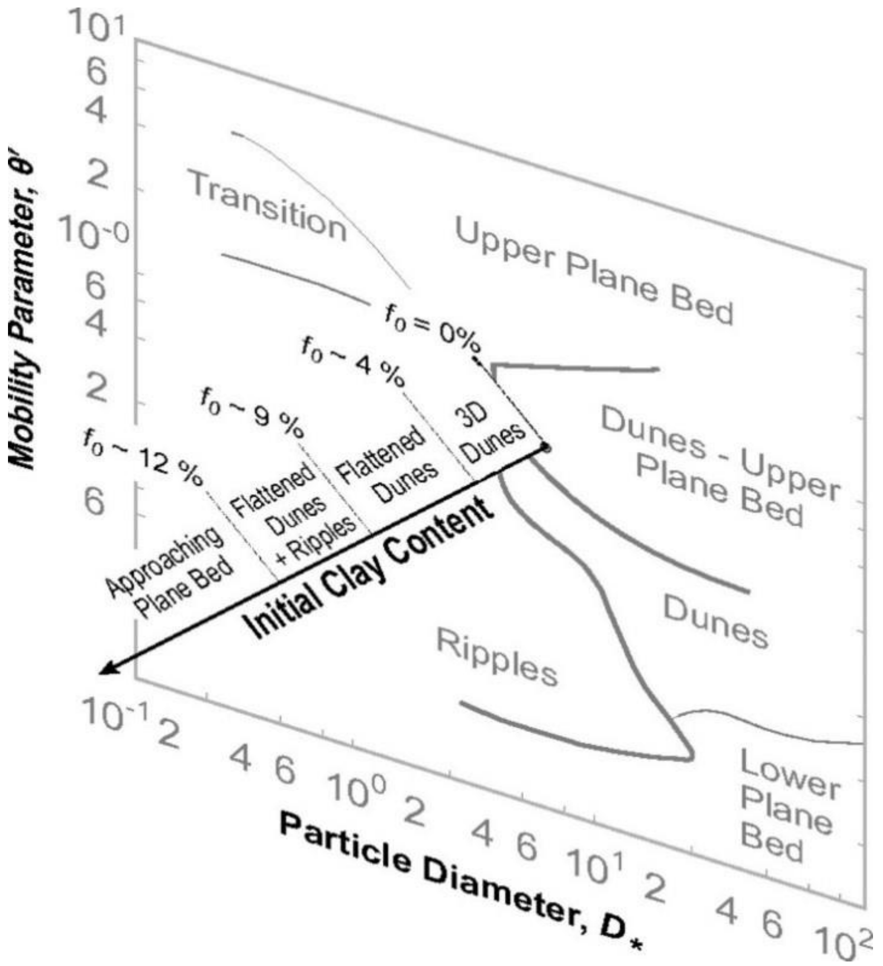

Figure 2-22. Conceptual modification of current bedform diagram of van der Berg and van Gelder (1993) by adding z axis of initial bed clay fraction, showing bedform chage with increasing initial bed clay content (from Schindler et al., 2015 and Ye, 2016).

CHAPTER 3 –Ripple evolution in mixed sand-clay substrates

3.1 Introduction

The near seafloor fluid in coastal environments and across shelf-seas frequently experiences a range of wave induced oscillatory motion, particularly when the water depth is sufficiently shallow (Clifton and Dingler, 1984). Bed sediment transport can be initiated if the wave-induced bed shear stress exceeds the critical shear stress for the initial motion of sediment. Such sediment transport results in the generation of wave ripples (van Rijn, 1993). The size of wave ripples is related to the sediment characteristics, including sediment particles size ranges, and the flow properties, such as maximum near-bed orbital velocity (Nelson, 1981; van Rijn, 1993; Nelson et al., 2013). Relationships built on both empirical measurements and theory allow a range of parameters to be predicted based on the wave ripple height. Therefore, wave ripple co-sets preserved in the rock record are significant tool to reconstruct paleo-environment (Clifton and Dingler, 1984; Yokokawa, 1995) allowing relations between wave-base and paleo-deposition water depth to be determined. Moreover, the presence of wave ripples are also an important parameter within modelling of sediment transport in coastal settings (van Rijn, 2007; Perillo et al., 2014b; Nelson et al., 2013).

Previous studies, however, have focused on the dynamics of bedforms within substrates composed only of well-sorted sand. This restrictive sediment type is far from being a realistic representation of natural sediment size distributions, particularly in European coastal and estuarine environments, where mixed sediments with and without fine cohesive components are common (Flemming, 2002). Cohesive mixed sediments (mud-sand) are known to heavily influence bedform characteristics (Baas et al., 2011, 2013) and, in turn, the near-bed boundary conditions for turbulence and sediment transport within dynamic sediment transport models. Baas et al. (2013) highlighted that cohesive clay particles added into sand bed substrates significantly slows the rate of current ripple development. In Particular, they reported that ripple dimensions decrease with increasing clay content under unidirectional flow (Baas et al., 2013). However, the influence of such cohesion under wave induced flows are yet to be determined.

This chapter therefore concentrates on examining the influence of cohesive clay contents of bed substrates on the ripple development under regular wave conditions. The aims can be outlined as: (1) identifying the relationship between the rate of wave ripple development and initial bed clay fraction; and (2) determining the equilibrium height and length of the wave ripples as a function of initial bed clay fraction.

3.2 Methodology

3.2.1 Experiment set-up

A large-scale flume experiment was conducted in the Total Environment Simulator, University of Hull. The effective length of flume is 11 m with additional inlet and outlet tanks for recirculation of the flow and sediment. The maximum internal depth and width of a central channel built within the basin are 1.6 m and 6 m, respectively (Figure 3-1). At the upstream end of the flume tank, there are 8 wave-generating paddles across the channel width. In the experiments reported here two of them were used to generate regular and irregular water surface waves in the present experiments (Figure 3-1). The working test section of the present experiment was approximately 9.8 m long, and around 1.6 m wide, and a detailed monitoring section was centred at 4.3 m distance from the flume inlet (Figure 3-1). An instrument frame with state-of-the-art measurements was mounted in the central monitoring section (Figure 3-2). At the downstream end of working test section, a perforated board with a porosity of 15% was mounted at an upstream-dipping angle of 6° (Figure 3-1). The purpose of the perforated board is to disperse wave energy and thus minimise wave reflections within the test section. The sediment substrate at the base of the flume was 0.1 m thick at the start of the experiments. All experiments used same mean water depth of 0.6 m and the salinity of water was held constant across all runs at ~ 19 psu (Table 3-1).

Experiment Run 01 and Run 02 consisted of a bed of well-sorted sand, with a median diameter of ~496 µm. Wet kaolin clay, which is most common clay type on Earth, and same sand in Run 01 and Run 02 were homogenously mixed to create substrates for Run 03 to Run 06, with initial clay fraction increasing from 4.2% to 7.4% (Table 3-1) across the runs. All of the experiment runs were conducted under regular (monochromatic) waves with the basically same freestream velocity of 0.35 ms^{-1} and wave period 2.48 s (Table 3-1), except Run 02. The experimental results of Run 02 that was conducted under irregular (poly-chromatic) wave are not discussed in this chapter.

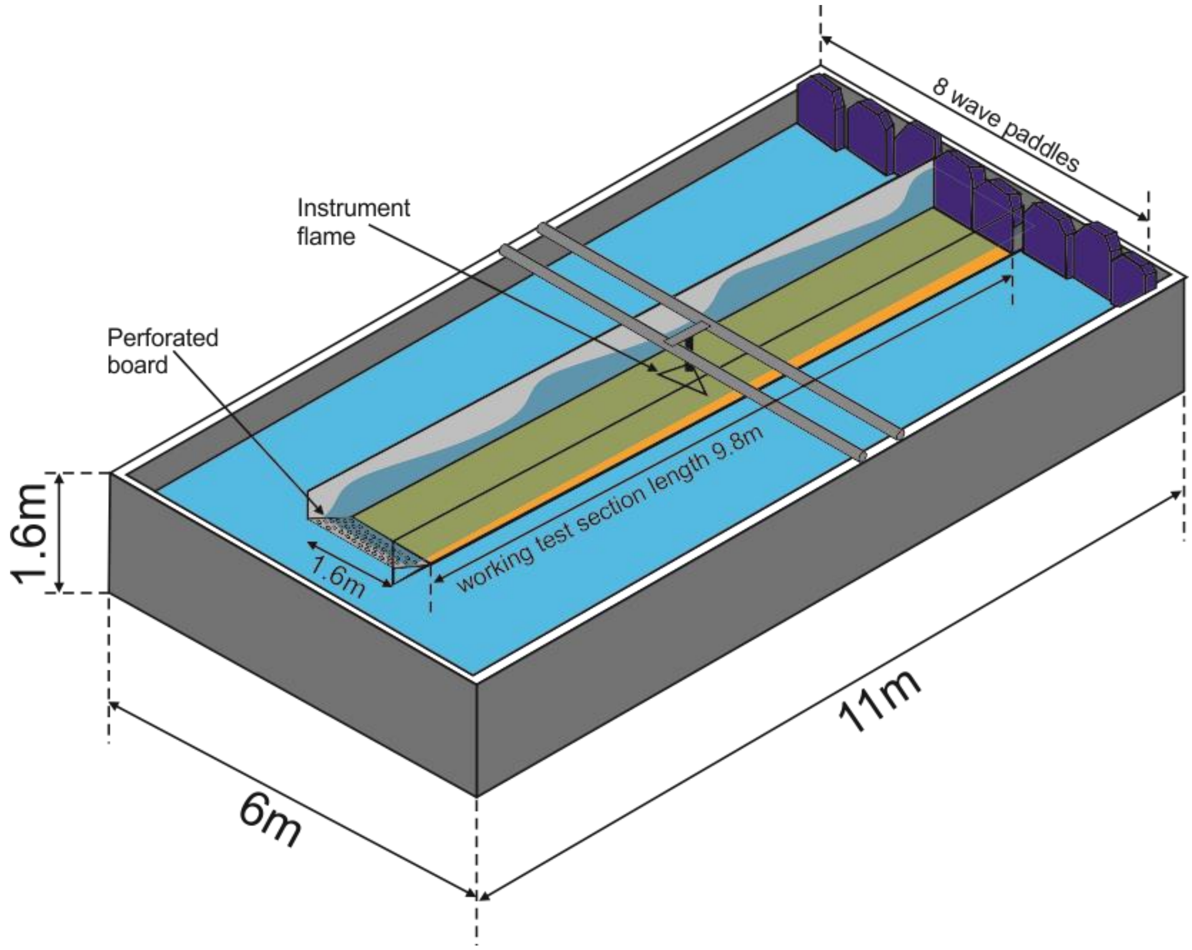

Figure 3-1. The Total Environment Simulator and the working test section for the experiment.

Table 3-1 Experimental parameters

Run	Duration (min)	Temp (°C)	Initial Clay fraction[a] (%)	Salinity (‰)	D_{50} (μm)	H_s Start (m)	H_s End (m)	U^*_{won} Start (ms^{-1})	U_{won} End (ms^{-1})	U_{woff} Start (ms^{-1})	U_{woff} End (ms^{-1})	$U_{\infty on}$ Start (ms^{-1})	$U_{\infty on}$ End (ms^{-1})	$U_{\infty off}$ Start (ms^{-1})	$U_{\infty off}$ End (ms^{-1})
1	290	16.3	0	17.8	496	0.16	0.15	0.30	0.30	0.25	0.24	0.36	0.35	0.32	0.31
3	300	15.4	4.2	19.2	457	0.22	0.19	0.31	0.31	0.26	0.26	0.36	0.36	0.31	0.30
4	250	15.4	6.2	17.2	435	0.22	0.21	0.29	0.28	0.27	0.27	0.37	0.36	0.31	0.30
5	510	14.6	7.2	20.4	431	0.24	0.19	0.29	0.31	0.26	0.26	0.35	0.33	0.32	0.28
6	630	15.9	7.4	19.1	421	0.21	0.21	0.29	0.29	0.25	0.23	0.35	0.33	0.31	0.30

H_S: Significant wave height

U_{won}: Maximum near-bed onshore orbital velocity

U_{woff}: Maximum near-bed offshore orbital velocity

$U_{\infty on}$: Maximum onshore free stream velocity

$U_{\infty off}$: Maximum offshore free stream velocity

a: Initial clay fraction percentage is by dry weight

b: Positive, “onshore” flow is defined as flow direction to the left.

3.2.2 Procedure

Prior to the commencement of each run where clay was mixed into the bed, the volume of kaolin mixed into the bed was carefully measured to control the clay: sand ratio. The bed was wetted and fully homogenised and was then flattened. Prior to the runs, syringe sediment cores with a diameter of 20 mm and a maximum length of 90 mm were collected at 7 equally-spaced locations at 3.4 m < x < 9.4 m from the wave paddles and y=0.4 m from the right-lateral side of the channel for subsequent grain size test (Figure 3-2).

The development of bedforms of each run from the initial flat bed was scanned by traverse ultrasonic sensor array (URS). The system consist of 8 probes, which were mounted above the centre monitoring section. However, probe 2 did not work in all experiments, hence some experiments only 7 probes functioned. The bed scanning length was about 2.7 m and scanning velocity was around 0.0093 m/s (Figure 3-2 B). The two wave generators were stopped every 30 minutes (every 15 minute in the first hour of Run 01, 03 and 04) to allow the URS scanning to complete. In addition, another two URS probes were fixed into position on the instrument frame and were used to record ripple migration form experiment start to the end of each run (Figure 3-2).

After each run, sediment cores were taken for comparison of substrate characteristics with those from initial flat bed. Sample cores were collected from both the ripple crest and trough. The sample cores were located at from 3.4 m <x < 7.4 m from wave generators and at from 0.4 m< y < 1.2 m from the right-lateral side of the channel (Figure 3-2 B).

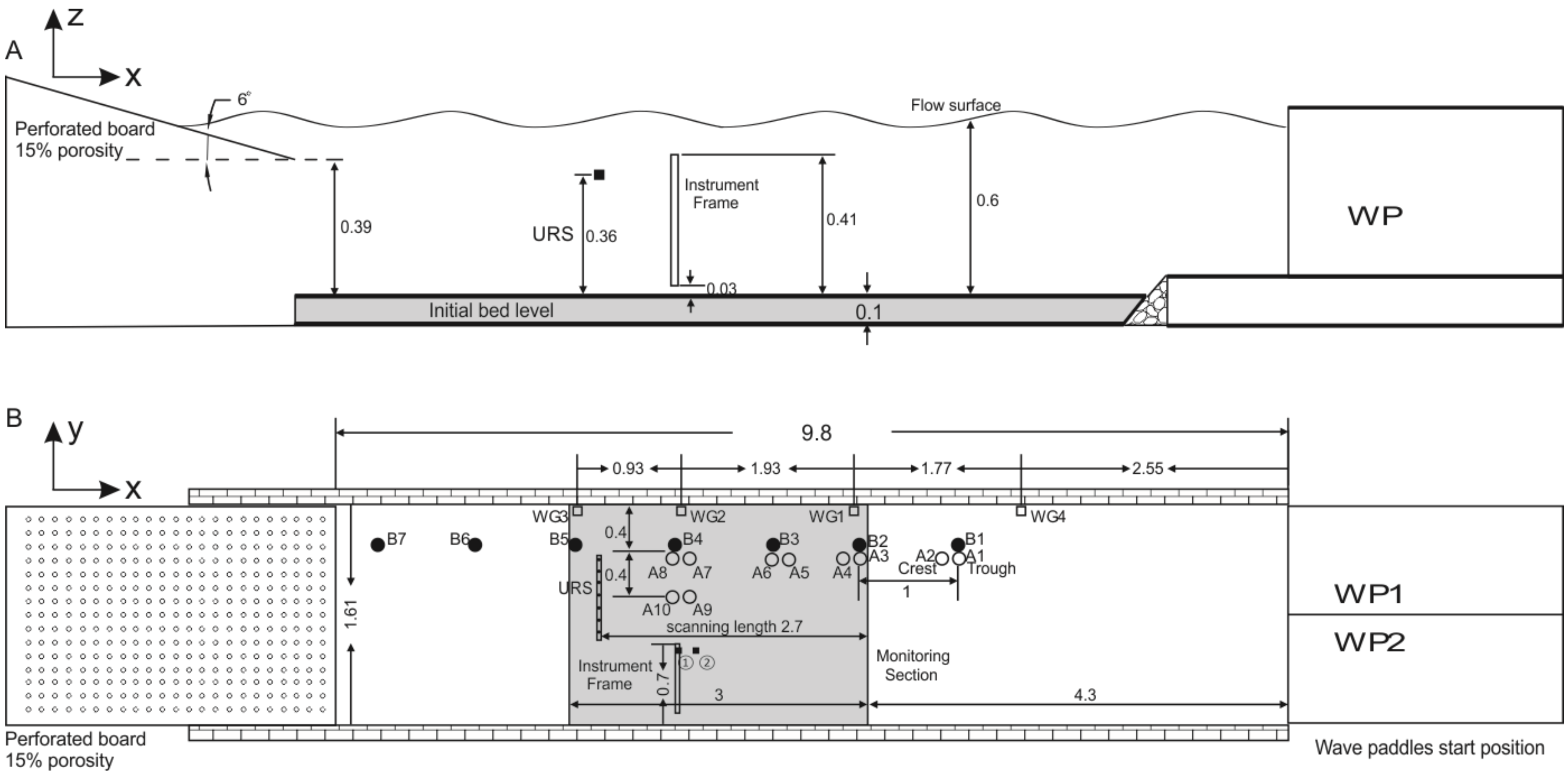

Figure 3-2. (A) Lateral schematic diagram of the experimental set-up. Planview schematic (B), with the traverse URS scanning area and locations of sediment cores collected before (black circles) and after (white circles) each run. WG denotes wave gauge. ① and ② represent the downstream and upstream fixed URS. The distance between the two URS probes was 0.03m. The shade area is the 3-m length central monitoring area where the instrument frame with measurement devices was mounted. The unit is metre.

3.2.3 Post processing of data

Seven bedform elevation profiles (BEPs) were recorded by the URS-traverse for each scanning period, across a time interval of 30 minutes. Longer and shorter time intervals were also used, depending on ripple development rate. These raw data of BEPs were processed by the method based on Bedform Tracking Tool (BTT) that is a numerical code in Matlab (Van der Mark et al., 2008; Van der Mark, 2009). The steps for processing raw data could be summarised as follows:

1. *Removing and replacing outliers*. The absolute vertical distance (*dz*) between two consecutive was calculated to get the averaged vertical distance (dz_m) that is used as a criterion to find outliers in the BEP. The outliers differing more than absolute 5 dz_m between the previous points and the next points were interpolated. In the current thesis, linear interpolation was used to replace outliers.

2. *Detrending and smoothing the bed elevation profile*. A linear trend line was subtracted by the filtered bed elevation profile. Then a detrend bed elevation profile fluctuates around the zero line. In order to avoid small disturbance crossing zero line, weighted moving average technique was used to smooth the dtrend bed elevation profile.

As shown in Figure 3-3 the black line is the original bed elevation profile collected from probe 7 in Run 03 at t=30 min. Two zero values caused by poor return voltages in the URS depth sounders were filtered using above mentioned method (red dot line).

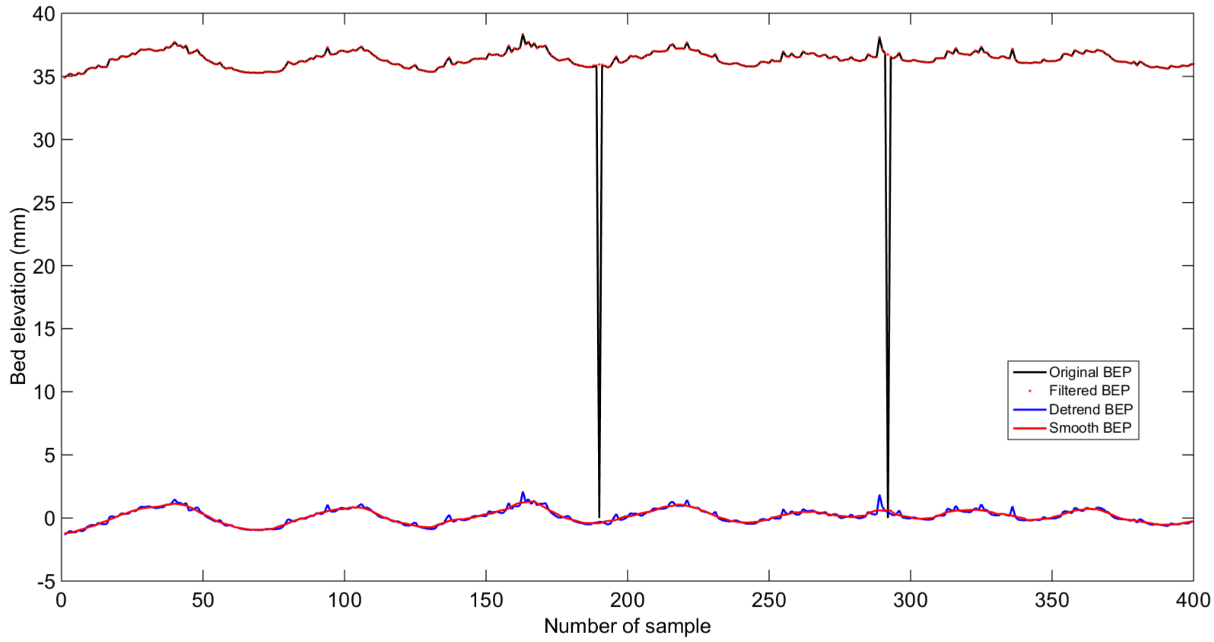

Figure 3-3. The produced data of probe 7 of Run 3 at t=30 min for calculation of ripple length and height. The black line is the origial bedform elevation profile (BEP) scanned by the URS. The red dot line is the data without outliers. The blue line dnotes the detrend BEP and the red line represents that the BEP has been smoothed.

The detrend method effectively enables the filtered BEP to fluctuates around a zero line (blue line). The red smooth BEP shows that the very small disturbances are eliminated. In conclusion, the first two steps of Bedform Tracking Tool are helpful to reduce negative influence of data noise on the next step calculation of ripple length and height.

3. *Determining zero crossings*. Two types of zero crossings are determined, which are up-crossings and down-crossings respectively. A zero up-crossing and down-crossing are located where the filtered bedform elevation profile crosses the zero line in upward and downward direction, respectively.

4. *Determining crests and troughs*. A crest point should be between a zero up-crossing and zero down-crossing, while a trough point is between a zero down-crossing and zero up-crossing. Van der Mark (2009) emphasized that local disturbance could be incorrectly selected as crest or trough. Actually for the present data, the local disturbances were effectively avoided using step 2. However, the method for finding crest and trough is inapplicable under certain circumstance.

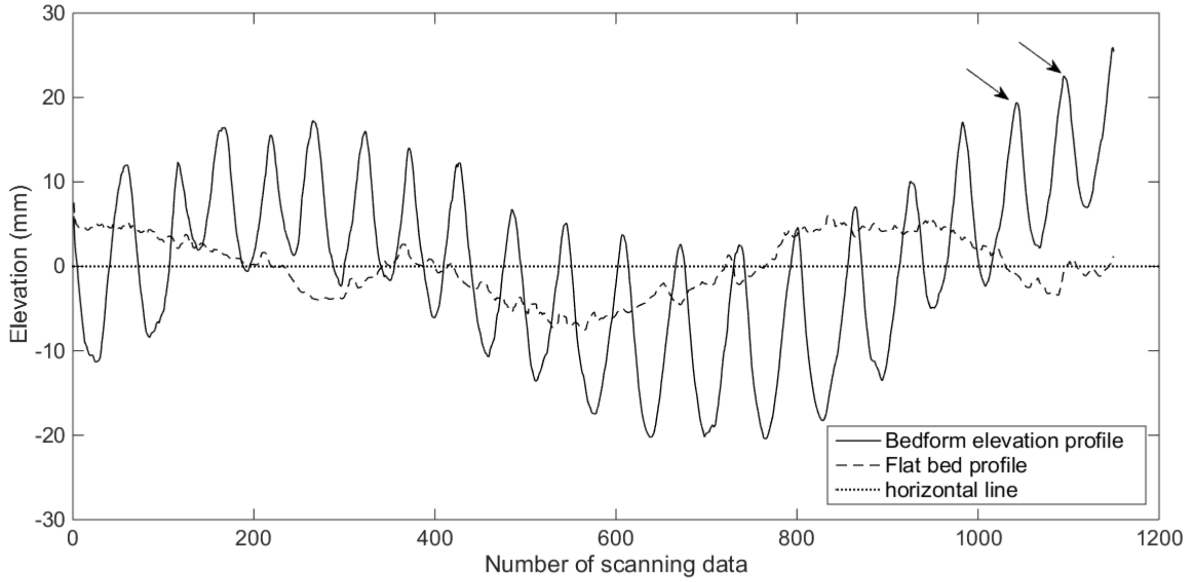

Figure 3-4. Comparison of bedform elevation profile (Run 03, t=240 min, scanned by probe 5 of URS) and flat bed profile to determine ripples crests and troughs. The two crests pointed by arrows will be discarded by the method of Van der Mark et al. (2008).

Figure 3-4 shows a bedform elevation profile collected by URS (probe 5) in Run 03 at t=240 min. The black dash line is the bed elevation profile before the start of Run 03. Comparing these two profiles, it is apparent that there are two ripples located beyond x=1000 as highlighting by the arrows. However, these two crests and troughs are not located between zero up-crossings and zero down-crossings and herein are discarded by BTT algorithm. Therefore, manually finding ripples and BTT algorithm are combined to process raw traverse URS scanning data in order to locate all of ripples.

For each traverse scanning period there are seven BEPs because probe 2 did not work during the experiment. For each profile, all of individual ripple were found and then calculating averaged ripple length and height. Therefore, there were seven averaged ripple lengths and heights at one scanning time, which were used to construct development curves of wave ripple length and height.

In addition, the ripple lengths and heights were used to analyse the ripple geometry in more detail. Figure 3-5 shows the definitions of the ripple geometry in a detrend bedform elevation profile.

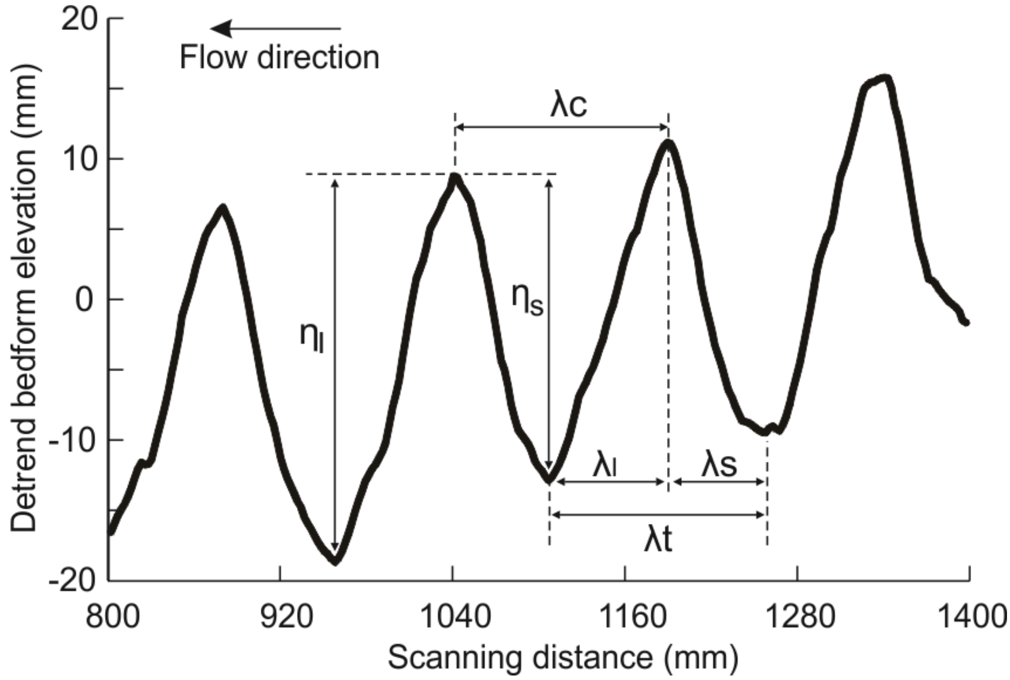

Figure 3-5. Definitions of the determined ripple geometry in a detrend BEP.

Symbol name	**description**
λ_t ripple length between troughs	horizontal distance between two consecutive troughs
λ_c ripple length between crests	horizontal distance between two consecutive crests
λ_s ripple length of stoss face	horizontal distance between crest and upstream trough
λ_l ripple length of lee face	horizontal distance between crest and downstream trough
η_s ripple height of stoss face	vertical distance between crest and upstream trough
η_l ripple height of lee face	vertical distance between crest and downstream trough

The bedform steepness (BI) and bedform symmetry (BSI) are computed as the following equations:

BI= $\lambda_c {\eta_l}^{-1}$ 3-1

BSI=$\lambda_a \lambda_b^{-1}$ 3-2

a and b refer to lager value and smaller value between leeside length and stoss side length.

For the data collected from the fixed URS, filtering of spikes caused by suspended sediment in the data was undertaken. Noise was found by setting a maximum threshold of the gradient between two consecutive points. This threshold was chosen as 0.5 times the standard deviation of each time series. Removed values are replaced with linearly interpolated values and every 300 data (5 Hz sampling) were averaged to represent value of each minute. Once filtering of fixed URS data was complete, detection of ripples was undertaken using the same steps as mentioned above for traverse URS data. The data collected by four fixed URS are used to acquire ripple migration rate by:

$\mathrm{c}_m = L/(t_2 - t_1)$ 3-3

where

c_m is wave ripple migration rate

t_1 is the time that the upstream fixed URS probe recording ripple crest.

t_2 is the time that the downstream fixed URS probe recording the same ripple crest moved from upstream. Noticed that t_1 and t_2 are the time after ripples reaching equilibrium.

L is the distance between upstream and downstream fixed URS probes, which is approximately 30 mm.

Then the bed sediment flux per unit width (q_b) of each run is computed by (Van Den Berg 1987):

q_b=0.6(1-p)c_m η 3-4

Where

P is bed porosity (p=0.35)

The equilibrium conditions could be established by the Baas *et al*. (2013) method, where the ripples development by the following equations:

$$\frac{\lambda_t - \lambda_0}{\lambda_e - \lambda_0} = 1 - (0.1)^{\frac{t - t_f}{T_\lambda - t_f}} \qquad 3\text{-}5$$

$$\frac{\eta_t}{\eta_e} = 1 - (0.1)^{\frac{t - t_f}{T_\eta - t_f}} \qquad 3\text{-}6$$

Where

λ_t: ripple length derive from BTT at time t after experiment start

η_t: ripple height derive from BTT at time t after experiment start

λ_e: equilibrium wave ripple length

η_e: equilibrium wave ripple height

λ_0: the length of the first appearance of wave ripple

T_λ : time for ripple length getting equilibrium

T_η: time for ripple height getting equilibrium

A non-linear fit using the Curve Fitting Tool in Matlab was used to find the best solution for Equations 3-1 and 3-2, therefore obtaining λ_e, η_e, λ_0, T_λ and T_η. In the present study, T_λ and T_η are defined as 90% of wave ripples reach equilibrium.

The delay time (t_f) for the formation of wave ripples firstly appeared on the flat bed is determined by the flowing method. According to the experimental observation wave ripples formed immediately after experiment started in Run 01, therefore no delay time was recorded for this run. However, there were no experimental observations of first appearance of wave ripples in other runs, therefore delay times are based on the URS generated 3D images. The middle time between experiment start or the last time recording flat time and the first time recording wave ripples were used as delay time for runs with cohesive materials (Table 3-2). In addition the initial wave ripple length (λ_0) is assumed to be undefined and the initial height is assumed to be zero at first time of wave ripples appearance (Baas, 1993). The best-fit lines given by Equation 3 and Equation 4 fit well with experimental data of each run with high R values and the fitting results are shown in Table 3-2.

The ripple length growth rate (r_λ) and height growth rate (r_η) are computed by equations as following:

r_λ =(λ_e-λ_0)/(T_λ- t_f) 3-7

r_η =η_e/(T_η-t_f) 3-8

To compute accurate wave height of each run, a least squares method is used to separate reflected wave from incident wave (Mansard and Funke, 1980). Simultaneous measurements at three positions (WG1, WG2, and WG3 in Figure 3-2) were used to decompose incident and reflected spectra.

All of the sediment cores were frozen shortly after sampling. Each sediment core was sliced into sample with 1cm thickness and then all the samples were dried less than 80 Celsius degrees about 4 hours. The grain size analysis results were acquired by laser particle analyser (Model: Malvern 2000). All of the measurements were undertaken in School of Ocean Science, University of Bangor.

3.3 Experimental results

Five runs were conducted under regular waves with fixed 2.48s period. The initial bed clay fraction increased from 4.2% in Run 03 to 7.4% in Run 06.

3.3.1 Ripple development under regular waves

Run 01 was the control experiment with pure sand and a median size 496 μm (Table 1). Therefore this was a reference for Runs 03-06 to study the influence of increasing initial bed clay fraction on bedform evolution and dynamics. Wave ripples appeared instantaneously from the flat bed when the experiment started, according to experimental observation in Run 01. The entire bed below the URS traverse was covered by the wave ripples at ~20 minutes of experimental time (Figure 3-6). Experimental observation proved the time ripples were covering complete scanning area at around 10 minutes after Run 01 beginning. Figure 3-6 clearly shows that the typical two dimensional wave ripples with quite straight crest lines developed well during the experiment.

Seven wave ripple length development curves of Run 01 with standard deviation are shown in Figure 3-7. The ripple length fluctuated slightly around ~125 mm (Table 3-2) notably at the initial scan (scanning time, t=20 min). The rather higher standard deviations suggest that individual ripple length varied heavily at the beginning of experiment. Ripple lengths experienced a relatively faster growth period from t= 20 min to t=50 min before tending to be stable (Figure 3-7). Precisely, the equilibrium times of ripple lengths determined from equation 1 were simultaneously at t=∼40 min (Table 3-2). Moreover the equilibrium ripple length was approached to 136 mm (Table 3-2). Figure 3-8 shows the photo of ripples taken after Run 01 in which the ripple lengths are about 140 mm and 145 mm, respectively. The actual wave ripple lengths are very close to the length calculated by Bedform Tracking Tool as mentioned in section 3.2.

In terms of ripple height, at very beginning of experiment the mean ripple height was approximately 16 mm. However, the difference among individual ripple height was large, with higher standard deviation again. In addition, all of ripple height development curves show that ripple height reached peaks at t=50 min before keeping level (Figure 3-7). Table 3-2 also shows the results of equilibrium height and equilibrium time for ripple height derived from equation 2. The equilibrium times of ripple heights slightly fluctuated around 26 minutes and the equilibrium ripple height reached to approximately 20 mm (Figure 3-7). In conclusion, seven ripple development curves reflect a quite similar wave ripple growth trend, which indicates that the pure sand bed enable wave ripples to develop homogeneously.

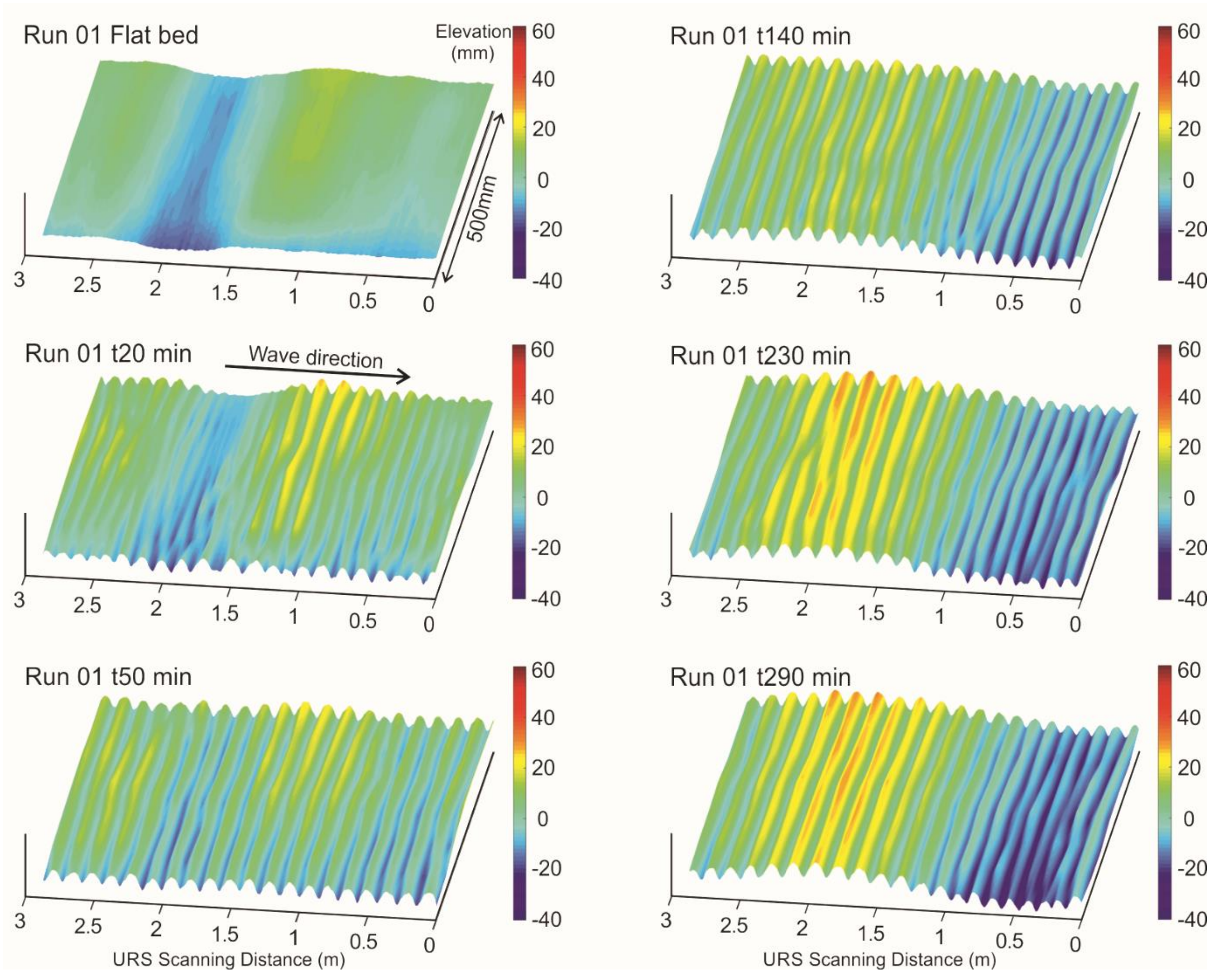

Figure 3-6.   3D image of wave ripples evolution of Run 01 with pure sand.

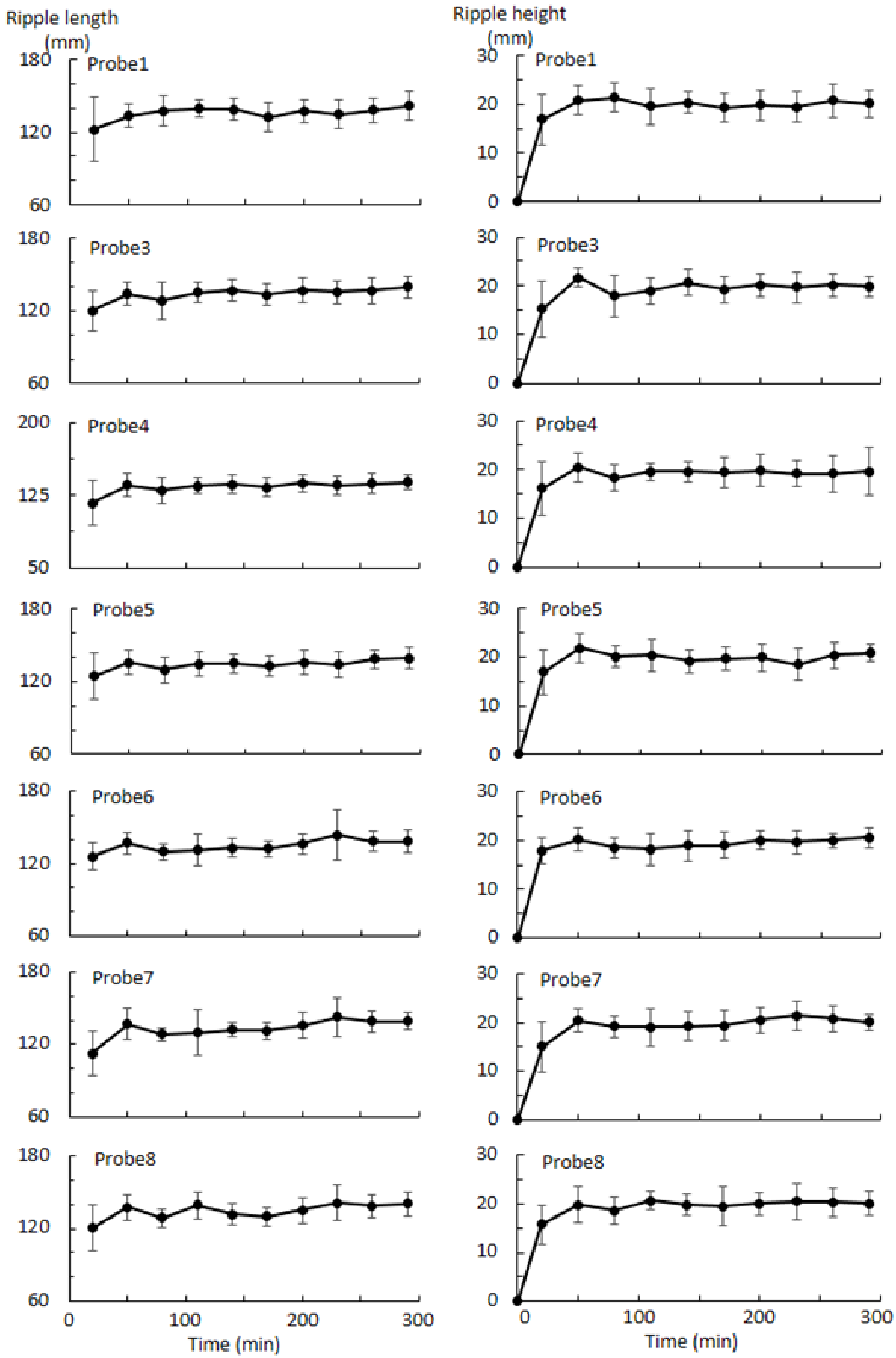

Figure 3-7. Development curves of ripple length and height of Run 01. The vertical black line denotes one standard deviation around the mean.

Figure 3-8. Photo of wave induced two dimensional ripples after Run 01.

Runs 03 to 06 investigated ripple evolution from mixed sand-clay beds at progressively higher clay fractions (Table1). Before each run, Kaolin clay was homogeneously mixed manually with the sand bed. Sediment cores collected from flat bed indicate that none of the flat bed before each run showed a significant vertical trend in sand fraction (Figure 3-25), suggesting that the clay was reasonably well mixed into the sand.

Run 03, with the lowest clay fraction, about 4.2%, exhibited reduced wave ripple growth rate than the ripples developed without clay (Run 01). At first 15 minutes scan, approximately two third of the URS scanning area was covered with two dimensional ripples. Beyond the 15 minutes the ripples continued to develop until after 30 minutes beyond the experiment start, all the URS probes recorded almost the whole scanning section to be covered by a continuous train of wave ripples (Figure 3-9).

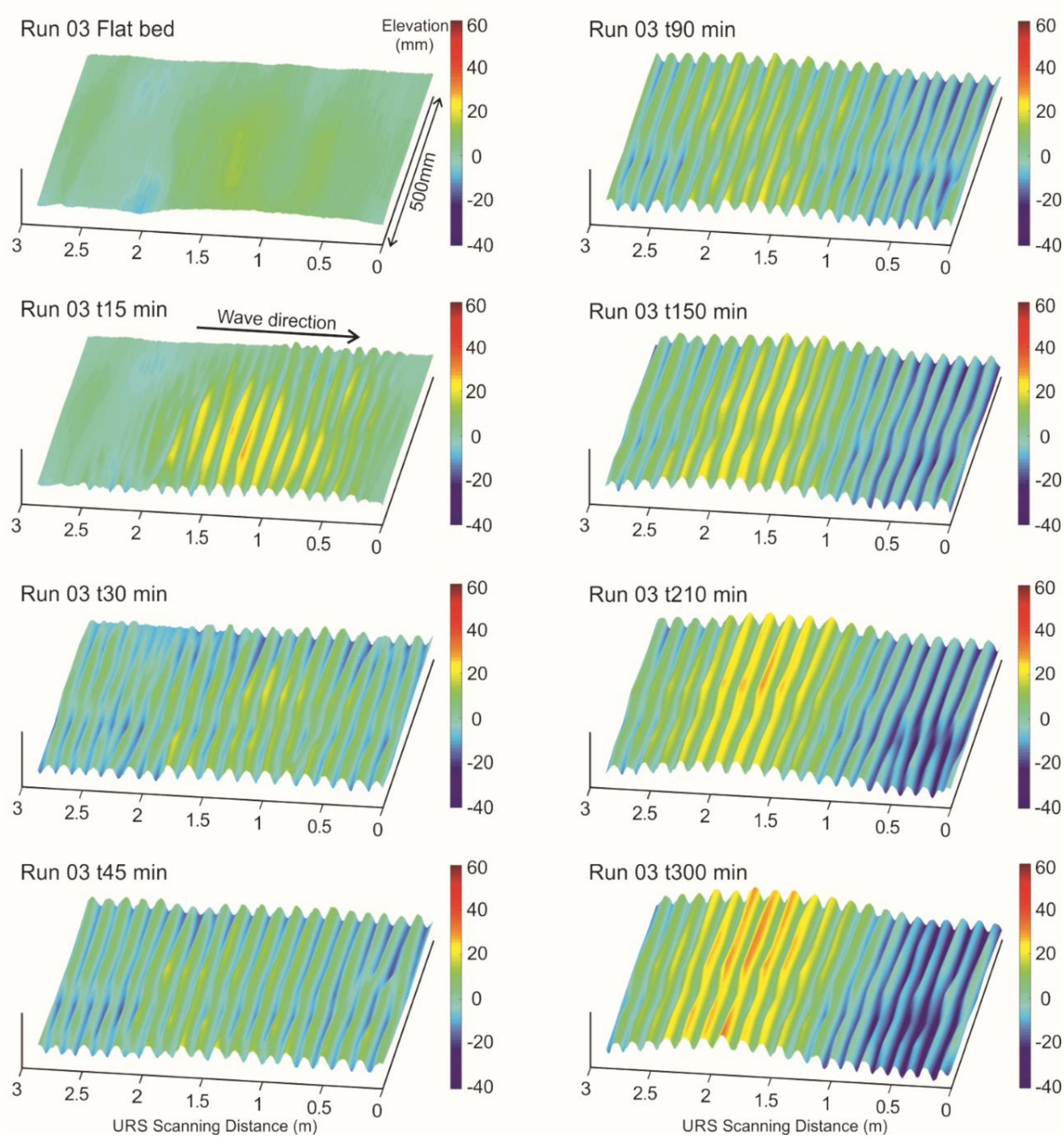

Figure 3-9. 3D images of wave ripples evolution of Run 03 with 4.2% clay fraction.

Figure 3-10 depicts progressive stages of ripple development in Run 03. In the first 15 minutes, ripples in the middle scanning area tended to develop more quickly, with the URS (Probes 2 to 6) initially recoded averaged ripple length of ~120 mm. While the ripple lengths recorded by side probes (Probes 1, 7 and 8) were shorter than 100 mm. In the following 45 minutes, ripple lengths slowly approached to ~140 mm in the most part of area. During the same period ripples below probes 7 and 8 had rather faster development rate, with ripple lengths reaching to 140 mm at t=60 min as well (Figure 3-10). The results of non-linear fit indicate most of ripple lengths attained equilibrium after t=60 min, with equilibrium length of ~138 mm (Table 3-2). However, wave ripples at below probes 7 and 8 spent longer time to reach equilibrium length, exceeding 70 minutes (Table 3-2).

Ripple heights developed in a similar trend set as the ripple lengths. During period from t=15 min to t=60 min, the heights of ripples at right edge of the scanning areas (Probe 7 and 8) grew more quickly than ripples at other places. Remarkably, ripple heights beneath probe 1 and 4 acquired equilibrium only after t= 15 min, while the equilibrium time for ripple height below probe 8 was 53 minutes. Although there was a large difference among the time for ripple height reaching equilibrium, the equilibrium height was uniformly around 20 mm (Table 3-2).

The bed of Run 04, comprising 6.2% of initial clay fraction, remained flat in the first 10 minutes of the experimental run. A couple of minutes thereafter, the wave forcing began to impact on the bed, which signalled the formation of a nucleus of ripples with mean ripple length of 100.6 mm and mean ripple height of 11.9 mm at right edge side along wave direction. The similar kind of wave ripple sets had been generated at opposite edge after 15 minutes, but the ripples size were marginally smaller with mean ripple length and height at 87.8 mm and 9.7 mm, respectively (Figure 3-11 and Figure 3-12). The erosional scouring was an irregular process and individual ripple size varied significantly, as evidenced by the higher standard deviations of both ripple length and height (Figure 3-12). Since then the nucleus expanded toward centre of the URS scanning section by growth of existing ripples, until the ripples occupied most of the bed with mean ripple length increasing to around 122 mm at t=70 min (Figure 3-11; Figure 3-12). Based on the above-mentioned growth mode, ripple lengths at edge attained equilibrium before t=90 min, which were much earlier than that developing at middle bed. However, the heights of ripples below probe 3 and 8 spent a rather loner time (~45 minutes) to reach equilibrium (Table 3-2). Furthermore, the equilibrium ripple size were consistent, with equilibrium length and height at approximately 137 mm and 20 mm, respectively (Table 3-2).

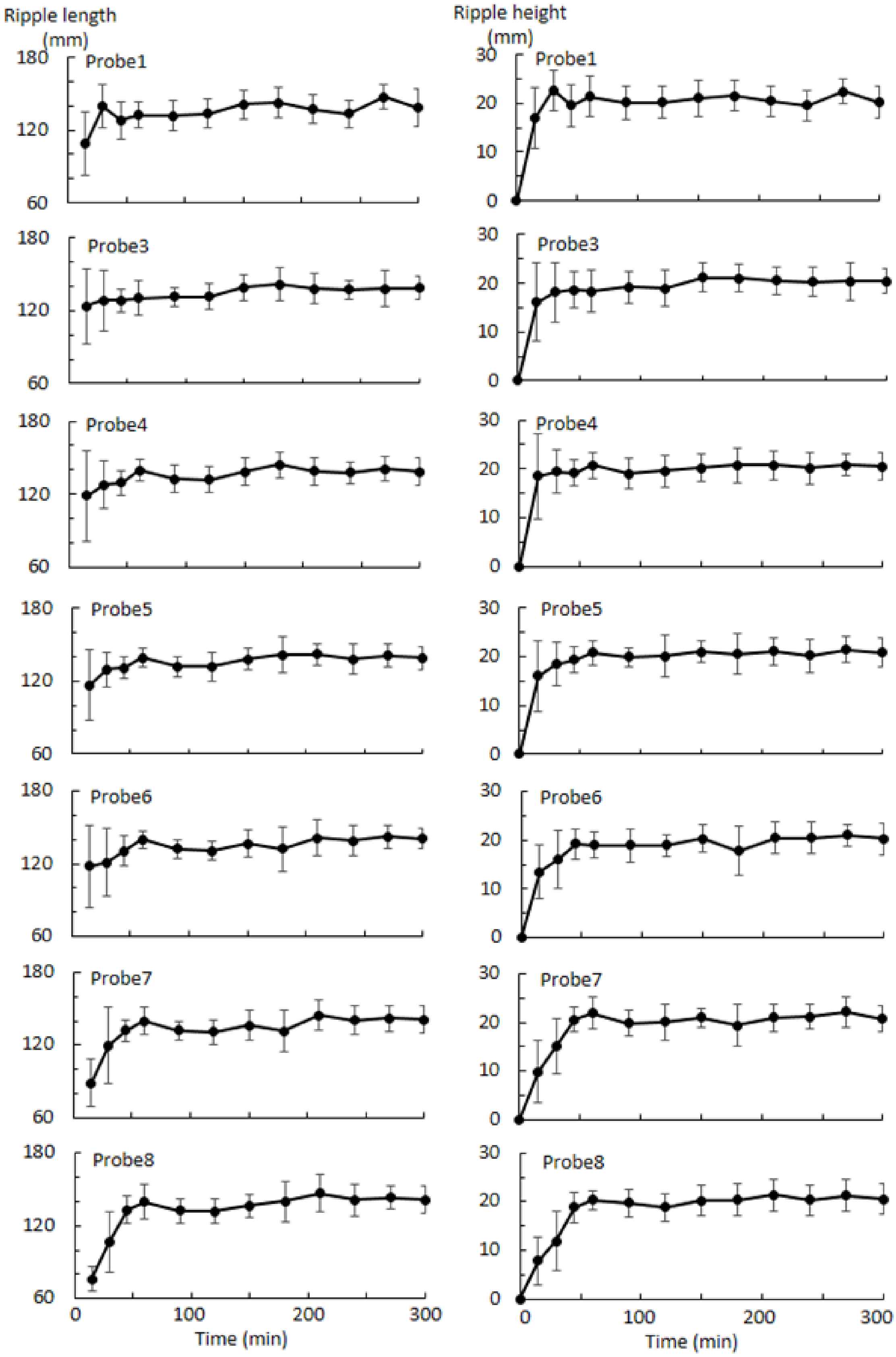

Figure 3-10.* *Development curves of ripple length and height of Run 03. The vertical black line denotes one standard deviation around the mean.

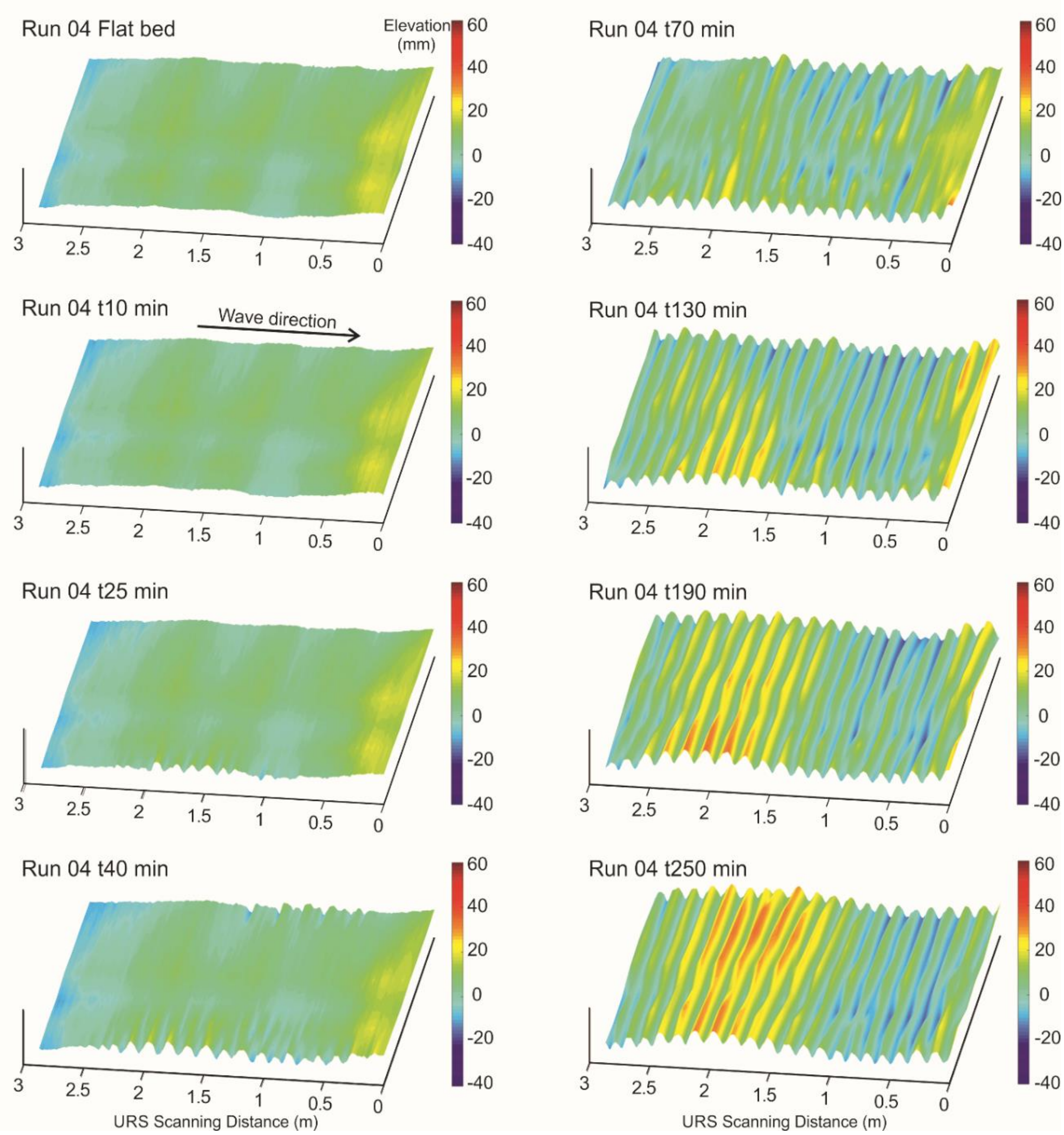

Figure 3-11. 3D images of wave ripples evolution of Run 04 with 6.2% clay fraction.

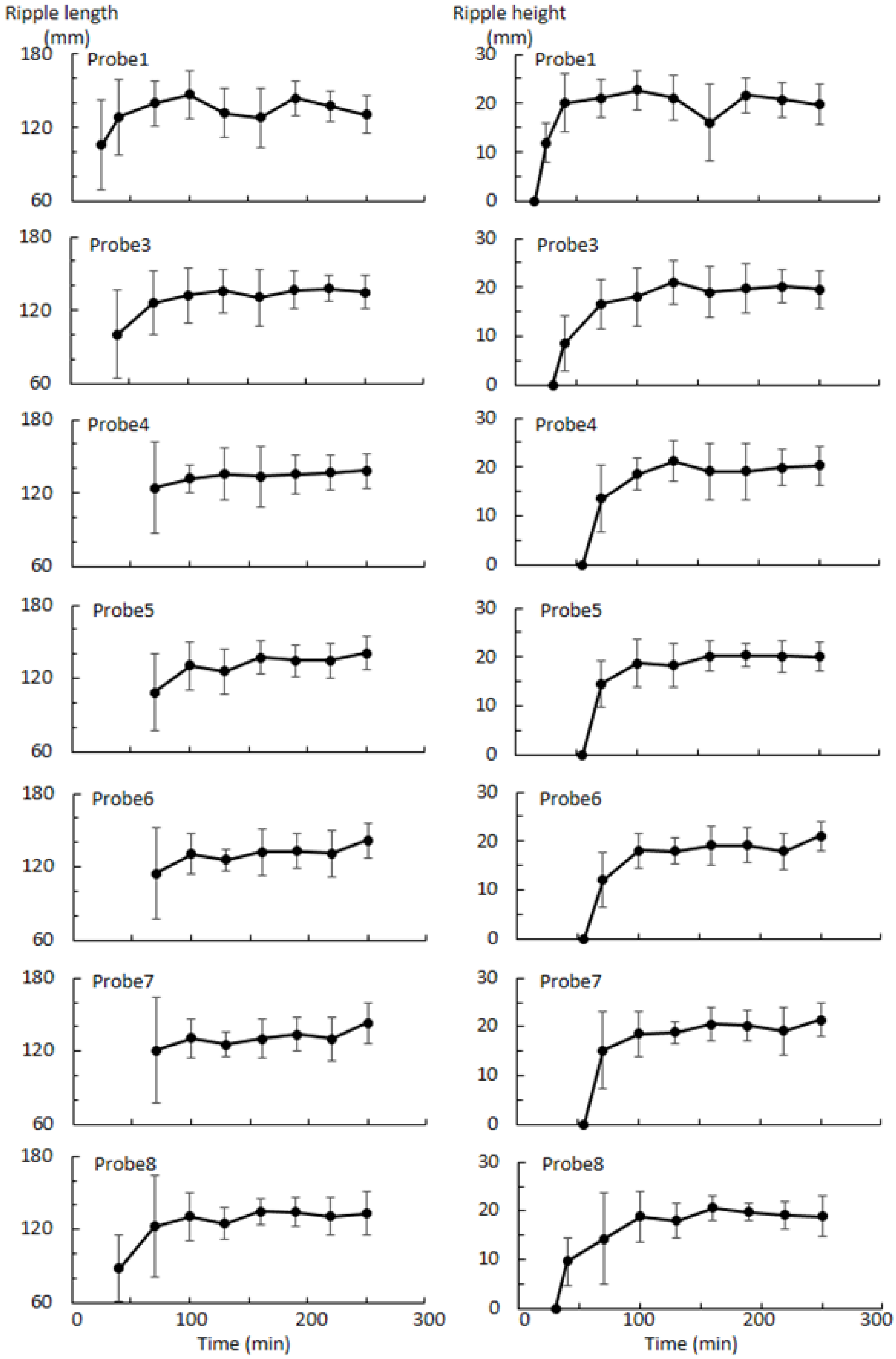

Figure 3-12. Development curves of ripple length and height of Run 04. The vertical black line denotes one standard deviation around the mean.

The experimental time of Run 05 and Run 06 were 510 minutes and 630 minutes, respectively. The wave-induced ripple developments of these two runs were quite similar, probably because of a minor difference of clay fraction between the two runs (7.2% for Run 05 and 7.4% for Run 06). The 3D images show the nucleus of wave ripples firstly appeared at edge at 30 minute and then the ripples expanded to other side of the flume. In the next 90 minutes the continuous train of ripples occupied scanning section. Three hours later most of the flume bed was covered by two-dimensional wave ripples (Figure 3-14; Figure 3-15) and the ripple dimension had evolved to be more stable. Yet, a patch of small, irregular bedforms formed at the downstream end (0-1 m) of the URS traverse in both runs (Figure 3-13). This patch of small ripples probably resulted from turbulent eddies around the instrument frame. Therefore, the enigmatic bedforms were ignored for the ripple length and height calculation by Bedform Tracking Tool.

Figure 3-13. Small and irregular bedforms generated beneath the instrument frame in Run 05.

It should be noted that the bed elevation changed dramatically when the wave ripples covered the entire bed. The middle and upstream elevation rose from flat bed to around 40mm, while the downstream elevation fall down to about～30mm (Figure 3-14; Figure 3-15).

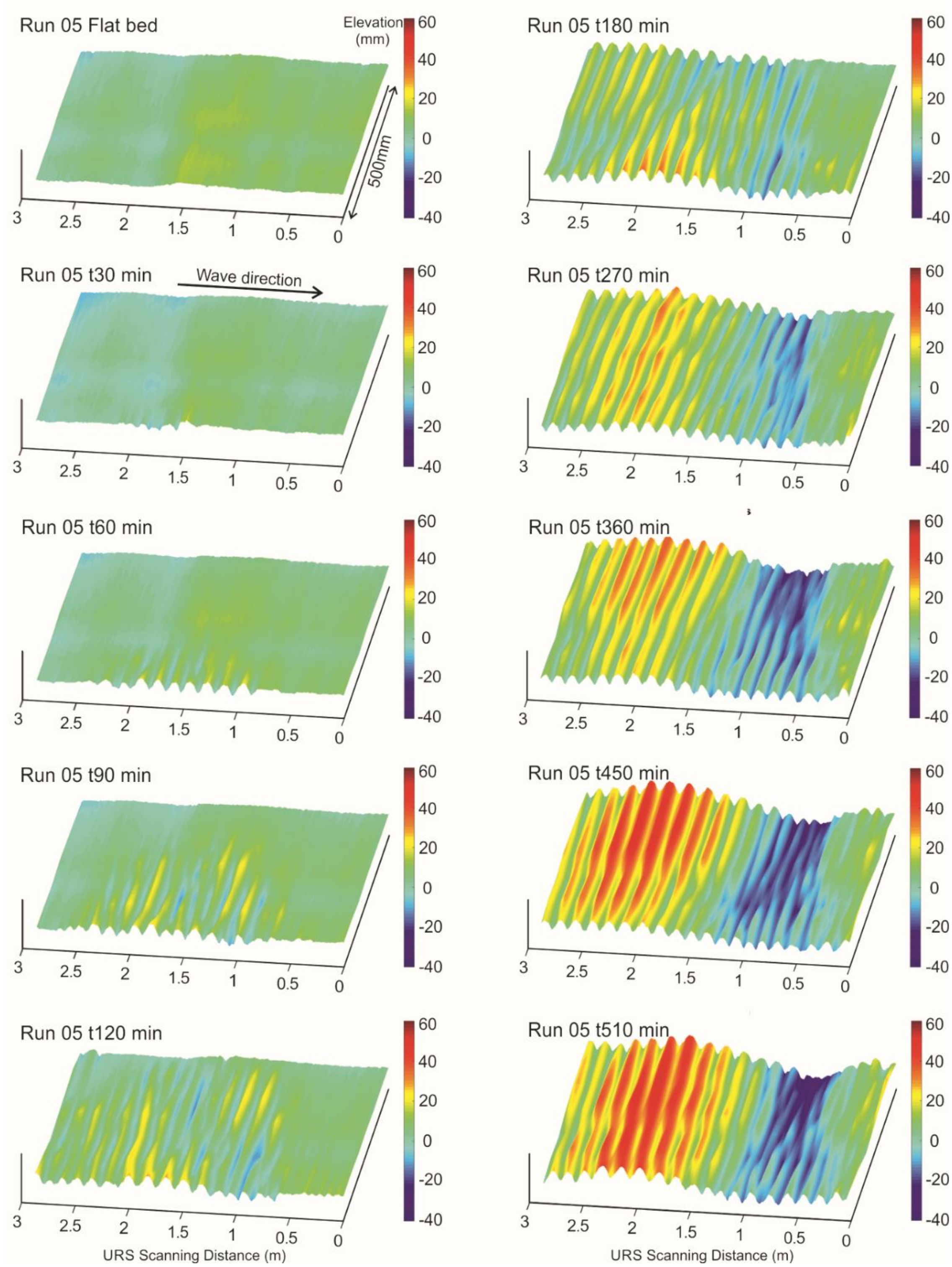

Figure 3-14. 3D images of wave ripples evolution of Run 05 with 7.2% clay fraction.

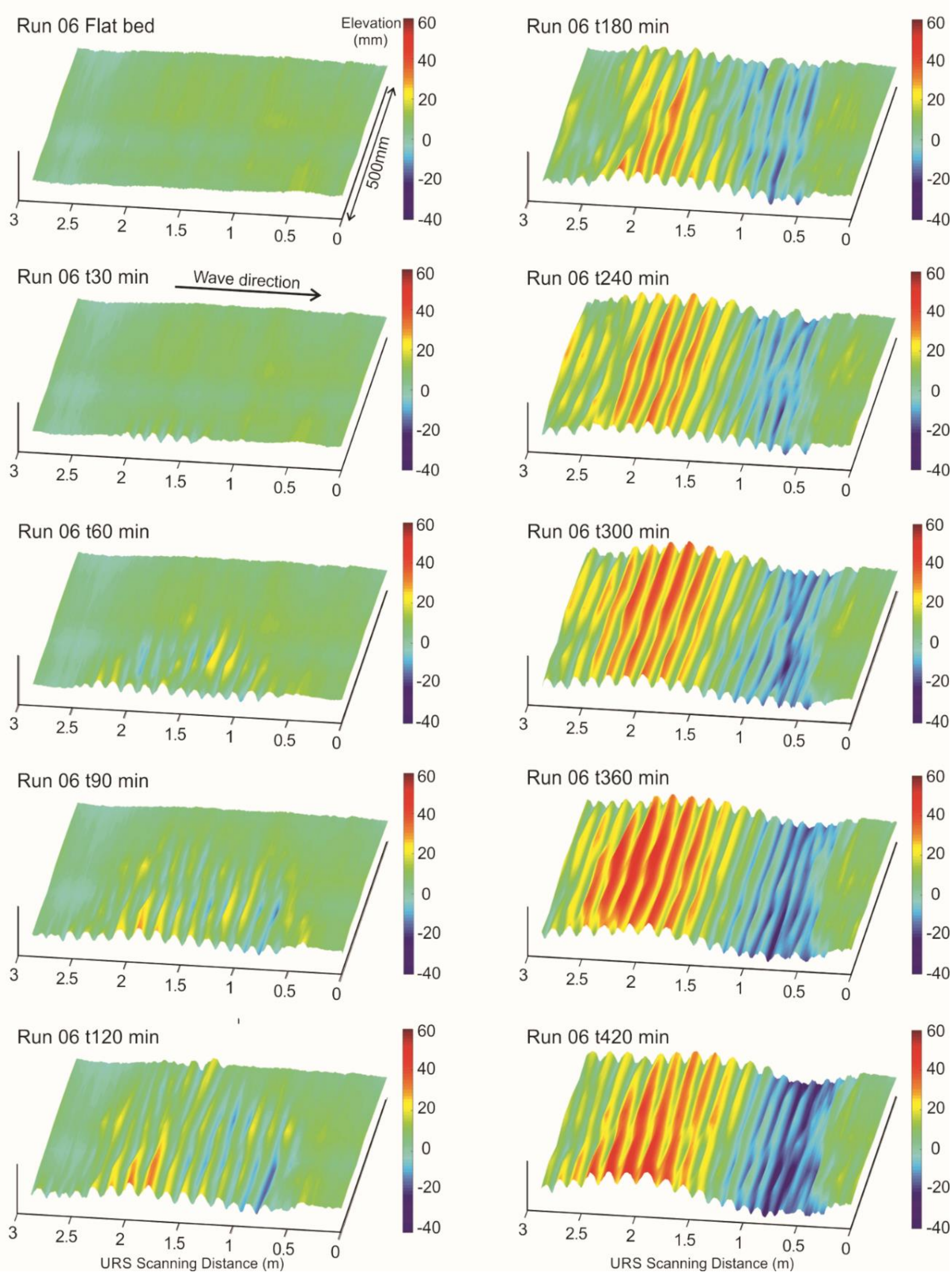

Figure 3-15. 3D images of wave ripples evolution of Run 06 with 7.4% clay fraction.

The ripple development curves (Figure 3-16, Figure 3-17, Figure 3-18, Figure 3-19) show more inhomogeneous growth of wave ripples in Run 05 and Run 06, comparing with the ones in the relatively lower clay fraction experiments. The nucleus of wave ripples firstly were detected by probe 1 in both Run 05 and Run 06, the mean length of these small wave ripples were 114.3mm and 103.5mm and the mean ripple height were 11.8mm and 11.1mm, respectively. The nucleus of ripples in Run 05 evolved to equilibrium at t=～145 min, with equilibrium length reaching to about 136 mm. During this period, ripples extended across the bed as well. Consequently, ripples at right edge of the bed along wave direction acquired equilibrium with a longer time, extending to 250 minutes. The equilibrium length slightly increased as well, standing at around 141 mm (Table 3-2). Similarly, the equilibrium time for ripple length in Run 06 varied heavily as well, the shortest equilibrium time standing at 131 minute for ripples beneath probe 1 and the longest time exceeding 260 minutes for ripples below probes 6 to 8. However the difference of equilibrium lengths among wave ripples was tiny, which were approach of 142 mm (Table 3-2).

The mean ripple height stood at 11.8 mm and 11.1 mm for Run 05 and Run 06 at t=30 min, respectively. Once wave ripples appeared from the flat bed in Run 05, the heights of most wave ripples developed very quickly in the following 30 minutes (Figure 3-17). Akin to the ripple length the inhomogeneous development led to large difference time for ripple height attaining to be stable. As shown in Table 3-2, the shortest equilibrium height time was 54 minutes for ripples that formed firstly. However, for the latest appearance of ripples, the equilibrium time for height was significantly increased to 169 minutes. In Run 06, there was a similar height growth mode as Run 05 (Figure 3-19), which resulted in the equilibrium height time increasing from 63 minutes for ripples beneath probe 1 to 189 minutes for ripples below probe 8 (Table 3-2). The equilibrium ripple heights in both high clay fraction runs were almost the same, reaching to approximately 20 mm (Table 3-2).

The relative higher standard deviations, comparing with other runs, reflects that the individual ripple size varied heavily even ripples had reached stable in Run 05 and Run 06. The significant change of bed elevation as mentioned above causes the remarkable difference of ripple size. As shown in Figure 3-14 and Figure 3-15, the middle upstream bed elevation (～1.8m<x<～2.5m) was higher, therefore the sizes of wave ripple developed in this area were bigger because of relative larger orbital velocity. Vice versa, the wave velocity reduced as declined bed elevation and the ripple sizes were smaller.

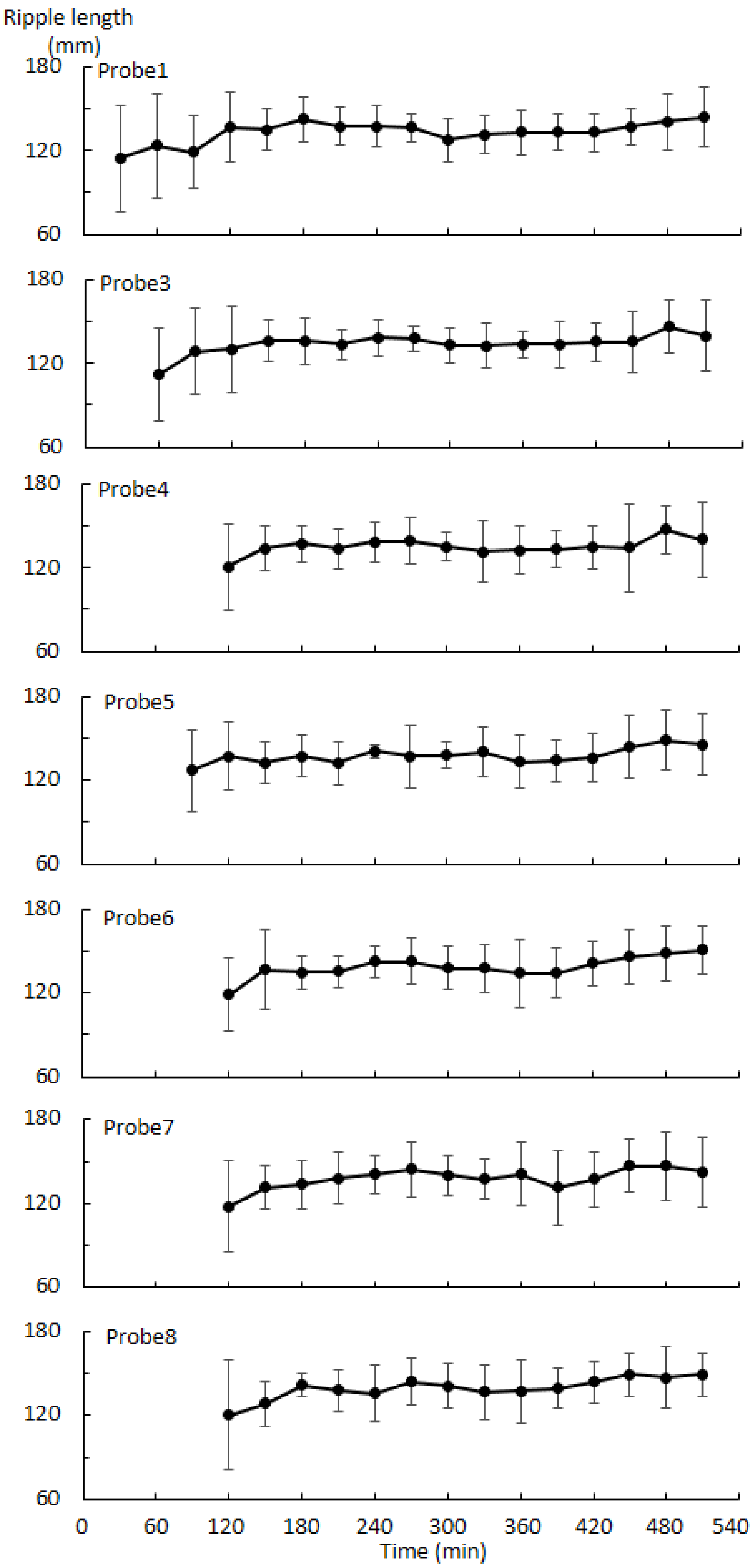

Figure 3-16. Wave ripple length development curves recorded by seven URS probes of Run 05 with clay content of 7.2%. The vertical black line denotes one standard deviation around the mean.

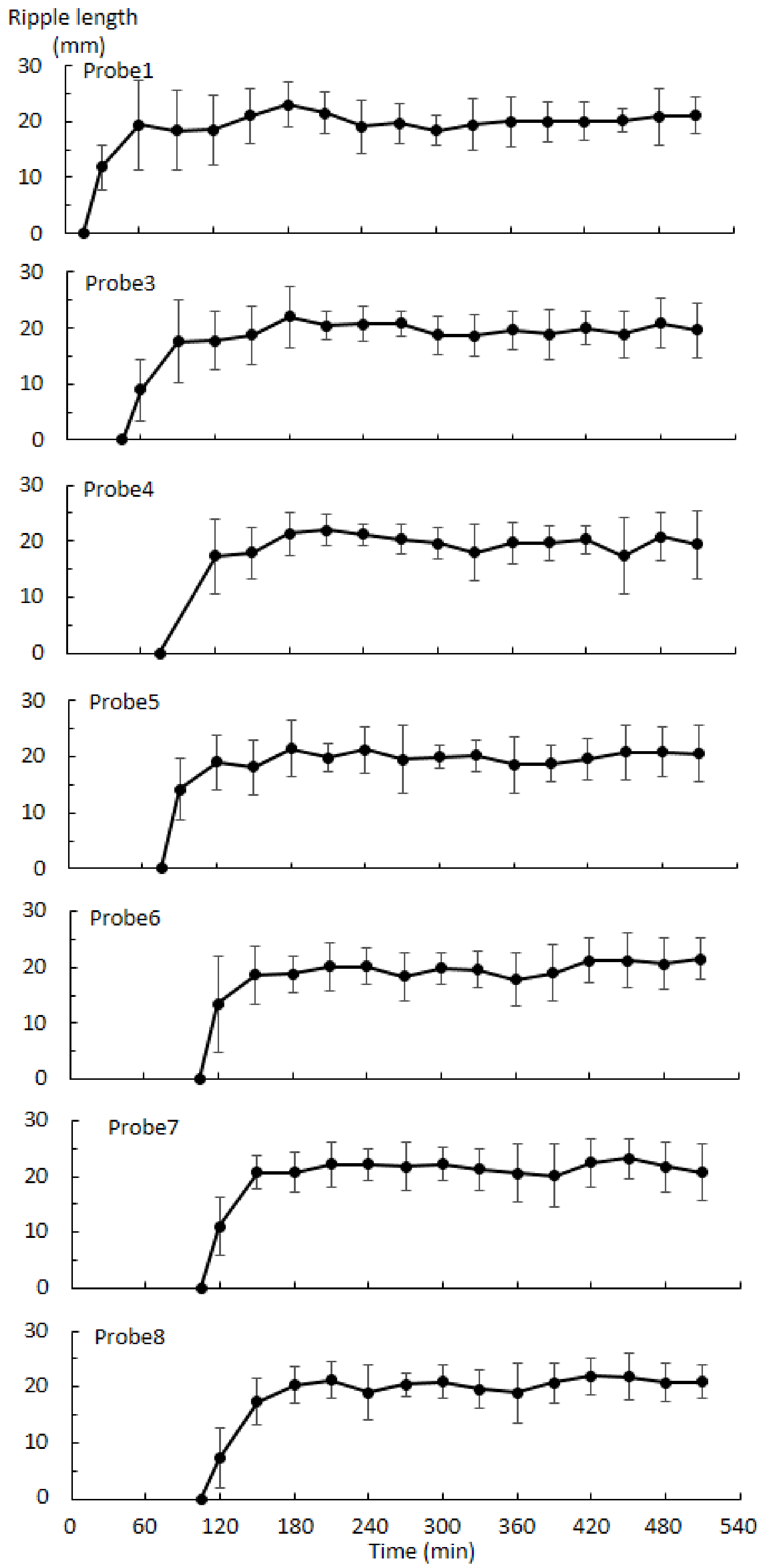

Figure 3-17. Wave ripple height development curves recorded by seven URS probes of Run 05 with clay content of 7.2%. The vertical black line denotes one standard deviation around the mean.

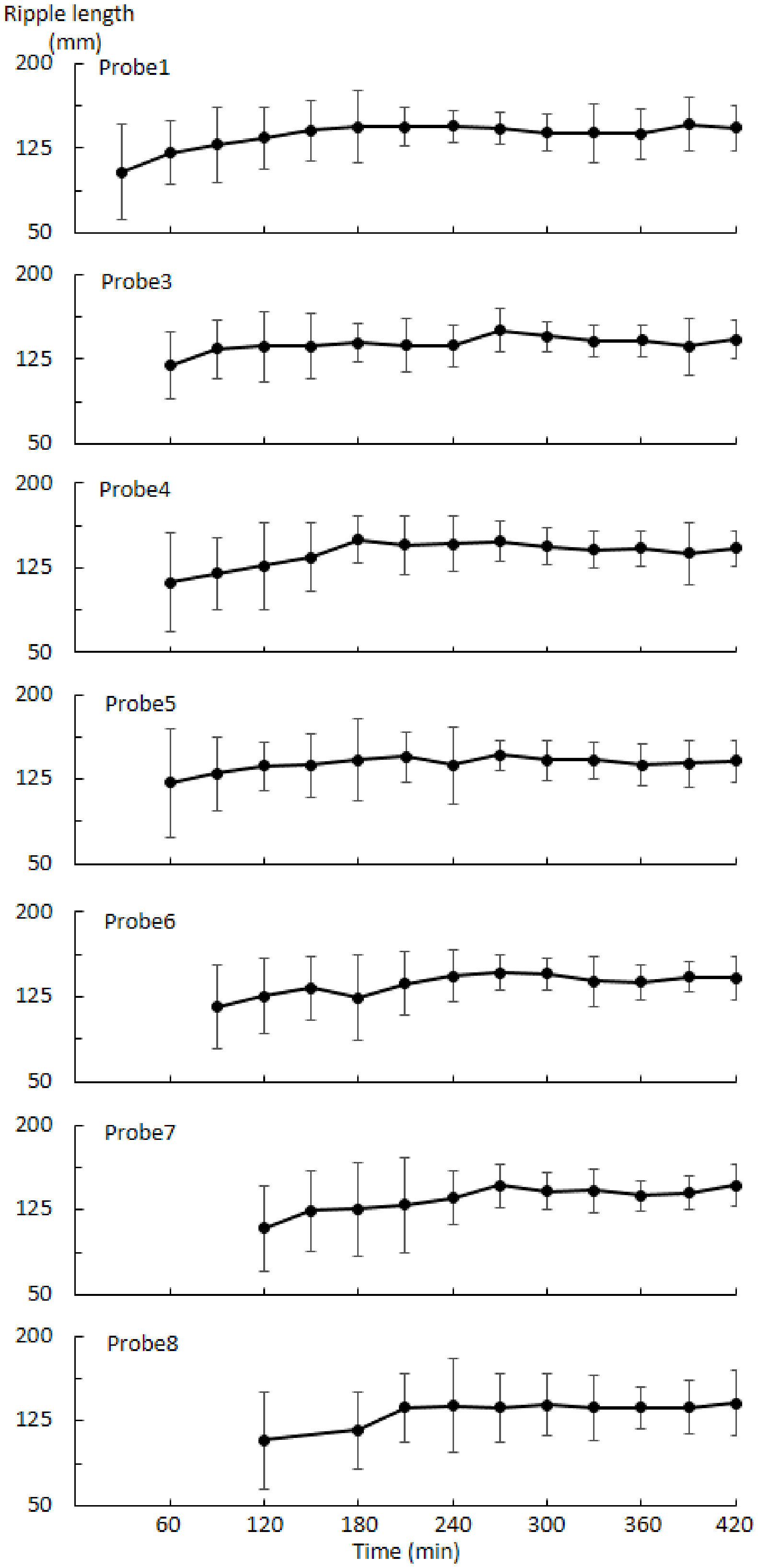

Figure 3-18. Wave ripple length development curves recorded by seven URS probes of Run 06 with clay content of 7.4%. The vertical black line denotes one standard deviation around the mean.

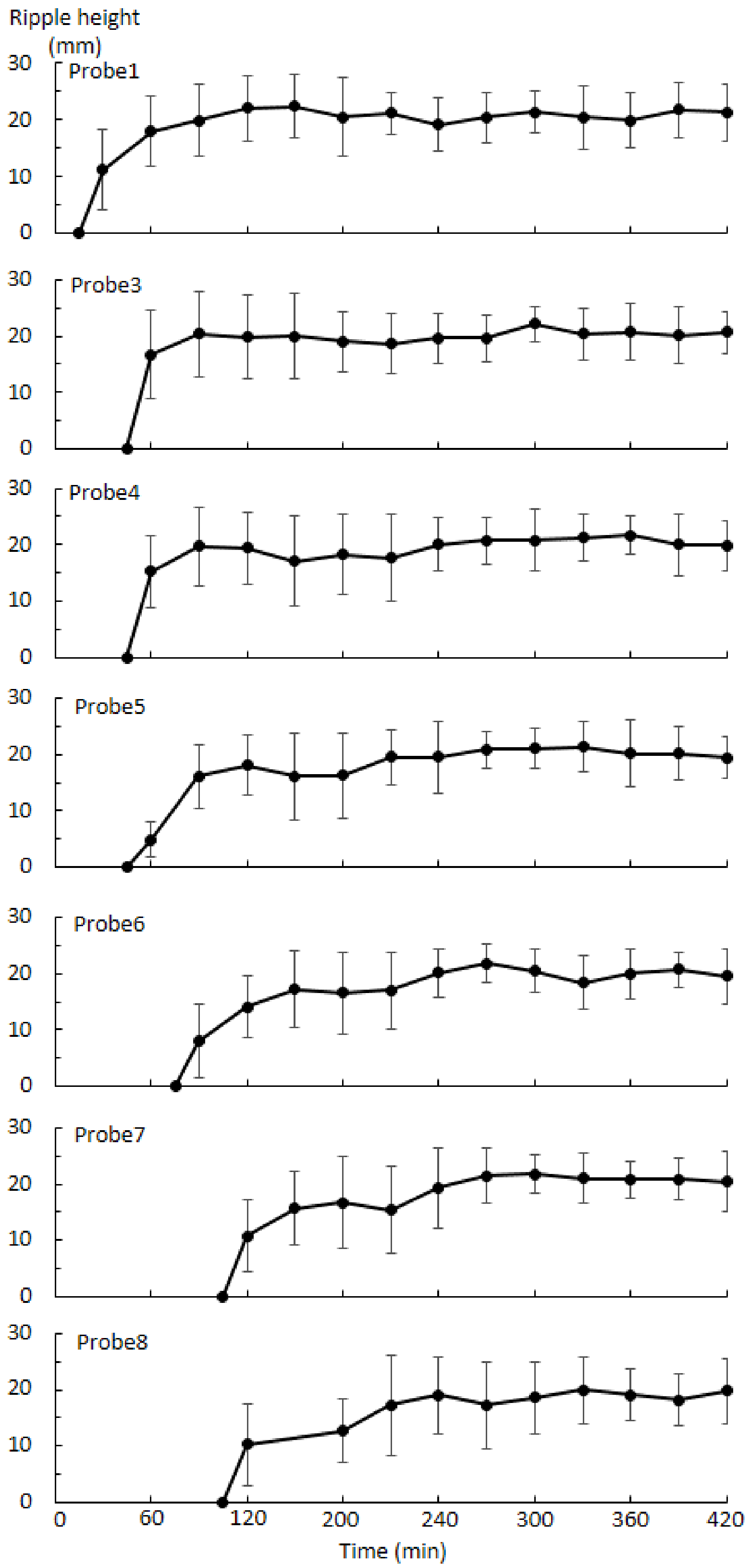

Figure 3-19. Wave ripple height development curves recorded by seven URS probes of Run 06 with clay content of 7.4%. The vertical black line denotes one standard deviation around the mean.

The final URS scanning revealed that the averaged ripple lengths calculated by Bedform Tracking Tool were 140.9mm for Run 03, 138.6mm for Run 04, 147.6mm for Run 05, and 150.1mm for Run 06. The results are very close to the actually measured ripple lengths after each run (Figure 3-20), which proves that the method for calculating ripple size mentioned in section 3.2 is suitable for the runs with clay as well.

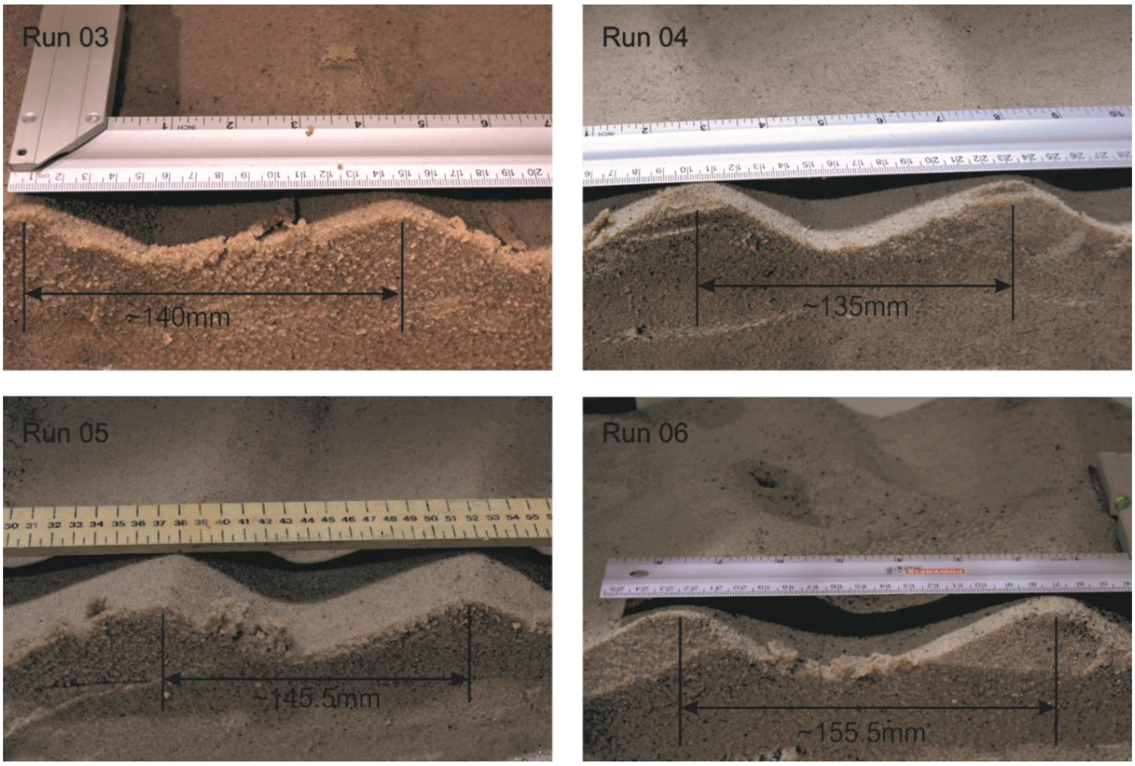

Figure 3-20. Measured ripple lengths after Run 03, Run 04, Run 05, and Run 06.

Table 3-2 Best solutions of Equations 3-5 and 3-6

Run	Probe	T_λ (min)	λ_e (mm)	λ_e Std (mm)	λ_0 (mm)	R(λ)	$T_{\lambda d}$ (min)	r_λ (mm/min)	T_η (min)	η_e (mm)	η_e Std (mm)	R(η)	$T_{\eta d}$ (min)	r_η (mm/min)	t_f (min)
	1	41	13.76	0.23	8.81	0.88	41	1.21	25	2.02	0.05	0.99	25	0.81	-
	3	38	13.55	0.24	8.23	0.86	38	1.40	30	1.98	0.09	0.98	30	0.66	-
	4	41	13.55	0.21	8.00	0.92	41	1.35	26	1.94	0.05	0.99	26	0.75	-
	5	35	13.51	0.23	9.56	0.77	35	1.13	24	2.01	0.07	0.99	24	0.84	-
	6	34	13.56	0.45	9.80	0.60	34	1.11	19	1.94	0.06	0.99	19	1.02	-
	7	45	13.57	0.43	7.56	0.82	45	1.34	33	2.01	0.07	0.99	33	0.61	-
	8	43	13.61	0.41	9.30	0.71	43	1.00	30	1.99	0.04	0.99	30	0.66	-
	1	58	13.81	0.46	10.65	0.77	31	1.02	18	2.08	0.07	0.98	11	1.89	7
	3	67	13.7	0.31	11.00	0.76	60	0.45	20	1.98	0.07	0.98	13	1.53	7
	4	62	13.83	0.3	10.83	0.87	55	0.55	15	2.01	0.04	0.99	7	2.87	7
	5	60	13.85	0.32	10.87	0.88	53	0.56	20	2.04	0.05	0.99	13	1.57	7
	6	65	13.75	0.37	10.58	0.84	58	0.55	26	1.95	0.08	0.98	18	1.08	7
	7	72	13.88	0.43	9.25	0.89	45	1.03	39	2.09	0.08	0.98	32	0.65	7
	8	77	14.12	0.51	7.65	0.93	56	1.16	53	2.05	0.09	0.98	46	0.45	7
	1	59	13.7	0.71	9.50	0.82	44	0.95	39	2.05	0.17	0.96	24	0.85	15
	3	84	13.51	0.3	8.16	0.98	54	0.99	76	1.96	0.08	0.99	46	0.43	30
	4	140	13.67	0.29	11.78	0.96	85	0.22	86	1.98	0.08	0.99	31	0.64	55
	5	133	13.68	0.87	9.43	0.93	78	0.54	82	1.97	0.07	0.99	27	0.73	55
	6	107	13.37	0.61	9.50	0.84	52	0.74	91	1.91	0.11	0.99	36	0.53	55
	7	134	13.41	0.85	10.90	0.68	79	0.32	80	1.98	0.10	0.99	25	0.79	55
	8	76	13.18	0.41	8.92	0.98	46	0.93	75	1.91	0.14	0.98	45	0.42	30
	1	145	13.61	0.36	10.61	0.75	130	0.23	54	2.01	0.95	0.97	39	0.52	15
	3	120	13.61	0.23	9.79	0.88	75	0.51	101	1.98	0.97	0.98	56	0.35	45
	4	175	13.67	0.32	10.20	0.67	100	0.35	128	1.99	0.94	0.97	53	0.38	75

Table 3-2 continued

Run	Probe	T_{λ} (min)	λ_e (mm)	λ_e Std (mm)	λ_0 (mm)	R(λ)	$T_{\lambda d}$ (min)	r_{λ} (mm/min)	T_{η} (min)	η_e (mm)	η_e Std (mm)	R(η)	$T_{\eta d}$ (min)	r_{η} (mm/min)	t_f (min)
	5	209	13.96	0.36	12.20	0.58	134	0.13	104	1.99	0.97	0.98	29	0.69	75
	6	187	14.12	0.4	10.85	0.76	72	0.45	137	1.98	0.96	0.98	32	0.62	105
	7	198	14.1	0.33	10.78	0.85	83	0.40	150	2.17	0.98	0.99	45	0.48	105
	8	253	14.37	0.44	11.95	0.71	138	0.21	169	2.07	0.97	0.98	64	0.32	105
	1	131	14.23	0.26	8.94	0.97	116	0.46	63	2.09	0.06	0.99	48	0.43	15
	3	132	14.13	0.33	10.96	0.85	87	0.36	65	2.01	0.06	0.99	20	1.00	45
	4	178	14.42	0.5	9.87	0.92	133	0.34	69	1.97	0.08	0.97	24	0.82	45
	5	146	14.13	0.25	11.28	0.92	101	0.28	134	2.00	0.12	0.97	89	0.22	45
	6	265	14.32	0.72	11.05	0.89	190	0.17	161	1.97	0.11	0.98	86	0.23	75
	7	284	14.38	0.67	10.24	0.95	179	0.23	172	2.01	0.15	0.96	67	0.30	105
	8	262	14.01	0.73	9.84	0.92	157	0.27	189	1.86	0.19	0.95	84	0.22	105

$T_{\lambda d}$: Ripple length development time from flat bed to reach equilibrium of each probe

$T_{\eta d}$: Ripple height development time from flat bed to reach equilibrium of each probe

R: Correlation coefficient of the best-fit curve

r_{λ} : Ripple length growth rate

r_{η} Ripple height growth rate

3.3.2 Equilibrium state of regular wave-induced ripple

The data of the seven URS probe were averaged to fully investigate the relationship between initial bed clay fraction and the main properties of the equilibrium wave ripples (Figure 3-21). The equilibrium wave ripple lengths were nearly constant slight fluctuating around 137 mm in the control run 01 and in the Run 03 and Run 04. The value at relative higher clay fraction (7.2% of Run 05; 7.4% of Run 06) were marginally longer, reaching to 139.2 mm and 142.3 mm, respectively (Figure 3-21C). In terms of equilibrium wave heights, the values are almost the same at around 20 mm from Run 01 to Run 06 (Figure 3-21D). In general the equilibrium wave length and height appeared to be independent of initial bed clay fraction for the applied experimental conditions.

However, there is a positive correlation between equilibrium time for wave ripple length and height and the initial bed clay fraction. The mean equilibrium time of ripple length increased exponentially with increasing clay fraction from 40 minutes of Run 01 to 200 minute of Run 06 (Figure 3-21A). The averaged equilibrium time of wave ripple height in Run 01 and Run 03 were quite close, standing at 27 minutes. It rapidly increases with clay fraction increasing from 4.2% to 7.2%, reaching to 120 min in Run 05. In Run06 with slightly higher clay fraction, the equilibrium time of ripple height almost the same with that of Run 05 (Figure 3-21B). The relative higher standard deviations of Run 05 and Run 06 indicate significantly different delay time of ripple appearance at different part of bed.

In addition, Figure 3-21E shows a negative relationship between the mean ripple length growth rate and the initial bed clay fraction. The mean ripple length growth rate reached to 1.2 $mmmin^{-1}$ with pure sand bed in Run 01. The rate declined dramatically to only 0.2$mmmin^{-1}$ in the highest clay fraction experiment (Run 06). The mean ripple height growth rate was 1.4 $mmmin^{-1}$ in Run 03, even much higher than the rate on the clay-free bed of Run 01 (0.8 $mmmin^{-1}$). The reason is the anomalously faster ripple height growth rate at the right half scanning area along wave direction (Table 3-2). However, the figure remarkably fell in the experiments with clay fraction over 6%, standing at around 0.5 $mmmin^{-1}$ in Run 06(Figure 3-21F).

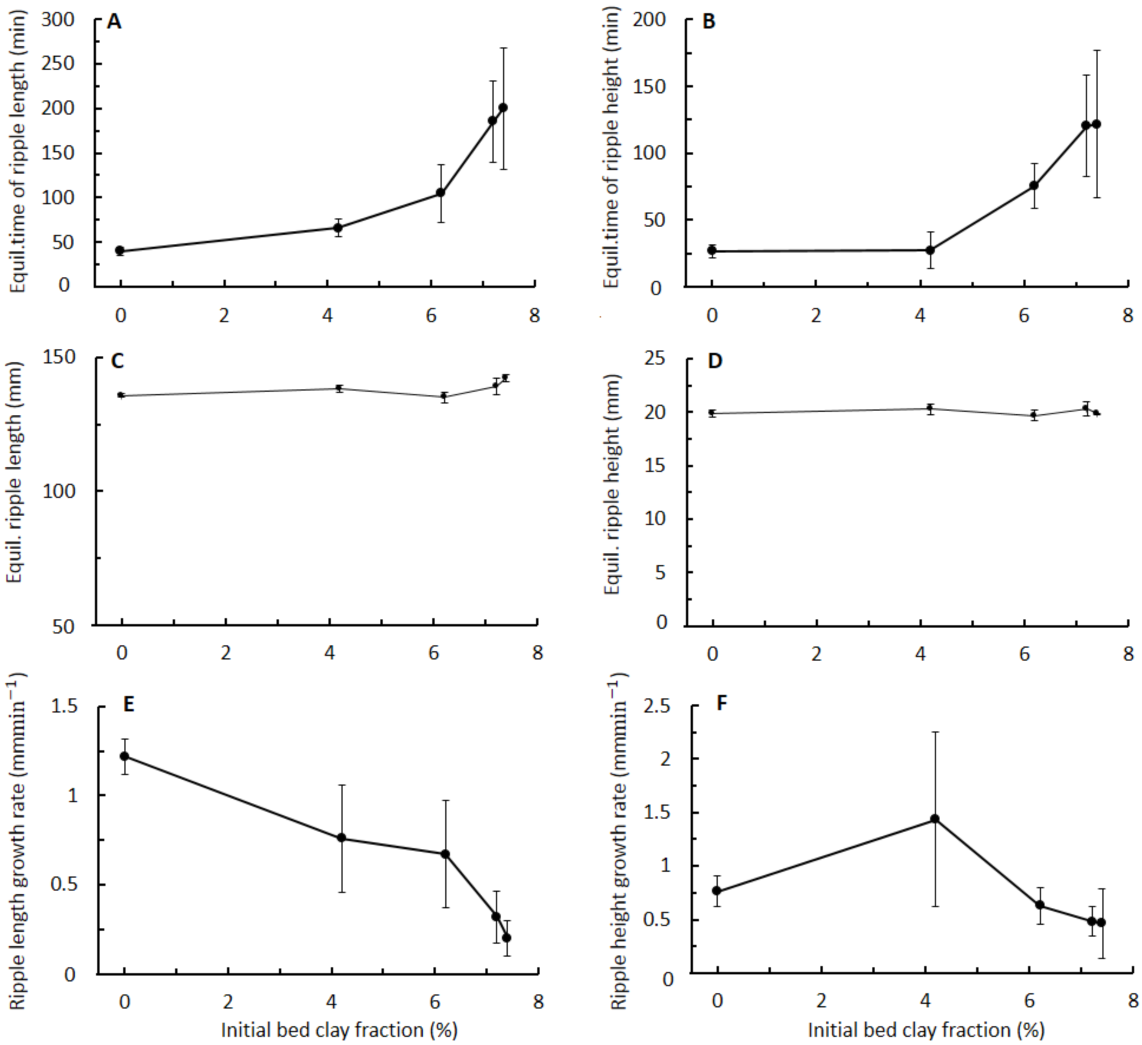

Figure 3-21. the main properties of the equilibrium wave ripples against initial bed clay fraction. The vertical black line denotes one standard deviation around the mean.

3.3.3 Wave ripple migration rate under regular waves

The ripple movements were observed in the experiments because of asymmetrical wave velocity that maximum onshore velocities were slightly higher than the maximum offshore velocities (Table 3-1). Two Bedform Elevation Profiles (BEP) were recorded by upstream and downstream fixed URS probes to investigate wave ripple migration of each run (Figure 3-22). In the control experiment (Run 01), the wave ripple did not move until t=53 min when the ripples had achieved equilibrium, with the migration rate reaching to 0.06 mm s^{-1}(Figure 3-22).

In Run 03, both fixed URS detected several small ripples movement in the first 50 minutes. The relatively bigger wave ripples started to pass through upstream probe and then downstream probe when the wave ripples attained equilibrium. The mean migration rate was 0.04 mm s^{-1}. The wave ripples crept until 135 minutes in Run 04 and since then they moved faster, with the migration speed at 0.03 mm s^{-1}. In Run 06, the bed elevation beneath the fixed URS was constant until t=$\sim$180 min, before gradual decreasing (Figure 3-22). The URS probes recorded mature wave ripple started to migrate at t=420 min, with the averaged migration rate of 0.02 mms^{-1}.

In Run 05, the upstream URS probe did not work, thus only one BEP is available to estimate ripple migration rate. Akin to Run 06 the bed remained flat in the first 110 minute, and beyond that the bed elevation fluctuated before it gradually decreased from t=265 min. The downstream probe recorded the first ripple crest at about t=331 min when the wave ripples had attained an equilibrium (Figure 3-23). The ripple migration is roughly determined as the equilibrium wave ripple length divided by the time between two successive crests. As a result, the mean ripple migration rate was around 0.04 mms^{-1}.

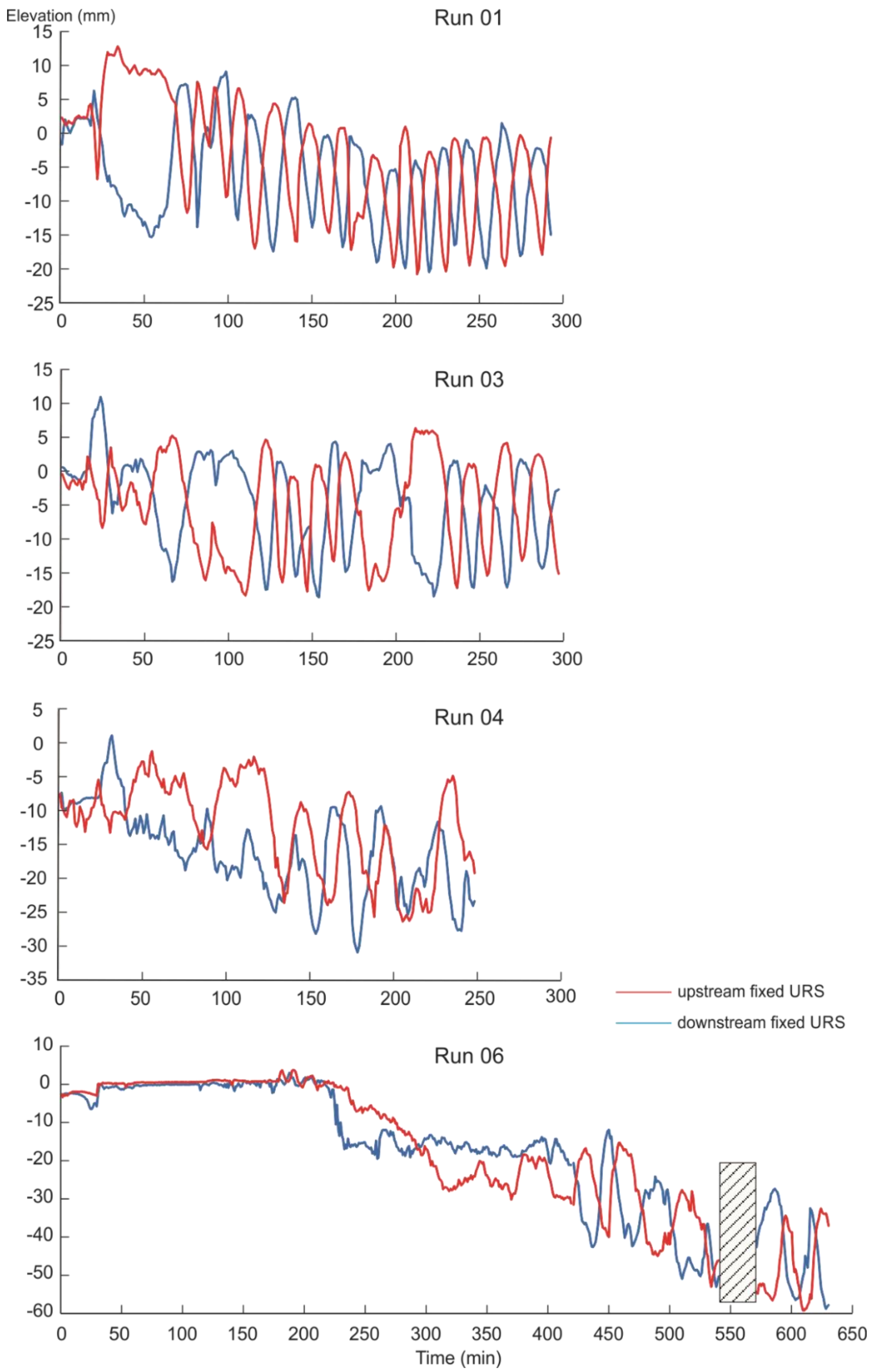

Figure 3-22. Bedform Eleavtion Profiles recorded by upstream and downstream URS (the red line and blue line repectively) are used to determine wave ripple migration rate. The rectangle shade area denote data lost as technical problem of URS probes.

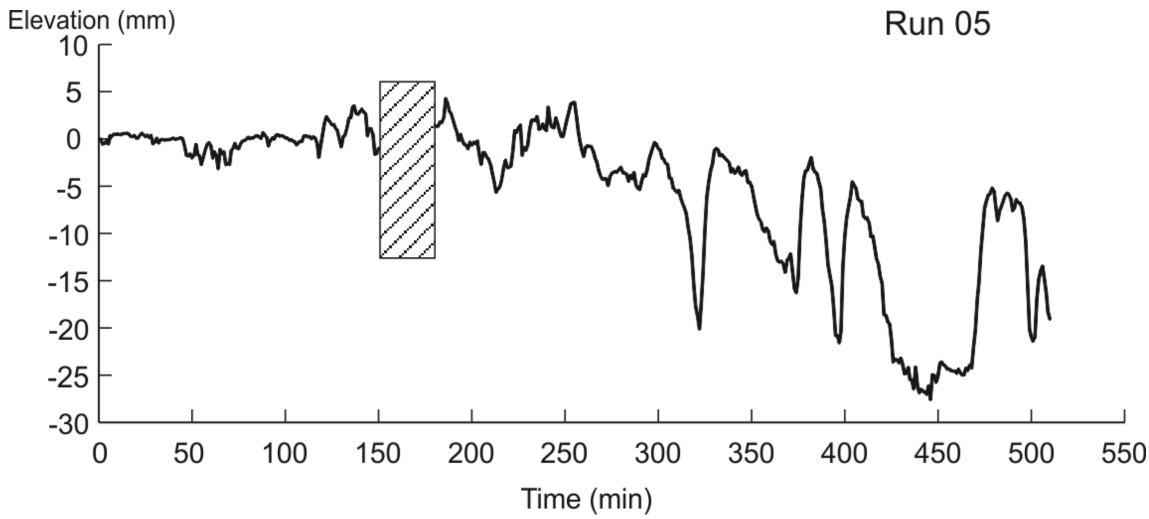

Figure 3-23. Bedform Eleavtion Profiles recorded by downstream URS is used for estimation of wave ripple migration of Run 05. The rectangle shade area denote data lost as technical problem of URS probe.

3.3.4 Regular wave-induced ripple cross-section form geometry

Steepness and symmetry are significant properties of wave-generated ripples. Therefore Bedform index (BI) and Bedform Symmetry Index (BSI) were introduced by Tanner (1967). In general, the wave ripple is defined as low angled if the BI is smaller than 3 and is defined as symmetric if the BSI is smaller than 1.5 (Perrilo et al., 2014). In the present study ripple height of lee face was used to calculate bedform steepness. Both results of bedform Index and bedform Symmetry Index reflect the wave ripple cross-section form geometry under equilibrium situation (Table 3-3).

Table 3-3 The mean Bedform Index (BI) and Bedform Symmetry Index (BSI) of each run with wave ripples reaching equilibrium.

Run	BI	Std Deviation	BSI	Std Deviation
1	6.88	0.14	1.17	0.04
3	6.81	0.08	1.11	0.04
4	6.85	0.10	1.07	0.02
5	6.86	0.19	1.08	0.04
6	7.16	0.34	1.11	0.03

The averaged Bedform Index of ripples formed under regular waves were around two times higher than 3 (Table 3-3), which suggests that all of the wave ripples under present experiment conditions were higher angled. In addition, as shown in Table 3-3, the regular wave-induced ripples were very symmetric with the mean BSI of each run was quite close to 1 (perfect symmetry).

Figure 3-24 shows that both BI and BSI are independent with initial bed clay fraction increasing. The results indicate that the cross-section form geometry of ripples generated under regular waves were basically the same without influence of initial bed clay fraction.

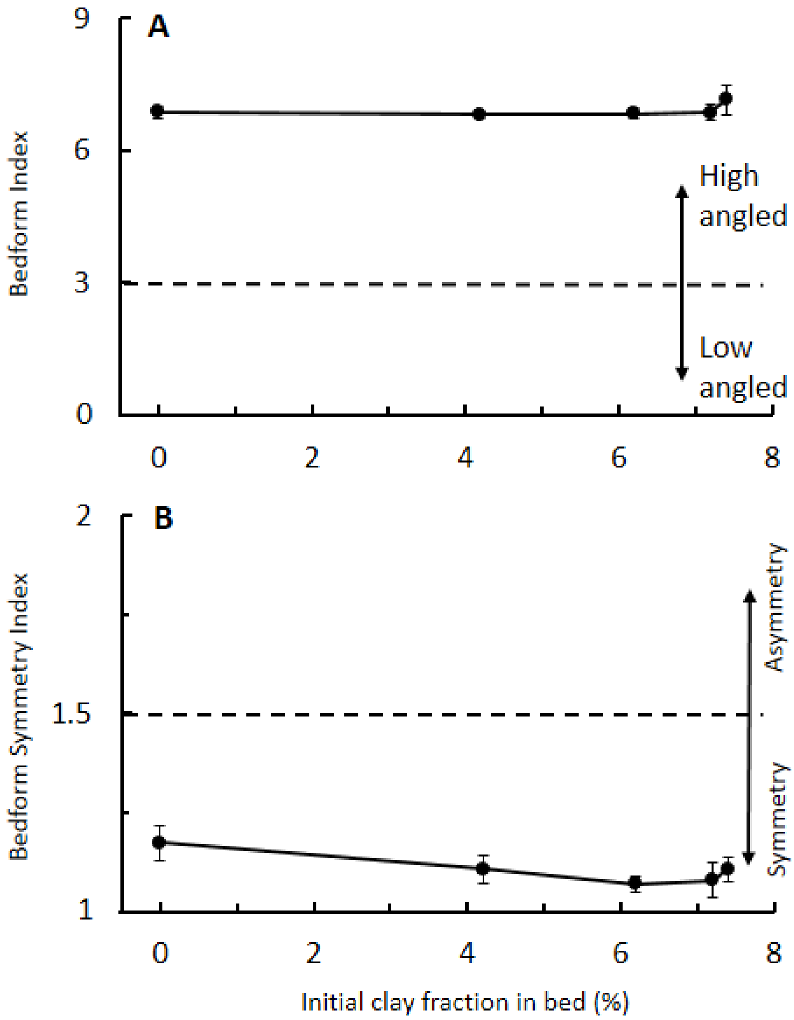

Figure 3-24. Bedform Index (A) and Bedform Symmetry Index (B) agaist initial bed caly fraction.

3.3.5 Granulometry

The post-run profiles of bed sand fraction reveal that the mixed-sediment beds experienced substantial changes in granulometry under wave-induced bed shear stress. Figure 3-25 shows characteristic profiles of bed sand fraction below ripples crests and troughs. There were pure sand layers (100% sand fraction) at top of cores collected from crests, thickness varying from 10 mm to 30 mm. However, the top clay-free layers were not formed for the cores collected from ripples troughs.

Changes in sand fraction of sediment cores between flat bed and rippled bed are shown in Figure 3-26. Sand fraction significantly increased at upper layers of cores from ripples crests, with around 10% of sand content increase in the top ripple crest in Run 05. Sand fraction increase at upper layers of ripples troughs was smaller than that beneath ripples crests except Run 04 in which sand fraction at trough top basically remained the same as flat bed. Moreover, comparing with original sand fraction, sand fraction of sediment cores declined at intermediate and lower layers. Additionally, at the bottom of most sediment cores, sand fraction tended to gradually exceed initial content before the experiments.

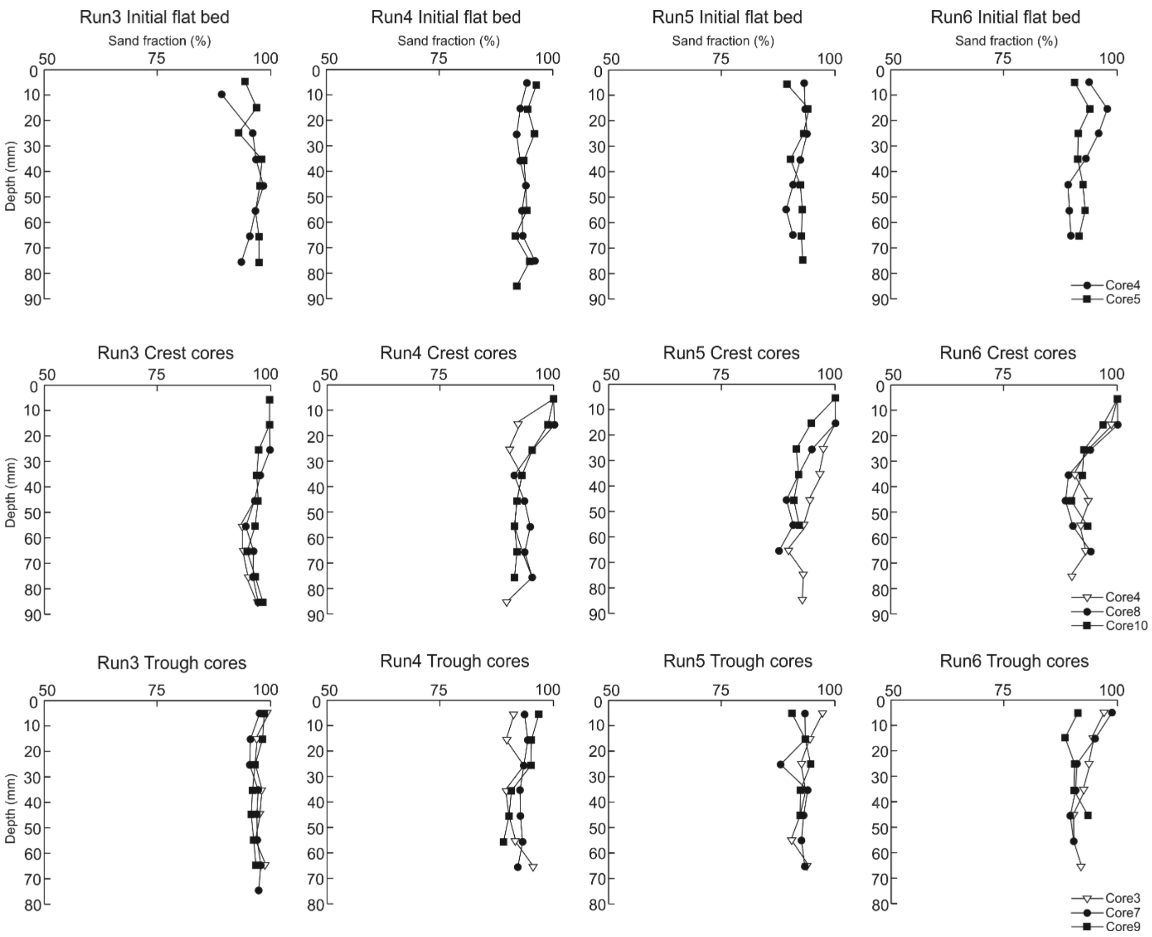

Figure 3-25. Vertical changes in bed sand fraction in cores collected before and after each run.

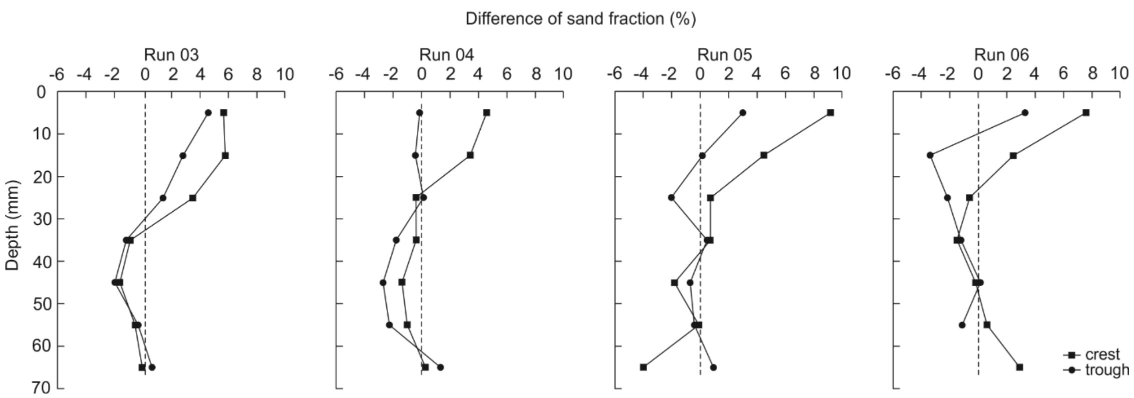

Figure 3-26. Sand fraction change compared with cores collected before and after each run. Black square line and dot line denote sand fraction change in cores collected at ripple crests and troughs, repectively. Vertical black dash line denote reference without change of sand fraction

3.4 Discussion

3.4.1 Wave ripples evolution stages

Previous studies investigated ripples with non-cohesive sands developed from flat bed to stable states under currents (e.g., Baas, 1993; Baas, 1994; Baas, 1999) and under waves (e.g., Perillo, 2013). In the experiments of Baas (1993, 1994, and 1999), four stages of ripples evolution, based on plan form evolution can be identified; including incipient ripples, 2D sinuous and straight ripples, 3D non-equilibrium ripples and 3D equilibrium ripples. Perillo (2013) identified four stages of ripples development according to ripple growth rate. They are incipient stage from flat bed to formation of small grain-rolling ripples, growing stage that ripple size significantly increasing, stabilizing stage that ripple growth rate rapidly declines, and fully-developed stage that ripples reaching equilibrium (Perillo, 2013). For the present experiment, as shown in Figure 3-7 ripple development curves in Run 01 with pure sand are similar with the experiment of Baas (1999) and Perillo (2014b). Nevertheless, the scenario is different with clay added into bed. The bed with cohesive clay was stable enough to resist wave erosion and remained basically flat with time varying from several minutes to around half an hour. Therefore, a pre-incipient ripples stage is introduced, from initial bed erosion to formation of the nucleus of wave ripples. As the first stage for ripples development with cohesive sediments, the most part of bed remains flat. This new step is absent, or precisely is immediately in the previous studies with pure sand bed (e.g., Baas, 1999; Perillo, 2014). Once the nucleuses of wave ripples are generated, the bed evolves to incipient ripple stage, with ripple crest lines gradual expanding until formation of two-dimensional ripples. Perillo (2014b) defined incipient step from initiation of beform until the first signs of ripple growth. The new definition emphasized change of planform geometry not only reflects characteristics of ripples development with cohesive bed, but also is an easier criterion to identify ripple evolution stage under experimental conditions. Then in the growth stage, both the average wavelength and height of two-dimensional ripple continue to increase. Finally, akin to ripples developed with pure sand bed, wave-induced ripples reach equilibrium, the mean ripple length and height converging to singular values and ceasing to sharp change with time.

3.4.2 The influence of clay on the ripple development

Bed critical shear stress for erosion could be significantly enhanced with increasing cohesive sediment added into noncohesive sand bed, because of electrochemical force leading to bind sand particles together (Collins, 1990; Alvarez-Hernandez, 1990; Amos et al., 1995; Mitchener and Torfs, 1996; Panagiotopoulos et al. 1997). Mitchener and Torfs (1996) collected data from both flume experiments and field works and suggested that mixture of mud and sand increases erosion resistance, particularly the bed behaviour transform from cohsionless to cohesive with gradually increase mud fraction from 3% to 15% by weight. Panagiotopoulos et al. (1997) found that clay fraction of 11% by weight is a threshold criterion, higher clay fraction changing deposit structure and finally increasing erosion rate. Thus the positive correlation between critical shear stress for erosion and clay fraction, and the negative correlation between bed erosion rate and clay fraction, may both contribute to these causes. The present experiment results show a relatively small increase in bed clay fraction (4.2% to 7.4%) is able to distinctly increase erosion resistance, which is consistent with previous findings. Most importantly, the results highlight the role of cohesive sediment on bedform dynamics by delaying ripples appearance on flat bed. Experimental results provide evidence cohesive force within clay-sand substrates proportionally slowed down ripple growth rate and then remarkably increased time of ripples growth to reach equilibrium from Run 03 to Run 06. However, the experiments that conducted under unidirectional flow conditions of Baas et al. (2013) did not display a reverse relationship between initial clay fraction (from 1.8% to 7.5%) and equilibrium time. The reason is probably due to the difference of ripple migration rate under different flow conditions. The ripple migration rate with pure sand under unidirectional flow reached to approximately 0.12 mms^{-1}, which is twice as fast as the figure in the present experiment (~0.065 mms^{-1}, Figure 3-27). In addition, ripple migration rate decreases to only 0.02 mms^{-1} in Run 06 with clay fraction of 7.4% (Figure 3-27), while the rate with similar clay fraction of bed in the study of Baas et al. (2013) varied from 0.04 mms^{-1} to 0.06 mms^{-1}. Moreover, the strong reverse relationship between clay fraction and ripple migration rate in the present study is not apparently in the experiment of Baas et al. (2013). Ripple development is closely related to bed erosion and ripple migration rate. Faster movement of current ripples contributes to a larger volume of the eroded bed in time than that due to slower migration of wave ripples. Therefore, wave ripples development is presumably by bed erosion in ripple troughs. With increasing initial clay fraction, the erosion efficiency of this mode of wave evolution gradually declines, therefore extending time for wave ripples reaching to equilibrium. In addition, comparing with bed sediment flux with pure sand, it was lower over the clay-sand mixture substrates (Figure 3-27), possibly due to the calculation largely related to ripple migration rate. Furthermore, increasing bed clay fraction contributes to bed stabilization, even eave ripples have formed. In the control experiment (Run 01), the wave ripples started to move quickly around 25 minutes after reaching equilibrium. While in Run 06, the URS probes detected wave ripple migration after 400 minute which around 2 hours after wave ripples reaching equilibrium (Figure 3-22). The progressive reduction of migration rate and sediment flux with the increase of be clay fraction enable the bed to be more stable, which is significant to the large reduction of sediment transport. It is crucial for sediment transport modelling in the natural estuarine environment, which the influence of cohesive materials on sediment transport is required to better parameterize the effect in future models.

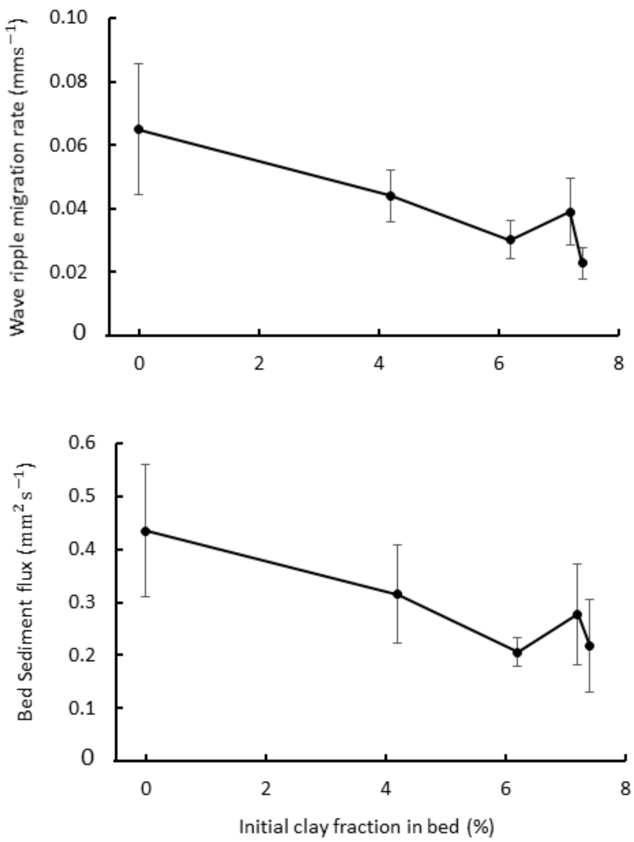

Figure 3-27. Relationship between initial bed clay fraction and (A) average ripple migration rate c_m, and (B) bed sediment flux per unit width, q_b. The black line denotes one standard deviation around the mean.

3.4.3 The role of winnowing on the bedform development

The equilibrium dimensions of the wave ripples in the present study were not affected by the initial bed clay faction. In other words, the equilibrium length (L_e～140mm) and height (H_e～20mm) for different f_0, provided that the ripples were given enough time to attain equilibrium. In addition the cross-section form geometry of wave ripples were similar with increasing clay fraction, with high angled (BI～6.9) and relatively symmetric (BSI～1.1). But, previous flume experiments under unidirectional flow condition found a negative relationship between bedform size and clay fraction (Baas et al., 2013; Schindler et al., 2015). When the bed is a mixture with two different size of sediments, the hydrodynamic force is able to suspend fine particles from the bed into upper flow, as a result relatively coarser sediments are left on the bed (Allen, 1984; Cizeau, 1999; Kleinhans, 2004; Lamb and Parsons, 2005; Liang et al., 2007; Malarkey et al., 2015; Ye, 2016). This kind of sorting process called sediment winnowing (McCrone, 1963) enables mixed clay-sand bed becoming to increasingly sandy bed (Baas et al., 2013). In the present experiments, visual observation of clean flow water transforming to turbid fluid during experiments implies that clay particles were also winnowed from the pores between sand grains. During the process that ripples gradually evolved to reach equilibrium, winnowing led to cohesive bed transforming noncohesive like pure sand bed. Herein, waves, under the same oscillatory flow condition for each run, can only erode into the bed as deep as the pure sand bed even with the highest initial clay fraction, because ripples have reached to equilibrium. As a result, equilibrium size of wave ripples were constant with initial clay fraction increasing from 4.2% to 7.4%.

In the present study, the products of winnowing were recorded in the sediment cores that penetrated ripple crests, with revealing a 100% pure sand at sediment cores top. Compared with winnowing under unidirectional flow (e.g., Baas et al. 2013), the experimental results presumably indicate that winnowing efficiency under waves is much higher. Although the depth-averaged current velocities (0.36ms^{-1}) in the experiment of Baas et al. (2013) were higher than the maximum orbital velocities (~0.30ms^{-1}), the pure sand layers were absent at ripples crest with similar initial bed clay fraction under current condition. It is consistent with that wave-induced bed shear stress entraining sediments are many times larger than current produced bed shear stress (Soulsby, 1997; Leeder, 2011). The clay particles were winnowed from ripples troughs as well, but the winnowing efficiency was lower as there are not top pure sand layers in the cores from ripple troughs.

Additionally, clay particles probably moved towards to intermediate layers as shown Figure 3-26 , presumably resulting in forming the clean sand ripples as well. The velocity gradient from ripple trough to ripple crest contributes pressure gradient between stoss face and lee face of wave ripples (Sato et al., 1984). According to Bernoulli’s principle, the pressure at ripple trough is quietly higher since relatively slower velocity, which pushes clay particles down. Thus the waves acted a pump that not only winnowed clay, but also pushed it deeper into bed. A conceptual model is constructed in order to reflect above mentioned clay removal process (Figure 3-28). Before the experiment, clay and sand are homogeneous mixture, with the initial bed fraction standing at a %. With waves exerted on the bed, clay removal including winnowing and downward movement contributes to form sandy equilibrium ripples. Herein, the characteristic sedimentary structures are generated, with clay content significant reducing at top layers, especially forming clay free layers beneath ripple crests. Furthermore, clay fraction is higher than initial reference at intermediate layer, gradual decreasing towards bottom of sediment cores.

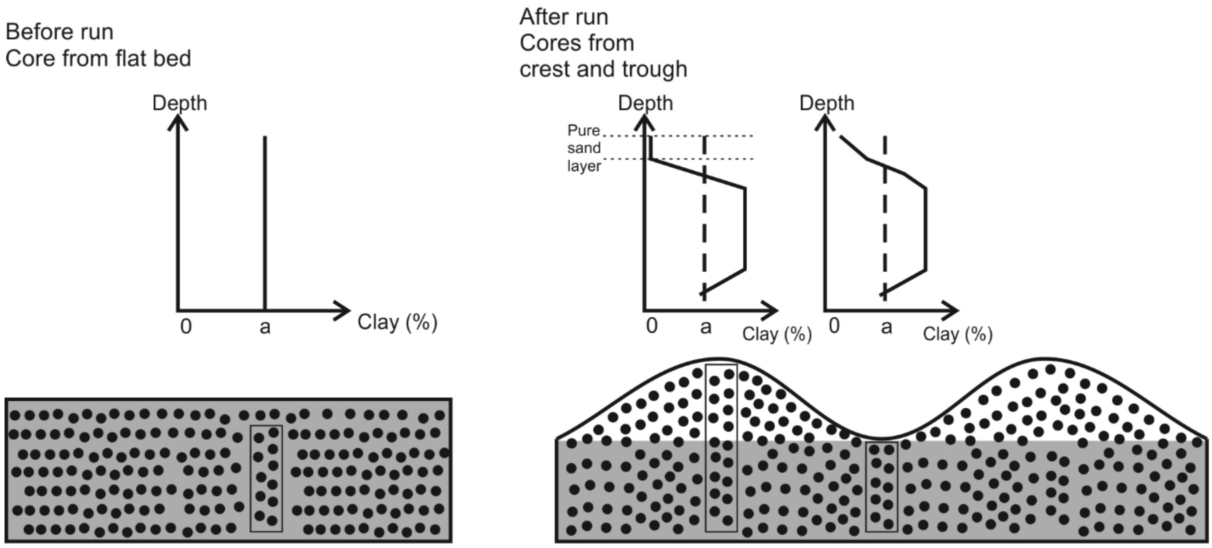

Figure 3-28. A conceptual model of clay removal process

3.5 Implications

The results of large flume experiments demonstrate that equilibrium wave ripples sizes are independent with initial clay fraction, which imply that the existing bedform models (e.g., Traykovski, 2007; Nelson et al., 2013) should be only restricted to wave ripples reaching equilibrium over the mixture of sand-clay beds. Since even small amount of bed clay fraction can heavily affect ripples developments under waves. The wave ripples models possibly overestimate bedform size if wave ripples are in the development stage, which in turn leads to mistakenly evaluate depositional conditions.

Granulometry in the present experiments highlights that wave-induced highly winnowing efficiency develops pure sand layers at ripples crests. This process contribute to sand-clay ripples evolving to pure sandy ripples, which potentially erroneously interpret the way in which the ripples were generated. However, downward movement clay particles forming clayey sand underneath sand ripples is helpful to avoid this mistake and to indicate that ripples were developed from mixed clay and sand sea bed.

In addition to implication for depositional environments, the present work will be helpful to predict the amount of clay winnowing into flow, which is beneficial for water-quality regulation in coastal area. Winnowing facilitates large amount of clay particles in the water column, leading to contain markedly higher chemical concentrations than sand particles (Horowitz, 1991; Svendsen et al., 1995; Horowitz, 2008). It is a double-edged sword. On the one hand the increasing release of nutrients into suspension will benefit aquatic ecosystem; on the other hand, an excess amount of nutrients and trace elements due to relatively higher fine suspended sediment concentration in water column easily leads to water pollution (e.g., Tyler et al., 2006), which seriously threatens coastal ecological balance.

3.6 Conclusions

The development of wave ripples with substrate that mixed cohesive clay and cohesionless sand under regular wave conditions was studied. Based on the results of the five runs of large flume experiments, following conclusion could be reached:

1. Relatively small increase of clay fraction from 4.2% to 7.4% in the present experiments dramatically slowed down the bed erosion rate and caused an inhomogeneous ripple development. The 2D wave ripples formed immediately

and developed uniformly with purse sand bed with length and height growth rate reaching to 1.2 $mmmin^{-1}$ and 0.8 $mmmin^{-1}$, while in the highest clay fraction experiment (Run 06), the rates declined to 0.2 $mmmin^{-1}$ and 0.5 $mmmin^{-1}$. Moreover, the increasing clay fraction resulted in progressive delaying wave ripples appearance on different part of bed.

2. Both equilibrium time of wave ripple length and height exponentially increased with clay content increase, from 40 minutes to 200 minutes for wavelength and from 30 minutes to 120 minutes for height.
3. The migration rate of wave ripples was inversely related to increase of the initial bed clay fraction, it decreasing from 0.06 mms^{-1} in Run 01 to 0.02 mms^{-1} in Run 06. The decline of migration rate led to smaller bed sediment flux over the clay-sand mixture bed, comparing with the pure sand bed. The figure in the control experiment was 0.43 mm^2s^{-1}, while it was only 0.22 mm^2s^{-1} in Run 06 with clay fraction of 7.4%.
4. Equilibrium dimensions of wave ripples were independent with clay fraction. The equilibrium length of wave ripples fluctuated around 140 mm, and the equilibrium height remained level approximately 20 mm. In addition, wave-induced ripple cross-section form geometry were constant without influence of clay fraction as well. Bedform index (BI) and Bedform Symmetry Index (BSI) indicate the wave ripples were high angled and very symmetric.
5. Wave-induced ripple with clay developed from flat be do reach equilibrium experience mainly four stage. Firstly, the pre-incipient stage starts from bed erosion until the nucleus of wave ripples appearance. The following stage is incipient stage with the nucleus of ripples expanding to two-dimensional ripples. Then the size of two-dimensional ripples continues to grow until reaching to final equilibrium stage, which is growth stage.
6. Clay removal including winnowing and downward movement from the bed enable cohesive bed to become less cohesive, which presumably contributes to constancy of equilibrium with wave ripple length and height. Laser granulometry shows that there were pure sand layer at top of cores collected from wave ripples crests with thickness varying from 10mm to 30mm, which were absent at cores collected from wave ripples troughs. This finding presumably indicates winnowing efficiency was much higher at wave ripples crests than that at troughs.

CHAPTER 4 – Near-bed turbulence dynamics and suspended sediment transport over mixed sand-clay substrates

4.1 Introduction

Sediment transport, which includes bedload and near-bed suspended load, is a dynamic process closely related to hydrodynamic forcing, turbulence, and bed substrate properties (Whitehouse et al., 2000; Leeder, 2011), which directly contributes to bedform formation (i.e., ripples; Liang et al., 2007). In the coastal environments, wave induced turbulence over flat bed (Sleath, 1987) and the spatially and temporally generated vortex at ripple lee side during oscillatory flow reversal (Ikeda et al., 1991) largely results in suspended sediments, which dominates sediment transport (Grass, 1981; Nielsen, 1986; Nielsen, 1992). Although a number of flume experiments and field investigations have previously studied sediment transport and morphodynamics under oscillatory flows (Longuet-Higgins, 1953; Bosman et al., 1987; Lee and Hanes, 1996; Davies and Villaret, 1997; Green and Black, 1999), the co-evolution of the bed morphology and oscillatory flow structures have only been examined for cases of cohesionless sand substrates (e.g., Thorne et al., 2002; Davies and Thorne 2005; van der Werf et al., 2007; O'Hara Murray et al., 2011). There is thus a significant knowledge gap concerning the influence of substrate cohesiveness on sediment transport and bedform generation.

This knowledge gap is significant as mixed sediments of cohesive clays and non-cohesive sands are ubiquitous in most coastal environments across the globe (Healy et al., 2002). Previous studies have focused on the influence of cohesivity on bed stabilization and a modulation of sediment transport, with the cohesive structure increasing erosion thresholds (e.g. Mitchener and Torfs, 1996; Van Rijn, 2007, Baas et al., 2013; Ye, 2016). Previous work has also highlighted the influence of suspended clay concentrations on flow turbulence modulation (e.g. Best and Leeder, 1993; Baas and Best 2008; Baas et al., 2016), where suspended clays reduced turbulence intensity. Indeed, Baas and Best (2008) noted that turbulence suppression occurs when suspended clay concentration is above 2.6 vol.%.

Recent experiments in unidirectional flows has shown the importance of winnowing clay from the bed and reducing both the size and the time for bedform development (Ye, 2016). Winnowing is shown to be a rate limiting step and has been highlighted as a key parameter during earlier experiments (e.g., Lamb and Parsons, 2005; Baas, 2013; Malarkey, 2015). The rate of winnowing from mixed substrates will also influence the volume of suspended clay within the water column. As such, there is a need to understand the feedback links between morphological evolution, turbulence production and suspended sediment modulation of turbulence intensity to be able to predict wave ripple formation across a range of environments.

As shown in the Chapter 3 the development rate of wave ripple dramatically decreases with initial bed clay fraction increase. The increasing bed resistance related to the initial bed clay fraction is speculated to play a vital role on slowing wave-induced ripple development. In the present chapter, near-bed wave generated turbulence and sediment transport dynamics are investigated over the evolving substrates. The objectives of this chapter are i) to quantify sediment transport rates and processes across the different substrates; ii) to examine the evolution of near-bed turbulence from the initial flat bed until ripple equilibrium morphologies are attained; iii) to find the relationship between initial bed clay fraction and rates of change in suspended sediment concentration through the experiments.

4.2 Methods

The details of experimental procedures are described in the Chapter 3. However, the specific instruments mounted to measure velocities and suspended sediment concentration are introduced in the present section, followed by a descriptions of the post-processing applied to the collected datasets.

4.2.1 Acoustic Doppler Velocimeter

A SonTek micro acoustic Doppler velocimeter (ADV) was used to provide reliable instantaneous three-dimensional velocity measurements. The instrument uses the Doppler shift principle to quantify the flow velocity towards or away from a set of transducers (Voulgaris and Trowbridge, 1998). As shown in the Figure 4-1 an ADV comprises a transmit transducer and three receive transducers positioned at 120 degree angles. Ultrasound pulses with a frequency of 10MHz are emitted by the transmit transducer and are scattered back particles within a 0.5 cm^3 sampling volume. The scattered acoustic echoes are recorded by the receive transducers and are converted to flow velocities. A combination of the returns and convolution between the 3D axis of the transducers results in the formation of a 3D flow velocity vector from within the sampling volume.

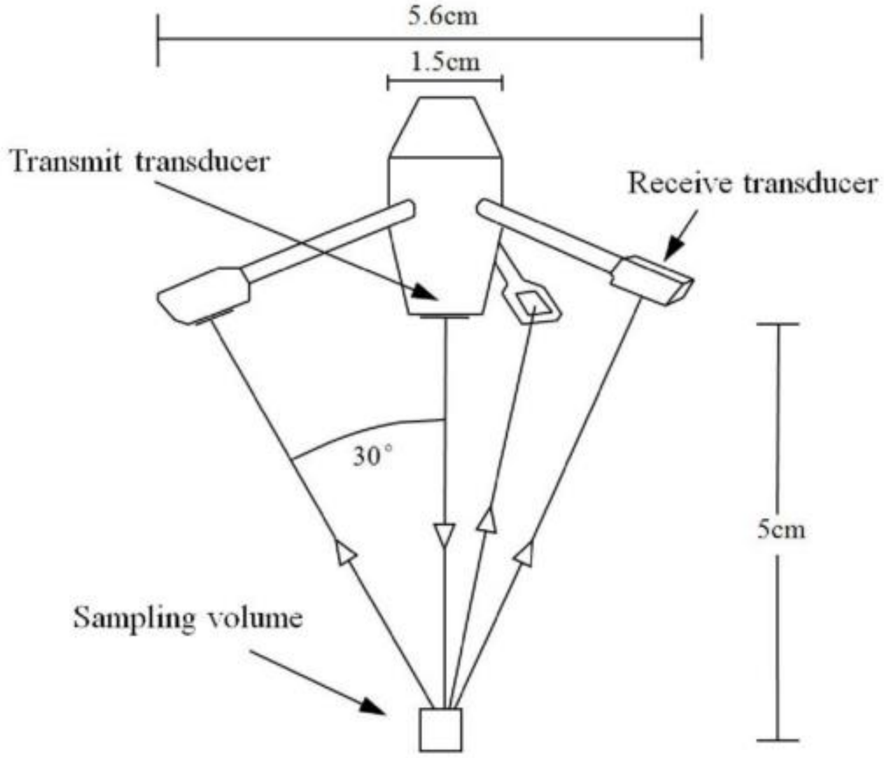

Figure 4-1 Schematic diagram of the ADV transmit and receive transducers layout (From Kraus et al., 1994)

A total five SonTek acoustic Doppler velocimeters with a temporal sampling frequency of 25Hz were positioned at five different heights to form a vertical array of measurements. Three of the ADVs were downward looking and two were sideward looking probes (Figure 4-2). In this chapter the velocity data recorded by probe closest to the bed (ADV 0) is primarily used in the analysis.

The Winadv software was used to process the measured velocities from the ADV array. This permitted calculation of instantaneous flow velocities and turbulence intensity. Data were filtered according to McLelland and Nicholas (2000) where velocities with signal-to-noise ratio <15 and correlation <70% were discarded. The despiking method of Goring and Nikora (2002) was also applied to the temporal series. The removed data were not interpolated and across all experiments >90% of the data were retained (e.g.,

Figure 4-3). The results are shown in Table 4-1. It is should be noted that the positive "onshore" flow is defined as flow direction to the left.

The filtered horizontal velocity is further processed to computer root-mean square deviation of the mean velocity, RMS(u'), which approximates horizontal component of turbulence intensity. Hussain and Reynolds (1970) inferred the wave horizontal velocity is constituted with Reynolds triple-decomposition as shown in the following equation:

$$u(\mathrm{t})=\bar{u}+\tilde{u}(\mathrm{t})+u'(\mathrm{t}) \qquad 4\text{-}1$$

where

u'(t) is the horizontal turbulent fluctuation

$\bar{u}$ is the averaged velocity,

$\tilde{u}$(t) is the periodic velocity

$\tilde{u}$(t) is described as the difference of the mean velocity $\bar{u}$ and the phase-averaged velocity $\langle u(\mathrm{t})\rangle$:

$$\tilde{u}(\mathrm{t})=\langle u(\mathrm{t})\rangle-\bar{u} \qquad 4\text{-}2$$

and

$$\langle u(\mathrm{t})\rangle=\frac{1}{N}\sum_{i=1}^{N}u\,(t+iT) \qquad 4\text{-}3$$

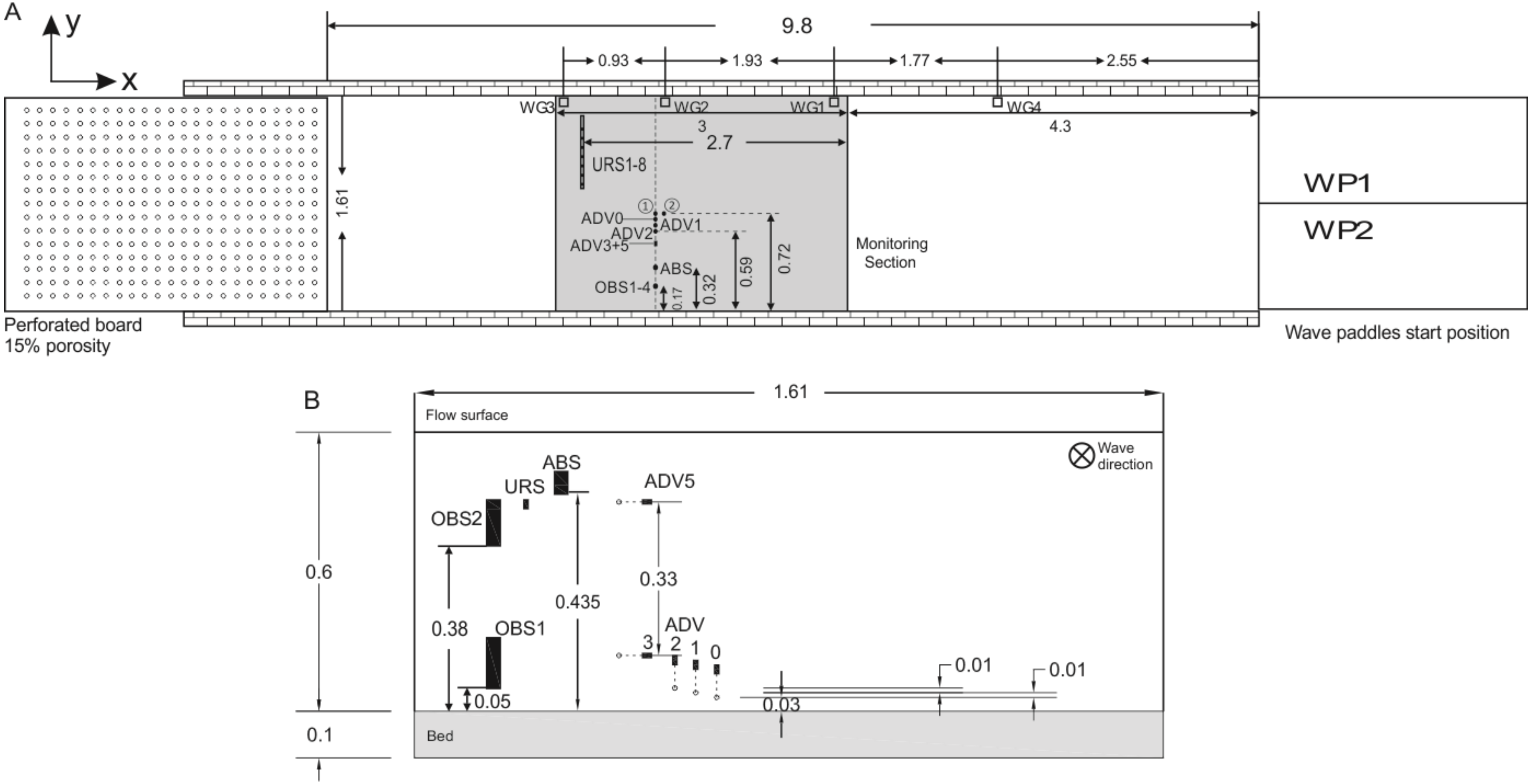

Figure 4-2 Schematic diagram of instrument set-up. (A) Plan view of the locations of instruments. ① and ② represent the downstream and upstream fixed URS. (B) Cross-section view to show the heights of instruments above from the initial flat bed. The unit is metre.

where T is the wave period and N are the number of cycles sampled. Each wave period is identified by zero-up cross points. Combined equation 4-1 and 4-2

$$u'(t) = u(t) - \langle u(t) \rangle \quad 4\text{-}4$$

then RMS($\boldsymbol{u'}$) could be derived by:

$$\mathrm{RMS}(u') = \sqrt{\frac{1}{N}\sum_{i=1}^{N} u'(t)} \quad 4\text{-}5$$

The wave Reynolds number R_W is calculated as:

$$R_W = \frac{U_W d_o}{2v} \quad 4\text{-}6$$

where

U_W is the maximum bottom orbital velocity

v is kinematic viscosity

d_o is the maximum orbital excursion:

$$d = \frac{U_W T}{\pi} \quad 4\text{-}7$$

Table 4-1 Experimental parameters.

Run	U_w(ms^{-1}) Start	U_w(ms^{-1}) End	d_o(m) Start	d_o(m) End	R_W Start ($\times 10^3$)	R_W End ($\times 10^3$)
1	0.30	0.30	0.24	0.24	30.9	30.9
3	0.31	0.31	0.24	0.24	33.0	33.0
4	0.29	0.28	0.23	0.22	28.8	26.9
5	0.29	0.31	0.23	0.24	28.8	33.0
6	0.29	0.29	0.23	0.23	28.8	28.8

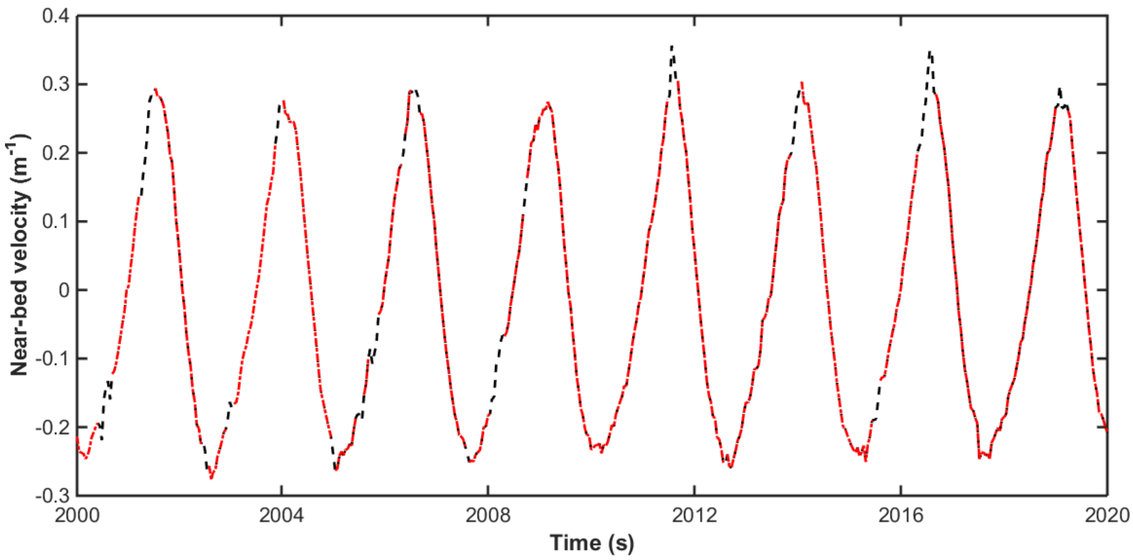

Figure 4-3 Raw near-bed wave velocity data (black dash line) recorded by Acoustic Doppler Velocimeter (ADV) 2000 seconds after experiment started in Run 05. The red dash line denotes filtered velocity with signal-to-noise ratio >15 and correlation >70% (McLelland and Nicholas, 2000) and with despiking method of Goring and Nikora (2002).

4.2.2 Acoustic backscatter system

An Aquascat^{TM} Acoustic backscatter system (ABS) was used to obtain suspended sediment concentration profiles during the experiments. The basic principle of ABS is that a sound source produces a pulse signal and acts as a receiver at the same time. The radiated sound is reflected by suspended matter within water column and is recorded by the transceiver. The scattering echo effectively carries the physical characteristics of suspended matter (Libicki et al., 1989; Thorne and Hanes, 2002). The concentration and grain size characteristics of suspended material can be recovered from the signal acoustic inversion algorithms that are based on the relationship between the backscattered intensity and the suspension concentration. Specifically, the suspended sediment concentration (SSC) is the function of sediment particles radius and recorded backscattering voltage (Thorne and Hanes, 2002).

$$ssc=\left(\frac{V_{rms}\psi r_d}{k_s k_t}\right)^2 e^{4r_d\alpha_m} \qquad 4\text{- }8$$

in which

V_{rms} is recorded voltage,

ψ is departure from spherical spreading within the transducer nearfield (Downing et al., 1995),

r_d is range from transducer,

α_m denotes sum of sound attenuation by water α_{w} and attenuation caused by suspended sediment α_s.

k_s is related to scattering properties of suspended sediment, which depends on sediment particle radius, particle size distribution and form function of suspended sediment backscatter.

k_t , the parameter of measurement system, is related to signal frequency, pulse width, transducer radius, and conversion function between sound and electricity.

The implicit iterative method based on single frequency was used in the current study to obtain suspended sediment concentration. Firstly, ssc_0 is calculated using equation (4-8), assuming α_{s0} =0. Then α_{s1} could be evaluated (see sampling below) by known ssc_0, therefore acquiring ssc_1, as shown below:

$$ssc_{i+1} = ssc_0 e^{4r_d\alpha_{m(ssc_0)}} \quad \text{for i=0, 1, 2…} \qquad 4\text{- }9$$

The iterative process is repeated until ssc_i and ssc_{i+1} are convergent.

In the above-mentioned algorithms, calibrating and evaluating k_t values is significant. The most common calibration method is to rearrange Eq. (4-7) (Thorne and Daniel, 2002).

$$k_t = \frac{V_{rms}\psi r_d e^{2r_d\alpha_m}}{k_s ssc} \qquad 4\text{- }10$$

In a sediment calibration tower, sound propagate through a homogenous suspension of known scatters at a known concentration. Hence,k_s, ssc, and α_m can be known and ψ=1 quantified (Thorne and Hanes, 2002). Theoretically, k_t could be calculated. The k_t values using in the present thesis were calibrated using the calibration sediment tower at National Oceanography Centre, Liverpool.

The ABS comprises three transducers operating at 1.0, 2.0 and 4.0 MHz, respectively. The pulse length and range sampling were set to 0.005 m with 92 samples recorded, thereby covering an overall range of 0.46m. In order to avoid contaminated signals from the bottom echo, the last three samples above the maximum signals are discarded. In order to assess the acoustic suspended sediment concentration, direct water samples were collected by the ISCO 6712 Portable Pump Samplers at positions of 20 mm, 30 mm, 40 mm, 50 mm, and 130 mm above the bed level. Figure 4-4 shows concentration profiles measured by 1MHz, 2MHz, and 4MHz over 5 minutes, respectively and measured by pumped water samples in Run 01. At a height lower than 60 mm, acoustic measurements at 4MHz are relatively close to measurements from the pumped samples, while measurements at 1MHz and 2MHz are higher than the realistic values. However, over 100 mm height, the pumped water measurement tends to be close to acoustic measurements with the 1MHz probe. Considering the focus of near bed sediment transport dynamics in present chapter, measurements from the 4MHz probe are utilized for the below results and discussions.

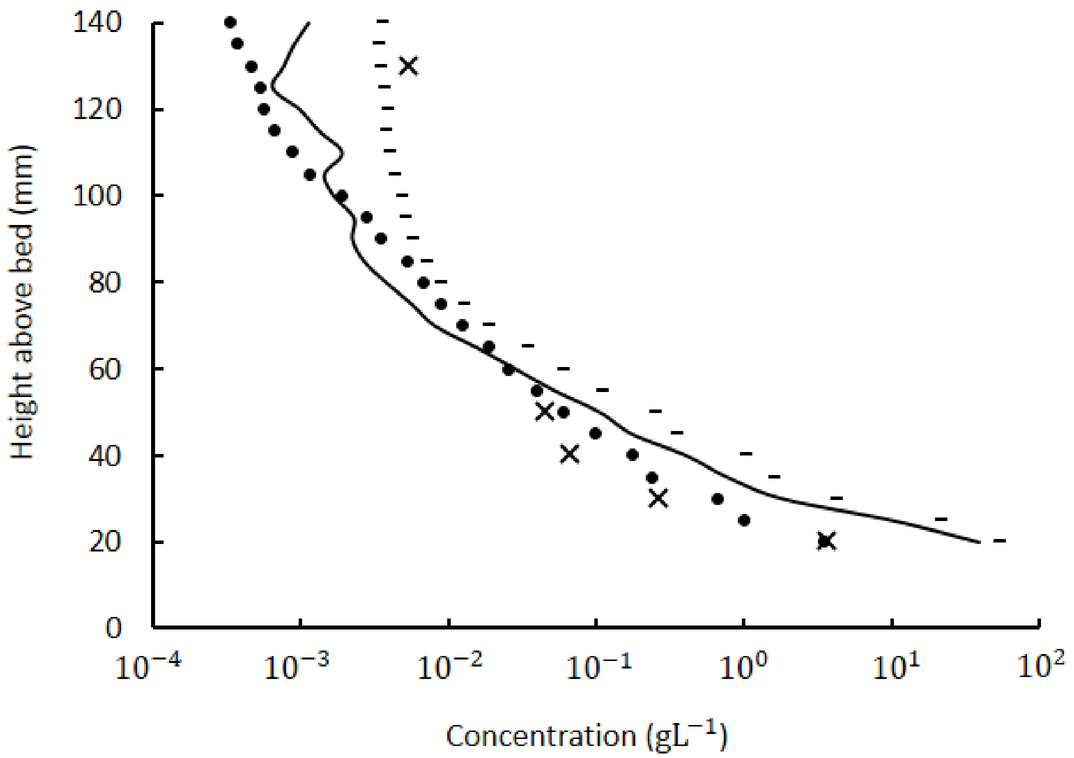

Figure 4-4 Measurements of acoustic and pumped sample suspended sediment concentration profiles in Run 01. Shown are acoustic measurements at 1MHz (dash line), 2MHz (solid line), 4MHz (dotted line), and pumped sample measurements (cross).

The ABS and the ADV array worked synchronously during the experiment, therefore individual wave period for inter-wave suspended sediment concentration could be identified using same time points corresponding with the imposed wave period. Once the SSC is separated periodically across the waves, the phase averaged SSC could be calculated. Figure 4-5A shows the ABS recorded SSC from 20 mm to 100 mm above the bed in one minute between t=368min and t=369min in Run 05. Correspondingly phase averaged SSC over 24 wave cycles across the same time period is shown in Figure 4-5B. This shows phase averaged SSC is better to reflect sediment laden by ejected vortex over the rippled bed (more details see below sections).

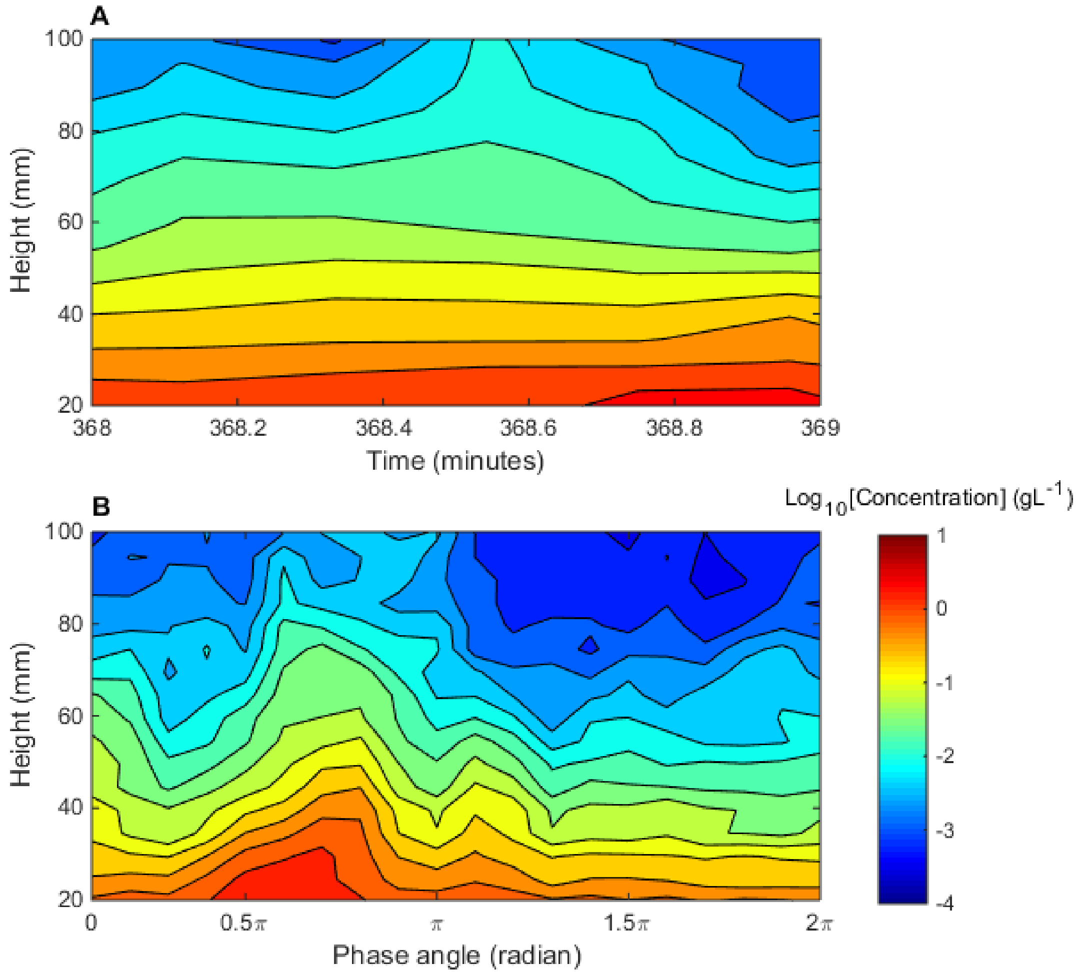

Figure 4-5 Suspended sediment concentration (SSC) recorded by 4MHz ABS transducer from 20mm to 100mm height above the bed in one minute between t=368min and t=369min in Run 05 (A). Phase averaged SSC over 24 wave cycles with the same height in the same one minute (B).

4.2.3 Optical Backscatter Sensor (OBS)

Two OBSs with 1Hz sampling frequency were set up at fixed positions in the vertical 50 mm and 380 mm above the initial flat bed, respectively. The operating principle of OBS is based on the light transmitted and light scattered (Downing, 2006). Light emitted from source can be scattered by suspended sediment particles. The photodetectors are able to convert the backscattered signal to photocurrent. The OBS provided a nephelometric-turbidity-unit (NTU) and a calibration is required to transfer the recorded NTU signal into a suspended sediment concentration (SSC). The direct water samples, collected close to the OBS sensors during experiments, were used to establish a relationship between the NTU and the SSC (Figure 4-6). Figure 4-6 shows good linear relationships between the NTU and the SSC with rather high correction coefficients (R).

4.2.4 Laser In-Situ Scattering and Transmissometry (LISST-100X)

LISST-100X produced by SEQUOIA is an in-situ laser particle size analyser, which is used to measure sediment particle size distribution and concentration suspended materials within water samples. The operation principles of LISST-100X is based on the theory of laser diffraction (Agrawal and Pottsmith, 2000). The scattering angle of sediment particles in the water is closely related to the particle size, the larger the particle size is, and the larger the scattering angle is, vice versa. When a collimated laser light illuminates suspended sediments in water, the scattered light by particles can be sensed and recorded by a multielement detector (Figure 4-7). The detector is constituted with 32 rings recoding 32 scattering angles from 0.1° to 20° in a logarithmical distribution. Each ring represents a small range of logarithmically increasing scattering angles, which corresponds with particle size varying from 2.5 μm to 500 μm. Based on Mie theory (Mie, 1908; Agrawal and Pottsmith, 2000), the scattering angles recorded by the ring detector are mathematically inverted to determine the particle volume concentration.

The LISST 100X was used to measure sediments within the direct water samples collected by the ISCO 6712 Portable Pump Samplers. These were sampled at the same heights as the two OBS, 50 mm and 380 mm heights, respectively. The direct sampled water was placed into the LISST-100x sample chamber, where the measurements were made immediately in order to capture the sediments size.

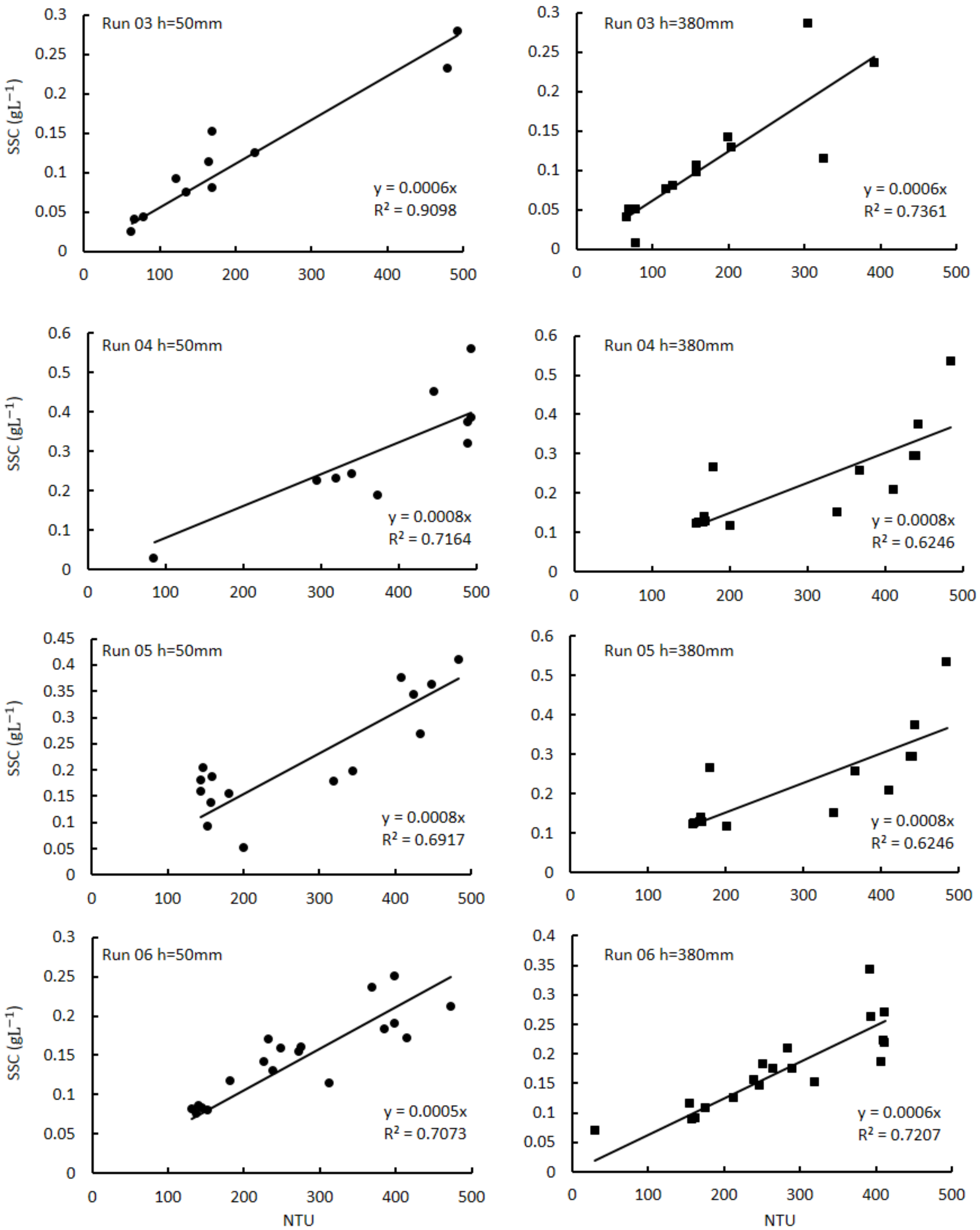

Figure 4-6 NTU-SSC relationship at 50 mm (black dot) and 380 mm height (black squares) above the initial flat bed from Run 03 to Run 06. The SSC are acquired from water sample immediately collected by ISCO 6712 Portable Pump Sample.

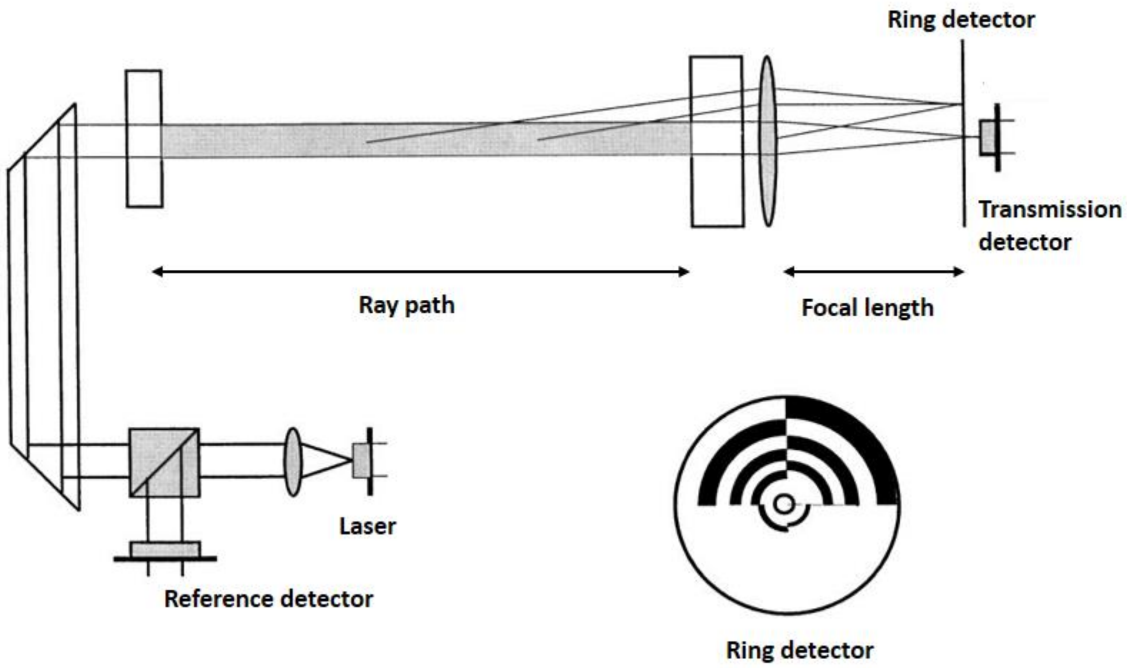

Figure 4-7 Schematic shows laser, optics and detectors (From Agrawal and Pottsmith, 2000).

4.3 Results

4.3.1 Time averaged horizontal velocity turbulence intensity

Figure 4-8 shows the relationship between the horizontal turbulence intensity (RMS (u')) and bed elevation for each of runs with mixed clay-sand substrates. Specifically the (RMS ($u^{'}$)) changes from beginning of experiment until formation of wave ripples, because spatially and temporally coherent vortices instead of random turbulence dominate in momentum transfer in the boundary layer of the rippled bed (Ranasoma and Sleath, 1992). Herein, the results of Run 01 with pure sand bed are not shown due to ripples formed immediately.

The initial bed clay fraction of Run 03 was 4.2%. It should be noted that bed elevation profiles in this section were acquired from the fixed downstream URS which was next to the ADV during the experiment (Figure 4-2). The sand-clay mixed bed remained flat until $\sim$ t=15 min when wave-induced ripples begin to form (Figure 4-8 A). RMS ($u^{'}$) fluctuated around 0.02 ms^{-1} whilst the bed remained flat. However, It markedly increased to 0.04 ms^{-1} at t=14 min and peaked to about 0.06 ms^{-1} at t=19 min, corresponding with the formation of the ripples within the substrate and the resultant changes in bed elevation.

In Run 04 the initial bed clay fraction was increased to 6.2%. This delayed the onset of bedform generation (see Chapter 3), with the URS probes recording bed morphology altering after t=25 min (Figure 4-8 B), which possibly indicates wave ripple started to form at that time. Figure 4-8 B depicts the RMS ($u^{'}$) remained at a rather lower value (<0.02 ms^{-1}) in the first 15 minutes. However, the following 20 minutes witnessed a rapid increase of RMS ($u^{'}$), peaking to almost 0.46 ms^{-1} at t=35 min (Figure 4-8 B).

In Run 05, the bed clay fraction was higher, reaching to 7.2%. Compared with Run 03 and Run 04, the time to formation of ripples extended over t= 120 min, with the bed remaining flat bed until this time (Figure 4-8 C). The value of the RMS (u') remained at a lower levels throughout this period, again fluctuating around 0.02 ms^{-1}. Noting that there was no bed elevation data recorded by fixed URS between t=150 min and t=180 min, it is assumed that during this 30 minute period ripples began to form, with the bed elevation declining to around -10 mm after t=180 min and rising slowly until t=250 min, followed by an another decrease. Concurrent to the likely generation of bedforms, the RMS (u') jumped to close 0.03 ms^{-1} at t=150 min and fluctuated at these elevated values, with peak value at $\sim$0.04 ms^{-1} between t=220 min and t=230 min (Figure 4-8 C).

Figure 4-8 D shows the change of RMS (u') and bed elevation with time in Run 06 which had the highest initial clay fraction at 7.4%. The higher clay fractions within substrate extended the period of flat bed conditions to over 120 mins. After 120 minutes, the bed began to be eroded and varied until t= $\sim$210 min, when significant erosion over a 20 minute period occurred (Figure 4-8 D). After t=230 min, the bed elevation tended to stabilised once more, but with larger variations in the bedform morphology, which approached 5 mm in height. In terms of RMS (u'), initially the values were relatively low (below 0.02 ms^{-1}). The RMS (u') gradually increased to around 0.03 ms^{-1} at t= 310 min, just before a large increase over the following period, coinciding with the change in morphology. RMS (u') series also showed larger variations and higher turbulence levels beyond t= 300 min (Figure 4-8 D).

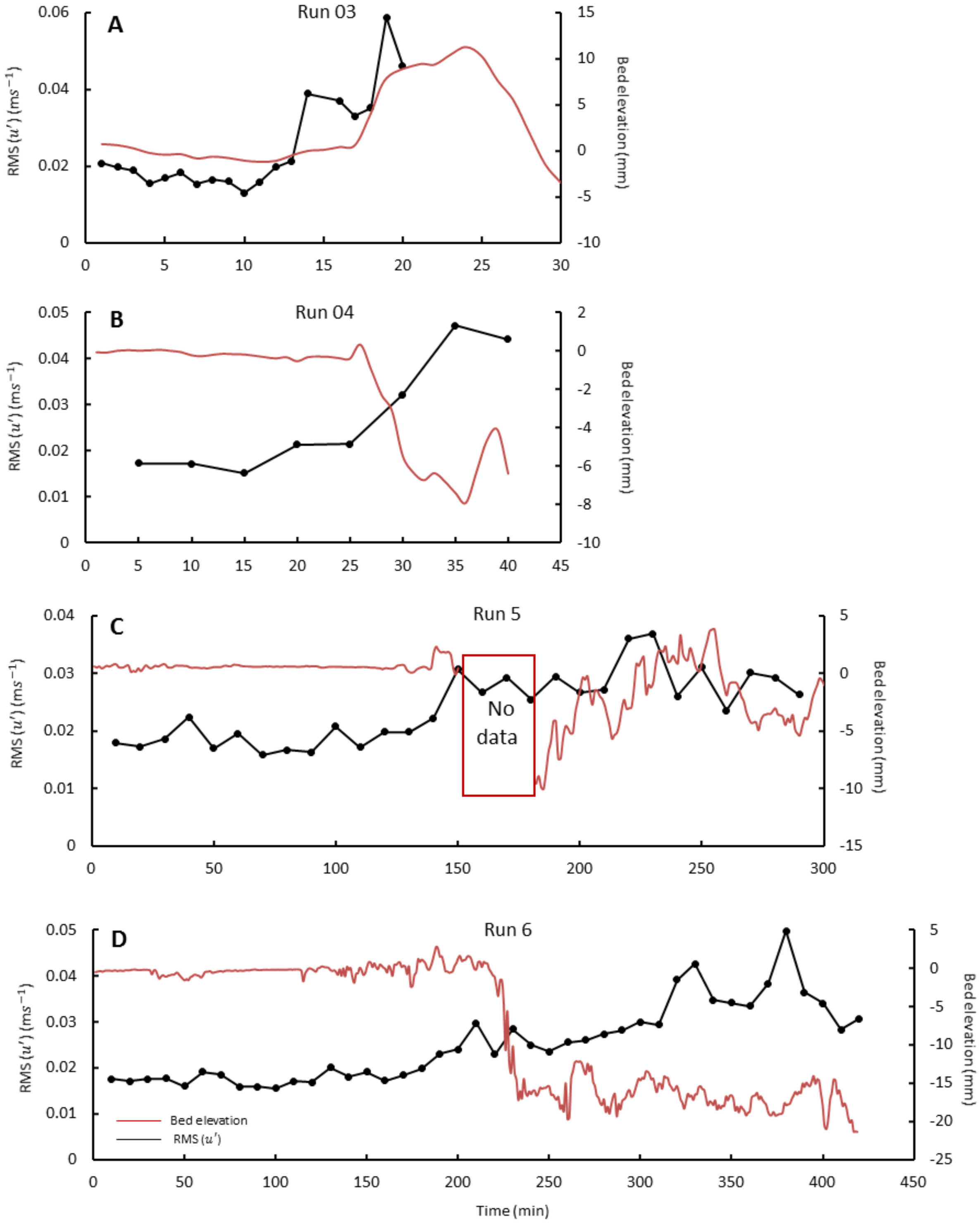

Figure 4-8 Near-bed horizontal velocity turbulence intensity (RMS (u')) change corresponds with bed elevation in each run. A) Run 03; B) Run 04; C) Run 05; D) Run 06. The red and black lines denote RMS (u') and bed elevation, respectively. The bed elevation profiles were acquired from fixed downstream URS.

4.2.2 Time averaged near-bed suspended sediment concentration

The suspended sediment concentration (SSC) at 20 mm above the flat bed fluctuated in the first 15 minutes of Run 03. In general, however, the SSC values were relatively lower at the start of the experiment. After t=15 min, the bed elevation, detecting by the ABS 4HMz probe, began to change and wave ripples formed. During this period, the SSC increased and peaked 1.2 $\mathrm{gL^{-1}}$ at t=25 min (Figure 4-9A).

Between t=200 min and t=290 min, the ABS probe detected four individual wave ripple migrations along wave direction (from right to left) below the sensing volume, therefore defining left side of ripple as lee side and the opposite as stoss side. Figure 4-9B shows the change of sediment suspended concentration at the different parts of the wave ripple after attaining equilibrium. The peak values in suspended sediment concentration, exceeding 1.3 $\mathrm{g\,L^{-1}}$, coincided occurred at the lee side of ripples. However, the impressive high concentrations were absence at the wave ripple stoss sides. Additionally, the suspended sediment concentration basically levelled off at ripple crest and stoss side, with mean values standing at about 0.8 $\mathrm{gL^{-1}}$.

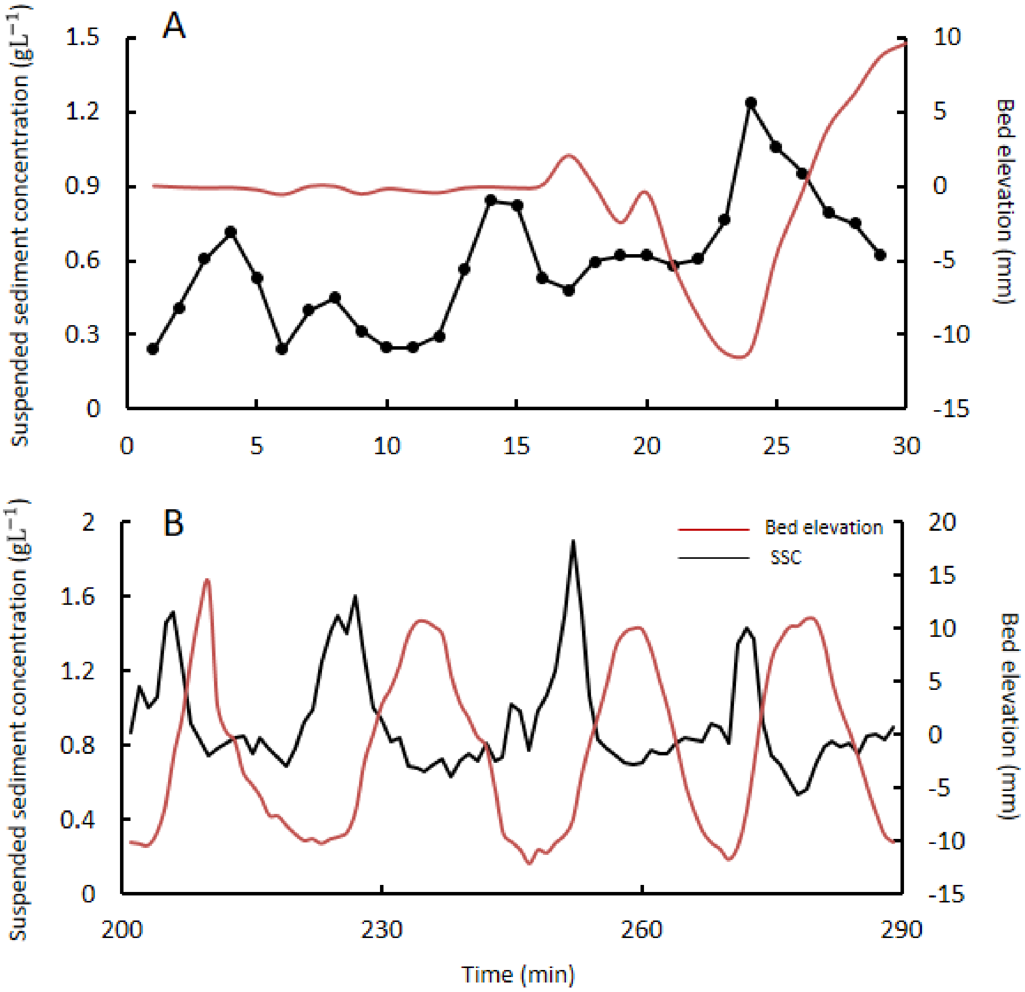

Figure 4-9 Suspended sediment concentration (black lines) at 20 mm over (A) flat and eroded bed and (B) rippled bed in Run 03. Wave moved from right to left. The bed elevation profiles (red lines) were obtained from the ABS 4HMz probe.

Compared with the SSC in the beginning of Run 03, the SSC in the first 40 minutes of Run 04 was very similar, except for low values (~0.2 gL^{-1}) at t=5 min. As shown in Figure 4-10A with distinct change of bed elevation, the SSC increased to 0.6gL^{-1} at t=50 min and then tended to be stable.

In Run 04 wave ripples reached an equilibrium after t=100 min. Three entire mature wave ripples appeared in the following 70 minutes (Figure 4-10B). Akin to Run 03, the peak values of SSC were found on the leeside of the wave ripples. Moreover, there is a positive relationship between ripple size and lee side peak SSC value. For example, the peak value at lee side of first big ripple between t=160 min and t=190 min was 1.6 gL^{-1}, while the values fell below 0.9 gL^{-1} at the following lee side of small ripple.

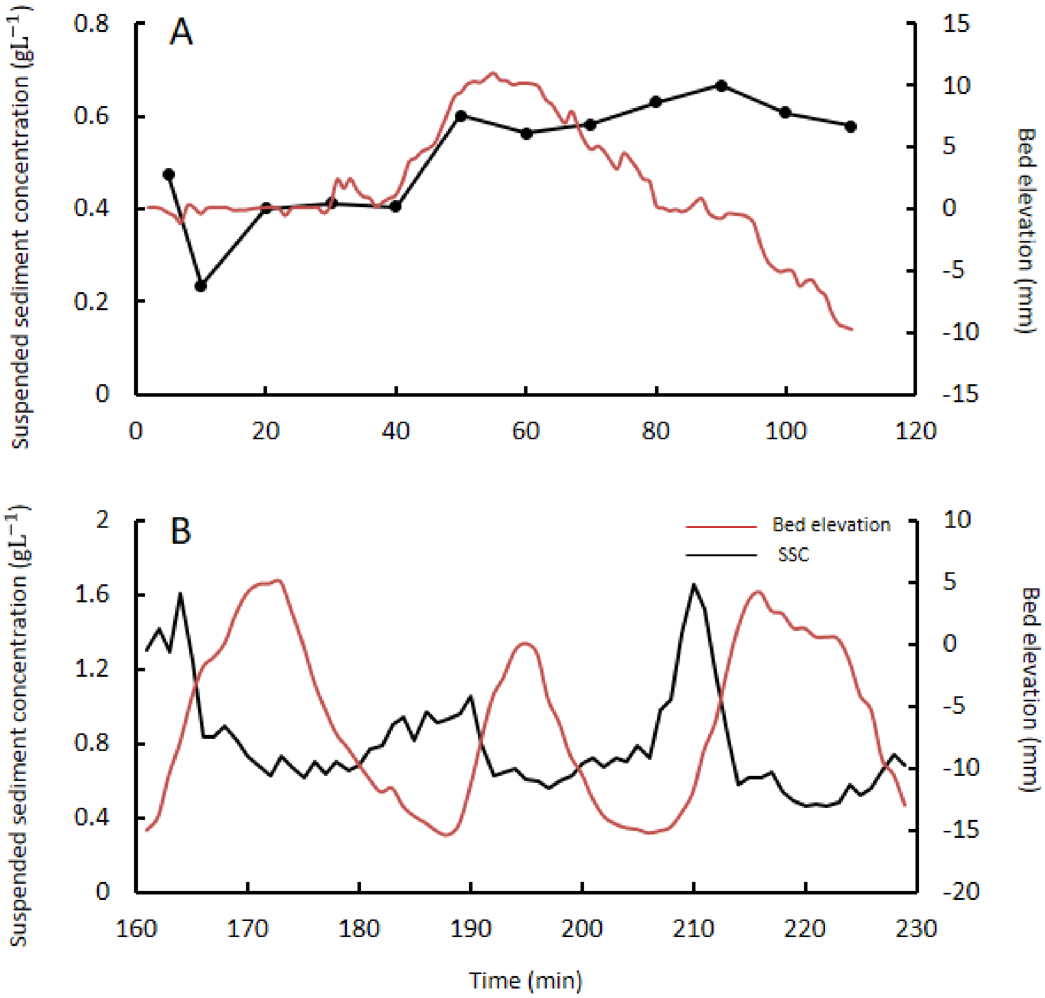

Figure 4-10 Suspended sediment concentration (black lines) at 20 mm over (A) flat and eroded bed and (B) rippled bed. Wave move from right to left in Run 04. Wave moved from right to left. The bed elevation profiles (red lines) were obtained from the ABS 4MHz probe.

The SSC remained at low level at around 0.3 gL^{-1} in the first 40 minutes of Run 05, though the figure jumped up to about 0.4 gL^{-1} at t=30min. After that the SSC increased until reaching a peak (0.7 gL^{-1}), coincident with the erosion of the bed. Once the wave ripples were fully established an equilibrium, as shown in Figure 4-11B, peak SSC values repeatedly appeared when the lee side of each mature wave ripple passed under the ABS probe.

In Run 06 the most of SSC values during the initial flat bed phase were 0.2 gL^{-1}, except an anomalously high value at t=30 min, that reaching to approximately 0.4 gL^{-1}. After t=70 min, the SSC increased rapidly, and at t=200min the value rose by as much as 0.4 gL^{-1} to 0.7 gL^{-1}. However, the SSC collapsed to less than 0.4 gL^{-1} at t=210 min. The experiment was suspended at t=210 min, with a night stop, leading to the majority of sediment settling back to the bed. Thus there was a sharp decrease of SSC at t=210 min when the experiment restarted in the second day. Since re-commencing, the sediments were re-suspended and the SSC started to slowly increase again (Figure 4-12A).

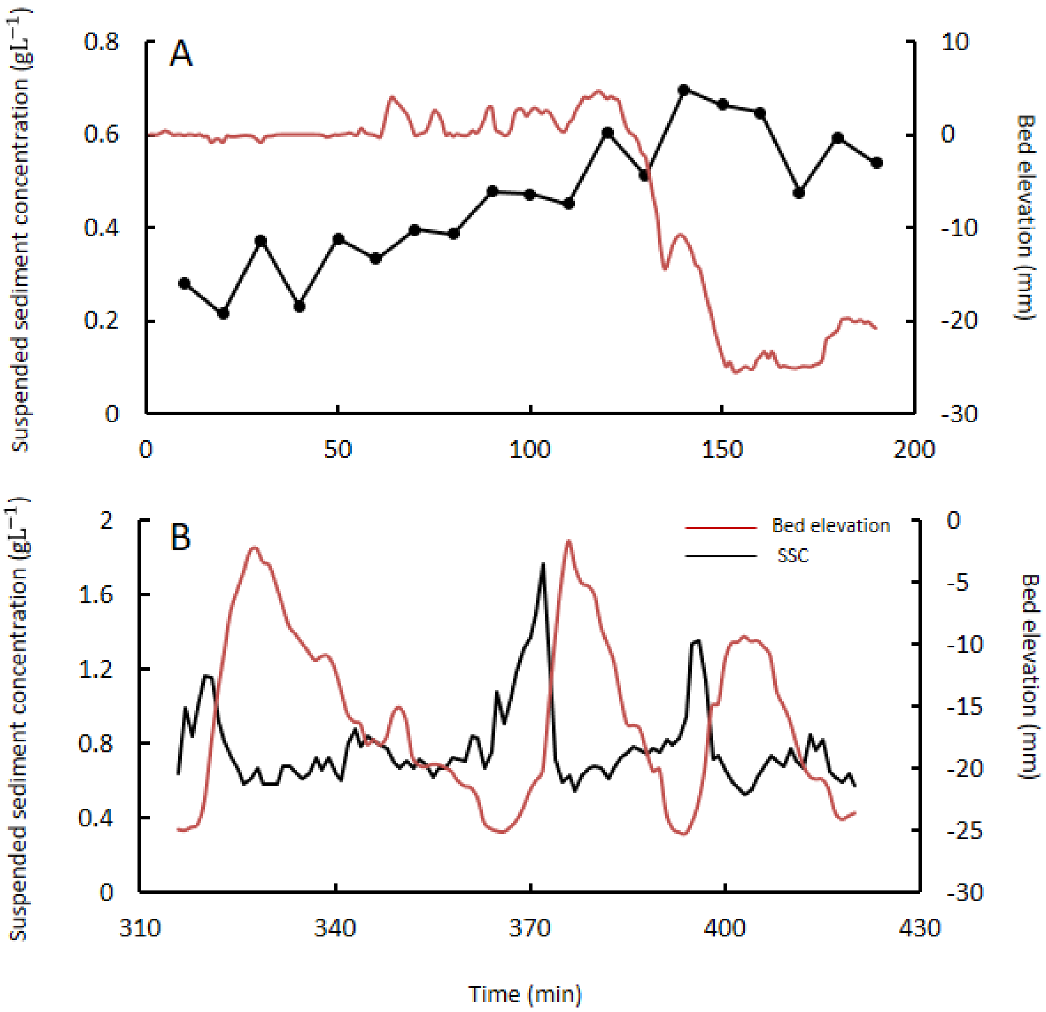

Figure 4-11 Suspended sediment concentration (black lines) at 20 mm over (A) flat and eroded bed and (B) rippled bed in Run 05. Wave moved from right to left. The bed elevation profiles (red lines) were obtained from the ABS 4MHz probe.

The wave ripples moved beneath the ABS probe had relatively smaller size in Run 06, compared with others in the previous runs. The distinct SSC peak values appeared at lee side of wave ripples as in the other runs, except at the third smaller ripple with ripple height of 10 mm (Figure 4-12 B).

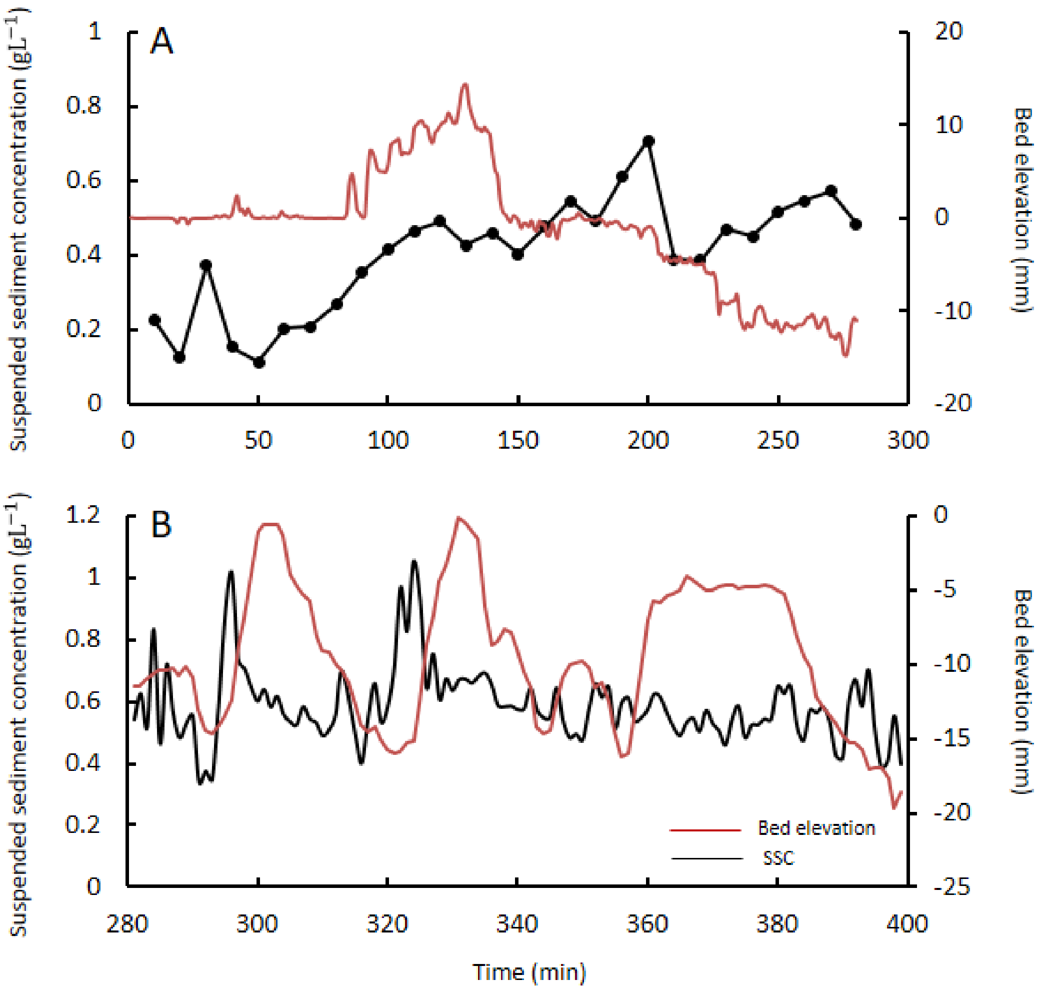

Figure 4-12 Suspended sediment concentration (Black lines) at 20 mm over (A) flat and eroded bed and (B) rippled bed in Run 06. Wave moved from right to left. The bed elevation profiles (red lines) were obtained from the ABS 4MHz probe.

Figure 4-13 reflects the vertical gradient of suspended sediment concentration over the different bed phases during each run. It is apparent that the gradient significantly decreased by several orders of magnitude from the near bed towards upper flow. Furthermore, over the flat bed, the vertical gradient of suspended sediment concentration (red square and line) was relatively smaller, especially in Run 05 and Run 06 with the higher initial bed clay fractions. In all cases it remarkably increased with ripple generation and peaked at ripple lee side (blue dot and line), which indicates that the lee side vortex was contributing to large vertical differences in suspended sediment concentration.

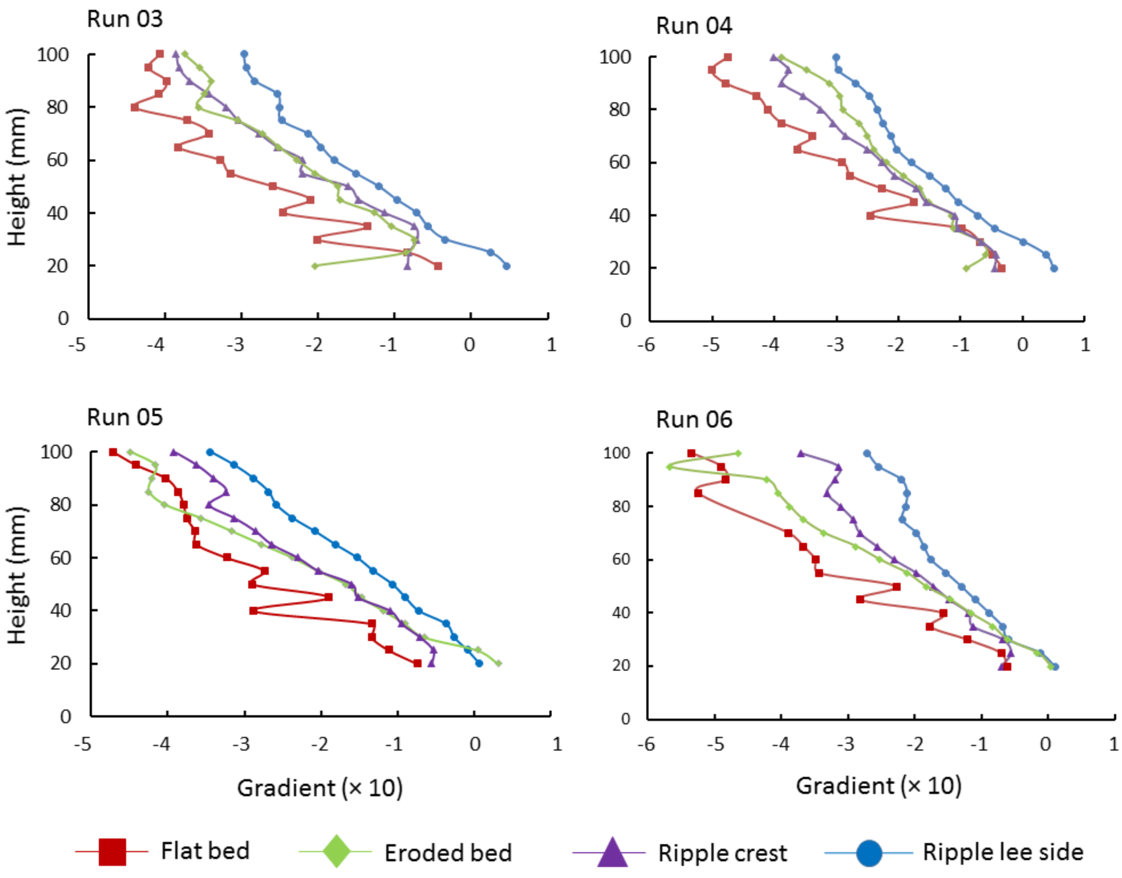

Figure 4-13 Vertical gradient of suspended sediment concentration over the flat bed (red square and line), the eroded bed (green diamond and line), ripple crest (purple triangle and line), and ripple lee side (blue dot and line).

4.3.3 Phase averaged suspended sediment concentration

The ABS data collected from 4-MHz transducer with vertical bin height of 5 mm were used to investigate intrawave suspended sediment concentration (SSC) from the flat bed to the rippled bed. The results show the suspended sediment concentration field bottom 100 mm of the flow down to 20 mm above bed, which equals to 4~ 5 wave-induced ripple heights.

In Figure 4-14, intrawave SSC results are shown for the beginning 20 minute of Run 03 with 4.2% initial clay fraction. The phase averaged velocity is also shown in the top left panel to display the regular and asymmetrical wave. A wave period starts from peak value at phase angle as 0°. The top right panel of Figure 4-14 shows the corresponding time of remaining numbered SSC contour plots. These contour plots reflect phase averaged intrawave SSC over 24 wave cycles. The colours in the contour plots are defined in the colour bar as $\log_{10}[\mathrm{SSC}]$.

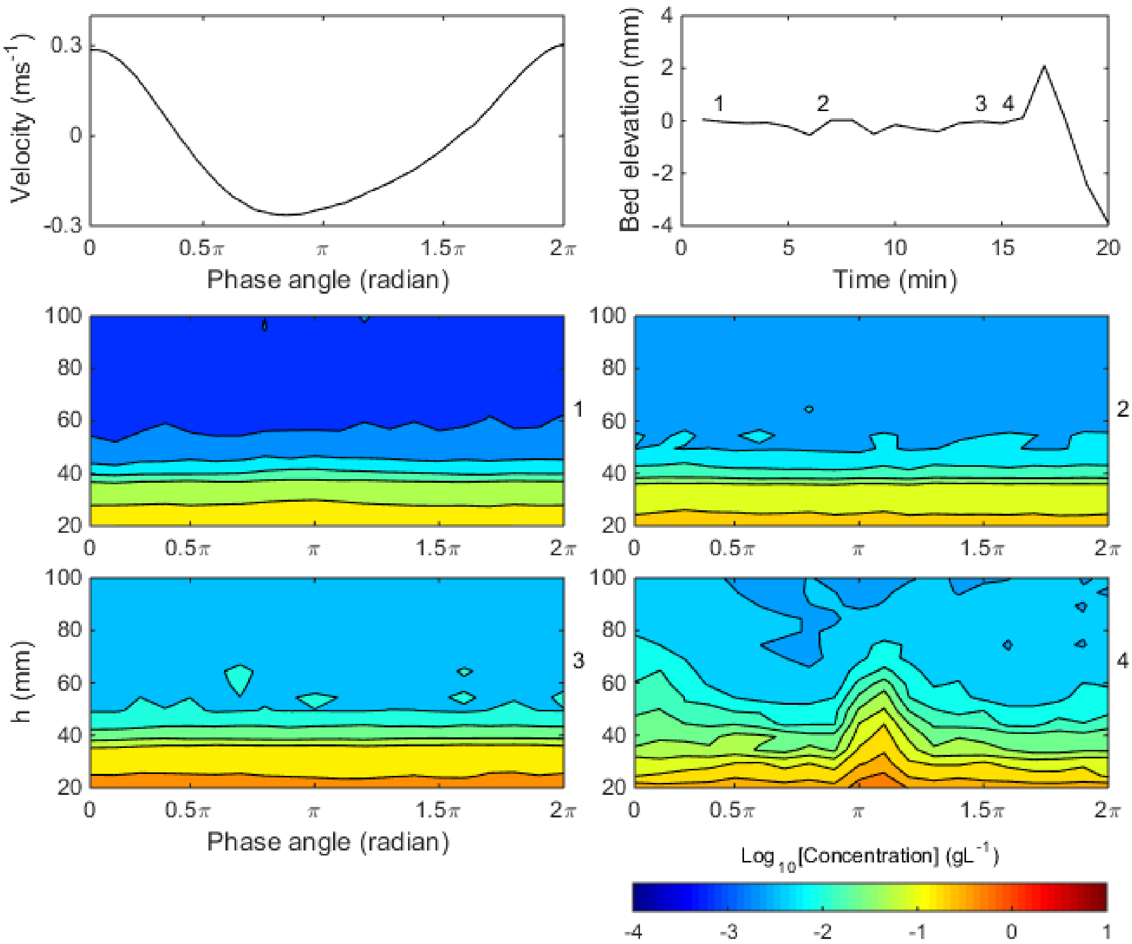

Figure 4-14 Wave velocity and phase averaged SSC profiles in the first 20 minutes of Run 03 with 4.2% of initial bed clay fraction. The top left panel displays measured freestream velocity for over 24 successive wave periods. The four numbered panels show phase-averaged suspended sediment concentration at respective time in the top right panel. The colours in the contour plots are defined in the colour bar as log_{10}[SSC].

Over the flat bed in very beginning of experiment, suspended sediment concentrations were clearly stratified and gradually decreased from the near bed zone higher into the flow, with the concentration increasing and remaining stratification until t=14 min (Panel 1 to 3, Figure 4-14). The stratified structure of suspended sediment profile was broken down at t=16 min just before formation of wave ripple, with a relatively high concentration appearing at a phase angle of more than 1.1 π rad (Panel 4, Figure 4-14).

During the time between t=271 min and t=294 min, an equilibrium wave ripple moved under the ABS probe. The ripple shape was kept more or less unchanged, which enables the study suspended sediment concentration field. Seven numbered locations were chosen as shown in the top right panel of Figure 4-15 and the following numbered contour plots correspond to these locations.

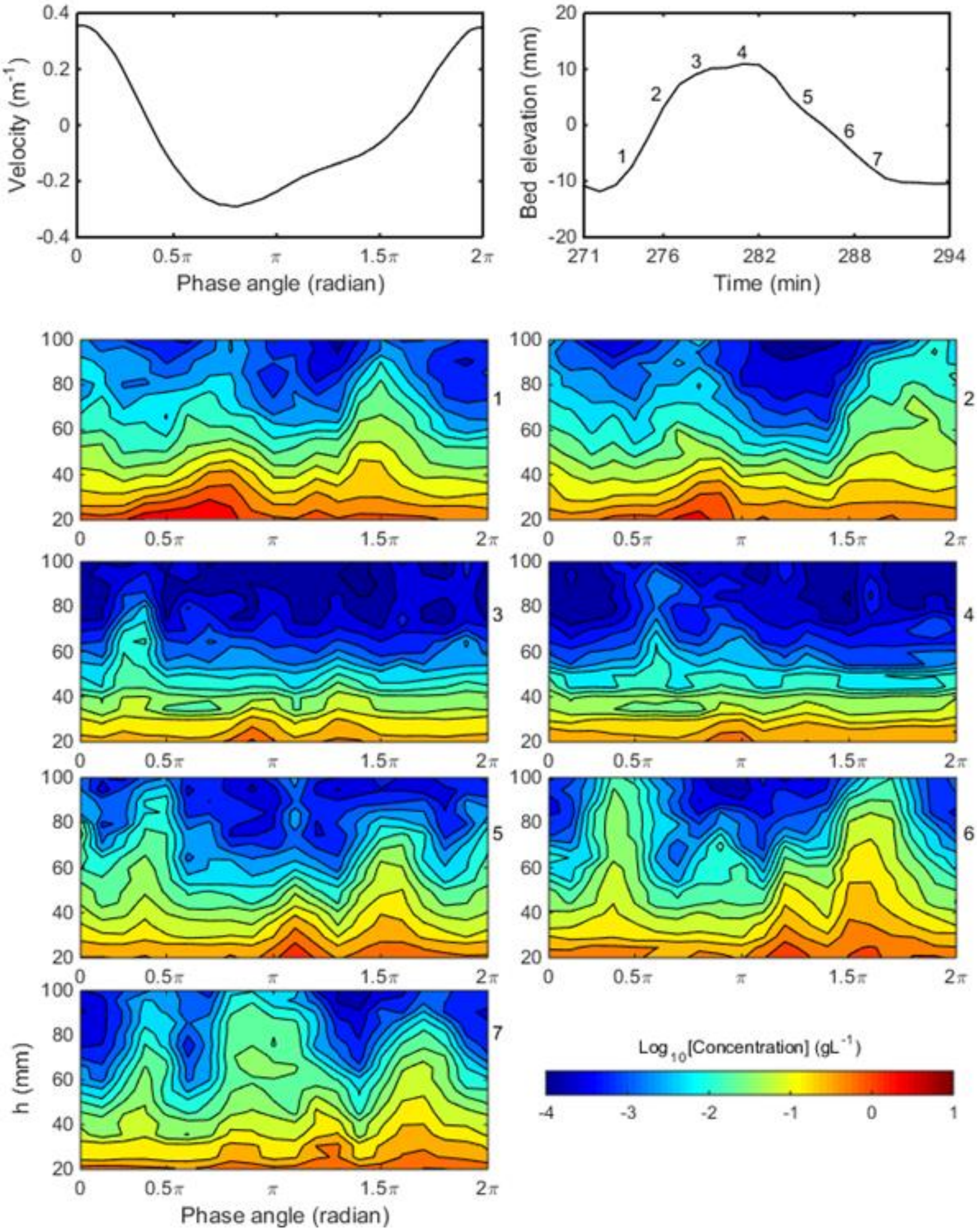

Figure 4-15 Wave velocity and phase averaged SSC profiles over the rippled bed of Run 03 with 4.2% of initial bed clay fraction. The top left panel displays measured freestream velocity for over 24 successive wave periods. The seven numbered panels show phase-averaged suspended sediment concentration at seven different locations of wave ripple as shown in top right panel. Wave

direction was from right to left. The colours in the contour plots are defined in the colour bar as log_10[SSC].

At the lee side of wave ripple (number 1 and 2), a high concentration cloud appeared after flow reversal from positive to negative in the first half wave cycle (Figure 4-15), matching the remarkable peak SSC value in Figure 4-9 B, which indicates sediments were trapped in the ejection of vortex formed during later part of the positive wave half cycle. The concentration peaks, with smaller magnitude in the second half of wave period above locations 1 and 2 (Figure 4-15), were probably associated with the passage of an advected suspension cloud forming at neighbouring downstream ripples.

As shown in Figure 4-15, there were not remarkable SSC peaks at ripple crest (locations 3 and 4). At locations 5 to 7 on the stoss slope of ripple, the SSC peaks in the first half wave cycle were presumably caused by the passage of an advercted suspension cloud from successive upstream ripples. In the succeeding half cycle, the formation of concentration peaks occurred at a phase angle of more than 1.5 π rad was similar as that above lee side due to vortex shedding during flow reversal. The ones generated between phase angle of 1 π and 1.5 π were assumed to relate with sediment trapped within new generated vortices (Figure 4-15). The different concentration field between the two wave half cycles is assumed to the weakly asymmetrical wave velocity.

As far as the concentration field over different bed phase in Run 04 with initial clay fraction of 6.2% is concerned, the stratified sediment concentration extended approximately 25 minutes longer than that in Run 03, with the bed keeping flat until t=40 min (Panel 1 to 3, Figure 4-16). During the period between t=40 min and t=120 min, bed elevation experienced a remarkable change, decreasing to -18mm (Figure 4-16). Whilst the stratified structure was completely disappeared, with minor concentration peaks appearing in each half of wave cycles (Panel 4 to 7, Figure 4-16).

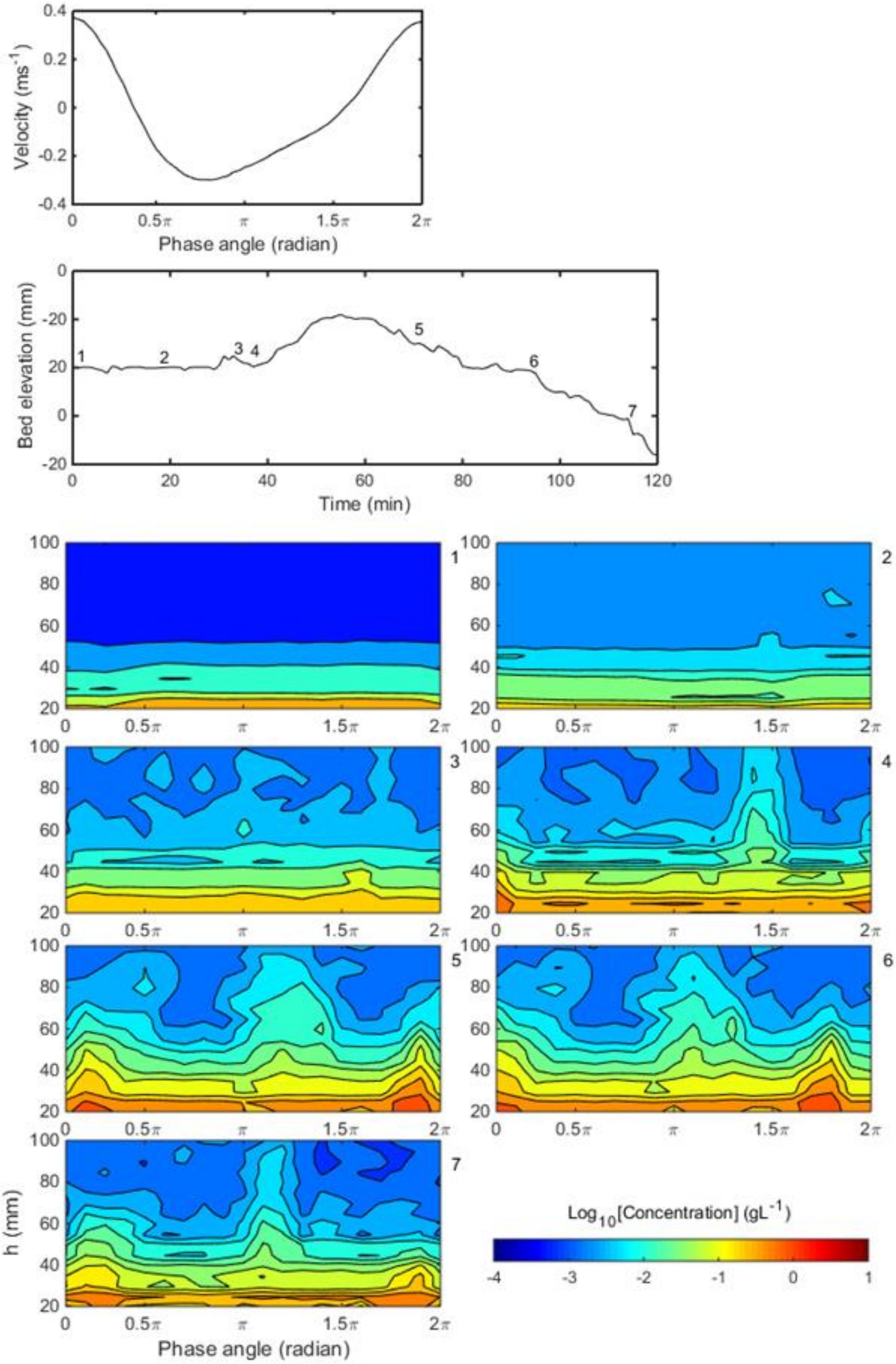

Figure 4-16 Wave velocity and phase averaged SSC profiles over the flat and the eroded bed between t=0 min and t=120 min of Run 04 with 6.2% of initial bed clay fraction. The top panel displays measured freestream velocity for over 24 successive wave periods. The seven numbered panels show phase-averaged suspended sediment concentration at respective time in the top second panel. The colours in the contour plots are defined in the colour bar as log_10 [SSC].

In Run 04, wave ripples reached equilibrium after t=100 min. An equilibrium wave ripple moved beneath the ABS probe between t=160 min and t= 190 min. Figure 4-17 shows the concentration field over the equilibrium ripple, with similar sequence of events in Run 03 observing as well. Again, vortex generated at lee side was able to carry more sediment than the counterpart forming at stoss side of ripple.

The initial bed clay fraction of Run 05 was increased to 7.2%, which enabled the bed beneath the ABS probe to remain flat for much longer time ($\sim$ 60 minutes) than Run 03 and Run 04 (Figure 4-18). Over the flat bed, suspended sediment concentration mainly stratified in 50 mm height above the bed, with sediment concentration in the bottom stratification gradual increasing (Panel 1 to 3, Figure 4-18). At t=105 min with bed eroded, a small suspended cloud appearing for phase angles 1.1 π rad cut down the stratification of suspended sediments (Panel 4, Figure 4-18). The bed was heavily eroded after t=120 min, with over 50 mm collapse of bed elevation. During this period, a larger suspended sediment cloud was observed just before flow reaching to maximum negative velocity of wave cycle, sediment expanding up over 70mm height at t=130 min (Panel 5, Figure 4-18). The stratified distribution of suspended sediment was totally disappeared after t=160 min, with concentration peak appearing in each half wave cycle and suspending sediments up to nearly 90 mm height (Panel 6, Figure 4-18).

Suspended sediment concentration over an equilibrium ripple between t=366 min and t=393 min is shown in Figure 4-19. At locations 1 and 2 above lee side of wave ripple, the distinct large suspended clouds with higher concentration were observed in the first half of wave cycles. However, in the succeeding half cycle, there were absence of concentration peaks. Over ripple crest (location 3), the suspended cloud with low concentration approaching to the height of 100 mm, which was possibly related to the advected suspension cloud from neighbouring ripple. At locations 4 to 7 on the stoss ripple side, three high-concentration regions were observed in a wave cycle, associating with vortex ejection and advection as mentioned above.

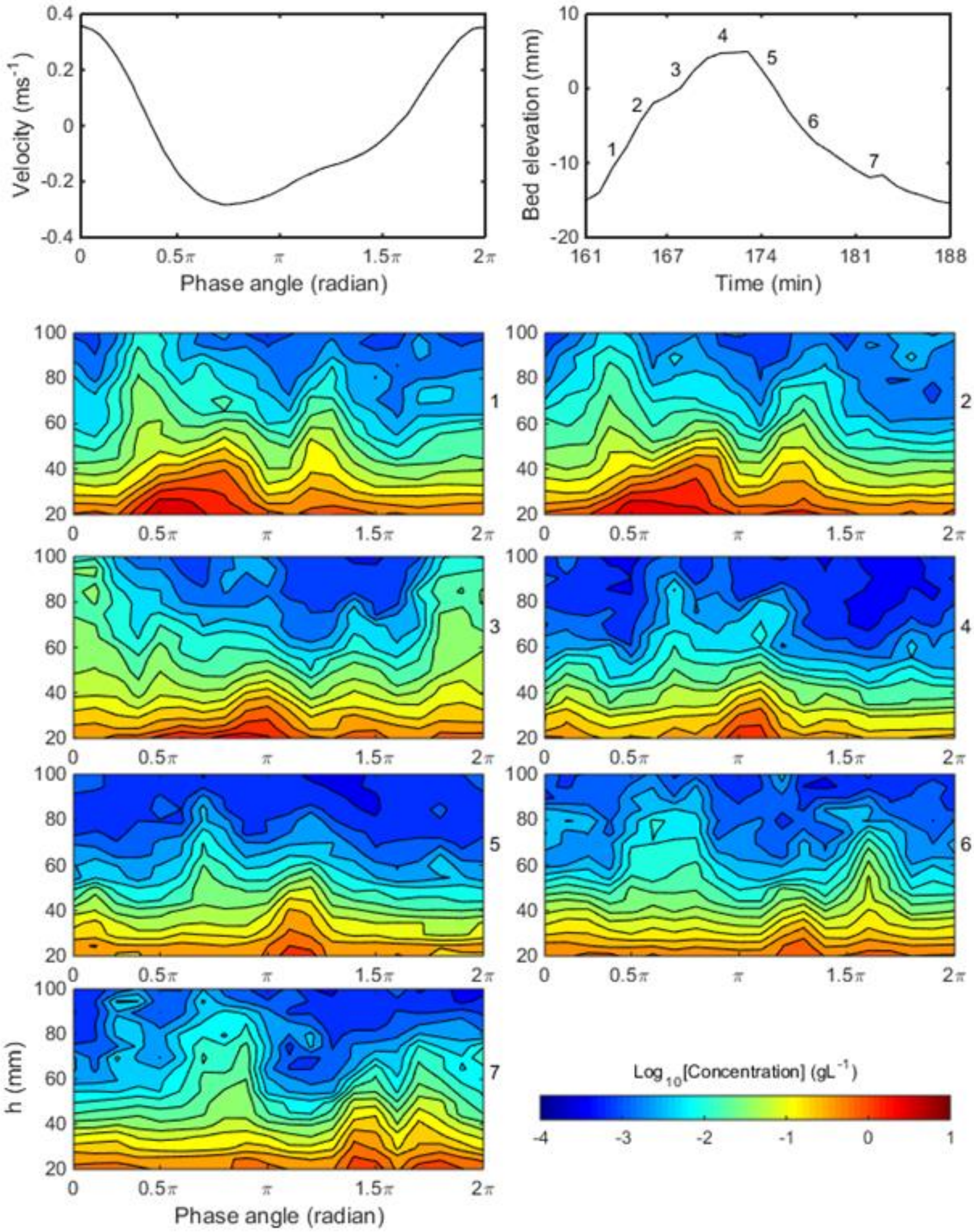

Figure 4-17 Wave velocity and phase averaged SSC profiles over the rippled bed of Run 04 with 6.2% of initial bed clay fraction. The top left panel displays measured freestream velocity for over 24 successive wave periods. The seven numbered panels show phase-averaged suspended sediment concentration at seven different locations of wave ripple as shown in top right panel. Wave direction was from right to left. The colours in the contour plots are defined in the colour bar as log_10[SSC].

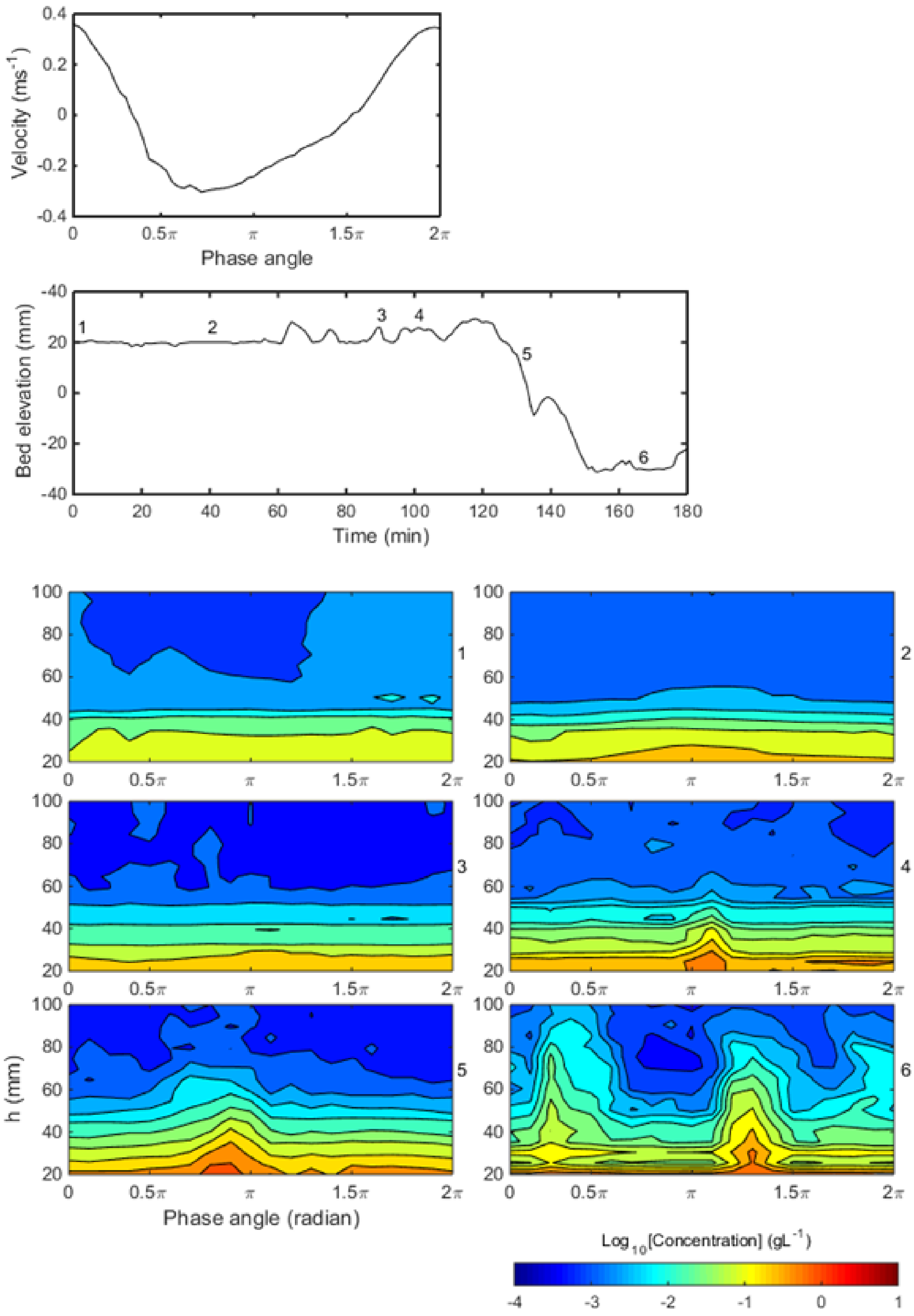

Figure 4-18 Wave velocity and phase averaged SSC profile over the flat and the eroded bed between t=2 min and t=180 min of Run 05 with 7.2% of initial bed clay fraction. The top panel displays measured free stream velocity for over 24 successive wave periods. The six numbered panels show phase-averaged suspended sediment concentration at respective time in the top second panel. The colours in the contour plots are defined in the colour bar as log_10[SSC].

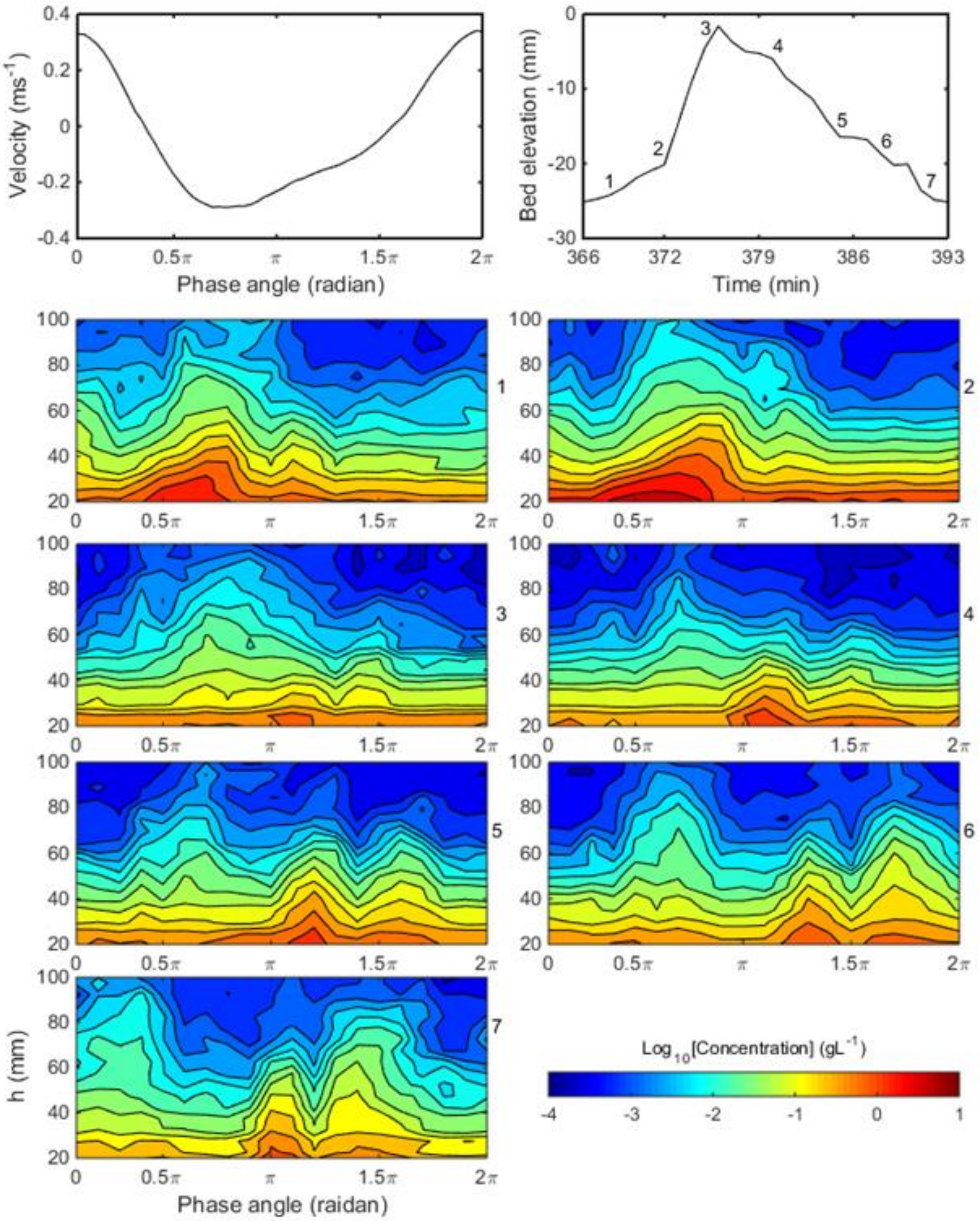

Figure 4-19 Wave velocity and phase averaged SSC profiles at different locations of an equilibrium ripple in Run 05 with 7.2% of initial bed clay fraction. The top left panel displays measured freestream velocity for over 24 successive wave periods. The seven numbered panels show phase-averaged suspended sediment concentration at seven different locations of wave ripple as shown in top right panel. Wave direction was from right to left. The colours in the contour plots are defined in the colour bar as log_10[SSC].

The stratified distribution in the concentration field lasted around 100 minutes even though the bed began to be eroded in Run 06 with the highest clay fraction of 7.4%

(Panel 1 to 5 Figure 4-20), with the majority of suspended sediments concentrating at the height below 50 mm. After t= 100 min, the stratification of suspended sediment was gradually disappeared and a small suspended sediment cloud was observed at a phase angle of 0.2 π rad when the bed elevation had risen to 10mm at t=120 min (Panel 6, Figure 4-20). During period from t=150 min to t=270 min, larger suspended sediment clouds were appeared between 1 π rad and 1.5 π rad in a wave cycle, carrying more sediment up to over height of 60 mm (Panel 7 and 8, Figure 4-20).

Figure 4-21 reflects the change of concentration field at different part of an equilibrium wave ripple migrating beneath ABS between t= 294 min and t= 321 min in Run 06. Similar as the results of previous runs, there was a distinct concentration peak in the first half wave cycle at the lee side of ripple (Panel 1 and 2, Figure 4-21). However, the concentration peak appearing above stoss side of ripple was only observed at location 6 that was close to ripple trough (Panel 6, Figure 4-21). Furthermore, compared with other runs, the magnitude of concentration peaks were much smaller not only at stoss side but also at lee side. It is possibly attributed to relatively smaller size of wave ripple with height of around 10 mm. While ripples in the previous runs beneath the ABS probe had heights over 20 mm. Consequently, relatively weak vortices formed above the smaller ripples can only suspend a small amount of sediments.

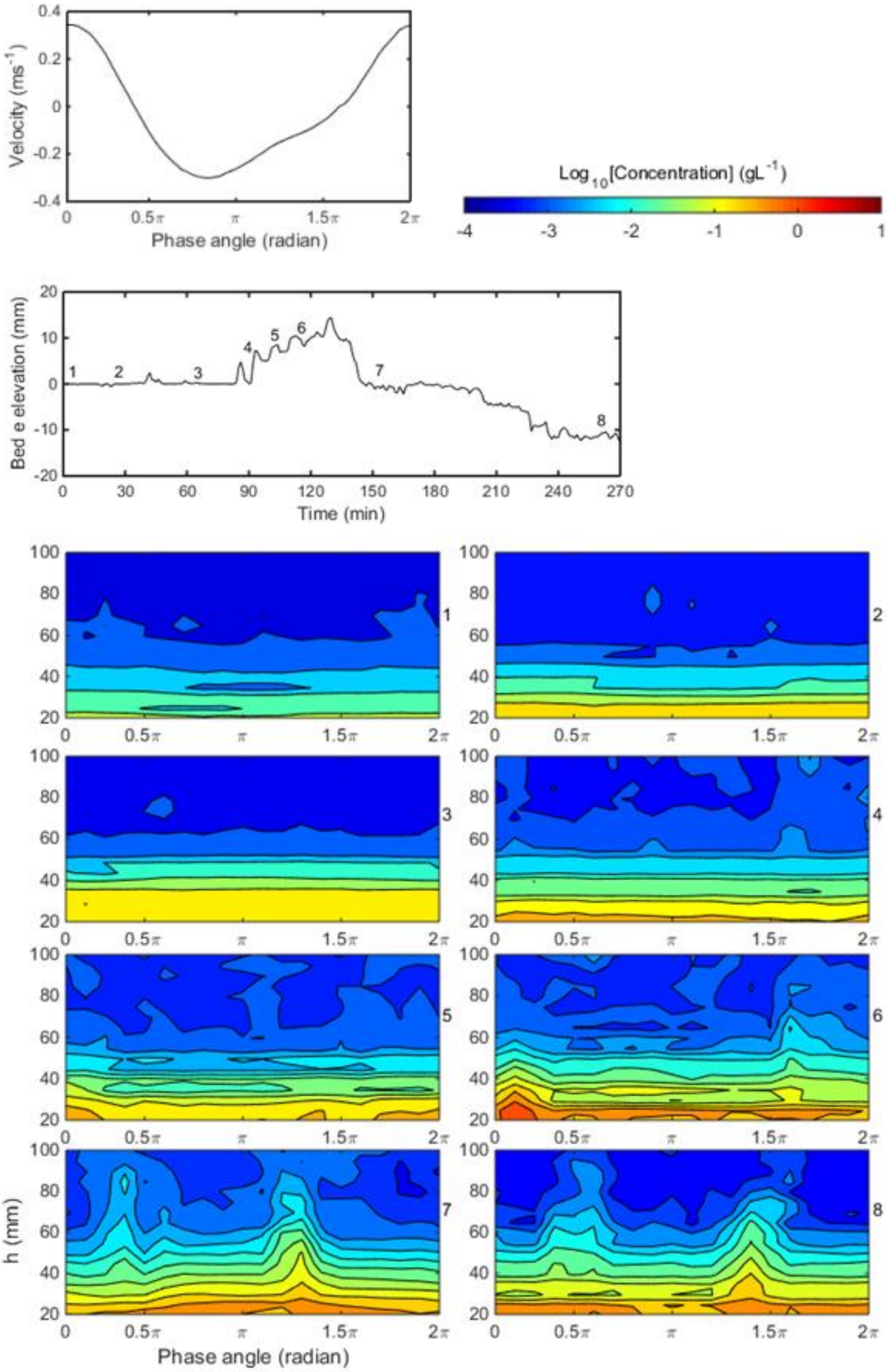

Figure 4-20 Wave velocity and phase averaged SSC profiles over the flat and the eroded bed between t=0 min and t=270 min of Run 06 with initial bed clay fraction of 7.4%. The top panel displays measured freestream velocity for over 24 successive wave periods. The eight numbered panels show phase-averaged suspended sediment concentration at respective time in the top second panel. The colours in the contour plots are defined in the colour bar as log_10[SSC].

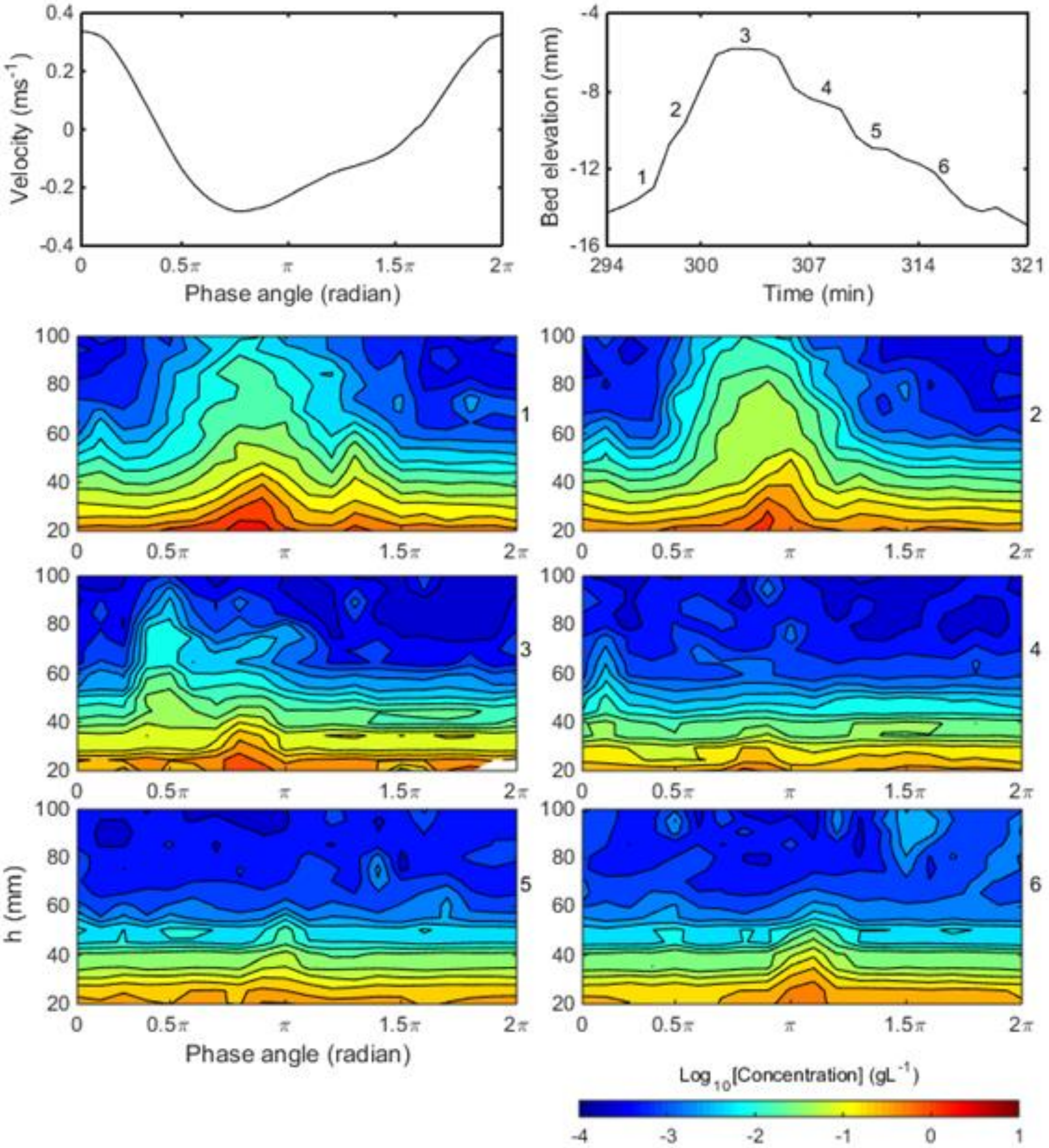

Figure 4-21 Wave velocity and phase averaged SSC profiles at different locations of a ripple in Run 06 with 7.4% of initial bed clay fraction. The top left panel displays measured freestream velocity for over 24 successive wave periods. The six numbered panels show phase-averaged suspended sediment concentration at seven different locations of wave ripple as shown in top right panel. Wave direction was from right to left. The colours in the contour plots are defined in the colour bar as log_10[SSC].

4.3.4 Suspended clay concentration change

In the current experiment, the OBS measured suspended sediment concentration along with the ABS. Downing (2006) suggested that OBS is more sensitive to fine sediment particles such as clay particles than the relatively coarse particles, especially with flow constituting two significant difference in sediment particle size. During each run, a large number of fine clay particles were winnowed from bed and mixed with coarse sand particles moving up by near bed turbulence, which transformed clean flow water to turbidity one during experiment (Figure 4-22). Thus, the OBS was likely biased towards the suspended clays concentration as shown in Figure 4-23.

A B

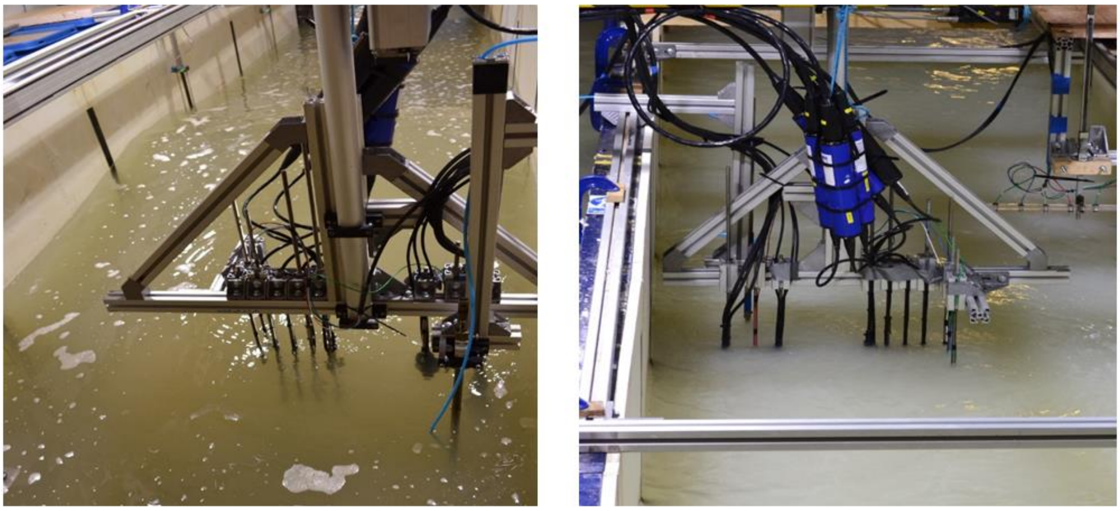

Beginning of Run 06 Approximately 1 hour later

Figure 4-22 Photos show the flow transforming from clean water (A) to turbidity water during Run 06 with the initial clay fraction of 7.4%.

Figure 4-23 shows the clay concentration at 50 mm height experienced a sharp increase in the first 10 minutes during each run, which indicates winnowing of clay particles from sand bed occurred immediately since waves imposed on the bed. At the same time clay particles continually moved upwards, resulting in the peak times of clay concentration were slightly later at 380 mm height. After that, the clay concentration basically uniform in the vertical direction except Run 04 in which the clay concentration at 50 mm height was distinctly higher than that at 380 mm height. Additionally, in Run 06 the suspended clay concentration reached to about 0.3 gL^{-1} at 380 mm height between t=10 min and t=15 min, which was unexpectedly higher than that at 50 mm height in the same time. There was a pronounced decline of clay concentration during each run. The reason for this phenomenon is clay particles expanding to outside of central working test. As Figure 3-1 shown, the working test section with mixed clay and sand bed was centred the area with 9.8 m length and 1.6 m width. The suspended clay particles were easily expanded outside area of central working section and settled back to flume floor as the still water in the outside area. Finally, the clay concentration gradually decreased without enough supplement of clay from the bed.

In general, the trends of suspended sediment concentration recorded by the OBS change were remarkably different with that recorded by the ABS. In this section, Figure 4-23 is closely linked to the suspended clay particles transport instead of both clay and sand transport in this flume experiment.

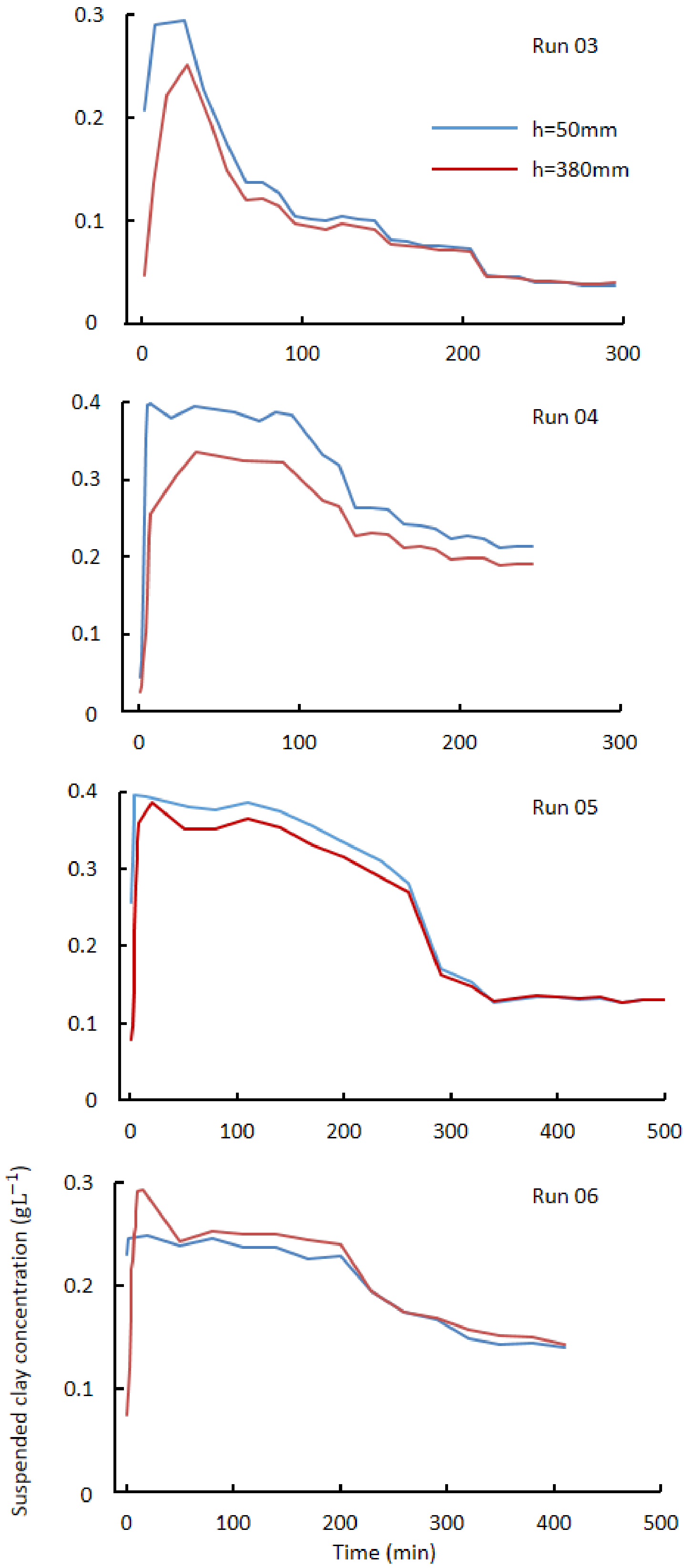

Figure 4-23 Suspended clay concentration during each run. The blue and red line denote clay concentration at 50 mm height and 380 mm height, respectively.

4.3.5 Volume distribution of suspended sediments

Figure 4-24 depicts volume distribution of suspended sediments at 50 mm (solid lines) and 380 mm (dash lines) height with log-log coordinate during each run. The results show the suspended sediment volume uniformly changed at different sampling heights, remarkable decreasing from fine to coarse sediment particle, though a slight increase was observed corresponding with very coarse sediment (500 µm). Furthermore, the results reflect the majority of suspended sediments were the fine particles that particle size was smaller than 30 µm. In particular, the volume of the very fine suspended sediments (< 3 µm) exceeded 100 μLL^{-1} at 50 mm height, which dominated suspended sediment volume distribution.

4.3.6 Time-averaged RMS (u') and the SSC changes over the different bed phases

The sand-clay mixed bed experienced three steps evolution during each run, including flat bed, eroded bed and rippled bed as shown above. The time-averaged near-bed horizontal velocity turbulence (RMS(u')) and suspended sediment concentration (SSC) at 20 mm height above the bed are used to investigate their changes over the different bed phases with the initial bed clay fraction.

Figure 4-25 depicts the time averaged RMS(u') is independent with increasing clay fraction over the flat bed (black circles), with the RMS(u') constant standing at approximately 0.019 ms^{-1}. The figure shapely increased when the bed was eroded during the experiments. Specifically, in Run 03 and Run 04 which had relatively lower clay fraction, the RMS(u') over the eroded bed reached to about 0.037 ms^{-1}. While the value decreased to around 0.028 ms^{-1} in Run 05 and Run 06 with clay fraction reaching to 7.2% and 7.4%, respectively (Figure 4-25).

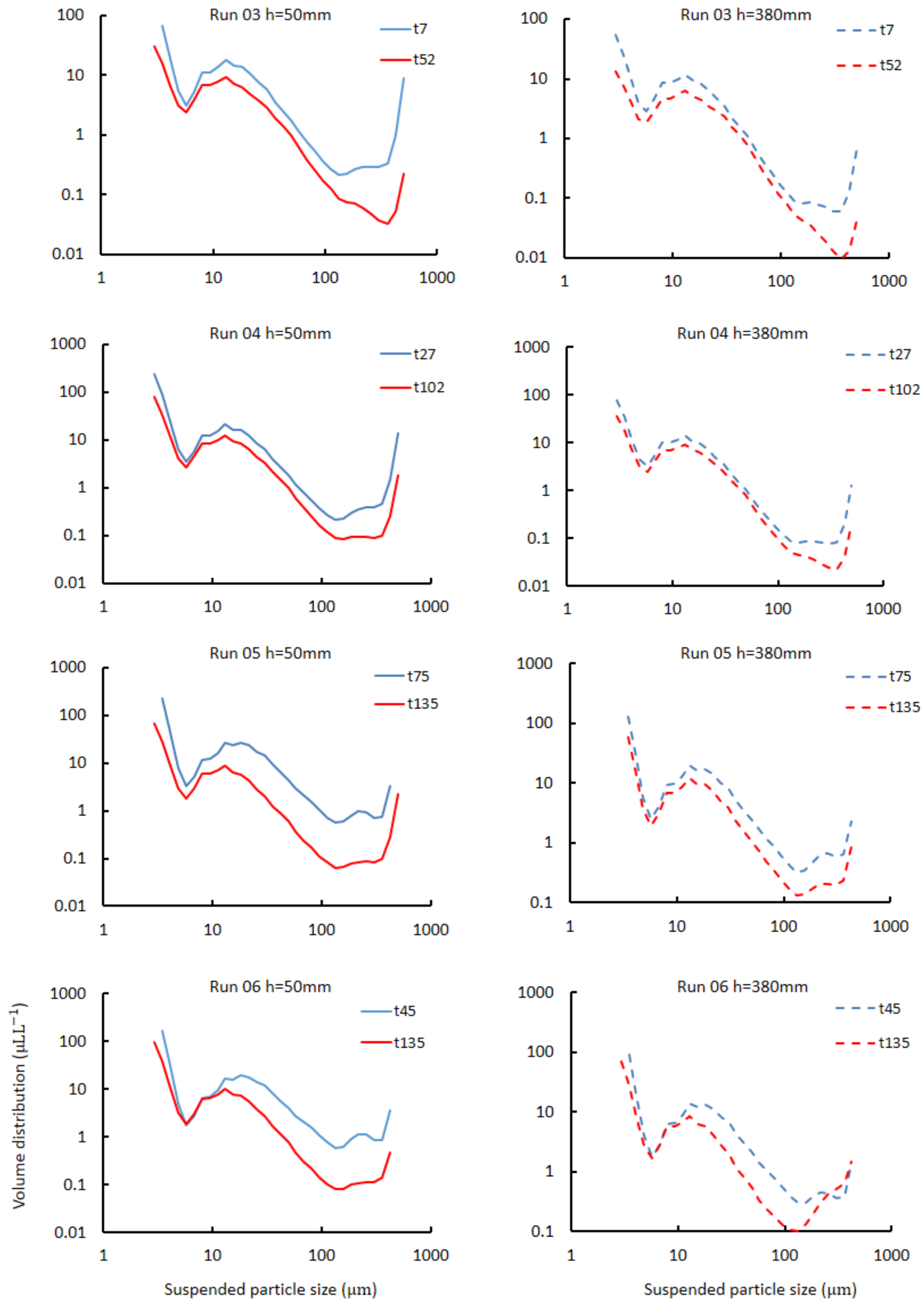

Figure 4-24 Volume distribution of suspended sediments with log-log coordinate. Solid lines and dash lines represent samples collected at 50 mm and 380 mm height respectively.

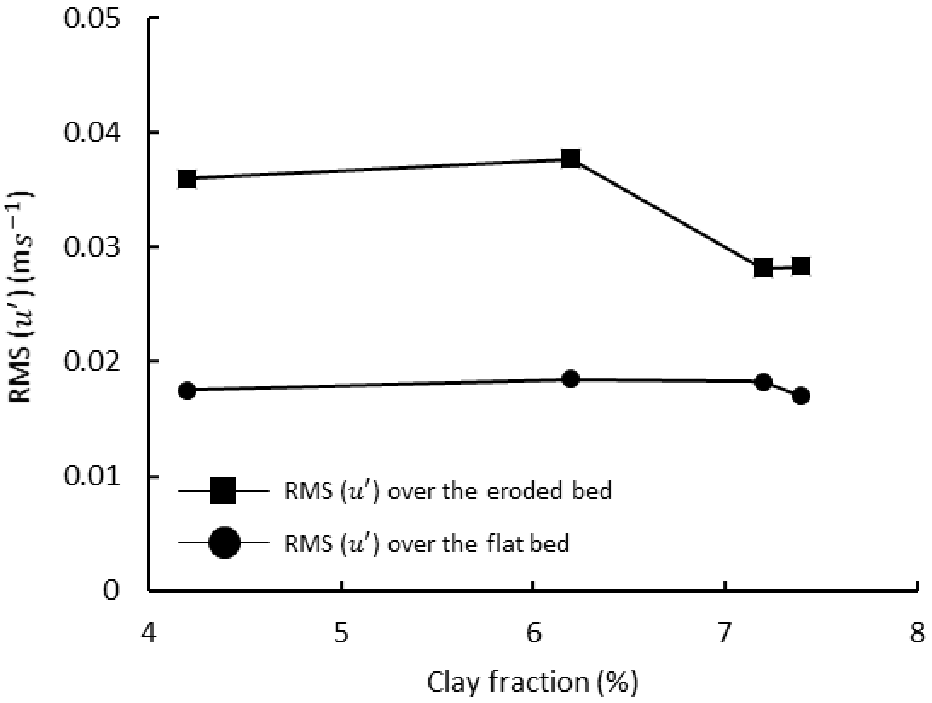

Figure 4-25 The time averaged Horizontal velocity turbulence RMS(u') at 20 mm above the bed with different bed phases against initial bed clay fraction. Black circle blcak square donates RMS(u') over the flat bed and the eroded bed, respectively.

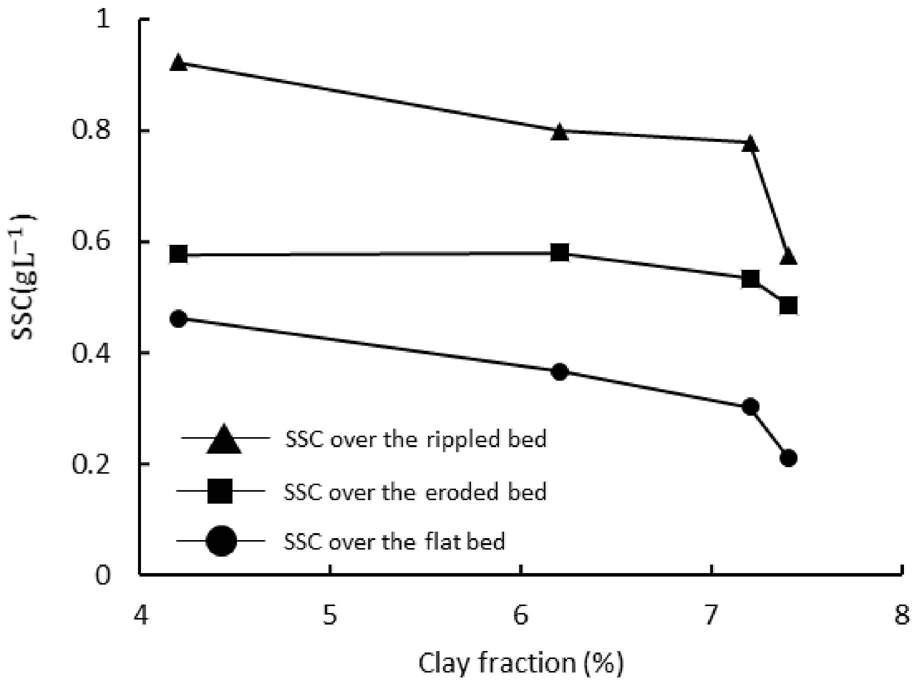

Figure 4-26 The time-averaged suspended sediment concentration (SSC) at 20 mm height above the different bed phases against initial bed clay fraction. Black circle donates SSC over the flat bed; Black square donates SSC over the eroded bed, and black triangle donates SSC over the rippled bed.

In terms of suspended sediment concentration (SSC), the SSC was the lowest over the flat bed (black circle) and remarkably increased over the eroded bed (black square) and rippled bed (black angle) as shown in Figure 4-26. When the bed remained flat, it decreased gradually from 0.46 $\mathrm{gL^{-1}}$ of Run 03 to 0.21 $\mathrm{gL^{-1}}$ of Run 06. Over the eroded bed, the figure was 0.58 $\mathrm{gL^{-1}}$ in Run 03, with slight decreasing to 0.52 $\mathrm{gL^{-1}}$ in Run 06 of 7.4% clay fraction. The SSC peaked to 0.92 $\mathrm{g\,L^{-1}}$ when the wave ripple reaching equilibrium in Run 03. The value dropped in the following runs with increasing initial bed clay fraction. Especially the SSC over the rippled bed significantly decreased to 0.57 $\mathrm{gL^{-1}}$ in Run 06 (Figure 4-26). The reason may be attributed to the relatively smaller size of wave ripple. As mentioned above, the ABS recorded only three small wave ripples with height about 10 mm in Run 06. The rather weak vortices were generated cross the lee side of smaller ripples, which lead to suspend a small amount of sediments.

4.4 Discussion

4.4.1 Causes of suppression of near-bed turbulence

The experimental results presented herein reveal that the near-bed horizontal velocity turbulence intensity was relatively lower when the bed remained flat (Figure 4-8). In addition, near bed vertical gradient of suspended sediment concentration significantly increased from the flat bed to the rippled bed (Figure 4-13), which also reflects turbulence suppression over the flat bed.

In the present experiments, the bed was constituted by sand and Kaolinite clays that is one of very common minerals in the earth. The clay particles were winnowed from the bed once the oscillatory flow moved over the bed. The suspended clay particles attract each other (cohesive force) because of molecular-scale electrostatic forces (Van Olphen, 1977). With increasing amounts of clay particles, the sufficiently small distance between clay particles causes the collisions of clay particles to form flocs (Van Olphen, 1977). The flocs grow to generate a gel with highly particle bonds, which possibly leads to turbulent suppression (Winterwerp and Van Kesteren, 2004). Therefore, the dynamics between cohesive force and turbulent force is heavily dependent on the suspended clay concentration in the experiments with similar flow condition. Baas et al. (2009) proposed that the 4 $\mathrm{g\,L^{-1}}$ of suspended clay fraction is the threshold to modulate turbulence. However, the highest suspended clay fractions in the present experiment were close to 0.4 $\mathrm{gL^{-1}}$ that were far less than the threshold fraction. Baas et al.(2013)

assumed that such small amount of clay fraction was unable to supress turbulence. Furthermore, the results of the volume distribution of suspended sediment suggest very fine clay particles with size smaller than 10 μm were dominated. In other worlds, only a very small amount of clay particles collided to form flocs with size when the bed kept flat (see Figure 4-24). Therefore, it is speculated that cohesive force in the flow was too weak to supress turbulence.

Another mechanism of turbulence suppression is that suspended clay particles thickening the viscous sublayer which has been shown to reduction of vertical mixing and momentum exchange, finally supressing turbulence (Gust, 1976; Li and Gust, 2000). Previous studies proved that a very small amount of suspended Kaolinite clay could damp turbulence in salt water, for example 0.01-0.15 $\mathrm{gL^{-1}}$ in the experiment of Gust and Walger (1976), 0.1 $\mathrm{gL^{-1}}$ of experiment of Li and Gust (2000). Based on this theory, the clay concentration in the flow during beginning of each run was possibly able to form thick viscous sublayer and finally damping near-bed turbulence.

In addition to suspended clay damping flow turbulence, the bed roughness seems to be another important cause contributing to suppression of turbulence. Over the flat bed the turbulence intensity was constant and was lower than 0.02 $\mathrm{ms^{-1}}$ (Figure 4-25). However, the turbulence intensity significantly increased when the bed started to be eroded (Figure 4-25), which presumably indicates increasing bed roughness promoting turbulence intensity. A number of studies found that increasing bed roughness is able to provide additional turbulence by comparing with gravel bed and smooth bed under unidirectional flow condition (e.g. Papanicolaou et al., 2001; Hardy et al., 2007; Baas and Best, 2009). At the very beginning of each run, the bed was flat mixed with clay and sand. On the surface layer, the gaps between sand particles were filled by very fine clay particles, hence the bed could be regarded as a smooth bed (Selby, 1997). Clay winnowing during experiments led to reduction of bed yield strength. As a result, near-bed sediment transport initiated and the bed gradually became rougher because of the change of bed topography, which increased velocity gradient in the boundary layer (Glenn and Grant, 1987; Leeder, 2011). This progress promotes energy change in the flow and then causes turbulence enhancement.

The stratified distribution of suspended sediment above the flat bed were observed during each run and this stratified structure was immediately disappeared when bed morphology started to change (e.g. Figure 4-14). Considering the suspended sediment including both sand and clay, the significantly different particle size of sediments might be much easier to form vertical gradients of density compared with uniform suspended sediments because of the difference fall velocity between sand particle and clay particle. Coincidentally, this stratification structure occurred only corresponding with relatively lower turbulence intensity. Many previous studies found similar results as well. For example, Adams and Weatherly (1981) investigated the bottom boundary layer of the Florida current and found 40% of turbulent kinetic reduction with suspended sediment stratification. The model of Ribberink and Al-Salem (1995) overpredicted suspended sediment concentration when the sediment stratification existed. The stratification of suspended sediments is considered as a main cause to damp turbulence (Sheng and Villaret, 1989; Winterwerp, 2001). Density interface in the stratification inhibits vertical energy transport, which results in near-bed turbulence suppression and finally decline of suspended sediment concentration (Sheng and Villaret, 1989). Herein, it is conjectured that the combination of stratification of suspended sediments and smooth flat bed played a vital role on turbulence suppression at the beginning of the experiments.

4.4.2 The role of turbulence suppression on the wave-induced ripple evolution

Wave-induced ripple evolution with mixture clay and sand substrates was investigated in the Chapter 3. The results show that the equilibrium ripple length and height kept constant with increasing initial clay fraction (Figure 3-21). However, the first appearance of the two-dimensional wave ripple from the flat bed gradually delayed. Furthermore the development rate of wave ripples significantly decreased with initial bed clay fraction increase as well (Figure 3-21). The increasing bed yield strength caused by increase initial bed clay fraction is thought to extend distinctly wave ripples development in the Chapter 3. In the present chapter, turbulence suppression is highlighted and discussed in the former sections. Best and Leeder (1993) investigated the influence of clay-laden (0.2 $\mathrm{g\,L^{-1}}$) current flow on ripple development. The experimental results showed that the flow within suspended clay apparently increased bed erosion threshold and then delayed the first ripple appearance. Best and Leeder (1993) hypothesized it was attributed to drag reduction by decreasing vertical turbulent momentum exchange. This theory about the relationship between turbulence suppression and drag reduction is supported by many flume experiments (e.g., Gust, 1976; Amos et al., 1992; Li and Gust, 2000). Thereby it is conjectured that both turbulence suppression to reduce shear stress acting on the bed and the increasing bed yield stress to increase bed resistance work together to slow wave ripple development rate. Considering the degree of turbulence suppression was constant, the increasing bed yield stress possibly dominated wave ripple evolution evidenced by the decrease suspended sediment concentration above the flat bed from Run 03 to Run 06 (Figure 4-26). The role of drag reduction, however, cannot be ignored and further work is needed to investigate more details about the influence of combined drag reduction and increasing yield strength on bed erosion resistance.

4.4.3 The near-bed suspended sediment dynamics

As discussed in the above, increasing initial clay fraction from Run 03 to Run 06 strengthened bed resistance. Considering the same level of bed shear stress exerted by waves of each runs, the clay added into the bed efficiently reduced sediment entrapment, especially the amount of sands movement (Figure 4-26). It is speculated that the back-and-forth orbital motion on the bed enable sand particles to move up just in the boundary layer. At the same time, clay particles can be winnowed up to relatively higher water column. As a result, stratification of suspended sediments was formed over the flat bed in each run.

Random turbulence events dominated sediment transport when the bed morphology started to change, which were strong enough to suspend more sediments into flow. It seems that the clay fraction over 6.4 % could increasingly resisted sediment transport in this period (Figure 4-26). The reason probably is related to rather lower erosion efficiency in runs with higher initial clay fraction. With the similar flow condition, waves entrained a small quantity of sediments due to higher bed resistance in these experiments.

Over the rippled bed, the majority of suspended sediment was closely linked with vortices, which is consistent with earlier work (e.g. Davis and Thorne, 2005; Admiraal et al., 2006). Moreover, there was a reverse relationship between clay fraction and the SSC over this bed phase (Figure 4-26). The decline of vortex strength that strongly related to ripple height (Marieu et al., 2008) is assumed to main cause of the gradual decrease of the near-bed SSC (see Figure 4-9 to Figure 4-12).

4.5 Conclusions

In this chapter, the near-bed turbulence and suspended sediment concentration over different bed phases of each run have been investigated. In addition, the interacting triad of cohesive bed, near-bed turbulence and suspended sediment dynamics is discussed as well. The conclusions can be drawn as following:

1. The near-bed turbulence intensity (RMS(u')) was supressed over the flat bed, consistently standing at 0.019 ms^{-1} without influence of increasing initial bed clay fraction from Run 03 to Run 06. It is remarkably enhanced when the bed started to be eroded. Furthermore, the near-bed RMS(u') over the eroded bed were 0.028 ms^{-1} in runs with high initial clay fraction, which were lower than that in Run 03 and Run 04, standing at around 0.036 ms^{-1}.

2. The suspended sediment concentration (SSC) field over the flat bed in each run was characterised by the stratification of suspended sediments, which was immediately disappeared with bed morphology eroded. Several peak values of the SSC that related to vortices ejection and advection were appeared in each wave cycle over the both side of wave ripples. Moreover, the peak concentrations at lee side of ripples were significantly larger magnitude than that at the opposite ripple side, which is probably due to the asymmetrical waves.

3. The time averaged SSC at height of 20 mm above bed was significantly increased from the flat bed evolving to equilibrium wave ripples. Furthermore, there is an inverse relationship between the near-bed SSC and increasing initial bed fraction over the same bed phase.

4. The interactions among cohesive force in bed, near-bed turbulence and suspended sediment dynamics play a vital role on wave ripple evolution. The combination of suspended sediments stratification presumably resulting in turbulence suppression and the increasing yield strength with increasing bed clay fraction enables the bed to remain flat longer time. Continual winnowing of clays, however, efficiently reduced bed yield strength and contributed to bed erosion. The near-bed turbulence is significantly enhanced with the increase of bed roughness, promoting large amount of near-bed sediment transport and finally generating wave ripples.

CHAPTER 5 –Bedform morphodynamcis under combined flow: field surveys

5.1 Introduction

Coastal zone, a transitional region between land and sea (Crossland et al., 2005), is providing richness and diversity of natural resources and ecosystem services. The coastal zone, broadly defined as areas within 100 km of the coastline, hosts approximately half of the world's population (Crossland et al., 2005). An estuary is an important part of coastal zone and is defined as a partially enclosed body of brackish water, which links terrestrial river catchments to coastal seas. Given their strategic locations over two third of the world's largest cities located on estuaries (Ross, 1995).

Estuaries are significantly influenced by tidal currents with gradients of salinity and density existing from the largely saline river mouth to the upper estuary zones fed by fresh water systems (Hansen and Rattary, 1966). The periodic flood and ebb tides along with periods of slack water contribute to settlement of large quantities of sediments that can be derived from both the coastal seas and from the upstream river system (Davidson et al., 1991), often forming complex bar and island deposits across the estuary zone. Additionally, there are abundant nutrients trapped with sediments in the estuaries, supporting primary source of food for animals and plants (Fairweather and Quinn, 1993).

At present the hydrodynamics and sediment dynamics in estuaries are sensitively affected by both climate change and human activity. Present trends in global warming has been shown to lead to extreme weather events and the strengthening of storm force (Rosenzweig et al., 2001), which can result in rapid morphological adjustments (Hay and Wilson, 1994; Green et al., 1995). Moreover, human activities directly affect sediment supply in estuaries. For example, reservoir construction within upstream river basins may significantly reduce sediment delivered to the lowland rivers and estuaries (Sybitski et al., 2005; Kummu and Varis, 2007). In addition, agricultural production including deforestation and reclamation can result in enhanced land run-off, and therefore a sharp increase in sediment load in the estuaries (Walling and Fang, 2003; Siakeu et al., 2004).

Bedforms are the primary sedimentological features within estuarine systems, and are found both in subtidal channels as well as across exposed bar tops at low tides. Bedform dynamics, via influences on bed roughness, regulate flow sediment transport processes and are sensitive to changes in flow forcing and thus above mentioned environmental changes concerned with storm forcing. Although previous flume experiments provided an excellent information set on their relationship between ripple dynamics in both unidirectional and combined (wave and current) flows (Yokokawa, 1995; Sekiguchi and Yokokawa, 2008; Dumas et al., 2005), the related knowledge is still far from achieving a full predictive framework for understanding bedform dynamics in natural estuarine environment. Moreover, recent research has shown the importance of biological cohesive extracellular polymeric substances (EPS), produced by micro-organisms, in stabilizing sediment surfaces in estuarine systems. EPS effectively reduces fluid erosion by binding the sediment particles to one another (Underwood and Paterson, 1993; Southerland et al., 1998; Tolhurst et al., 2002; Lundkvist et al, 2007). Recent flume experimental results have also highlighted the bedform growth rate is significantly slowed with the addition of EPS to the substrate. Indeed, even with low levels (0.016%-0.5%) of EPS fraction in the bed (Malarkey et al., 2015; Ye, 2016) significantly changes in bedform size and dynamics. Specially, Malarkey et al (2015) indicated, compared with ripples formed from pure sand bed, both ripple lengths and heights were smaller due to existence of EPS within the substrate.

Fully understanding the complex relationship between hydrodynamics, bedform dynamics and the role of biological cohesion on bedform evolution in estuarine environment are important in order to improve management of coastal environment. In this chapter, a suite of fieldwork was conducted in the Humber Estuary, NE England, in order to examine the relationship between flow forcing, waves and bed cohesion. A state-of-the-art 3D laser scanner was used in order to acquire high resolution ripple geometry. The primary aim of the field surveys was to study the influence of wave-induced bottom oscillatory motion combined with unidirectional motion on bedform geometry changes under windy condition. Additionally, this chapter also tried to investigate if the biological cohesive EPS seasonally affect ripple size in the study estuary.

5.2 Background of the Humber Estuary

The Humber estuary, one of the largest estuaries in the UK, is located on the east coast of northern England (Figure 5-1). The estuary begins at Trent Falls where the Ouse and Trent confluence. The combined rivers are about 1 km wide at confluence and expand towards the sea, expanding to a width of around 8 km at Spurn Head (Figure 5-1), along a length of approximately 62 km (IECS 1987). The catchment of the Humber estuary is of some 24,000 km^2, which covers approximately one fifth of England's land area (Figure 5-1, Jarvie et al., 1997). The majority of freshwater source of the Humber is from the rivers Ouse and Trent, with the long-term mean total flow discharge reaching 240 m^3s^{-1} (IECS, 1987).

The Humber estuary can be divided into three units that includes upper estuary, middle estuary, and lower estuary (Figure 5-1). The estuarine morphology exhibits a range of depositional forms, with mud or sand flats occupying approximately one third of estuary during low water (IECS, 1987; Aubry and Elliott, 2006). Additionally, saltmarsh, sand dunes and sand beaches are widespread in the middle and lower estuary (IECS, 1987).

Another prominent characteristic of the Humber estuary is high suspended sediment concentration. The suspended particulate matter (SPM) concentration can be over 10 gL^{-1} in upper estuary and gradually falls towards estuary mouth (Uncles et al., 1998; Uncles et al., 2005). The high SPM concentration combined with the salt intrusion contribute to create a significant estuarine turbidity maximum (ETM), which has a large impact on local ecology (Mortimer et al., 1999; Paterson et al., 2000; Boyes and Elliott, 2006).

The Humber estuary has the second-largest tidal range in the U.K., with tidal range of 6.5 m at the Humber mouth and peaking to 7.2 m at Saltend (IECS, 1987; Figure 5-1). Tidal influence can extend to over 100 km inland along both river Trent and Ouse (Rouse and Hardisty, 1996). Tides are typically semi-diurnal featuring a significant neap-spring inequality (IECS, 1987). For example, maximum spring tide range at Saltend reaches to 7.2 m which is 3.3 m larger than tide range of the minimum neap tide. In addition, current velocities mainly contributed to gradual tides asymmetry from Humber mouth to the upper estuary (IECS, 1987). At Spurn, the tide is roughly sinusoidal with a symmetric (6.25 hours) flood and ebb phase. Into the estuary, at Brough, asymmetry in the tide extends, with a decline in flood time to 4.5 hours whilst ebb time increases to 8 hours.

The Humber estuary is bounded by significant development of socioeconomic activities such as agricultural production, fisheries infrastructure, chemical industry, ports and shipping and seaborne trade (Gray, 1995; NRA, 1993; Jarvie, 2000; DETR, 2000). Moreover, the floodplain of the Humber estuary hosts a third of a million people (Edwards and Winn, 2006). Furthermore, the Humber estuary is of outstanding habitat for a variety range of wildlife (Edwards and Winn, 2006) and provides abundant ecosystem services, particularly for migratory birds.

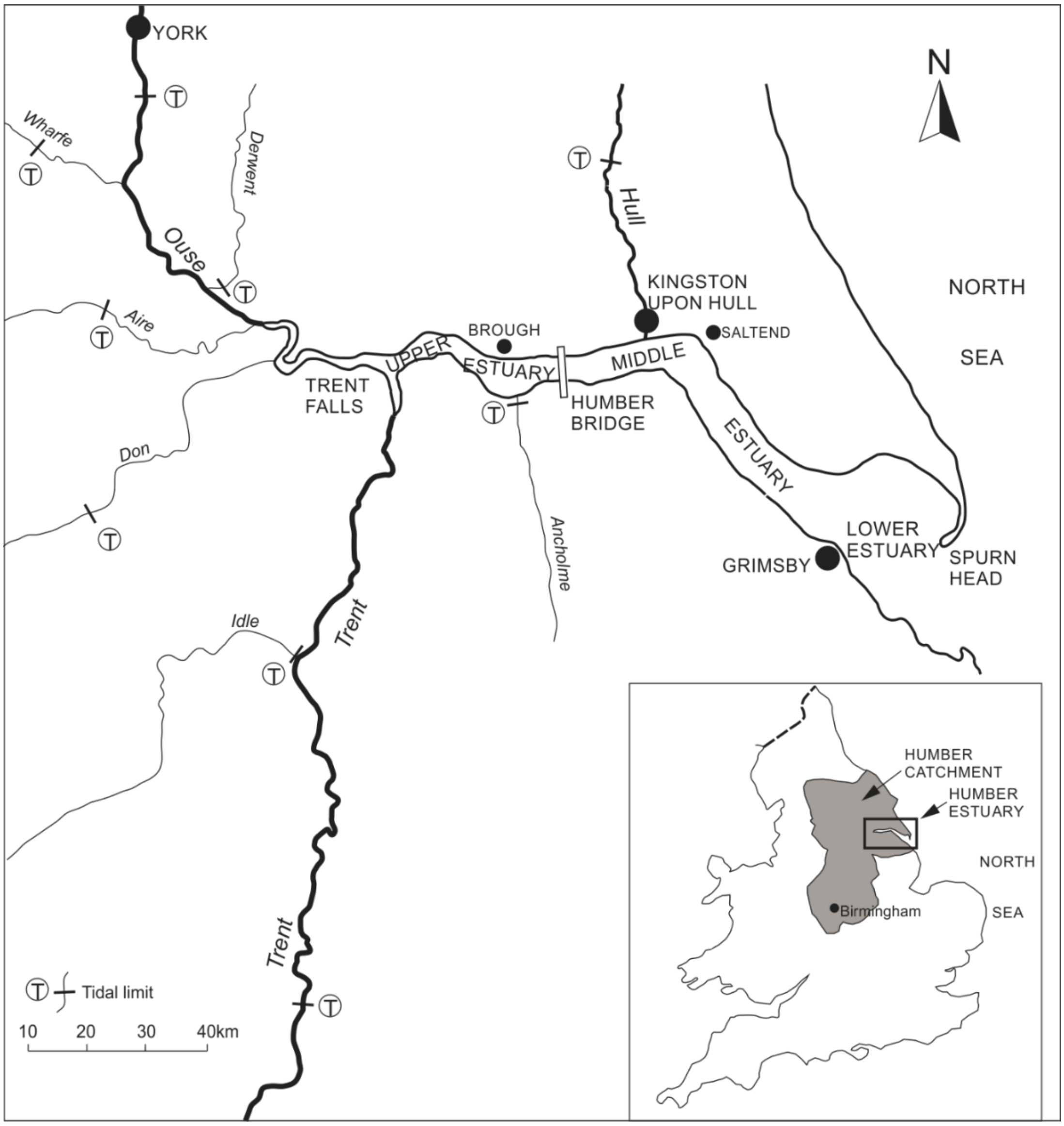

Figure 5-1. The Humber estuary and its catchment (modified after Edwards and Winn, 2006).

5.2 Methodology

5.2.1 Sandbar ripples surveys and instrumentation

Six periods of field surveys and samples collections were conducted at the red cliff sand bar (Figure 5-2), which is located in upper estuary. The south channel is the main shipping channel with an average depth around 3.5 m and the north channel is about 3 m deep at mean high water. This sand bar was exposed periodically during low tides.

The topography of the middle sand bar is flat, with topographic variations across the bar of below 1 meter. At the north edge of sand bar, the elevation gradually decreases, and thus exposure of the sand surface is only for a short period during lowermost tides. For this reason, the survey site was chosen at the north edge (Figure 5-2).

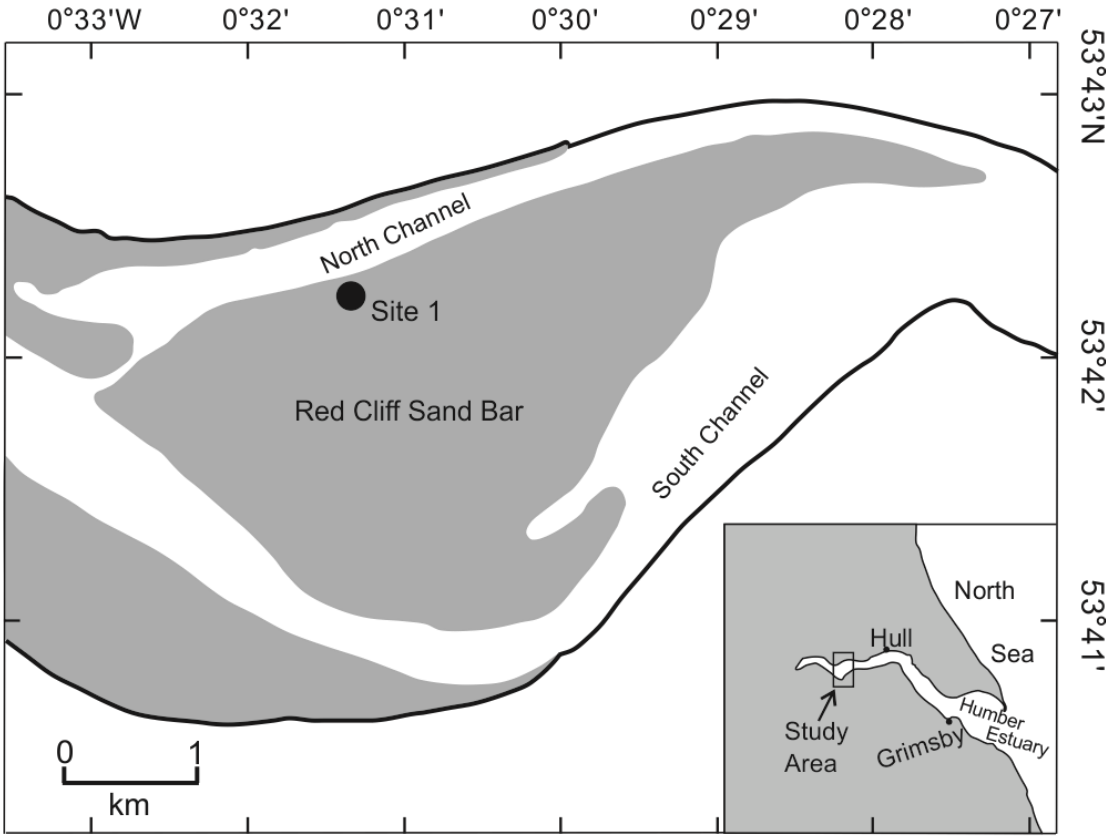

Figure 5-2. The location of the Red cliff sand bar, upper Humber Estuary, NE England.

Each round of the field work included two consecutive surveying days. Surveys were conducted across spring and neap tide periods in the winter of 2014 and summer of 2015 (0). This gave a broad range of flow and wave conditions at the site. Especially high waves were recorded during two high winds events which occurred during the spring tide and neap tide in the December of 2014 and March of 2015, respectively. The wind speed at field site reached to 28 knots and 25 knots during these two rounds of surveys (https://www. Windguru.cz), describing as moderate gale and strong breeze respectively based on the Beaufort wind force scale.

Field work date and tide condition

Season	Round*	Date	Spring	Neap
	WS1	24/11-26/11/2014	Calm	–
	WS2	08/12-14/12/2014	Moderate gale	–
	WN1	10/02-14/02/2015	–	Calm
	WN2	25/02-04/03/2015	–	Strong breeze
	SN1	23/07-31/07/2015	–	Calm
	SS1	05/08-07/08/2015	Calm	–

*Explanation of the nomenclature of the fieldwork round: the first capital letter indicates the season when field survey was conducted, and the second one denotes tide condition. The number represents the order of fieldwork. For example, SS1 denotes the first field survey during spring tide in summer.

The data collection for each field survey included deployment of a MIDAS DWR Directional Wave Recorder across the survey period in order to capture the flow and wave conditions at the site. This deployment was complemented 3D topographic scanning at low water, using a 3D FARO Laser Scanner and sampling of short sediment cores, which were collected from both a ripple crest and tough during each survey.

5.2.2 Wave and tide current measurement

The Valeport MIDAS DWR Directional Wave and Tide Recorder (Figure 5-3) was set up to measure both wave and tidally-driven currents at the site. The device obtains the real wave and current data by converting the measurements of flow-induced pressure variations. Meanwhile it calculates directions of both wave and current using Doppler shift principles. The details of operations of measurements are reported in *MIDAS DWR Manual* (Valeport Limited, 2004). The basic principle of wave measurement is based on the Linear Wave Theory, considering individual wave superimposed on top of each other with varying wavelengths and frequencies. The wave and current parameters, including significant wave height, mean zero upcrossing period, current velocity, could be calculated by measuring a burst of data of period of several minutes.

Figure 5-3. MIDAS DWR Directional Wave and Tide Recorder was set up during low tide time.

The data logged by the MIDAS DWR Directional Wave and Tide Recorder excludes the bottom orbital wave velocity that could be computed using significant wave height, mean zero upcrossing period. Soulsby (1986) hypothesised that a spectrum of random waves produce a series of orbital wave velocity under natural conditions, which can be approximated by its standard deviation (U_{rms}). In addition, Soulsby (1986) established the relationships between measured wave parameters and U_{rms}, as showing in the following equations:

$$U_{rms} = \frac{0.25H_s}{(1+At^2)^3 T_n} \quad 5\text{- }1$$

where

$$A = [6500 + (0.56 + 15.54T)^6]^{1/6} \quad 5\text{- }2$$

and

$$t = \frac{T_n}{T_z} \quad 5\text{- }3$$

$$T_n = (\frac{h}{g})^{1/2} \quad 5\text{- }4$$

h: flow depth

T_z: mean zero upcrossing period

5.2.3 Laser scan of ripples

The state-of-the-art terrestrial 3D laser scanner instrument (FARO Focus3D X 330) was used to capture detailed topography of the ripples. Based on the laser technology, it is able to produce three-dimensional images with high accuracy and resolution (Nield et al., 2014).

The detailed operating principle of FARO Focus3D X 330 is elaborated in *FARO Laser Scanner Focus^{3D} X 330 Manual* (2013). An infrared laser beam is projected into the centre of the rotating mirror which deflects the laser in a vertical axis direction. Then the light is scattered from scanning objective and finally is reflected back into the scanner from the surrounding area (Figure 5-4).

Distance measurement is based on the phase shift technology modulating laser beam with constant waves of infrared light of varying length. The light contacts the scanned object and is then reflected. The distance between the laser scanner and the object is accurately computed by measuring the phase shift in the waves of the infrared light. At the same time the measured distance is used with the mirror angle encoded and the horizontal rotation of the scanner. The x, y, z coordinates of each scanning point can thus be acquired by the instrument. The measurements over a period of time create a 3D Point Cloud. In the present fieldworks, the 3D clouds consisted of approximately 177 million of scan points for each survey. The scan distance of FARO Focus3D X 330 is up to 330 metres, but the site surveyed herein were restricted and bounded to a maximum of 15m by white spheres, which were also used to rectify the positioning of the system (Figure 5-5).

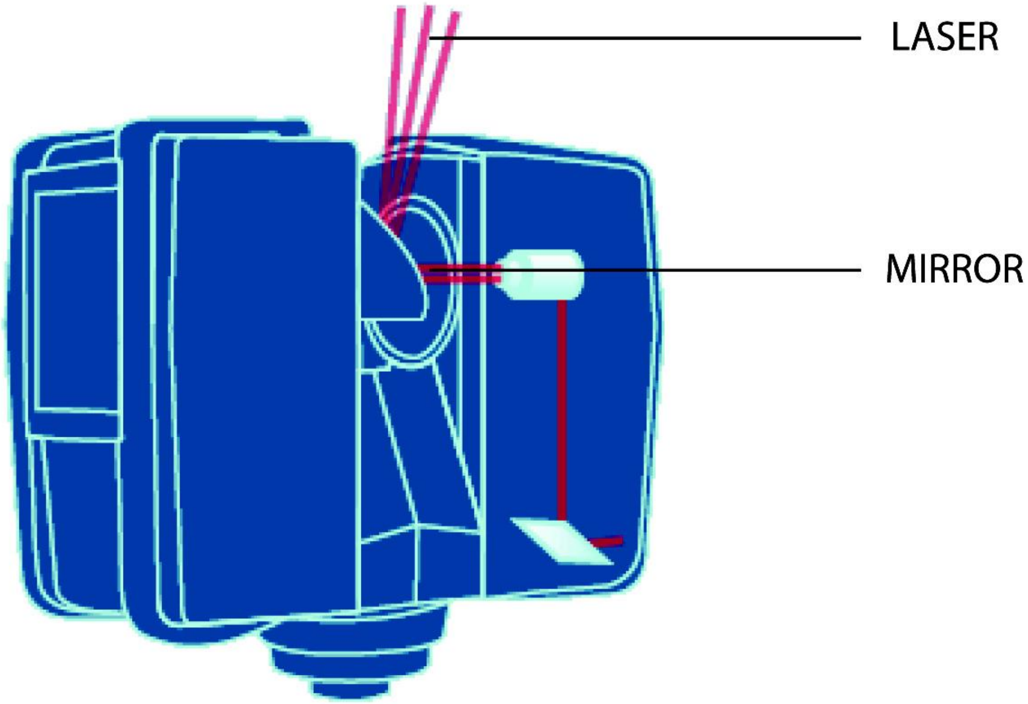

Figure 5-4. Schematic shows laser deflection (FARO Laser Scanner Focus^{3D} X 330 Manual (2013))

The scan 3D Cloud is processed by SCENE which is a software specially designed for data collected by FARO. The software enables users to simply measure, create 3D visualizations, and export raw data (Figure 5-4). For the purpose of ripple geometry measurement, SCENE is used as a media to export .xyz format files. In the next step, these files were further processed using ArcMap 10 software in order to obtain ripple profiles. ArcMap 10 is able to convert the point cloud file into a raster object, then outputting ripples profiles through scan data (e.g., Figure 5-29). Finally, the exported profiles are analysed in order to acquire ripple length and height using methodologies explained in the Section 3.2.3.

Figure 5-5. FARO Focus3D X 330 scan area in the fieldwork. The white spheres are the scan boundary.

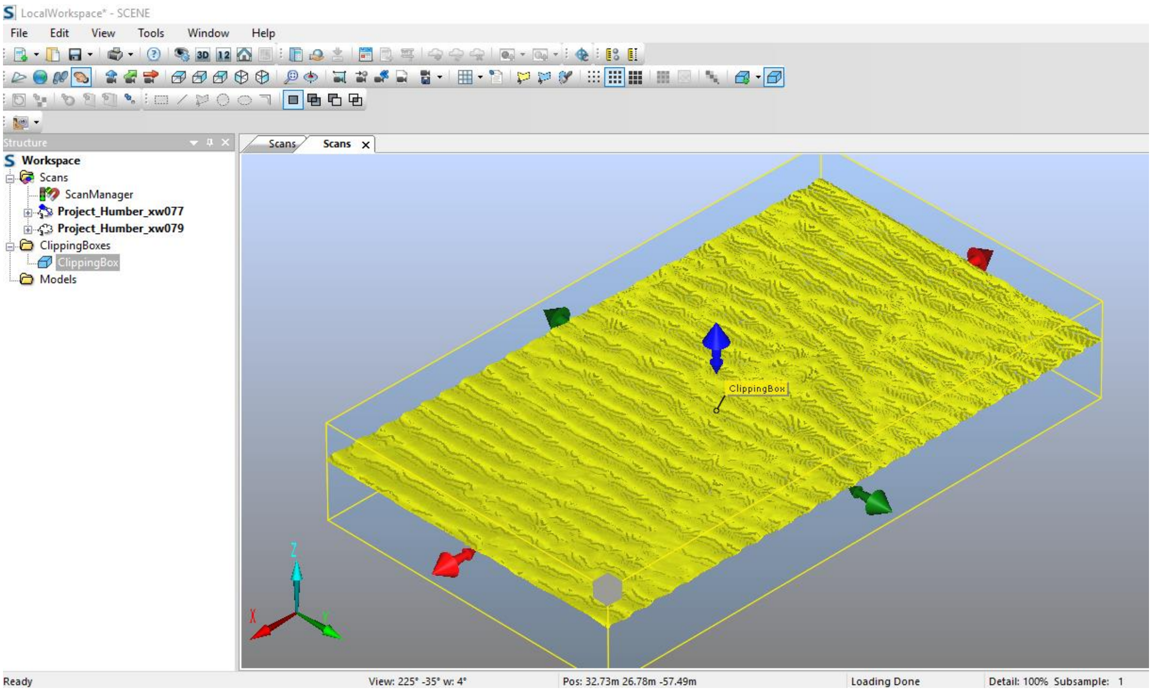

Figure 5-6. 3D visualization of scan ripples in the SCENE software.

5.2.4 Sediment cores

A handheld sediment corer (Figure 5-7) was used to collect sediment cores during each sand bar ripple survey. The sediment core length varied from 160 mm to 300 mm and were obtained from ripple crests and troughs, respectively. A total of 24 cores were collected across the field campaigns to determine the characteristics of the substrate material.

Sediment cores were frozen before further processing. Each sediment core was then evenly sliced into the samples with a 1 cm thickness. These sliced samples were dried at 80 Celsius degrees before granulometry was undertaken. The sedimental particles size test used a Malvern Mastersizer 2000 Particle Size Analyser. All of the measurements were undertaken in the Institute of Estuarine and Coastal Studies, University of Hull.

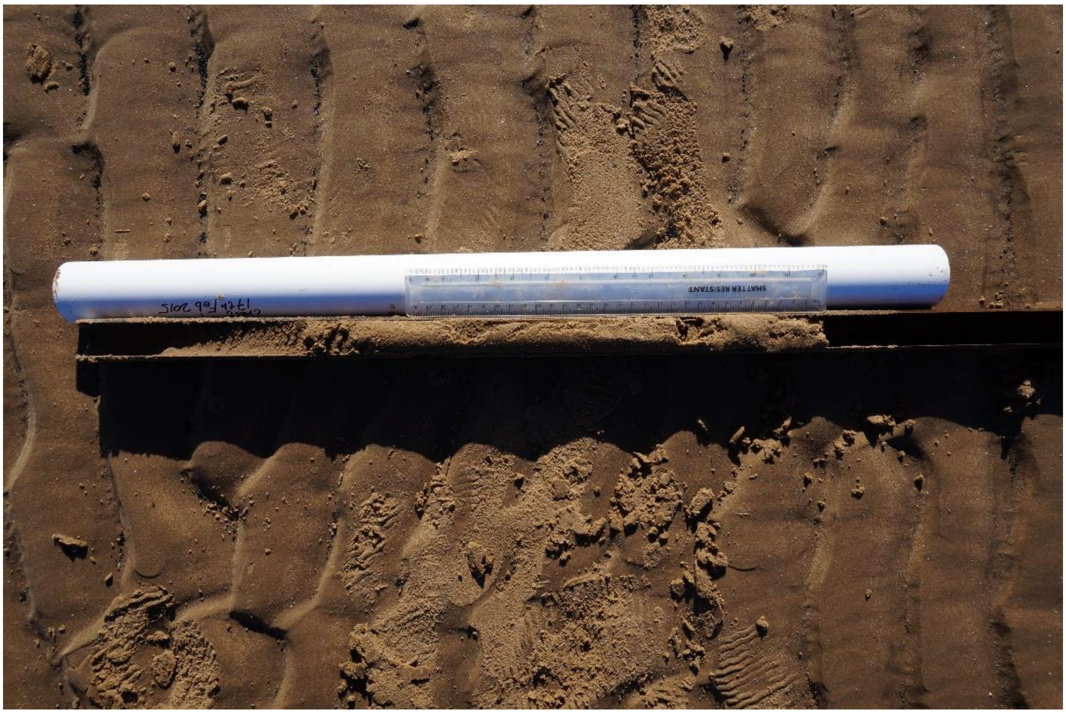

Figure 5-7. The collecting sediment core.

5.2.5 EPS Concentrations

The Extracellular polymeric substances (EPS) content of the bed sediment samples collected in each field survey were determined via carbohydrate analysis based on glucose equivalents and using a phenol sulphuric acid method (Dubois et al., 1956). The first step is to extract EPS from sediment samples by adding 10 ml of 0.5 molml^{-1}

Ethylene Diamine Tetraacetic Acid (EDTA) solution before a water bath at 40℃ and centrifuging. 35 ml of ethanol is added to the supernatant which is left at 4℃ for 8 hours before centrifuging again. The final precipitate is dissolved in a total of 1 ml MilliQ water for the measurement the amount of carbohydrate using the phenol sulphuric acid method. This is achieved through a 200µl of phenol solution and 1ml of concentrated sulphuric acid that are added into a 200µl dissolved precipitate before measuring the absorbance using a spectrophotometer at 490 nm. In addition, a set of standards dissolved by phenol and sulphuric acid as well with increasing known glucose concentration are necessary to establish relationship between glucose content and spectrophotometer absorbance. Finally, the actual EPS content for sample could be determined by converting measured absorbance through a simple arithmetic expression.

5.3 Results

5.3.1 Ripple geometry under unidirectional flows

i) Winter spring tide

The first round (WS1) of sand bar ripple survey was conducted on 24 November and 26 November 2014 within spring tide under quite calm weather condition. As shown in Figure 5-8, the high water level was over 5 m while the low water level was less than 1 m for each tidal cycle. It should be noted that the onshore current velocity during the flood period is regarded as positive value whereas the velocity during the ebb period is negative value. Current velocity quickly reached peak value around 1.5 ms^{-1} after water level rose. Similarly, the maximum velocity occurred again at the end of the ebb period.

Ripple surveys within the spring tide found ripple trains were two-dimensional with very straight crest lines (Figure 5-9). Aspect direction of ripples peaked at around 90 and 270 degree (Figure 5-30), which were coincident with the tidal current directions (Figure 5-8). As far as ripple size is concerned, on the first day of WS1 (24 November 2014), over one third of ripple lengths were between 75 mm and 85 mm and the majority of ripple heights varied from 5 mm to 9 mm (Figure 5-10). The average ripple length and height were 78.5 mm and 6.9 mm, respectively (0). On the second surveying day (26 November 2014), the mean ripple length and height slightly increased to 83.4 mm and 9 mm. Almost half of ripple lengths were from 75 mm to 90 mm and over half of ripple heights ranged from 7 mm to 11 mm (Figure 5-10). Ripple cross-section geometries were almost the same across the two days, and were dominated by the weakly asymmetrical ripples oriented towards an ebb tide direction (Figure 5-29 A). Furthermore, statistical results of ripple cross-section geometries indicate that ripple symmetry index (RSI, ratio of lee side length to stoss side length) of ripples on 24 November peaks at between 1 and 1.2 and ripples on 26 November were slightly more asymmetric (Figure 5-11). As far as ripple index (RI, ratio between ripple length and height) is concerned, the most frequent RI for ripples during the spring tides concentrates on between 8 and 10. In addition, on the first survey day, some extreme large RI values, for example RI>20, were found, which indicates these ripples were primarily flat (Figure 5-11).

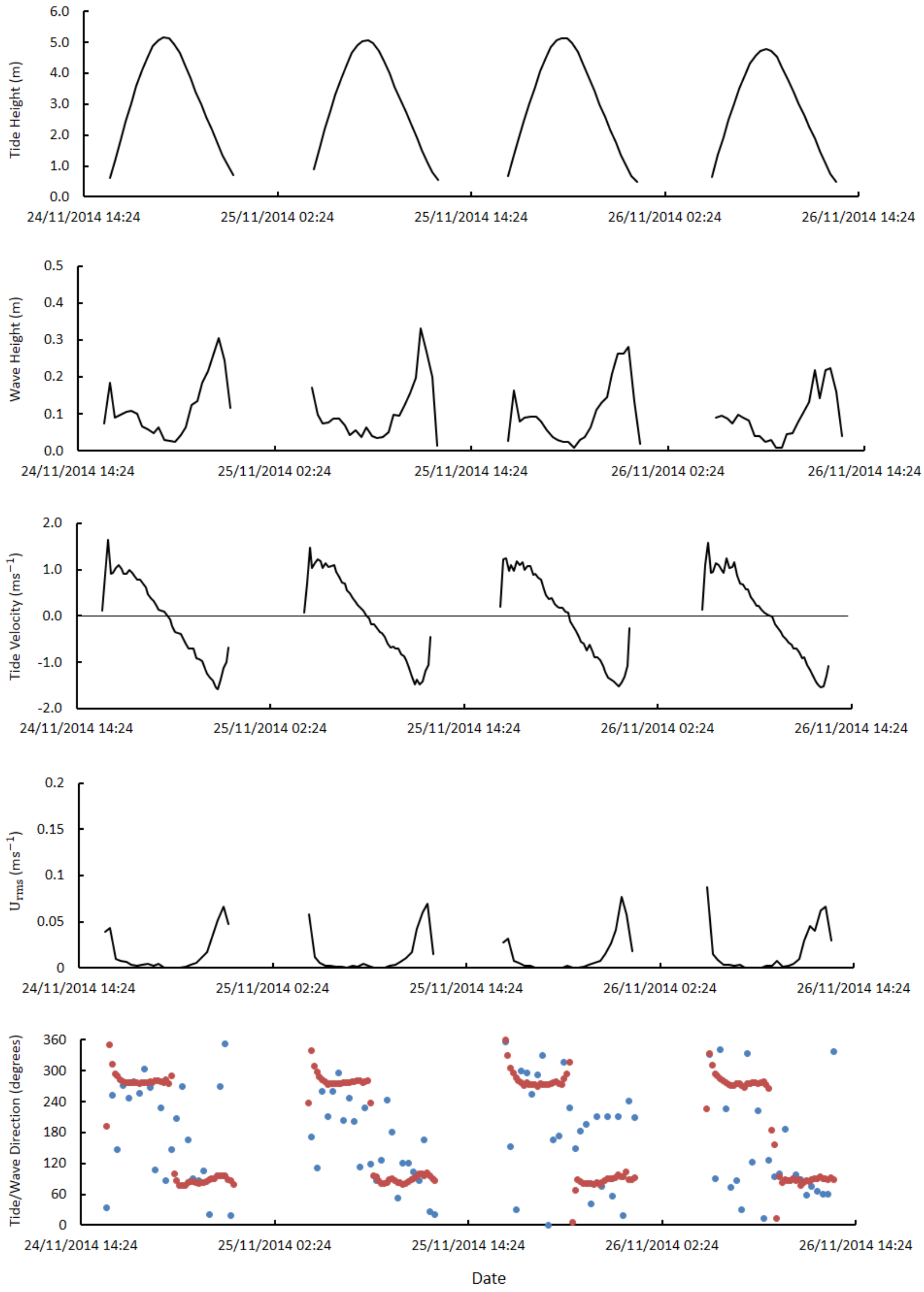

Figure 5-8. Tide height, wave height, tide velocity, bottom orbital velocity, tide and wave directions time series from 24 November to 26 November 2014 (WS1). Red and blue dots denote tide direction and wave direction respectively.

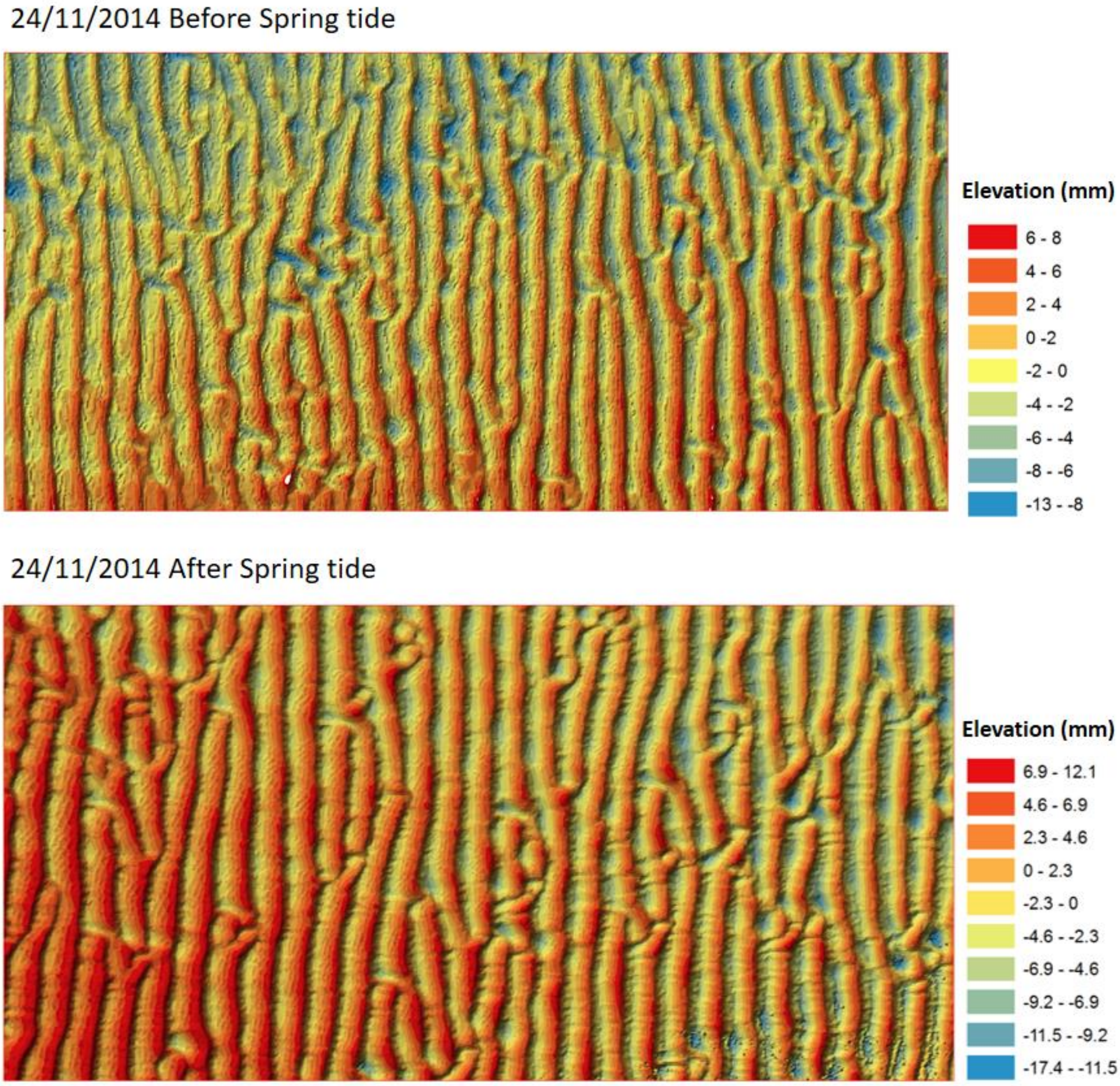

Figure 5-9. Plan view of ripples on 24 and 26 November 2014 (WS1). The scanning areas were around 3 square meters (2m lenth × 1.5m width).

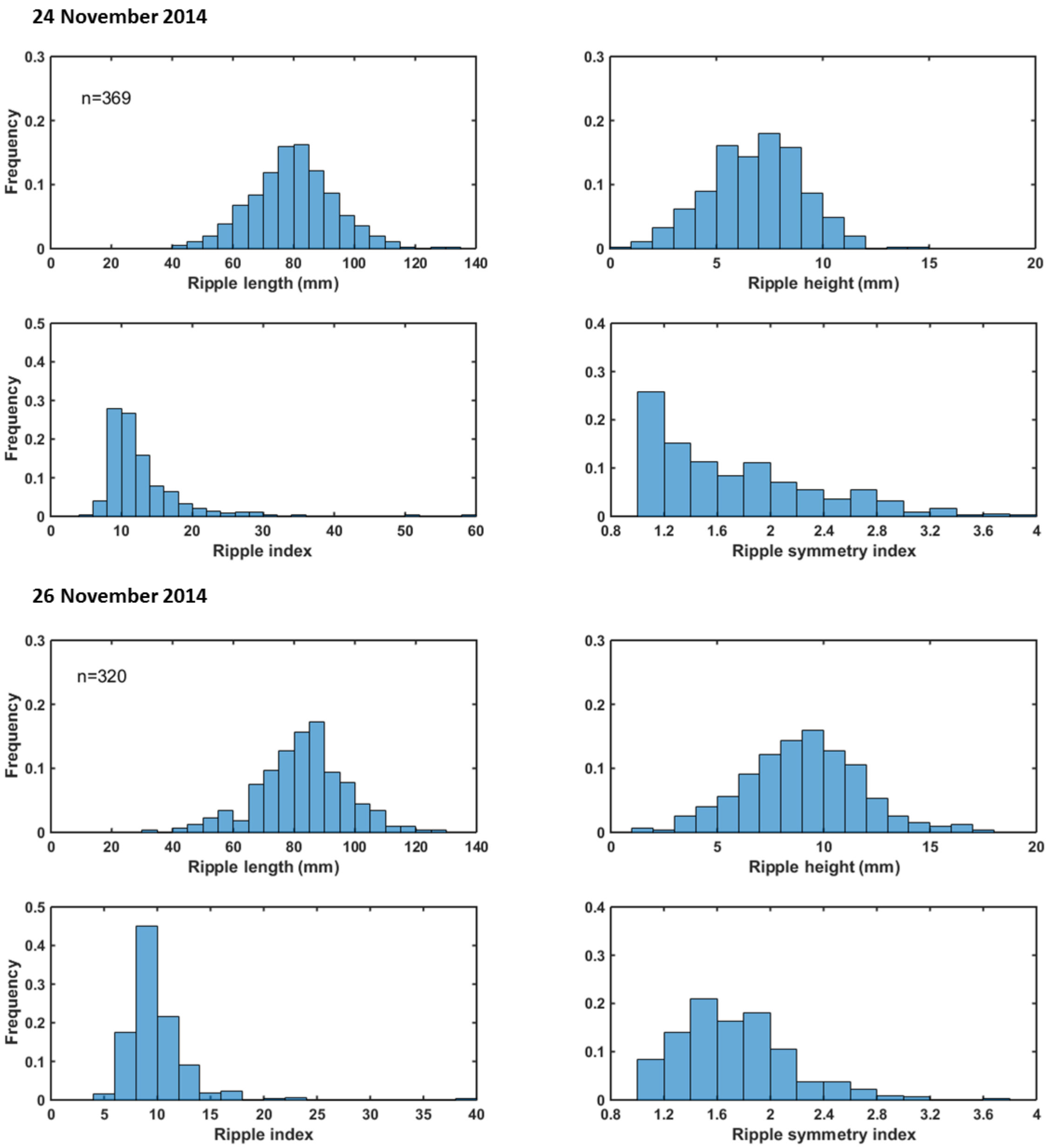

Figure 5-10. Histograms of all measured ripples' heights, wavelengths, ripple index and ripple symmetry index on 24 and 26 November 2014 (WS1), respectively.

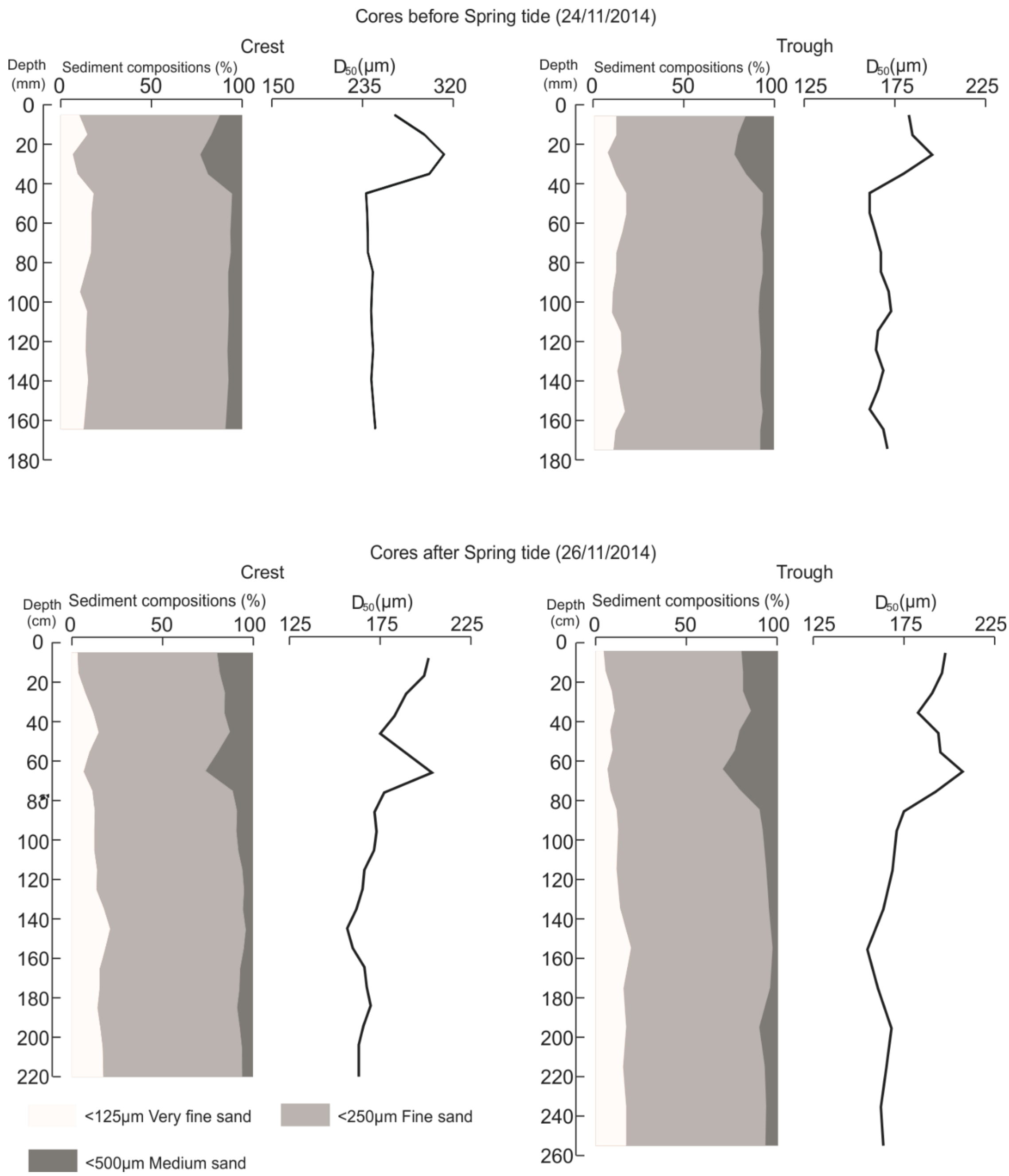

Figure 5-11. Sediment copositions and median grain size of sediment cores collected from ripple crest and trough (WS1).

Figure 5-11 shows bed sediments were mainly constituted of pure sand, with a grain size of 250 μm, both before and after spring tide. The cores show that sediments change across both the crest and trough of the ripples with sediments gradually becoming finer from top to bottom.

Summary of ripple-geometry characteristics and EPS content

Date	Conditions	λ (mm)	$\lambda\sigma$ (mm)	η (mm)	$\eta\sigma$ (mm)	λ_s (mm)	$\lambda_s\sigma$ (mm)	λ_l (mm)	$\lambda_l\sigma$ (mm)	RSI	RSI σ	RI	RIσ	EPS (%)
24/11/14	Calm/Spring	78.5	13.7	6.9	2.2	45.6	12.2	32.8	10.5	1.7	0.6	12.8	5.5	0.003
26/11/14	Calm/Spring	83.4	14.1	9.0	2.7	52.0	11.0	31.4	6.6	1.7	0.4	9.9	3.0	0.002
08/12/14	Calm/Spring	86.5	13.8	5.0	1.9	53.1	13.1	33.3	8.8	1.8	0.8	20.4	11.1	0.003
11/12/14	Moderate gale/Spring	-	-	-	-	-	-	-	-	-	-	-	-	0.003
10/02/15	Calm/Neap	171.4	57.6	20.1	10.8	98.7	35.4	72.7	32.6	1.7	0.7	11.0	7.4	0.003
17/02/15	Calm/Neap	81.9	12.9	7.2	1.9	46.9	9.8	35.0	7.7	1.5	0.3	12.1	3.1	0.004
25/02/15	Calm/Neap	92.6	17.1	9.2	2.4	58.5	13.5	34.1	11.1	1.9	0.8	10.7	3.1	0.005
04/03/15	Strong breeze/Neap	90.9	19.8	4.3	2.1	50.7	15.2	40.3	12.0	1.5	0.5	28.1	20.3	0.007
23/07/15	Calm/Neap	78.2	10.8	8.8	2.5	45.2	9.1	33.0	6.4	1.5	0.4	9.5	2.5	0.013
31/07/15	Calm/Neap	78.2	17.9	8.0	4.0	39.9	11.8	38.3	12.1	1.4	0.4	12.0	5.9	0.010
05/08/15	Calm/Spring	69.9	9.9	6.4	1.8	38.3	7.6	31.6	5.5	1.3	0.3	11.6	3.3	0.013
07/08/15	Calm/Spring	72.8	11.2	6.8	1.9	37.2	8.2	35.6	7.6	1.3	0.3	11.4	3.1	0.012

λ: Ripple length; η: Ripple height; λ_s: Stoss side length of ripple; λ_l: Lee side length of ripple; RSI: Ripple symmetry index; RI: Ripple index; σ: Standard deviation.

ii)Winter neap tide

A neap tide occurred between 10 February and 17 February, 2015. The tidal velocities were significantly lower, compared with spring tide, with maximum velocities of 0.96 ms^{-1} compared with 1.64 ms^{-1} under spring conditions (Figure 5-12).

The bed topography measured across the bar was dominated by linguoid ripples (1st of round WN1; Figure 5-13). The aspect directions of these ripples were not constrained into tight distributions but were distributed widely in terms of their (Figure 5-30). These kind of ripples, with short and curved crest lines, can be defined as 3D ripple in plan view (Perillo et al., 2014). The 3D ripples were replaced by 2D current ripples on the second day of the survey (WN1; Figure 5-13). The cross-section geometries of 3D ripples significantly differ from that of 2D current ripples. As shown in Figure 5-29B, the cross-section geometries of 3D ripples are much more irregular and heavily varied, with the evidence of broader distribution of RI and RSI values (Figure 5-14). In contrast, the majority of ripple indices of 2D ripples were concentrated between 8 and 14 and over two third of ripple symmetry indices of ripples were between 1 and 1.6 (Figure 5-14).

The sizes of 3D ripples were much larger than that of 2D ripples, with mean ripple length reaching to 171.4 mm and mean ripple height achieving to 20.1 mm (0). In particular, some extremely large ripples were observed, with length reaching to 350 mm and height reaching to 48 mm. The mean ripple length and height of 2D ripples sharply declined to 81.9 mm and 7.2 mm, respectively. As shown in Figure 5-14, over 60% of 3D ripple lengths were distributed between 100 mm and 200 mm and approximately 25% of ripple lengths longer than 200 mm. For the 2D ripples, most of ripple lengths were between 75 mm to 90 mm, with mean ripple length of 81.9 mm and standard deviation of 12.9 mm. In terms of ripple height, the statistic results of ripple heights show that there is not apparent peak value for 3D ripple heights, with most of ripple height broad ranging from 4 mm to 32 mm. The results also reflect a large proportion (about 60%) of ripple heights varied from 6 mm to 9 mm (Figure 5-14).

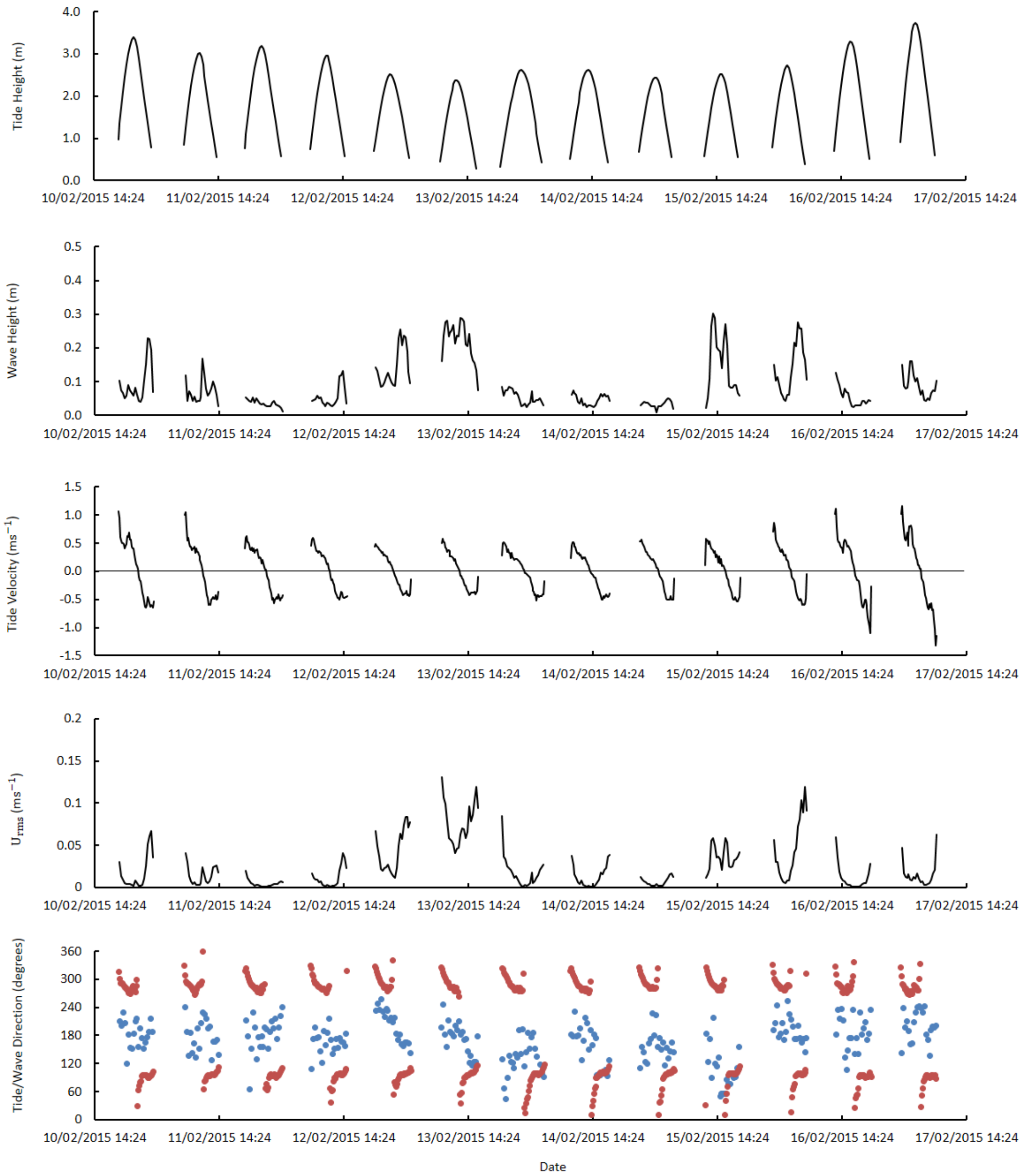

Figure 5-12. Tide height, wave height, tide velocity,bottom orbital velocity, tide and wave directions time series from 10 February to 17 February, 2015 (WN1). Red and blue dots denote tide direction and wave direction respectively.

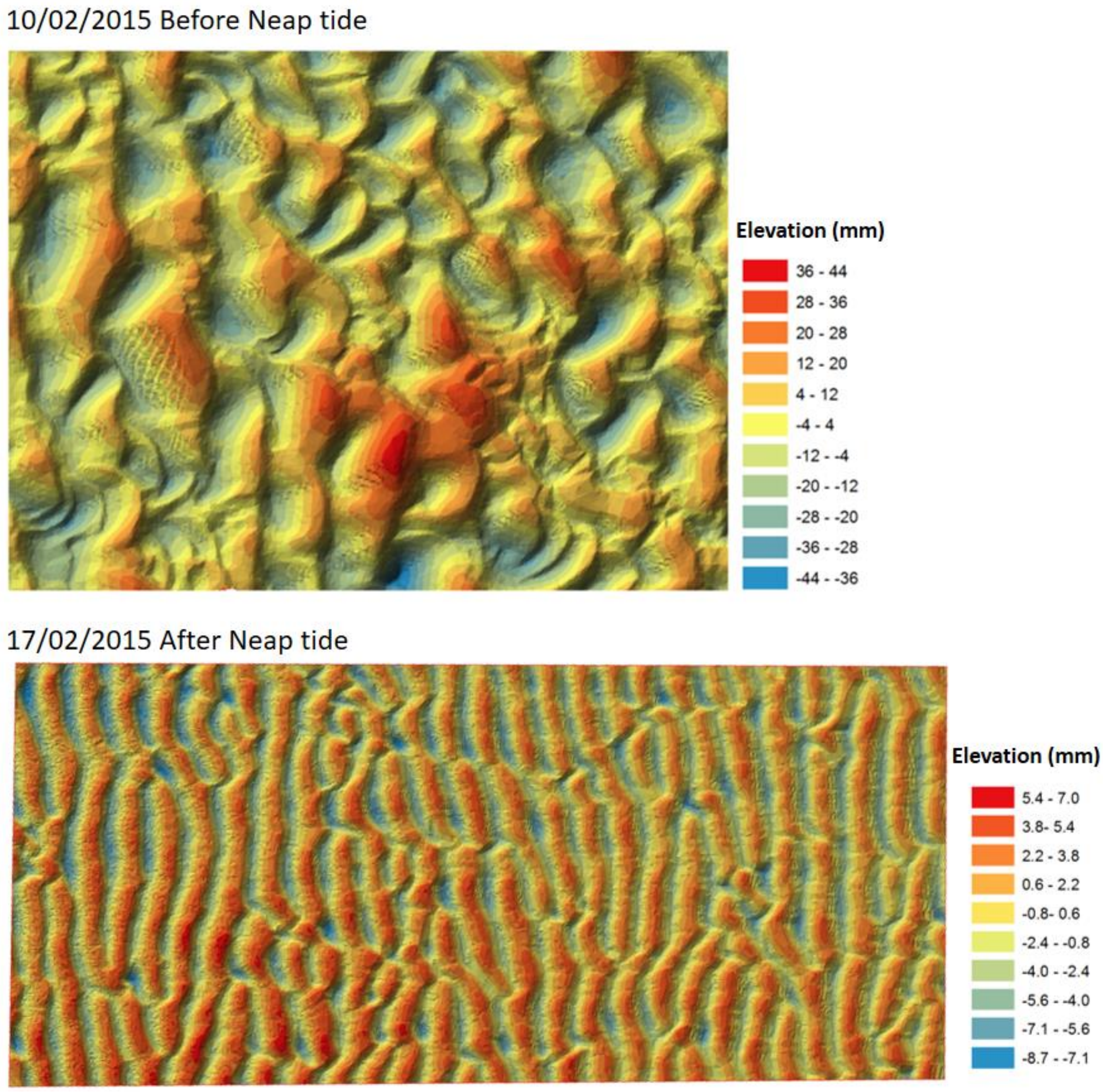

Figure 5-13. Plan view of ripples on sand bar on 10 Feburary and 17 Feburary 2015 (WN1), respectively. Both photos show ripples on 3 sqaure meters area with the first one 1.5m length and 2m width, and with the second one 2.5m length and 1.2m width. Ebb current direction from left to right.

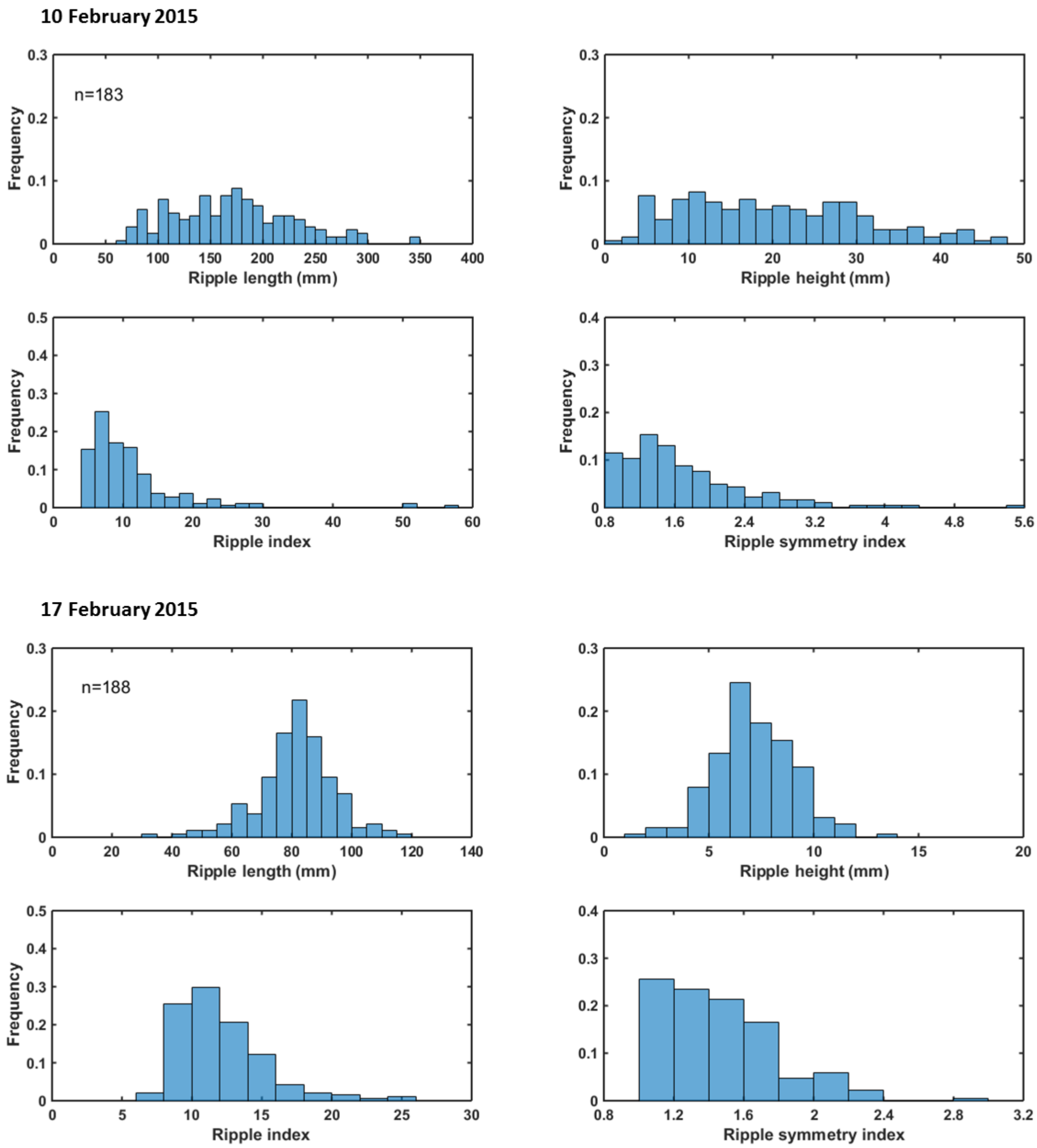

Figure 5-14. Histograms of all measured ripples' heights, wavelengths, ripple index and ripple symmetry index on 10 and 17 February 2015 (WN1), respectively.

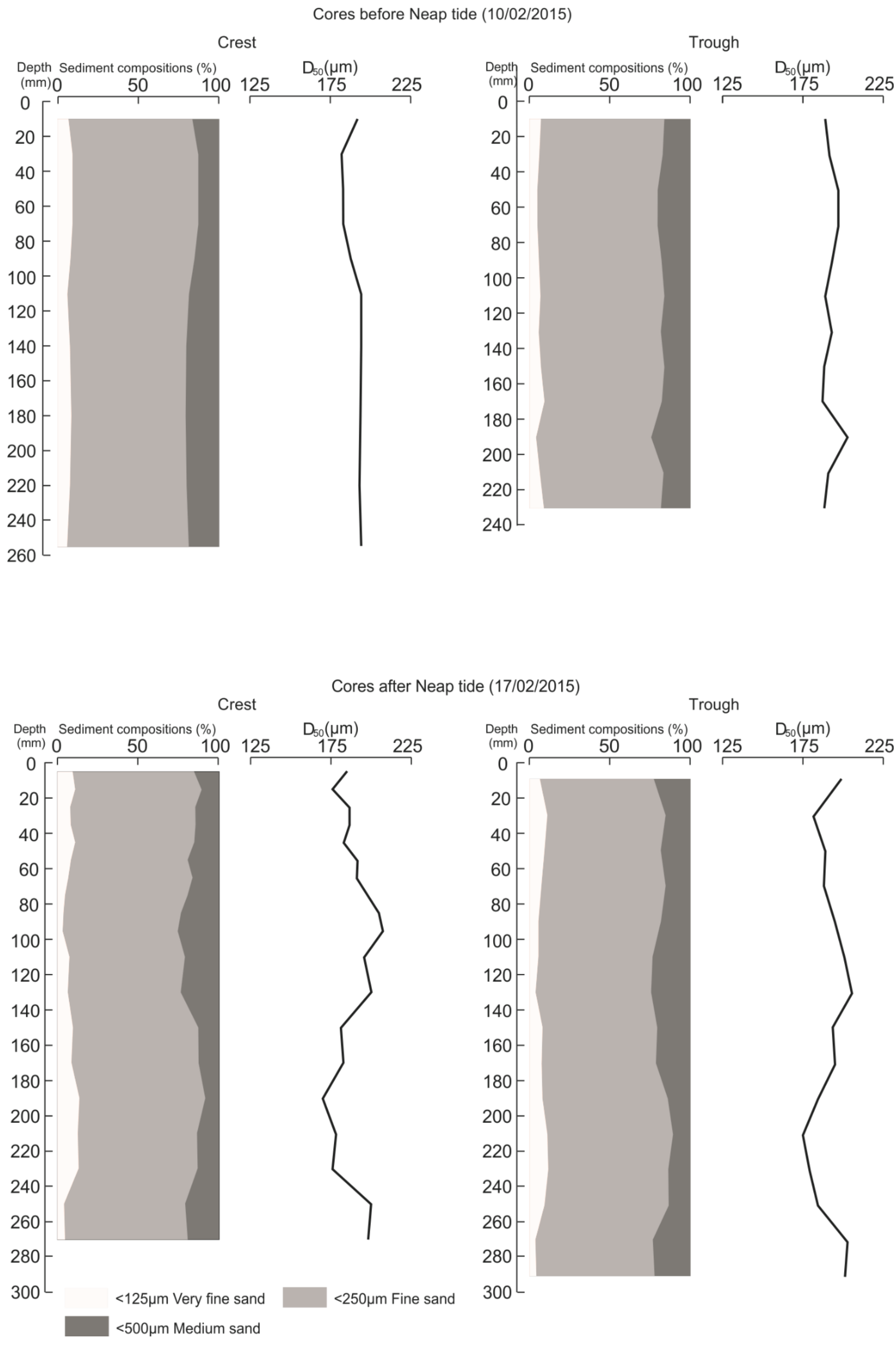

Figure 5-15. Sediment copositions and median grain size of sediment cores collected from ripple crest and trough (WN1).

Sediment cores from 3D ripple's crest and trough collected before neap tide show that median grain size was constant from top to bottom, at about 180 µm. For cores collected after neap tide, the median grain size gradually increased within the upper layers to about 200 µm. Grain size declined to 170 µm within intermediate and lower layers before another increase again at bottom layer (Figure 5-15).

iii) Summer neap tide

Field survey period SN1 in summer was conducted between 23 and 31 July 2015 during a neap tide period. On 23 July the high water level reached to about 3.2 m and the maximum tide current velocity was very close to 1 ms^{-1} (Figure 5-16). On 31 July, as shown in Figure 5-16 the high water level increased to around 4.4 m. The current velocity was slightly asymmetry with ebb tide current velocity marginally higher, reaching to 1.5 ms^{-1}. During these two days, wind was weak, therefore the wave height was relatively small than 0.2 m (Figure 5-16).

On the first surveying day of round SN1, typical 2D current ripple trains were observed on the sand bar (Figure 5-17). Ripples profile shows these ripples were weakly asymmetric with mean RSI of 1.5 (Figure 5-29 C; 0). Moreover the sizes of summer 2D ripples were very close to the 2D ripples found in winter, with averaged ripple length and height close to 78.2mm and 8.8mm respectively (0). Figure 5-18 depicts the peak frequency of ripple length corresponds to length between 80 mm to 85 mm. Over two third of ripple heights are in the range between 7 mm and 12 mm.

Plan view of ripples on the second survey day of SN1 was neither the plan view of typical 2D ripples nor the 3D ripples (Figure 5-17). The crest lines of these ripples were either continuous or straight. Additionally, two distinct peaks of aspect direction indicates ripples were tend to be two-dimensional (Figure 5-30). Some earlier flume experiment studies (e.g. Dumas et al., 2005; Perrilo et al., 2014) defined this kind of ripple as 2.5D ripples. Contrast with the preceding uniform size of 2D ripples, the individual ripple steepness heavily differed (Figure 5-29C). The statistical result of ripple index is the evidence for the remarkable change, with RI wide ranging from 2 to 40 (Figure 5-18). Correspondingly, there were larger differences of lengths and heights among the single ripple as well (Figure 5-18). However, the degree of asymmetry of each single ripple was quietly similar, which was independent with ripple size (Figure 5-

29C). The RSI value of individual ripple slightly varied, with mean RSI of 1.4 and lower standard deviation of 0.4 (0).

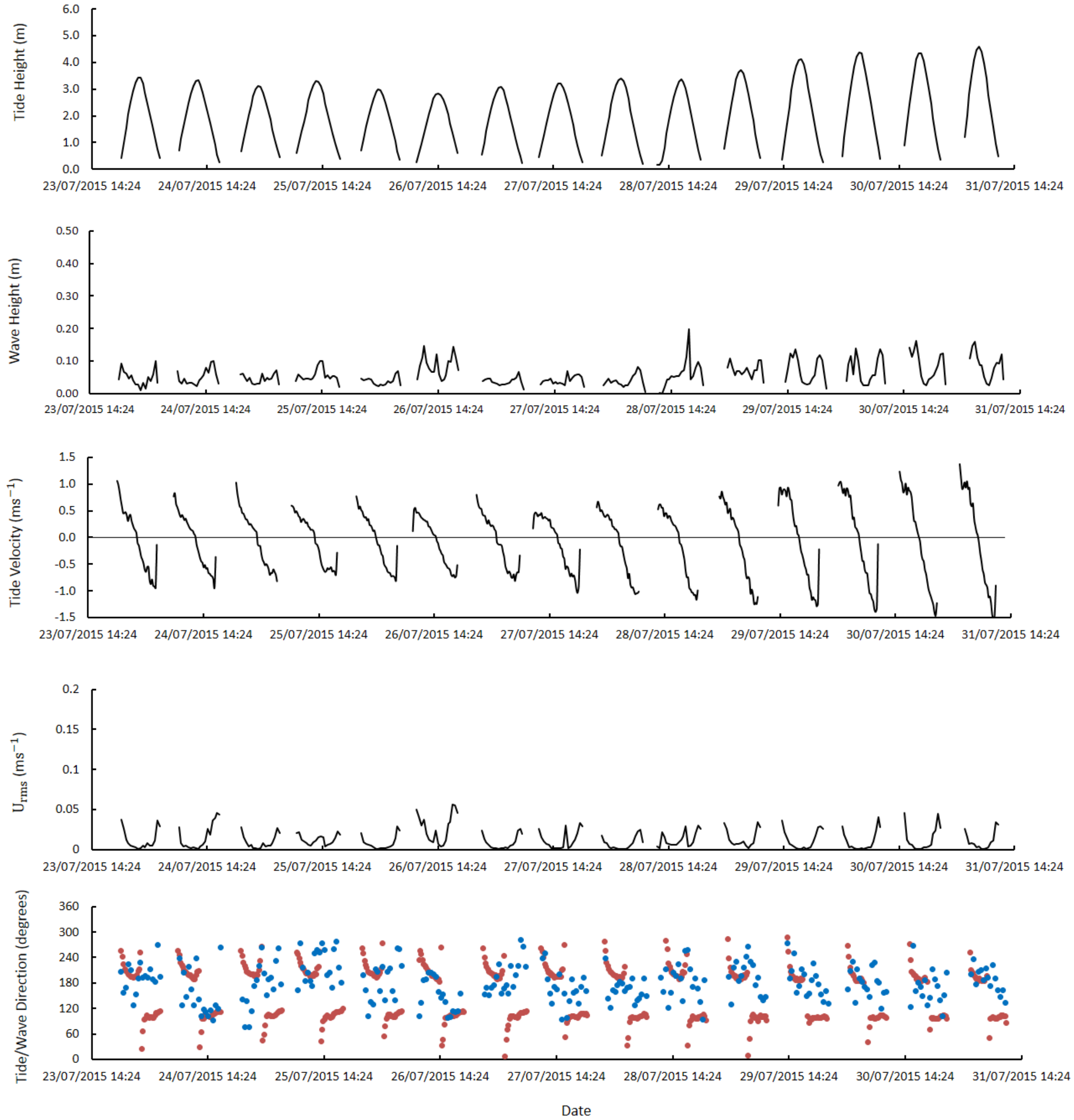

Figure 5-16. Tide height, wave height, tide velocity,bottom orbital velocity, tide and wave directions time series from 23 July to 31 July (SN1), 2015. Red and blue dots denote tide direction and wave direction respectively.

23/07/2015 Before Neap tide

31/07/2015 After Neap tide

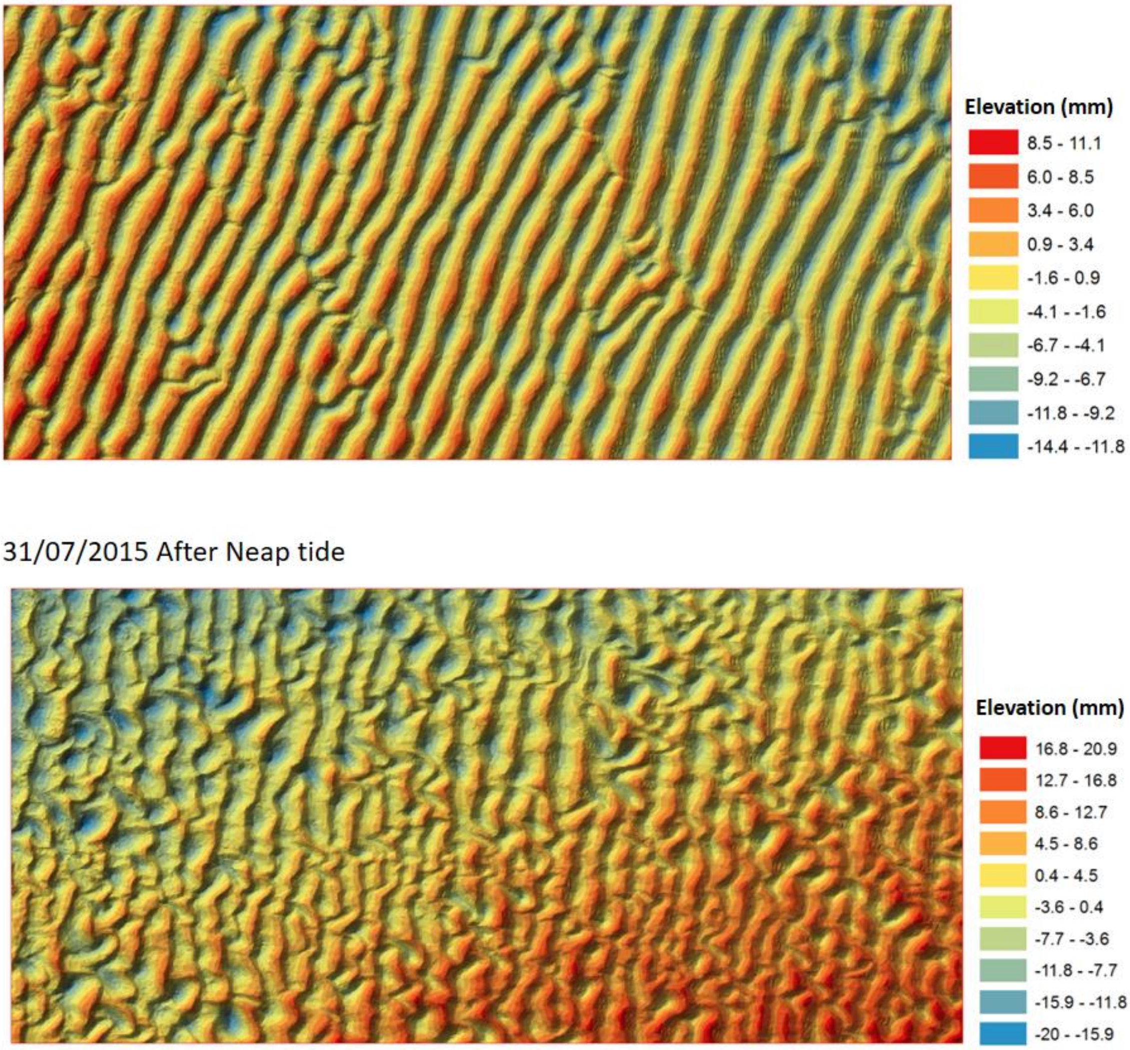

Figure 5-17. Plan view of ripples on 23 and 31 July 2015 (SN1). The scanning areas were around 3 square meters (2m lenth × 1.5m width).

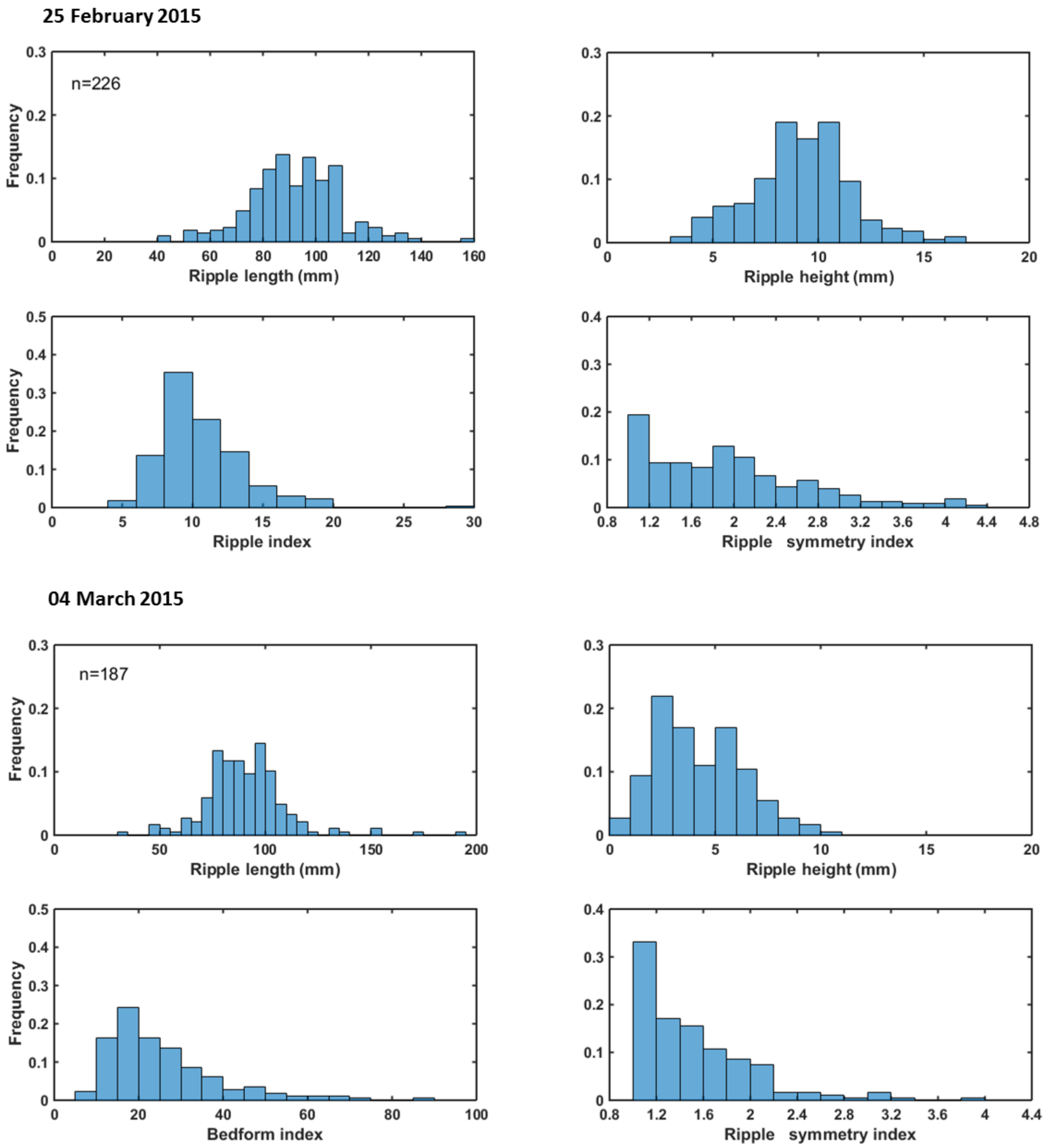

Figure 5-18. Histograms of all measured ripples' heights, wavelengths, ripple index and ripple symmetry index on 23 and 31 July 2015 (SN1), respectively.

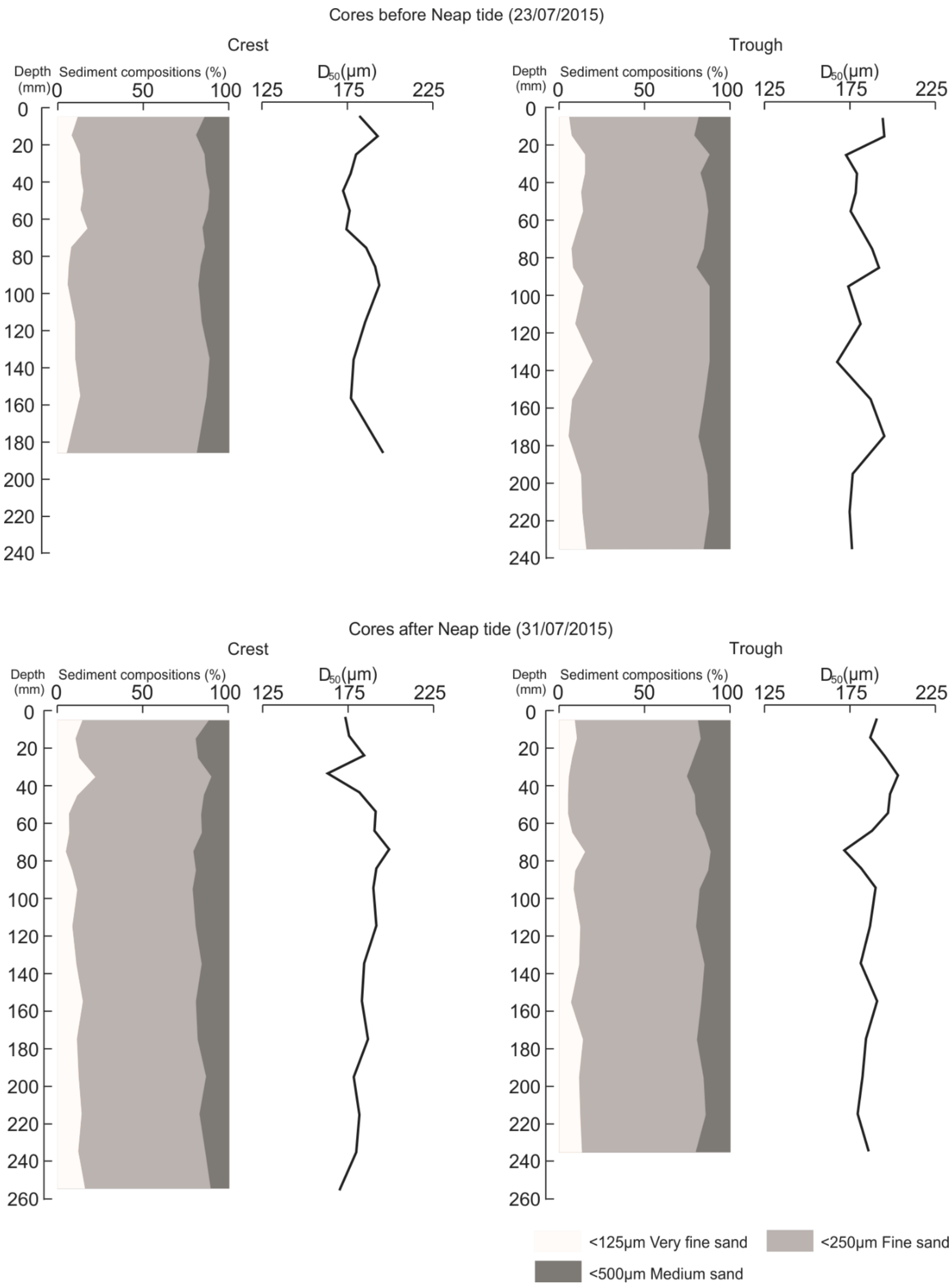

Figure 5-19. Sediment copositions and median grain size of sediment cores collected from ripple crest and trough (SN1).

However, ripple length and height statistical results indicate that the percentage of smaller sized ripples with lengths shorter than 80 mm and heights lower than 8 mm increased significantly compared with ripple size on 23 July. Moreover some extreme larger size ripples (length > 120 mm and height > 20 mm) appeared as well, which were absent in the first surveying day in summer (Figure 5-18).

Granulometry shows that sediment still constituted by the pure sand, furthermore fine sand was dominated sediment cores (Figure 5-19). In addition median grain size slightly fluctuated around 175 µm from upper layer to lower layer (Figure 5-19).

5.3.2 Ripple geometry under combined flows

On night 9 December 2014 (Round WS2), the wind speed was 28 knots, which resulted in the maximum wave height reaching above 0.8 m and maximum computed bottom orbital velocity of > 0.19 ms^{-1} (Figure 5-20). Soulsby (1997) hypothesized that waves are able to produce an oscillatory velocity at sea bed and to act on sediment transport if water depth is smaller than ten times of wave height. It is speculated that the relatively high wave height corresponding with water depth meets the condition. Therefore, the ripples were developed with influence of combined oscillatory and unidirectional flows under this circumstance. The high tide during flood phase reduced to 2.8 m and the maximum tide current velocity decreased to 1.1 ms^{-1}. The strong wind lasted two days until 11 December, with wave height exceeding 0.3 m.

Before gale, the sand bar ripple survey held on 8 December 2014 (1^{st} day of WS2) found that ripples with straight and continuous crests line were common. However, the individual ripple shape was quite different from the shape of previous ripple found in round of WS1 (Figure 5-29). Nevertheless, ripple aspect directions with two peaks suggest they can be defined as two-dimensional ripples (Figure 5-30). The lee side slope of each ripple became much gentler and the brinkpoint was vague (Figure 5-29D). The ripple trains were much flatter (Figure 5-21) because slightly increased mean ripple length (86.5 mm) and a sharp decline of mean ripple height (5 mm). As a result, compared with 2D ripples observed in the first round, the mean ripple index significantly rose to 20.4 (0).

After strong wind, on 11 December 2014 (2nd day of WS2), the 2D ripples were replaced with a flat planar bed (Figure 5-21; Figure 5-29D). The photo shows that there were patterns on the flat sand bar with khaki sand and dark blue clastic coal (Figure 5-22).

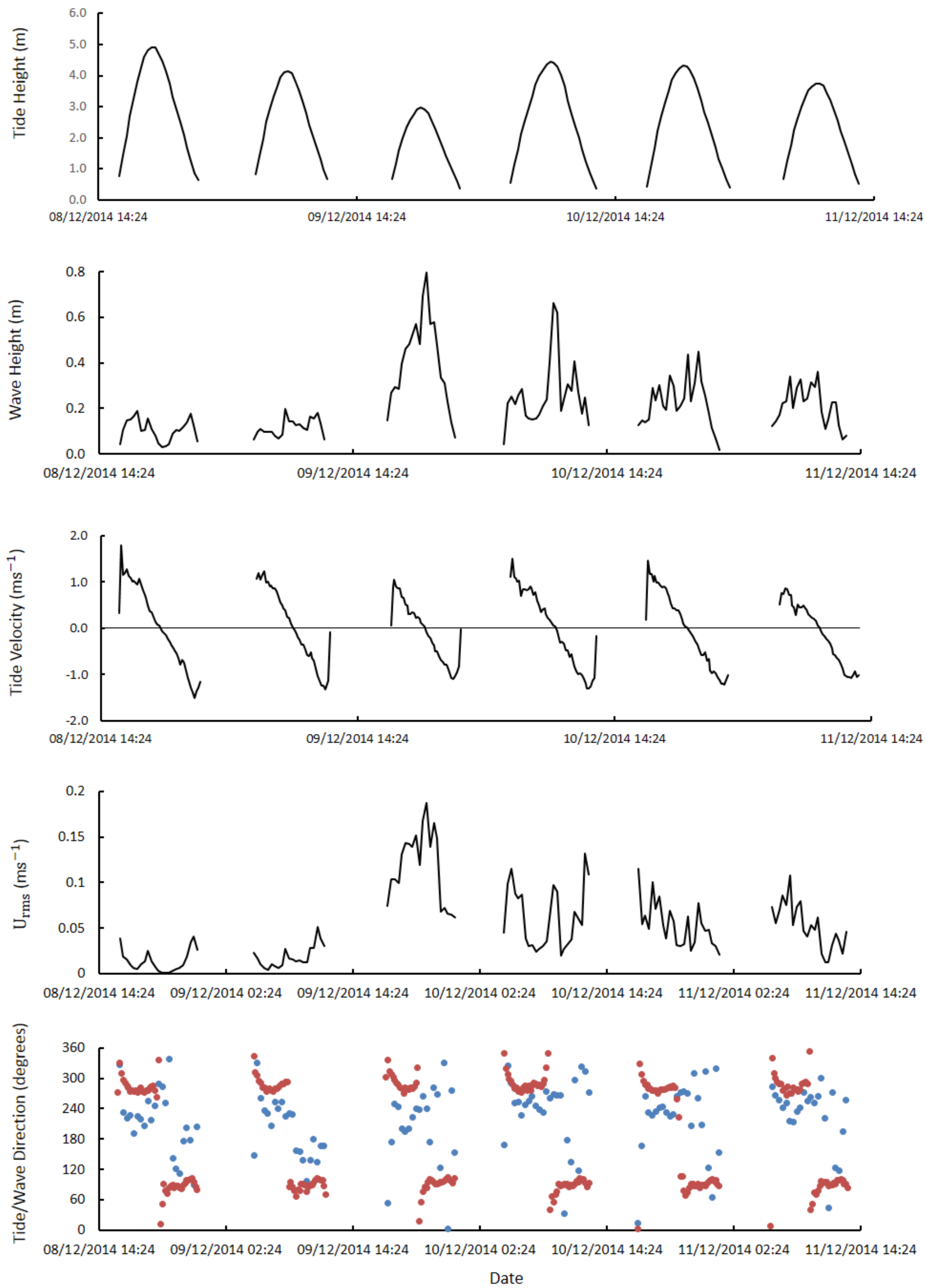

Figure 5-20. Tide height, wave height, tide velocity,bottom orbital velocity, tide and wave directions time series from 8 December to 11 December, 2014 (WS2). Red and blue dots denote tide direction and wave direction respectively.

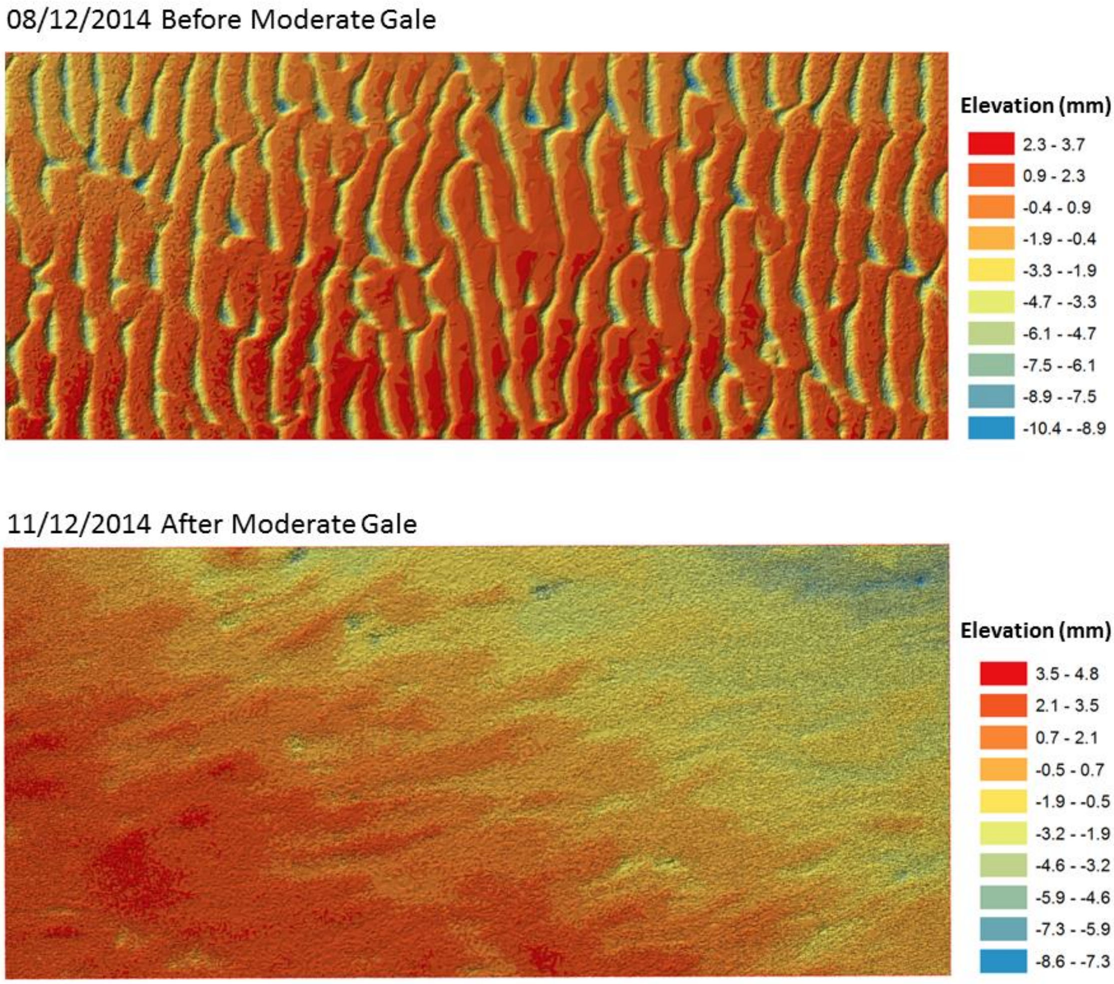

Figure 5-21. Plan view of ripples on 8 and 11 December 2014 (WS2). The scanning areas were around 3 square meters (2m lenth × 1.5m width).

Before the moderate gale event, sediment cores collected from both ripple crest and trough show that sediment gradually became finer towards the surface. A similar trend was also found in the core collected from the flat sand bar (Figure 5-23).

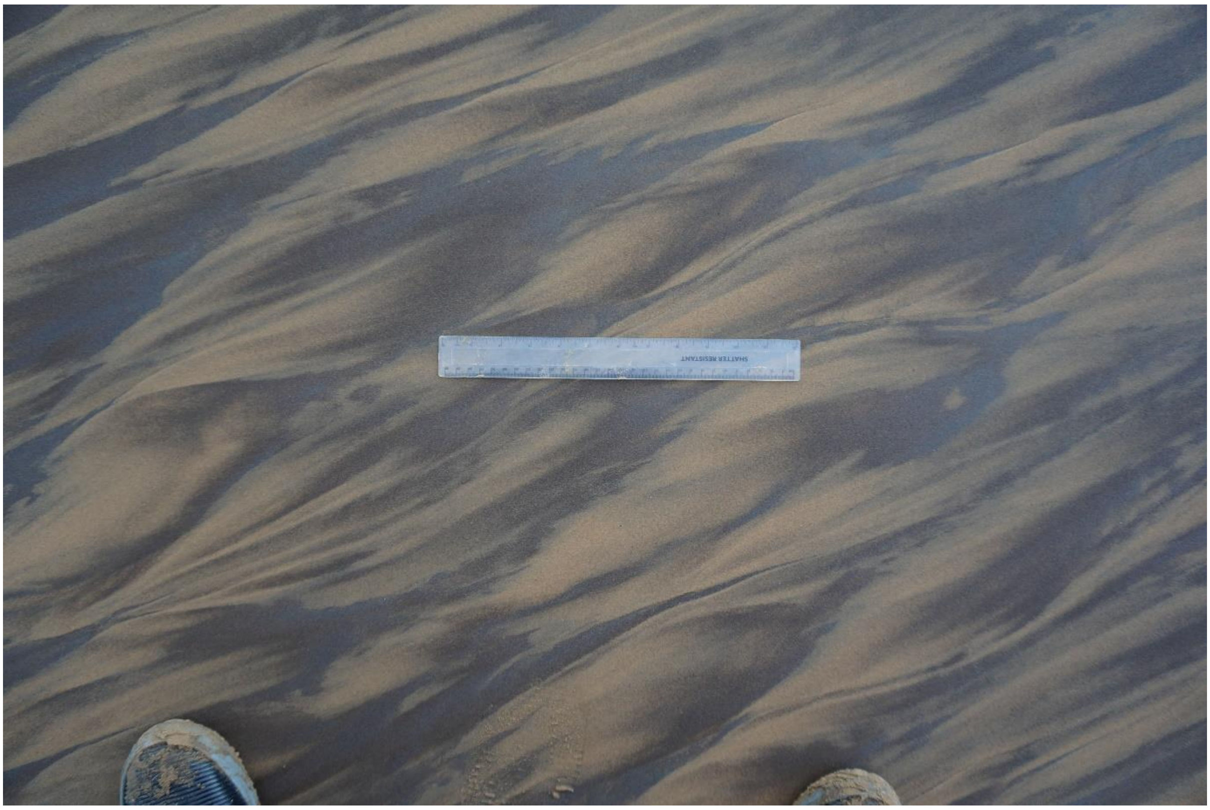

Figure 5-22. Photo showing the sand bar was flat after storm on 11 December 2014 (WS2).

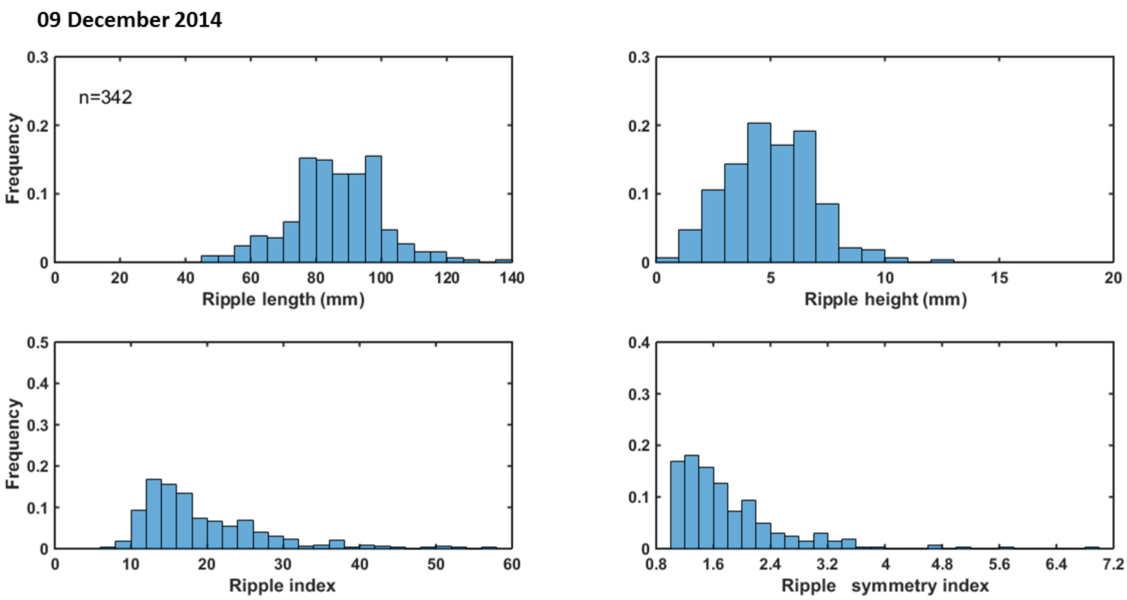

Figure 5-23. Histograms of all measured ripples' heights, wavelengths, ripple index and ripple symmetry index on 8 November 2014 (WS2).

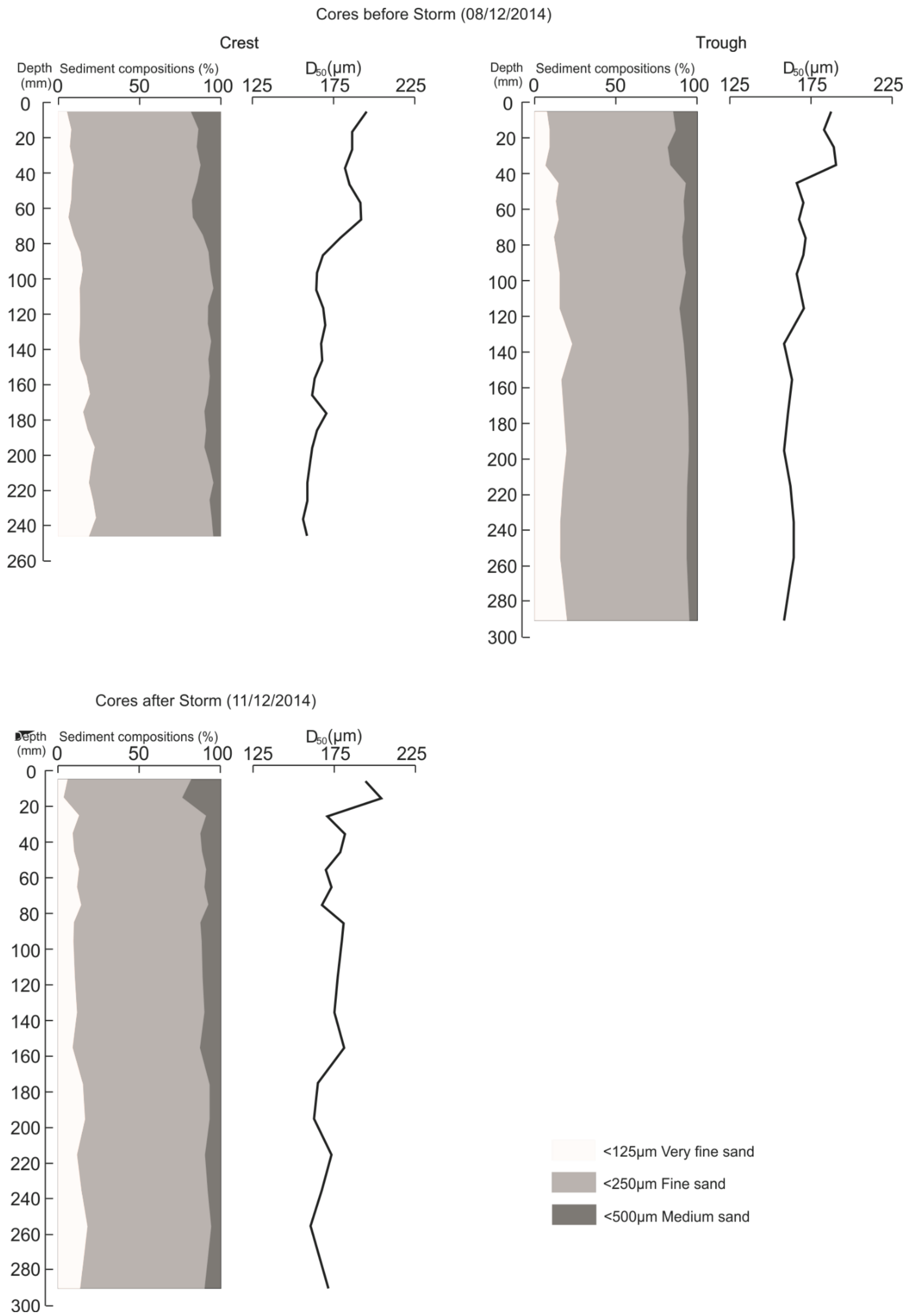

Figure 5-24. Sediment copositions and median grain size of sediment cores collected from ripple crest and trough (WS2).

Another high wind event was recorded between 25 February and 4 March 2015. During this period, the maximum wave height was 0.63m and the maximum bottom orbital velocity reached to 0.19 ms^{-1} (Figure 5-25). The round WN2 of ripple survey was conducted on 25 February under relatively calm condition and on 4 March after strong breeze event. On 25 February before neap tide, the high water level was around 4 m. The tide velocity was asymmetric with relatively faster ebb tide velocity reaching to 0.75 ms^{-1}. After neap tide, on 4 March, high water level increased to 4.2 m. Meanwhile, the maximum tide velocity increased as well, with maximum ebb velocity reaching to approximately 1 ms^{-1} (Figure 5-25).

The two-dimensional ripples with straight crest lines dominated the bar surface on the 1st surveying day of round WN2 (25 February 2015) as shown in Figure 5-26. There is a little difference of the plan view between the present ripples and the previous ones (e.g. Figure 5-9). That because some water covering ripple during scanning, which obscures ripple geometry, especially the relatively lower elevation area, for example top left of the scanning photo. Single ripple cross-section geometry shows an asymmetrical shape and ripple moving in the direction of the simultaneously occurring ebb tide (Figure 5-29E). Furthermore, the highest mean RSI (1.9) suggests these ripples were the most asymmetrical among six rounds of ripple surveys (0). Most of ripple lengths were between 80 mm and 110 mm (Figure 5-27), with averaged ripple length around 92.6 mm (0). The mean ripple height attained to 9.2 mm (0), over 50% of ripple height concentrating between 8 mm and 11 mm (Figure 5-27).

After the moderate gale, the ripples geometries had been completely changed. The plan view shows the rippled bed was much more flat. Additionally, ripple crests sometimes were merged to form sporadic flat bed (Figure 5-26), for example, as shown the black box in Figure 5-26, ripple crests had merged. Furthermore, at ripple troughs, some flow separation were observed (Figure 5-26 black circle). Individual ripple was featured with long gently-curved crest and very low ripple height (Figure 5-29E). In addition, the ripple aspects slightly tend to ebb tide direction because of quietly flat rippled bed (Figure 5-30). These were wash-out ripples (Jopling and Forbes, 1979) with mean ripple length reaching to 90.9 mm and a small mean ripple height of around 4.3 mm, therefore contributing to extremely high mean ripple index of 28.1 (0).

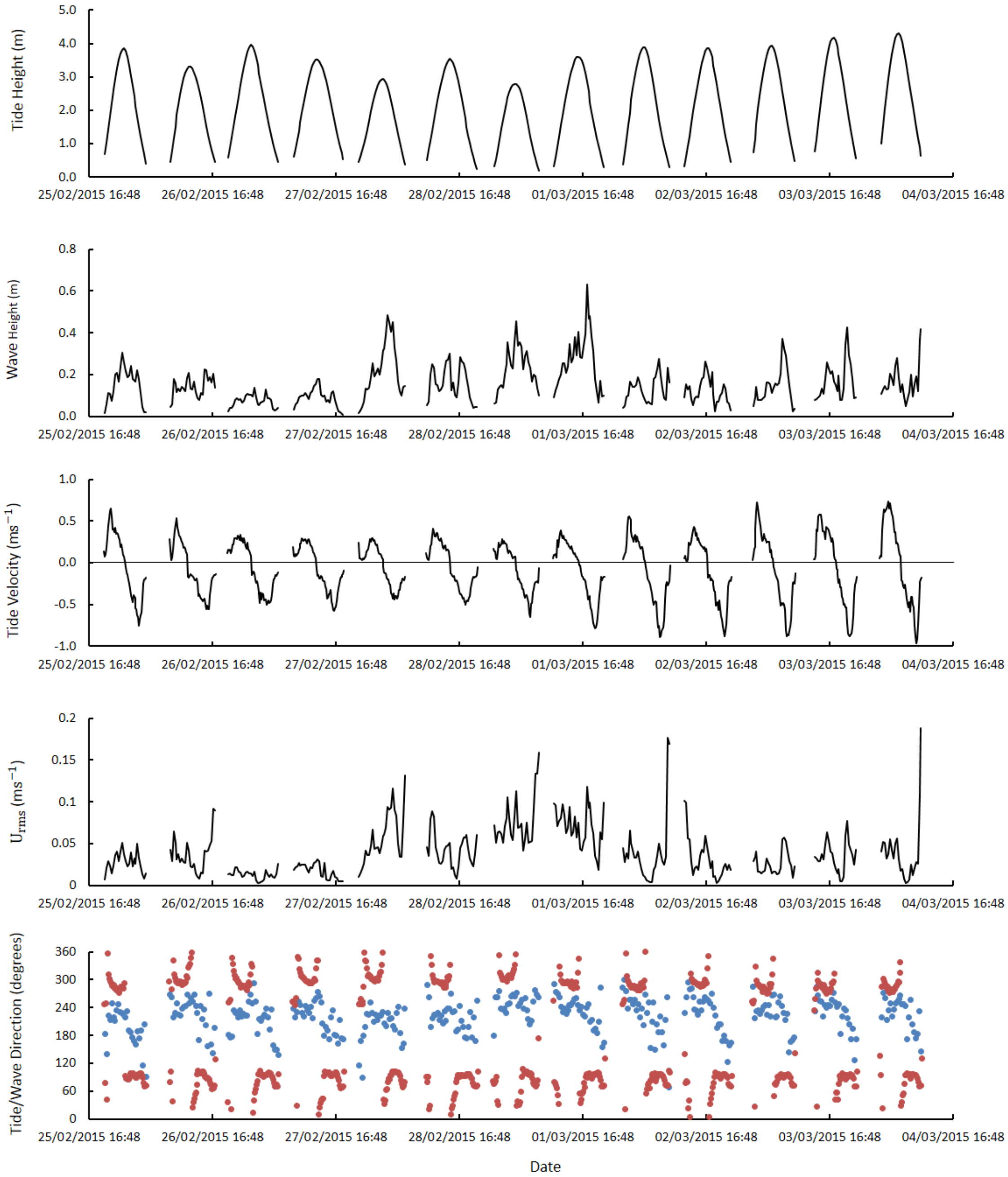

Figure 5-25. Tide height, wave height, tide velocity,bottom orbital velocity, tide and wave directions time series from 25 February to 4 March, 2015 (WN2). Red and blue dots denote tide direction and wave direction respectively.

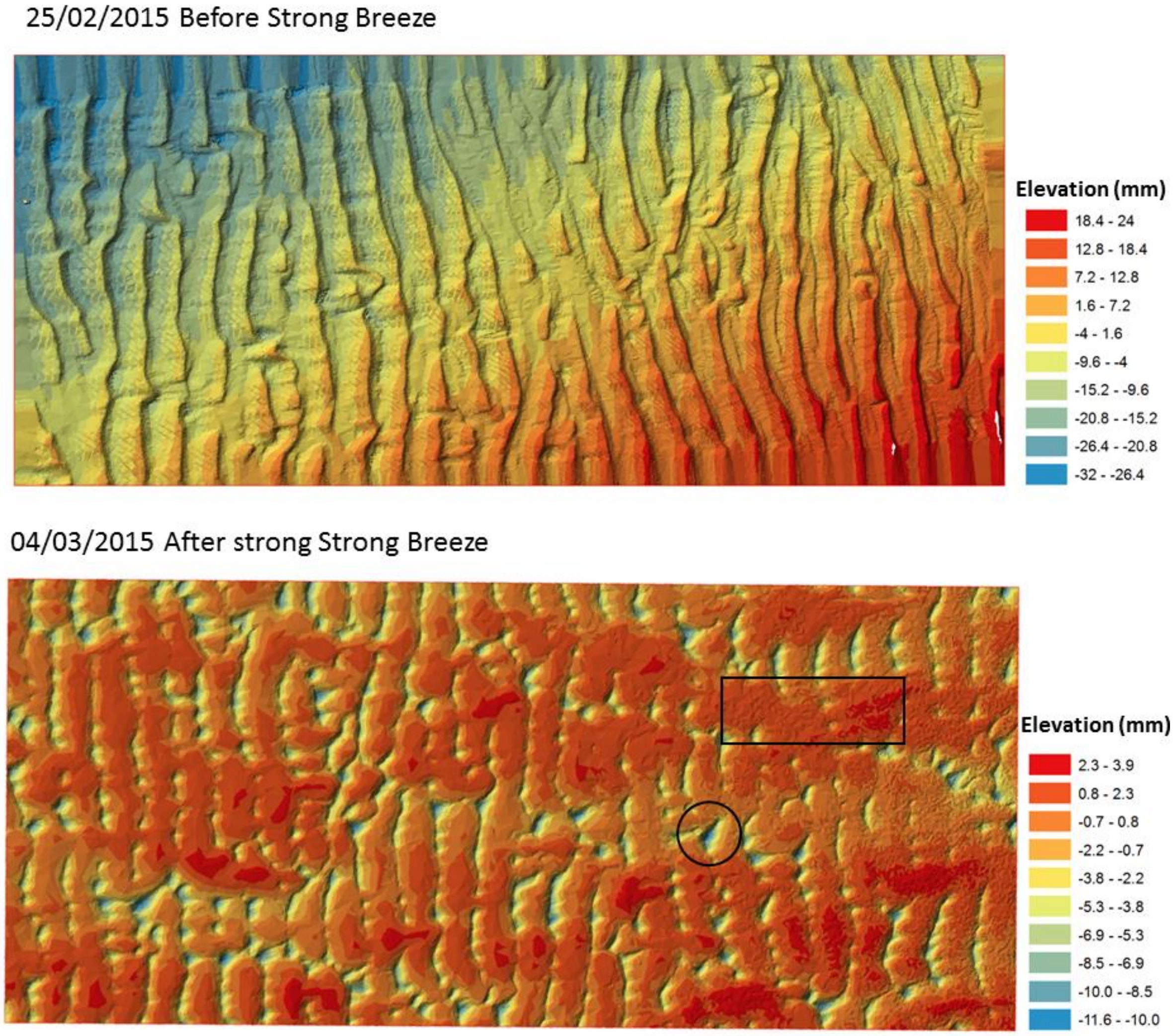

Figure 5-26. Plan view of ripples on 25 Febuary and 4 March 2015 (WN2). The scanning areas were around 3 square meters (2m lenth × 1.5m width). The black box shows ripple crests had merged and the black circle shows flow seperation at ripple trough.

Figure 5-21 depicts that bed sediment composition was constant with median grain size about 175µm from top layer to bottom layer of core collected from crest before the moderate gale event. While the sediment grain size slightly declined from the top trough core. For the crest core collected after the strong event, the composition of medium sand increased at intermediate layer and gradually decreased towards lower layer. Similarly, a relatively higher medium sand layer is found at middle upper layer of the trough core. Below this layer, sediment grain size slightly decreased finer than 175µm (Figure 5-21).

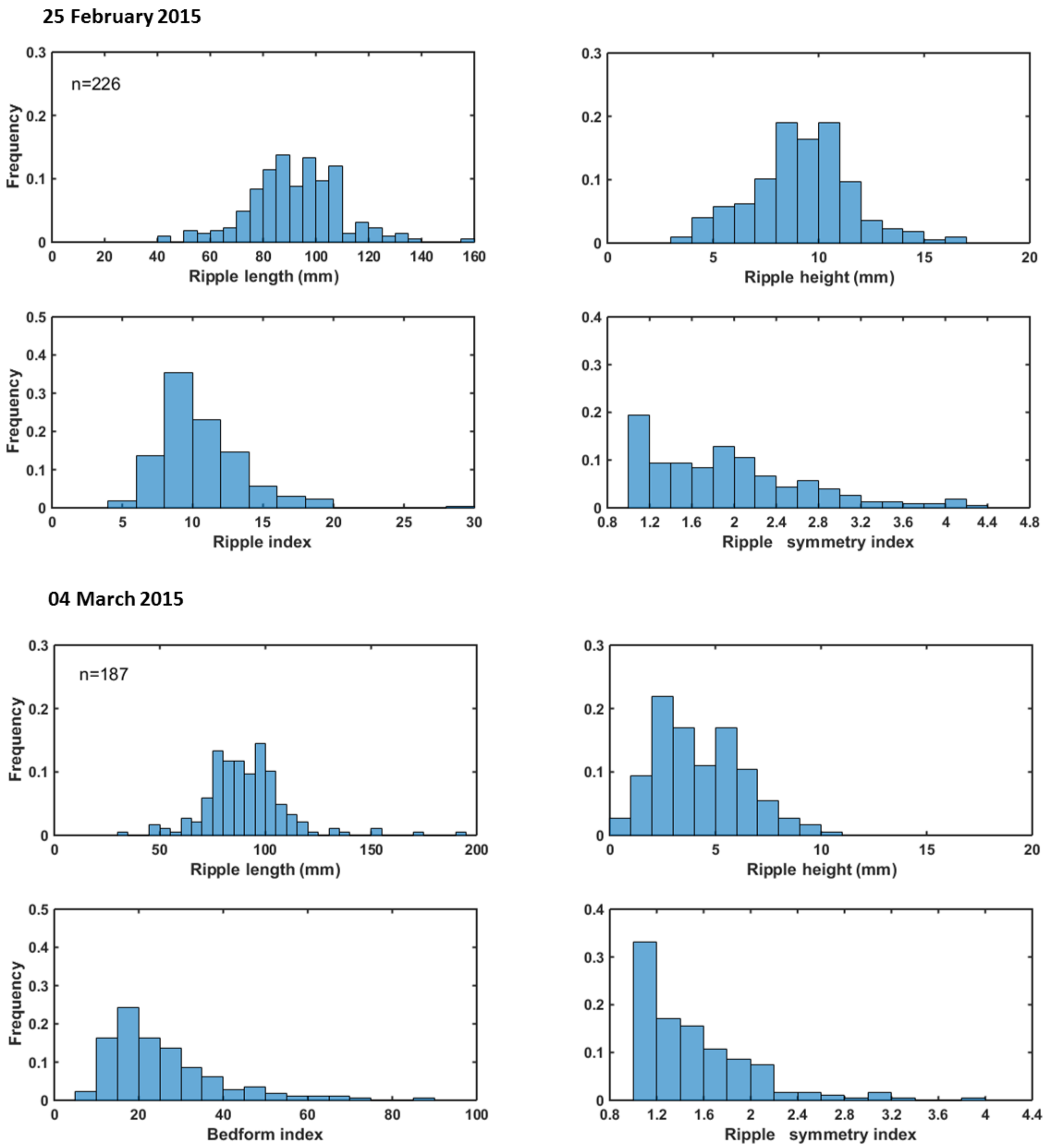

Figure 5-27. Histograms of all measured ripples' heights, wavelengths, ripple index and ripple symmetry index on 25 Febuary and 4 March 2015 (WN2), respectively.

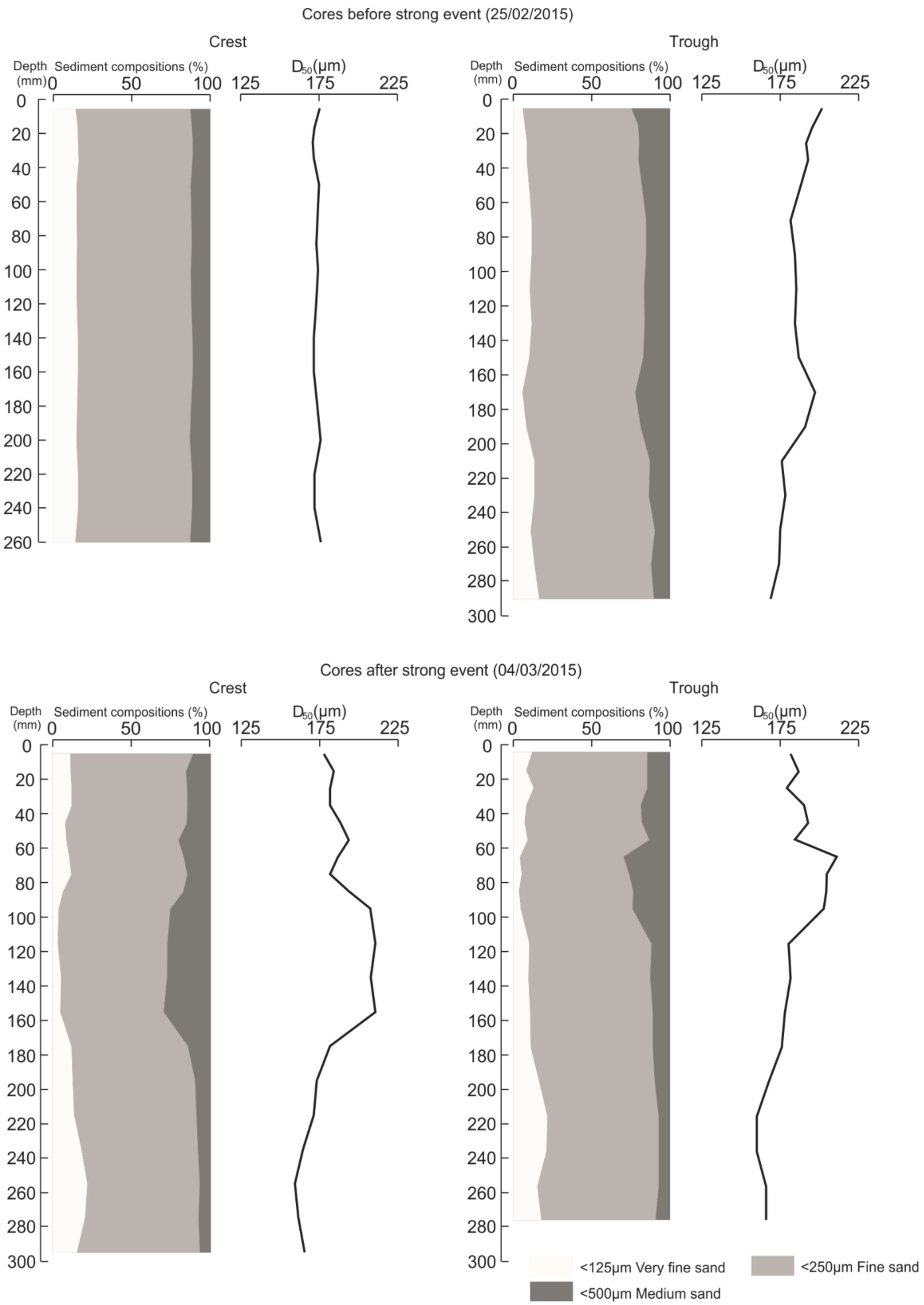

Figure 5-28. Sediment copositions and median grain size of sediment cores collected from ripple crest and trough (WN2).

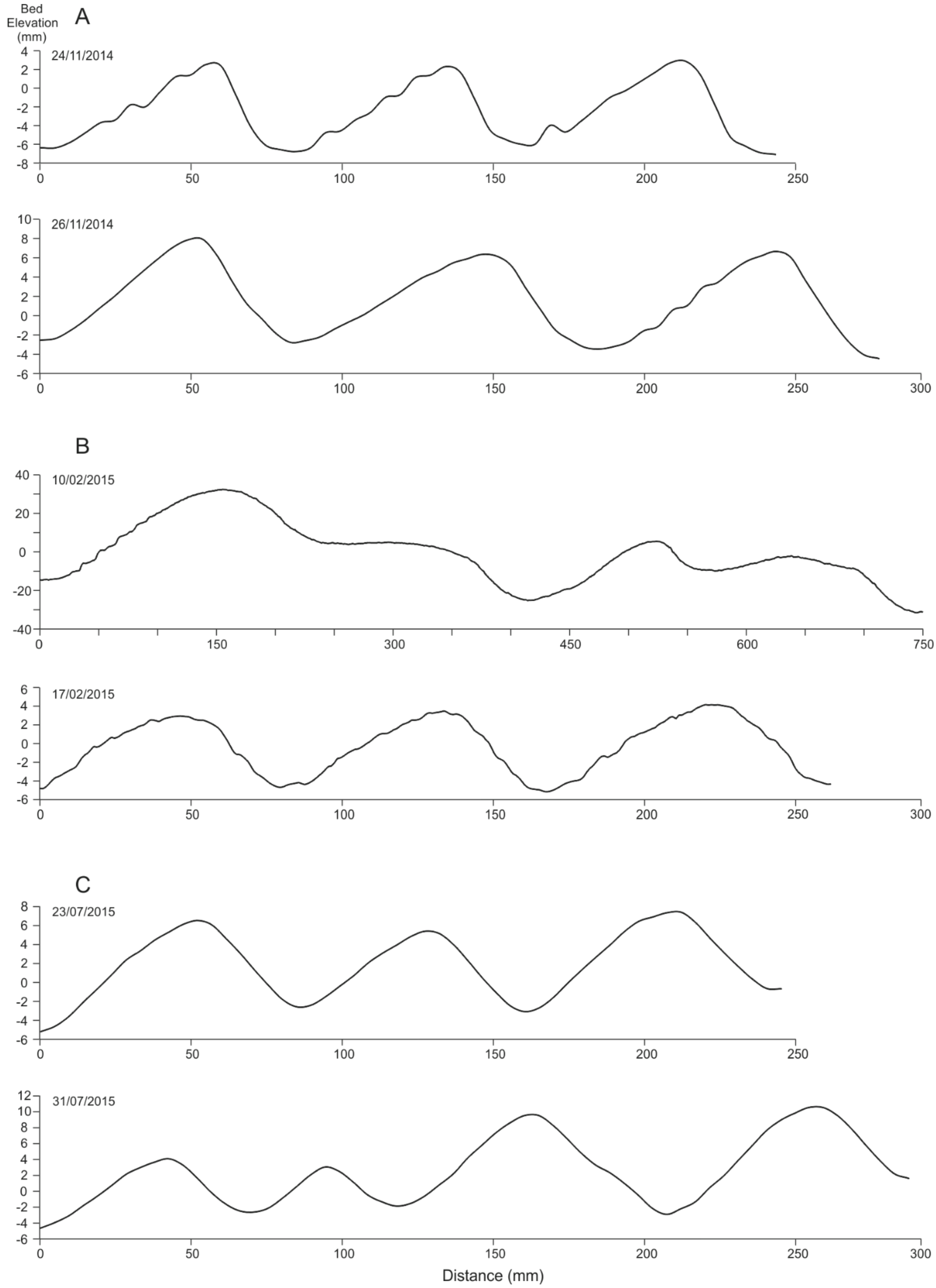

Figure 5-29. Typical ripple cross-section geometries observing in the field surveys. A-C: ripples were generated under calm condtions. Ebb direction from left to right.

Figure 5-29 continued

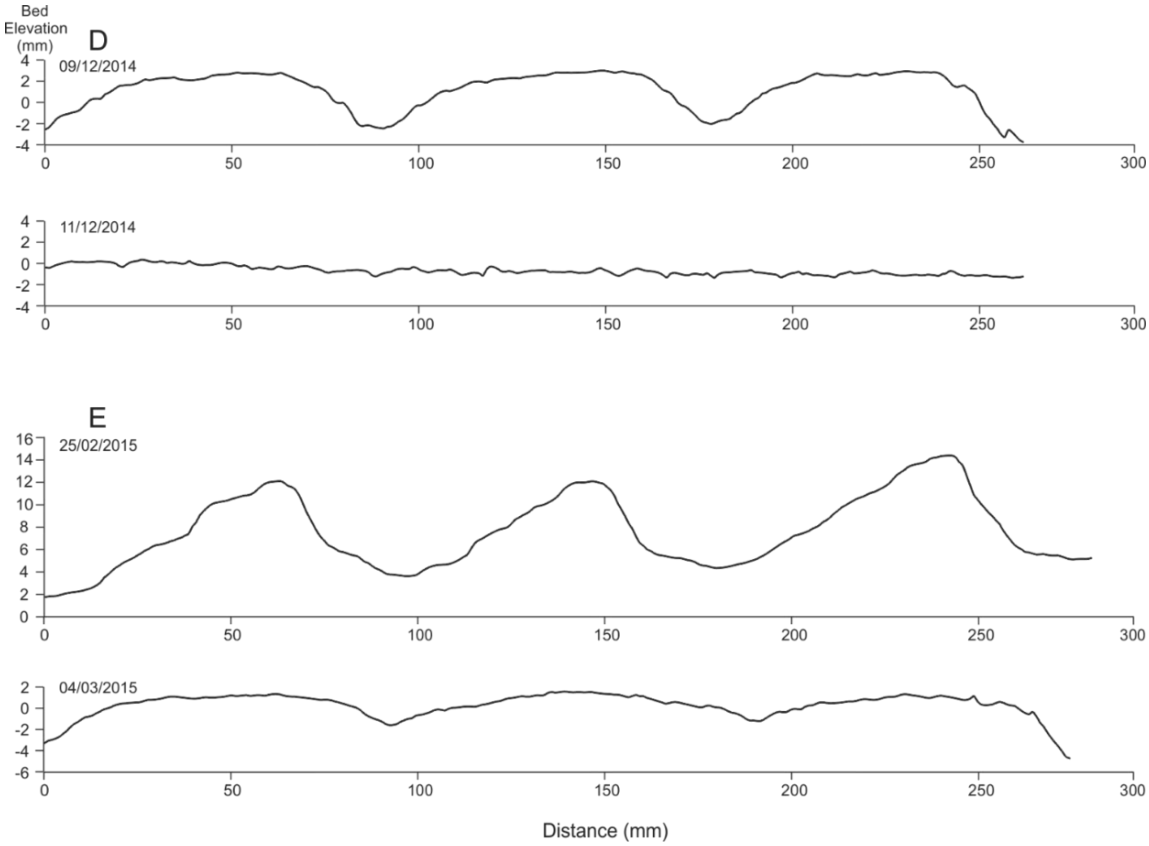

Figure 5-29. Typical ripple cross-section geometry observing in the field surveys. D-E: Ripples were generated under high wind conditions. Ebb direction from left to right.

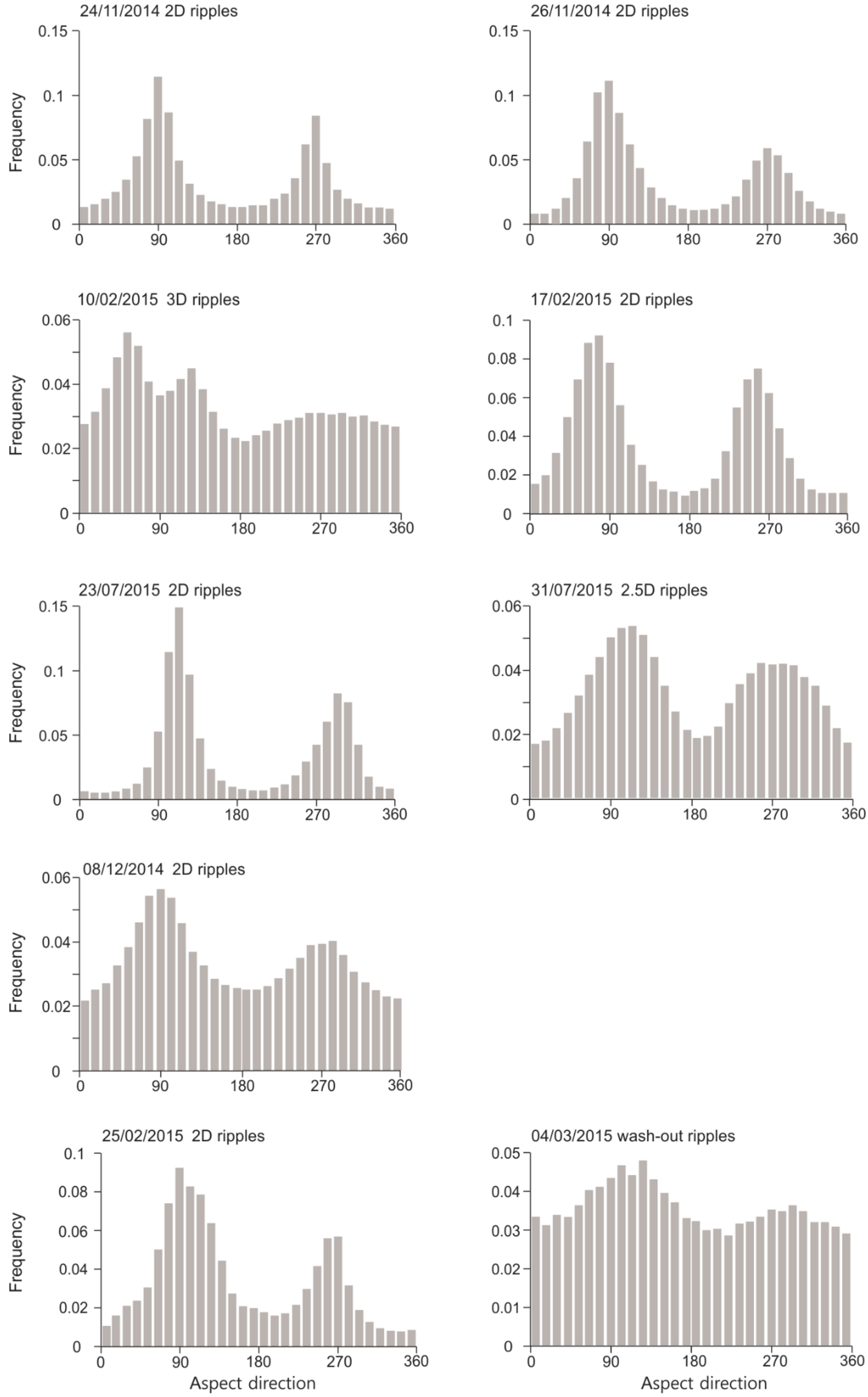

Figure 5-30. Frequency histogram of aspect direction of ripples obseving in the field survey.

5.4 Discussion

5.4.1 Cross-sectional bedform geometry

Field surveys at Red Cliff sand bar located in the upper Humber Estuary found ripples formed under unidirectional flow and combined flow conditions. Knowledge of the relationship between ripple geometry and flow conditions play a significant role on bridging the gap in understanding modern and ancient depositional environments (Harms, 1979; Clifton and Dingler 1984; Leeder, 2006). Detailed 3D scanning photos and ArcGIS analysis in this chapter to allow a greater quantification of the factors controlling ripple morphology. The most useful attributes to describe ripples include steepness (Ripple index) and symmetry (Ripple symmetry index).

i) *Ripple index (RI)*

Figure 5-31 A depicts changes of RI values with different hydrodynamic forces. The RI values of ripples generated under unidirectional flow varied marginally, and remained around 11. The exception is the observation on 8 December 2014 (WS2), when ripple crests were milder and ripple heights were smaller, contributing to the extremely high mean RI values of over 20. The averaged RI of washed-out ripples generated after strong breeze on 4 March 2015 (WN2) reached RI of 28. The results tend to demonstrate that RI could be used to differentiate between ripples forming under combined flow and unidirectional flow conditions. However simple using RI to identify depositional environments possibly leads to errors, because previous experiments under combined flow condition showed RI with greater range, from 5 to over 30 (Inman and Bowen 1963; Southard et al. 1990; Dumas et al., 2005; Perillo et al., 2014).

ii) *Ripple symmetry index (RSI)*

There is no precise boundary value of RSI between symmetrical and asymmetrical ripples, especially for the small-scale ripples with length smaller 40 mm. In common, ripples are regarded as the symmetric if the value of RSI is between 1 and 1.2 (Dumas et al., 2005). Ripples forming under unidirectional flow tend to be more asymmetric with increasing unidirectional flow (Dumas et al., 2005; Perillo et al., 2014). Yokokawa (1995) reported the asymmetrical ripples with RSI exceeding 4 under only unidirectional flow. But in present study the mean RSI of ripples generating under only tide current are smaller than 2, even the maximum RSI was smaller than 3 (Figure 5-31 B). Moreover, the results indicate that ripples forming in winter tend to be more asymmetrical (Figure 5-31 B). The previous studies highlight ripple cross geometry is dominated by the unidirectional velocity (Dumas et al., 2005; Perillo et al., 2014), the faster the unidirectional velocity is, the more asymmetrical the ripple is. Additionally, seasonal change of freshwater input (runoff) is observed at Humber Estuary, with it significant declining in summer (Uncles et al., 2006). However, it seems that the current velocity is not only element controlling ripple geometry. The ebb velocities measured on 10 February 2015 were slower than that recorded on 31 July 2015 (Figure 5-12; Figure 5-16). Nevertheless, the RSI on 10 February 2015 was 1.7, which indicate ripples were more asymmetrical than ripples found on 31 July 2015 with 1.4 of RSI. The reason for this discrepancy between flume experiment and field observation is still vague, therefore the further study is needed in future to bridge the knowledge gap.

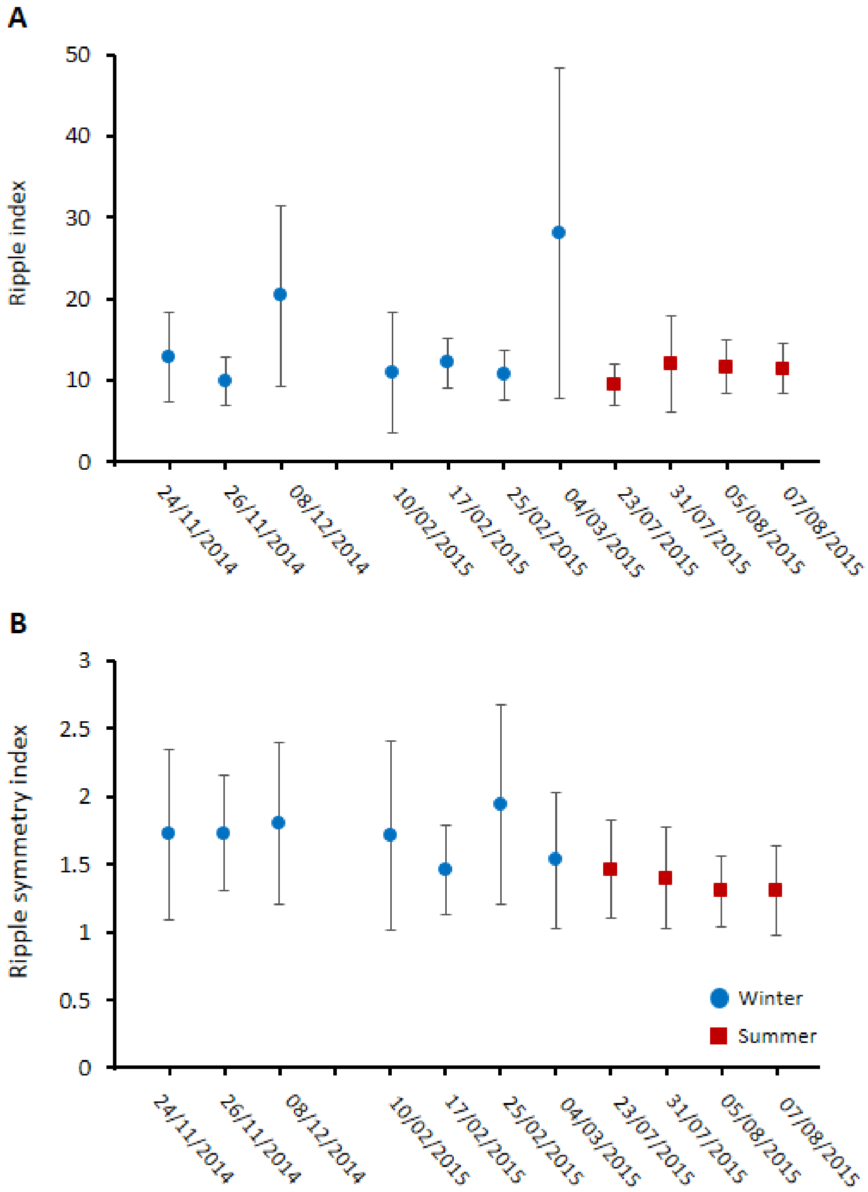

Figure 5-31. Ripple index (A) and ripple symmetry index (B) of ripples obseving in field surveys in winter (blue dot) and summer (red square). The vertical black line denote standard deviation.

5.4.2 Ripple development in unsteady flow

i) *Current alone*

The results of field surveys indicate that 2D ripples with straight crest lines were generated in the spring tide under calm conditions. Figure 5-32 shows unsteady tide velocity of last cycle before the ripple scans were undertaken, which is closely linked to ripple development. The stability fields of bedforms derived from Southard and Boguchawl (1990), with corresponding current velocity, are shown as well. Considering each ripple survey undertaken during low water, ripple fields were significantly affected by the magnitude of the ebb tide velocity. The ebb velocities, notably of spring tides, covered all stability fields within the phase diagram, from no movement to upper stage plane bed except the one on 26 November 2014 (Figure 5-32 A). The observed patterns of 2D ripples obtained on 5 and 7 August 2015 (SS1) map to the phase diagram zones. According to the phase diagram, however, the bed configuration on 26 November 2014 should be plane bed instead of 2D ripples. Similarly, the final ebb velocities of the neap tide on 17 February and 31 July remained in the stability field of upper stage plane bed (Figure 5-32 B). But the current-induced 2D ripples and 2.5D ripples were formed under these tide velocities. The discrepancy between observed bed form and prediction from the phase diagram could be explained by the existence of a significant estuarine turbidity maximum (ETM) in the Humber Estuary. The suspended particle matter (SPM) in the ETM progressively increases from the estuarine mouth to the upper Humber (Uncles et al., 2006). SPM stratification was found in the ETM (Uncles et al., 2006), which contributes to significant reduction of turbulent shear stress (Sheng and Villaret, 1989; Li and Gust, 2000). However, the study of Uncles et al., (2006) also revealed prominent flocculation processes in the ETM water column, for forming cohesive gels. This cohesive force enables a suppression of turbulence in the flow and a reduction of bed shear stress (Winterwerp and Van Kesteren, 2004; Baas and Best, 2008; Baas et al., 2009).

The tide velocity forming 3D ripples on 10 February was not recorded. However, following the velocity of the neap tide shown as the red dot line in Figure 5-32 B indicates that the ebb velocity remained over 2 hours within the stability field of current ripples, which enable the ripples to reach equilibrium. Seminal work of Baas (1993) revealed ripple development stages, including the transition from 2D ripples to equilibrium 3D linguiod ripples, given enough time. Therefore, it is speculated that the observed 3D ripples had attained equilibrium before low water. However, the 2D ripples, for example the ones observing on 17 February 2015 (Figure 5-9), developed under unsteady current flow (green dash line, Figure 5-32) and needed more time to attain equilibrium before they were exposed on the sand bar at low tide. Furthermore, there was longer time for ripples development on 31 July 2015 (blue dash line, Figure 5-32), thus the 2.5D ripples that is a transition between two-dimensional and three-dimensional were finally found.

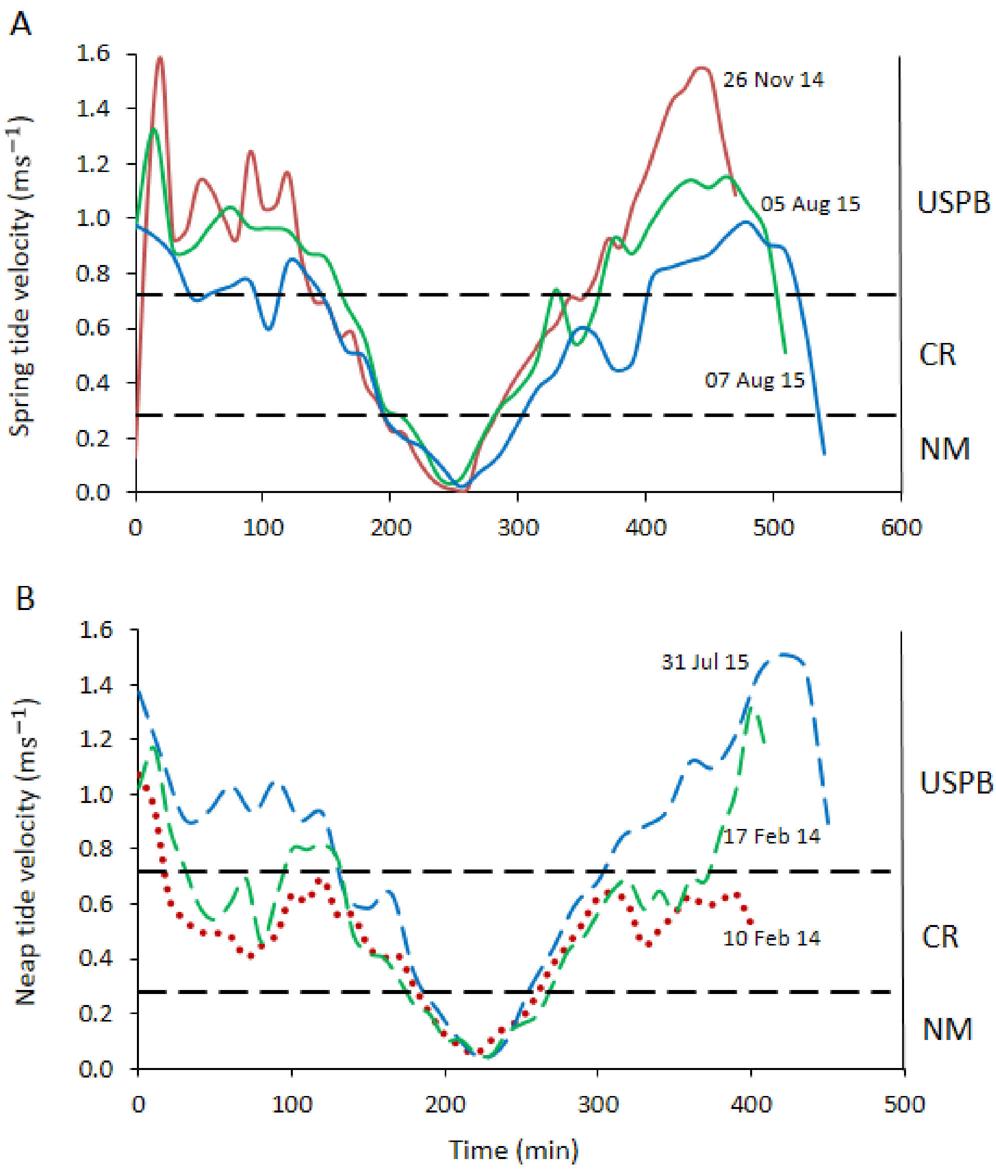

Figure 5-32. Current velocity change of last tide cycle just before ripple scaninning in spring tide (A) and neap tide (B). The corresponing dates are marked near the velocity lines. The black dash line repersents boudary of stability field of bedform. These two boudaries are derived from phase diagram of Southard and Boguchawl (1990) with median grain size D_{50}=0.19mm. USPB: Upper Stage Plane Bed; CR: Current Ripple; NM: No Movement.

ii) *Combined flow*

Two high wind events were recoded between 8 and 11 December 2014 and between 25 February and 4 March 2015, which induced bottom oscillatory motion that played a vital role in reworking bedforms. Without this motion, 2D current ripples were found as the tide current velocities were similar as in the calm condition. But the combined velocities generated flat bed on 11 December 2014 (Figure 5-21) and formed mild and flat crested wash-out ripples (Figure 5-26) on 4 March 2015. Theoretically, both plane bed and wash-out ripples are formed under relatively higher bed shear stress for the same grain size sediments (Van Rijn 1993; Leeder 2011). Past works indicated storm induced strong oscillatory motion changed bedform type and promoted wave-formed ripples (Amos et al., 1988; Allen and Hoffman, 2005). The present field observations reflect that strong wind, instead of storm generated wave energy, is strong enough to form transitions into upper regime bedform states. It agrees with the previous viewpoint (e.g. Hammond and Collins, 1979; Grant and Madsen, 1979) that wave-induced bed shear stress is enhanced with presence of tide current.

Before the sand bar was exposed on 11 December 2014, ebb tide velocity and maximum orbital velocity entered in the stability field of plane bed (Figure 5-33), which matches up with the actual observation. According to phase diagram of Mayrow and Southard (1991), tide velocity and maximum orbital velocity in the last 30 minutes of tide cycle on 4 March 2015 should corresponds with stability field of small strongly asymmetrical 3D ripples. However, the actual 2D wash-out ripples were appeared. The reason for the discrepancy between the field observation and prediction may be concluded as following. Firstly, bedform regions (Mayrow and Southard, 1991), with unidirectional currents exceeding $0.25ms^{-1}$, were extrapolated without support of experimental results and field observations. Secondly phase diagram of Mayrow and Southard (1991) neglected the influence of both sediment grain size and wave period, which are known as important factors in controlling the stability fields of bedorms (Dumas et al., 2005; Sekiguchi and Yokokawa, 2008; Perillo et al., 2014). Sekiguchi and Yokokawa (2008) highlighted that the bedform phase diagram significantly changes with wave periods between 1 s and 1.5 s which are very close to the actual wave period during surveys. Unfortunately, the study of Sekiguchi and Yokokawa (2008) was also restricted the unidirectional velocities smaller than $0.5ms^{-1}$. Therefore, more detailed studies are needed to understand bed configurations under relatively higher combined flow velocity, expanding the present bedform phase diagrams to applicability under field condition.

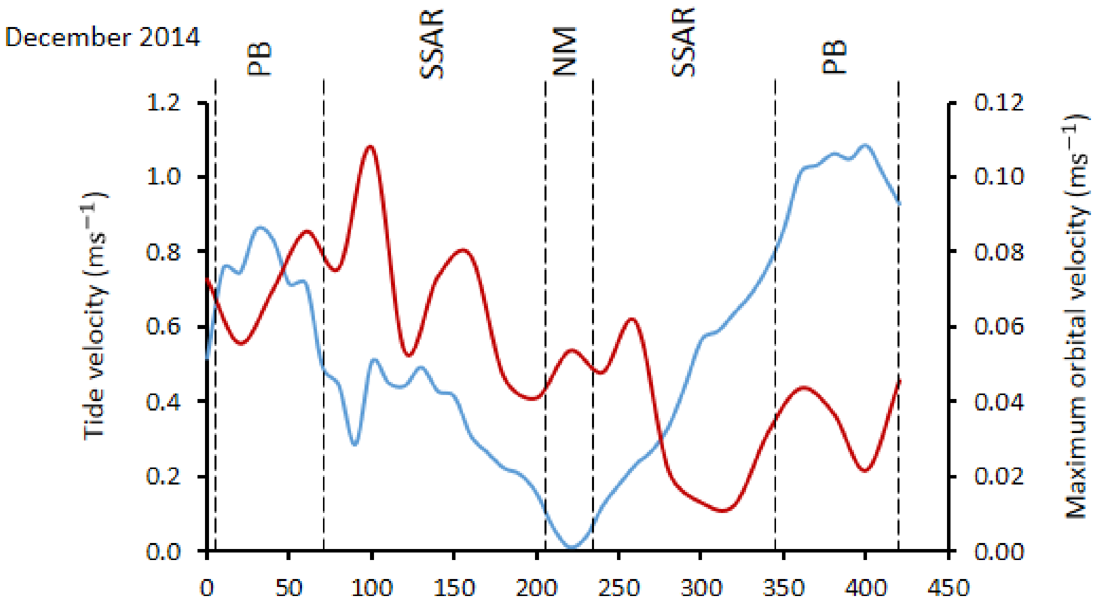

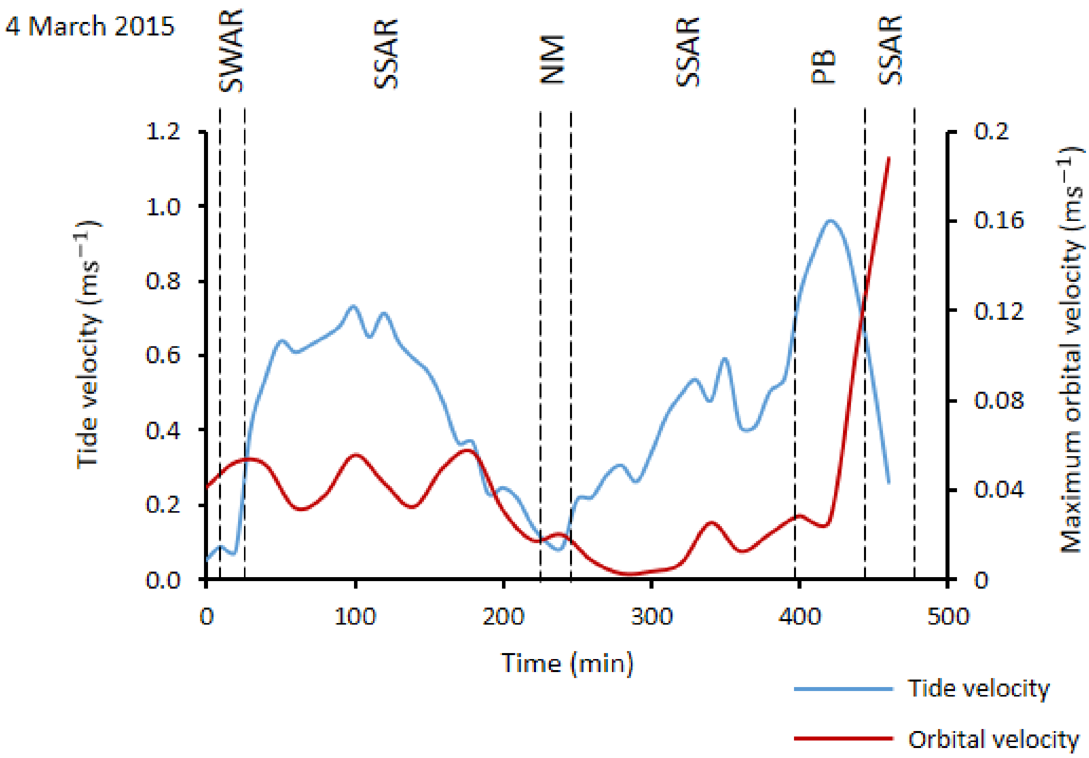

Figure 5-33. The change of both tide velocity (blue line) and maximum orbital velocity (red line) in the last tide cycle before ripples scanning. The black dash line repersents boudary of stability field of bedform of Mayrow and Southard (1991). NM: No Movement; SWAR: Small Weakly Asymmetrical Ripples; SSAR: Small Strongly Asymmetrical Ripples; PB: Plane Bed.

5.4.3 The role of EPS on ripple size

EPS, as the production of benthic micro-organisms, is known as a key factor in increase sediment bed resistance to erosive forces (e.g., Tolhurst et al., 2002; Lundkvist et al, 2007). This kind of biological cohesion has also been linked to restricting bedforms heights and lengths, even at low concentrations of EPS (Malarkey et al., 2015; Ye, 2016). The EPS contents of sediments for field surveys performed in the winter 2014 are shown in 0, showing very low level of EPS around 0.003%. In the summer 2015, EPS contents of sediments were one order of magnitude higher than those collected in the winter (0), standing at around 0.012%. It indicates relatively higher micro-organism activities in the summer, which is consistent with previous findings (Paterson, 2009). The delay of first ripple appearance and significant slow ripple growth rate were found in the experiment of Malarkey et al (2015), even the EPS content was only 0.016% that is close to EPS content in present sediments. However, the size difference between ripples forming with 0.016% EPS and with pure sand was tiny (Malarkey et al., 2015). In the present field surveys, the mean ripple length in summer marginally shorter than that in winter (0). In terms of ripple height, there is only a small difference between ripples observed in summer and winter, respectively. Considering similar hydrodynamics and sediments conditions, the results seem to be indicative for the low influence of EPS on ripple geometry, likely due to very low EPS content in sediments.

5.5 Conclusions

Ripple field surveys were conducted at Red Cliff sand bar in the upper Humber estuary NE England between November 2014 and July 2015. A 3D laser scanner was used in order to acquire detailed information of ripples formed on the bar top under tidal currents and during wave forcing of different magnitude. The results can be concluded as follows.

1. Under calm conditions, ripples were mainly two-dimensional and asymmetrical, except for 3D ripples surveyed on 10 February 2014 and the 2.5D ripples on 31 July 2015. Based on the theory of Baas (1993), it is speculated that the 2D ripples were still in the development stage and the 3D ripples were at equilibrium with enough evolution time.
2. The bed morphology was significantly altered during periods of high strong wind . Plane bed and 2D wash-out ripples appeared after the strong wind, induced

waves, which reflect the remarkable influence of combined flows and the enhanced shear stress on the change of bed configuration.

3. Ripple index of the wash-out ripples after high events was significantly higher, with the mean RI reaching to 28. Ripple asymmetry indexes, however, were not significantly different between ripples formed under calm and high wind conditions. However, suggestions of a seasonal change trend were detected, with ripples forming in winter being more asymmetrical.
4. The phase diagram of Southard and Boguchawl 1990 does not match observed bedforms. Especially with velocities exceeding 0.8 ms^{-1}, when the predicted bedform should be plane bed instead of actual 2D ripples. The high concentrations of suspended particles likely causes stratification and leads to turbulence suppression, which is possibly the main reason for the discrepancy.
5. The stability field of the phase diagram of Mayrow and Southard (1991) with unidirectional flows larger than 0.25ms^{-1} was extrapolated. It successfully predicts plane bed under observed combined flow conditions on 11 December 2014. But the 2D weak asymmetric ripples instead of expected small 3D strongly asymmetric ripples were generated under strong breeze condition on 4 March 2015. Therefore, further work is needed to improve present phase diagrams to enhance their applicability under natural estuarine conditions.
6. The EPS concentrations of sediment in winter were extremely low, with values of approximately 0.003%. EPS concentrations increased to about 0.013% in summer. However, the increased EPS content is seems to not significantly restrict ripple dimensions in a similar manner to the flume study of Malarkey et al. (2015).

CHAPTER 6 –Discussion

6.1 Vertical sorting caused by strong winnowing under waves

Previous studies indicate winnowing of fine grains from the bed is one of key mechanisms contributing to vertical sorting in bedforms (Willis, 1988; Wilcock and Southard, 1989; Klaassen, 1990; Blom et al., 2003). Blom et al. (2003) selected three different types of sediments with median grain size of 0.68 mm, 2.1 mm and 5.7 mm, respectively and argued that winnowing of relatively fine sands enabled the bed to become downward coarse. In the present flume study, two types of sediment (clay and fine sands) were much finer than that of Blom et al. (2003) and the vertical sorting in the observed wave ripples was identified. In particular, high winnowing efficiencies under waves resulted in the formation of pure sand layers at ripple crests (see Figure 3-25, Chapter 3). Additionally, clay particles winnowed from the bed resulted in higher suspended sediment concentrations, forming stratified structure of suspended sediments and also damping turbulence prior to the formation of ripples (see Chapter 4). Such fine clay particles winnowing has previously been observed in flume experiments under unidirectional flow (e.g., Baas et al., 2013; Schindler et al., 2015; Ye, 2016). However, it seems that winnowing efficiency under oscillatory condition is much higher than that under unidirectional flow conditions. For similar initial bed clay contents, rates of winnowing were much higher in the experiments herein compared with previous experiments (Baas et al., 2013; Ye, 2016) where pure sand layers within ripple crests were not produced in these previous unidirectional flow experiments. The mechanism of winnowing fine sediments from coarse sediments is attributed to pressure gradient exerting by flow forcing along bed surface (Kalf, 2013). Kalf (2013) emphasized three significant elements controlling the entrainment of fines including flow velocity, layer thickness and difference of grain sizes between surface and sub-surface layer. Considering tiny differences of flow velocities (0.36 ms^{-1} for the experiment of Baas et al. (2013) and 0.3 ms^{-1} for present maximum orbital velocity) and bed properties, it is hypothesised that oscillatory flow possibly leads to larger difference in dynamic pressure over different part of ripple, therefore winnowing more fines from bed. This is consistent with finding of van Rijn (1993) that waves are more efficient at entraining sediment than currents. It is should be noted that an upward coarsening trend within wave ripples is contradictory to the trend observed in the experiments of

Blom et al. (2003). This is likely due to sediment properties in that clay particles are relatively easily winnowed because of water pressure as discussed in the section 3.4.3. However rather coarser sediments (D_{50}>2 mm) used by Blom et al. (2003) were likely deposited at the lower location of bedforms due to being gravity. Furthermore, the study of Blom et al. (2003) ignored winnowing process at ripple crests where the winnowing efficiency is much higher. Although winnowing processes were not directly measured in the current study, it plays a vital role on both sediment and bedform dynamics and full understanding this process will benefit to improve sediment transport models to account for vertical sorting process.

6.2 Availability of present bedform phase diagrams and a new three dimensional phase diagram

As mentioned in the chapter 2, bedform phase diagrams are widely used to predict bed states with known flow and sediment conditions and to reconstruct ancient depositional environments from known sedimentary structure persevered in rocks (Schwartz, 1982; Clifton and Dingler, 1984; Schindler et al., 2015). In general phase diagrams of bedforms drawn either dimension variables (e.g., maximum orbital velocity and median size, Figure 2-15) or non-dimensional variables (e.g., wave mobility parameter and particle parameter, Figure 2-17). The phase diagram of Allen (1984) is based on both data derived from laboratories and field observations, highlighting contour lines of ripple index (Figure 2-17). In the present large flume experiment, the maximum orbital velocities were around 0.3 ms^{-1} and median sediment grain size were smaller than 500 µm (Table 3-1). Under this experimental conditions, wave-induced ripples dimensions were constant, with ripple length and height slight fluctuating around 140 mm and 20 mm, respectively. Based on the prediction of the phase diagram of Allen (1984), the ripple index should be smaller than 4.5. But the actual ripple indices were close to 7, which indicates this phase diagram tend to overestimate ripple steepness. As far as the phase diagram of Kleinhans (2005) is concerned (Figure 2-17), the boundaries between different bed configurations are defined as existing models, emphasizing the existence of hummocks as a transition from wave ripples to upper stage plane bed. The present 2D wave ripples corresponded with wave mobility parameters of 0.26 and particle parameters of 11 computed by equation 3-21 and equation 3-22, which is consistent with Kleinhans (2005)'s prediction.

Schindler et al. (2015) recently introduced a new version of bedform phase diagram by schematically adding the z-axis to show the influence of initial bed clay fraction on bed state change under unidirectional flow (Figure 2-22). The new three dimensional phase diagram highlights bed configuration change as a function of bed clay content, current mobility parameter and particle parameters. Under wave condition, a similar three dimensional phase diagram is built, even though the present study only focuses on single location (Figure 6-1). As discussed before, high winnowing efficiencies contributes to a sand-clay mixed bed transforming to pure sand bed, which results in wave ripple size that is independent with initial clay fraction with range from 0 to 7.4%. This finding is undoubtedly helpful to fully understand the role of cohesive sediments on bedform dynamics with relatively lower clay content. Moreover, it is reasonable to expect further studies that expand to higher initial bed clay fractions and develop the next generation of bedform prediction models.

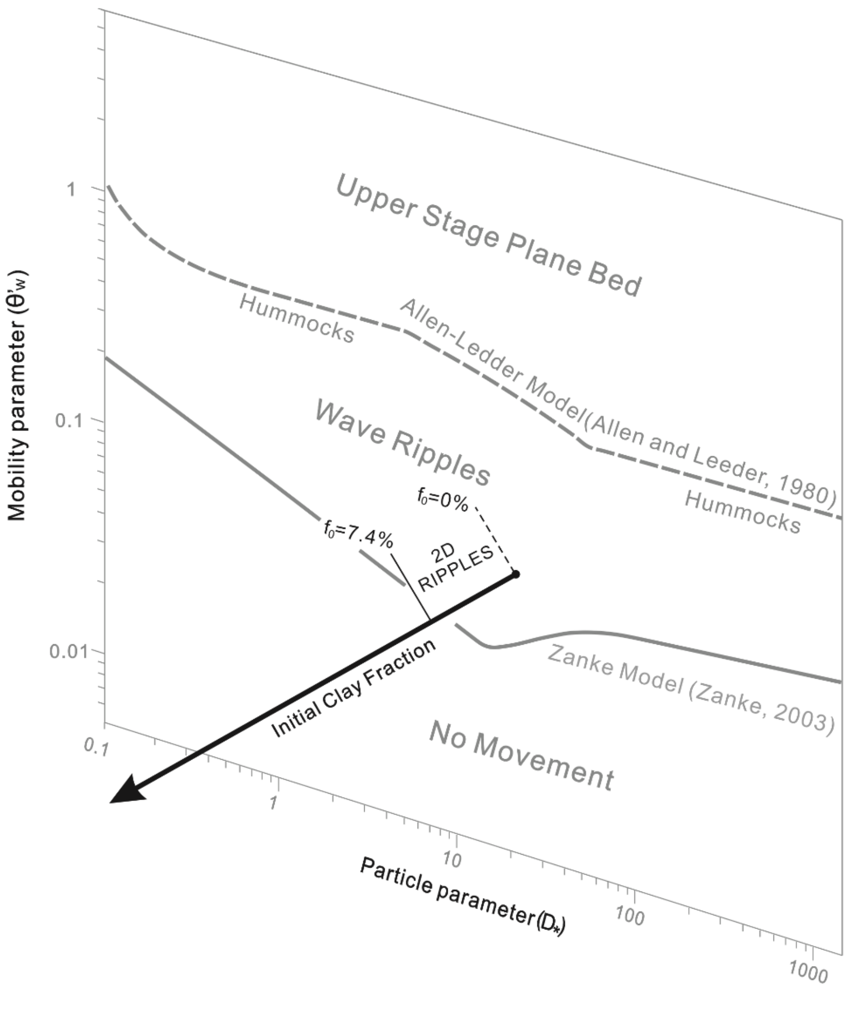

Figure 6-1 New three dimensional phase diagram of bedform generated under wave conditions (modified after Kleinhans, 2005).

6.3 The interacting triad of cohesive bed, near-bed turbulence and suspended sediment dynamics

Chapter 3 of this thesis shows wave-induced ripple dynamics over mixtures of clay-sand bed and investigates the influence of cohesive clay on ripples development. In Chapter 4, near-bed turbulence and sediment dynamics from flat bed to rippled bed are revealed. Based on the findings of both Chapter 3 and Chapter 4, a conceptual model is built in order to reflect the dynamic processes acting on sand-clay mixed beds, near-bed turbulence and suspended sediment transport (Figure 6-2). At the beginning of the experiment, the fine clay particles fill gaps between sand particles, forming a texture which is similar with a 'blocked layer' (Bartzke et al., 2013) and enabling the bed to be smooth. Clay winnowing immediately happens when the oscillatory flow moves over the flat bed. At the same time, a small amount of sand particles suspended very close to bed. The gravity difference between individual sand particle and clay particle leads to stratification of suspended sediments, which mainly contributes to suppress near-bed turbulence. Both bed yield strength and drag reduction caused by suppression of near-bed turbulence ensure that the bed remains flat, accompanying with a small amount of sediments transport (Figure 6-2 II). As the experiment progresses, increasing winnowing of clays from the bed reduces bed yield strength. As a result, the flat bed starts to be eroded, with gradual transition from smooth to rough. The increasing bed roughness promotes a vertical gradient of velocities, which enhances near-bed turbulence. However, the enhancing turbulent force is unable to break the structure of stratified distribution of suspended sediments. Additionally, in this stage, the yield strength and drag reduction still play a vital role in the inhibition of suspended sediment (Figure 6-2 III). With continual bed erosion, bed morphology development causes a significant increase of bed roughness. Under this circumstance, the increasing vertical momentum transports through density interfaces in stratification. Finally the stratification of suspended sediment disappears and random turbulence dominantly controls suspended sediments distribution, thereby suspended sediment concentration increasing in this stage (Figure 6-2 IV). It should be noted that the process from step 2 to step 4 remarkably prolongs with increasing initial bed clay fraction (i.e. from Run 03 to Run 06). The bed with increasing yield strength becomes more resistant to flow shear stress. However, the drag reduction effectively reduces the wave-induced force acting on the bed.

When wave ripples approach equilibrium, suspended sediment clouds occur that are closely related to the spatial and temporal production of vortices (Figure 6-2 V). Additionally, the asymmetric wave velocities cause relatively strong vortices generated across the lee sides, which leads to an imbalance in suspended sediment transport between lee side and stoss side. Clay winnowing continues when wave ripples are evolving and approaching equilibrium. Especially relatively higher winnowing efficiency occurs at ripple crests where formed pure sand layers varying by 1~3 cm (Figure 6-2 V).

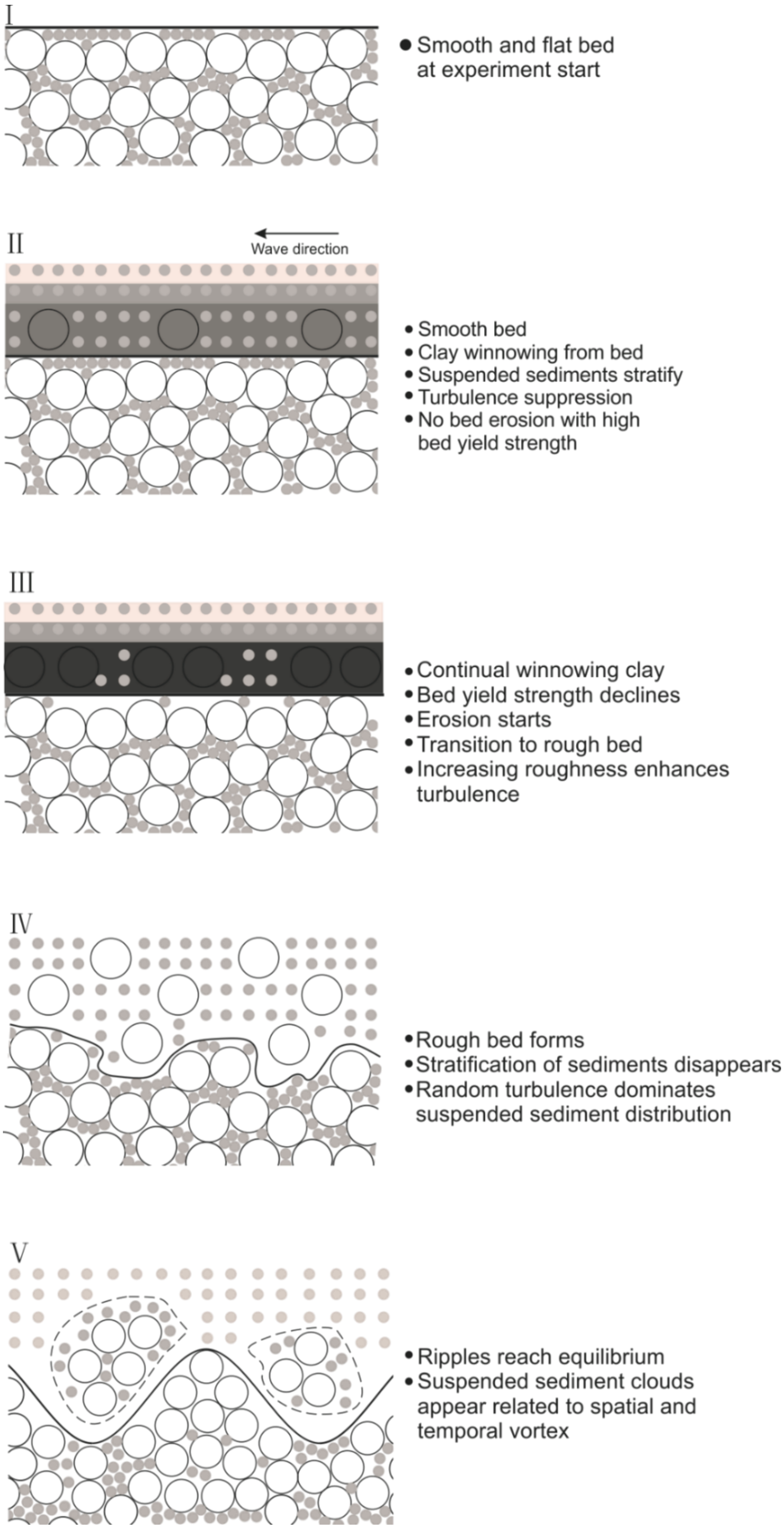

Figure 6-2 Conceptual model of the interactions among cohesive bed, near-bed turbulence and suspended sediment transport

CHAPTER 7- Synthesis and future research

7.1 Research questions revisited

The thesis sought to discover the influence of cohesion on bedform dynamics in combined wave-current flows. Chapters of 3 and 4 present new experimental results showing the influence of physical (substrate clay percentages) cohesion in mixed substrates on the development of wave-induced ripples. The experiments allow for the detailed quantification of the triad of bed stability, near-bed turbulence and sediment dynamics. Chapter 5 of thesis investigates how ripples change in response to hydrodynamics and the role of biological cohesion (via EPS on contents) bedform morphology on a large sand bar in the upper Humber estuary, NE England. The first part of this synthesis section will answer the research questions posed in the Chapter 1 and will draw on the findings from both the laboratory and the field work to provide set of implications for improvement of present sediment transport models and coastal management.

7.1.1 Bedform dynamics

1) How does mixed-sediment substrate, compared with a pure sand bed, affect i) the first appearance of wave-induced ripples, and ii) the bedform development rate.

The cohesive clay particles play a vital role in delaying the onset of wave ripples formation from flat bed, extending the time of first wave ripple appearance from few seconds in pure sand runs to over 30 minutes in the run with relatively high clay contents. Furthermore, the higher the initial clay fraction is, the slower ripple development and evolution (Figure 3-21 E and F, Chapter 3). Over a pure sand bed, the growth rate of ripple length and height, reached 1.2 mmmin^{-1} and 0.8 mmmin^{-1}, respectively. The figures, however, were significantly lower at 0.2mmmin^{-1} and 0.5mmmin^{-1} in the run with the highest clay fraction (Run 06).

2) Does a relationship exist between initial bed fraction and equilibrium wave ripples lengths and heights?

The results of non-linear fit using the method of Baas et al. (2013) highlight that equilibrium time of wave ripple length and height exponentially increased with clay content increase. But the equilibrium dimensions of wave ripples were independent with increasing clay fraction during the experiments, with ripple lengths and heights were constant around 140 mm and 20 mm (Figure 3-21 C and D, Chapter 3), respectively. Additionally, wave ripple cross-section geometry was little influenced by increasing clay fraction from 4.2% to 7.4%.

3) Does wave-induced bottom orbital motion and combined flows significantly change bedform morphology compared with calmer, low-wave height conditions?

Field surveys of ripples in the upper Humber estuary reveal that ripples were basically the same in both cross-section and plan view geometry without an influence of tidal strength. However, ripple morphology was strongly altered by combined flow induced by high winds. After strong wind events, 2D wave ripples were replaced by either plane bed or 2D wash-out ripples.

4) Does the quantity of EPS alter bedform morphology ?

Though EPS content increased from 0.003% in the winter surveys to around 0.013% in the summer, the influence on changing ripple size is tiny. Malarkey et al (2015) indicated that EPS content of 0.016% is able to significantly slow down ripple growth rate, but it is not sufficient to decrease ripple dimension.

7.1.2 Suspended sediment dynamics

1) What is the rate of winnowing and how does winnowing influence wave ripples development?

Winnowing of clay particles from the bed occurred during the entire set of experiments and during the transition from a flat bed to a rippled bed, which is important to wave ripple evolution. At the beginning of the experiments, clay winnowing contributed to the bed substrate becoming less cohesive, which resulted in a decline of bed yield strength and the formation of wave ripples. Winnowing process continued even when wave ripples reached equilibrium, leading to cohesive ripples transforming to non-cohesive ripples and constancy of equilibrium ripple length and height with increasing initial clay fraction.

2) How does near-bed turbulence intensity and suspended sediment concentration change during wave ripple evolution?

The near-bed turbulence intensity was suppressed by the stratification of suspended sediments over the flat bed and the near-bed turbulence kept level even though initial clay fraction increased to 7.4%, standing at approximately 0.018 ms^{-1}. The near-bed turbulence intensity significantly increased once bed began to be eroded. In particular, the results highlight that the near-bed turbulence was relatively lower in runs with clay fractions exceeding 7% over the eroded bed.

As far as suspended sediment concentration is concerned, it experienced a sharp increase from the flat bed conditions as ripples initiated and evolved. Additionally, the results indicate that peak values of suspended sediment concentration periodically occurred at the lee side of the wave ripples, which were associated with rather stronger vortices shedding across the lee side of ripples.

3) How does the dynamics system including cohesive bed, near-bed turbulence and sediment transport work?

The experimental results reveal a dynamic process of interacting cohesive bed, near-bed turbulence and sediment transport, which contribute to characteristic wave ripples developing over clay-sand bed. At the beginning of experiments, winnowing of clay particles leads to formation of suspended sediment stratification over smooth and flat bed, which suppresses near-bed turbulence. With increasing number of clay particles removed from bed, a gradual decrease bed yield strength results in increased sediment transport and bed erosion, resulting in the formation and acceleration in the evolution of wave ripples. This enhances bed roughness, thereby significantly increasing near-bed turbulence intensity. Finally, wave ripples develop to reach equilibrium, and these are characteristically formed of pure sand ripples overlying a mixed substrate below.

7.2 Future research

7.2.1 Extending experimental flume simulations

Strong clay winnowing efficiency under wave forcing governs the rate of formation of a rippled bed within mixed substrates. However, ripples of the same size are ultimately produced in the concentrations of clay investigated herein. These results in the independent relationship between initial bed clay fraction and ripple size. Compared with work of Schindler et al. (2015), with clay content widely varying from 1.9% to 14.1%, the clay fraction range of present flume experiment was narrower. Therefore, future work should increase the parameter range of the initial clay fraction to extend the knowledge of ripple evolution over sand-clay bed from present study and thus improve accessibility of three dimensional phase diagram of bedforms (e.g. Figure 6-1) generated under waves. In addition, regular waves with period of 2.5 s used in present experiments may also lead to different bedform evolution when compared to the poly-chromatic superimposed (irregular) waves often occurring in the natural environment. Hence, future flume experiments should also consider this complex parameterization and thus more fully represent natural depositional environments for bedforms.

7.2.2 Coastal management

The Humber estuary, like other estuaries in the world, is a significant locale for human activities and a range of ecosystem services. Therefore, scientific management will benefit to sustainable development of these fragile systems. The present thesis has provided elaborate information about ripples and have revealed that bedforms in the upper Humber estuary are sensitive with changes in hydrodynamics. In particular, the bed configurations have significantly altered after high wind generated wave events. The present field study is only a first step to link bedform dynamics with hydrodynamics since this kind of depositional environment is very complex and effected by physical, chemical and ecological elements. Herein further detailed field surveys are necessary to fully understand the mechanisms of the above mentioned changes. For example, future surveys, recording high resolution of three dimensional velocities by Acoustic Doppler Velocity Profiler (ADCP) during tide cycles will be helpful to examine in more detail the relationships between bedform dynamics and bed shear stress. Furthermore, using optical or acoustic devices (e.g. OBS, LISST) to record suspended sediment concentration in near bed zone will allow the influence of estuarine turbidity maximum (ETM) on bedform dynamics to be more fully explored.

References

Adams, C.E. & Weatherly, G.L. 1981, "Suspended-sediment transport and benthic boundary-layer dynamics", *Marine Geology,* vol. 42, no. 1-4, pp. 1-18.

Admiraal, D., Musalem-Jara, R., García, M. & Niño, Y. 2006, "Vortex trajectory hysteresis above self-formed vortex ripples", *Journal of Hydraulic Research,* vol. 44, no. 4, pp. 437-450.

Agrawal, Y. & Pottsmith, H. 2000, "Instruments for particle size and settling velocity observations in sediment transport", *Marine Geology,* vol. 168, no. 1, pp. 89-114.

Allen, J.L. 1968, *Current ripples*, Elseiver, Amsterdam, Netherland.

Allen, J.L. 1984, "Development in sedimentology, 30, Sedimentary structures their character and physical basis", Elsevier, Amsterdam.

Allen, J.L. 2012, *Principles of physical sedimentology,* Springer Science & Business Media.

Allen, J.L. & Leeder, M. 1980, "Criteria for the instability of upper-stage plane beds", *Sedimentology,* vol. 27, no. 2, pp. 209-217.

Allen, P.A. & Hoffman, P.F. 2005, "Extreme winds and waves in the aftermath of a Neoproterozoic glaciation", *Nature,* vol. 433, no. 7022, pp. 123.

Alvarez-Hernandez, E.M. 1990, *The influence of cohesion on sediment movement in channels of circular cross-section*, PhD edn, University of Newcastle upon Tyne, UK.

Amos, C.L., Bowen, A., Huntley, D. & Lewis, C. 1988, "Ripple generation under the combined influences of waves and currents on the Canadian continental shelf", *Continental Shelf Research,* vol. 8, no. 10, pp. 1129-1153.

Amos, C.L., Grant, J., Daborn, G. & Black, K. 1992, "Sea carousel—a benthic, annular flume", *Estuarine, Coastal and Shelf Science,* vol. 34, no. 6, pp. 557-577.

Amos, C.L., Sutherland, T.F. & Zevenhuizen, J. 1995, "The stability of fine-grained sediments in Manitouk Sound, Hudson Bay, Canada", *Sedimentology*.

Amoudry, L.O., Bell, P., Souza, A.J. & Thorne, P.D. 2011, "Intrawave modeling of turbulent flow and sediment transport over rippled beds", In Wang, P.; Rosati, J.D.; Roberts, T.M. (Eds), The Proceeding of the Coastal Sediments 2011, Singapore, World Scientific, pp. 1048-1059.

Amoudry, L.O. & Souza, A.J. 2011, "Deterministic coastal morphological and sediment transport modeling: A review and discussion", *Reviews of Geophysics,* vol. 49, no. 2.

Andersen, K.H. 2001, "A particle model of rolling grain ripples under waves", *Physics of Fluids,* vol. 13, no. 1, pp. 58-64.

Arnott, R.W. & Southard, J.B. 1990, "Exploratory flow-duct experiments on combined-flow bed configurations, and some implications for interpreting storm-event stratification", *Journal of Sedimentary Research,* vol. 60, no. 2.

Ashley, G.M. 1990, "Classification of large-scale subaqueous bedforms: a new look at an old problem-SEPM bedforms and bedding structures", *Journal of Sedimentary Research,* vol. 60, no. 1.

Aubry, A. & Elliott, M. 2006, "The use of environmental integrative indicators to assess seabed disturbance in estuaries and coasts: application to the Humber Estuary, UK", *Marine pollution bulletin,* vol. 53, no. 1, pp. 175-185.

Baas, J.H. 1993, *Dimensional analysis of current ripples in recent and ancient depositional environments,* Faculteit Aardwetenschappen.

Baas, J.H. 1994, "A flume study on the development and equilibrium morphology of current ripples in very fine sand", *Sedimentology,* vol. 41, no. 2, pp. 185-209.

Baas, J.H. 1999, "An empirical model for the development and equilibrium morphology of current ripples in fine sand", *Sedimentology,* vol. 46, no. 1, pp. 123-138.

Baas, J.H. & Best, J.L. 2002, "Turbulence modulation in clay-rich sediment-laden flows and some implications for sediment deposition", *Journal of Sedimentary Research,* vol. 72, no. 3, pp. 336-340.

Baas, J.H. & Best, J.L. 2008, "The dynamics of turbulent, transitional and laminar clay-laden flow over a fixed current ripple", *Sedimentology,* vol. 55, no. 3, pp. 635-666.

Baas, J.H. & Best, J.B. 2009, "On the flow of natural clay suspensions over smooth and rough beds", *ERCOFTAC Bulletin,* vol. 78, pp. 32-37.

Baas, J.H., Best, J.L. & Peakall, J. 2011, "Depositional processes, bedform development and hybrid bed formation in rapidly decelerated cohesive (mud–sand) sediment flows", *Sedimentology,* vol. 58, no. 7, pp. 1953-1987.

Baas, J.H., Best, J.L. & Peakall, J. 2016, "Predicting bedforms and primary current stratification in cohesive mixtures of mud and sand", *Journal of the Geological Society,* vol. 173, no. 1, pp. 12-45.

Baas, J.H., Best, J.L., Peakall, J. & Wang, M. 2009, "A phase diagram for turbulent, transitional, and laminar clay suspension flows", *Journal of Sedimentary Research,* vol. 79, no. 4, pp. 162-183.

Baas, J.H., Davies, A.G. & Malarkey, J. 2013, "Bedform development in mixed sand–mud: The contrasting role of cohesive forces in flow and bed", *Geomorphology,* vol. 182, pp. 19-32.

Baas, J.H. & De Koning, H. 1995, "Washed-out ripples: their equilibrium dimensions, migration rate, and relation to suspended-sediment concentration in very fine sand", *Journal of Sedimentary Research,* vol. 65, no. 2.

Bagnold, R.A. & Taylor, G. 1946, "Motion of waves in shallow water. Interaction between waves and sand bottoms", *Proceedings of the Royal Society of London. Series A, Mathematical and Physical Sciences,* 185, pp. 1-18.

Bagnold, R.A. 1966, *An approach to the sediment transport problem from general physics,* US government printing office.

Bakker, W.T. & Van Doorn, T. 1978, "Near-bottom velocities in waves with a current" in *Coastal Engineering 1978*, pp. 1394-1413.

Banasiak, R. & Verhoeven, R. 2008, "Transport of sand and partly cohesive sediments in a circular pipe run partially full", *Journal of Hydraulic Engineering,* vol. 134, no. 2, pp. 216-224.

Bartholdy, J., Ernstsen, V.B., Flemming, B.W., Winter, C., Bartholoma, A. & Kroon, A. 2015, "On the formation of current ripples", *Scientific reports,* vol. 5, pp. 11390.

Bartzke, G., Bryan, K.R., Pilditch, C.A. & Huhn, K. 2013, "On the stabilizing influence of silt on sand beds", *Journal of Sedimentary Research,* vol. 83, no. 8, pp. 691-703.

Belorgey, M., Rajaona, R.D. & Sleath, F.A. 1993, "Flow regime and eddy structure into a boundary layer gerenated by the swell above a rippled bed", *The EUROMECH 310 Conference*Le Havre, France, 13-17 September, 1993.

Bennett, S. & Best, J. 1995, "Mean flow and turbulence structure over fixed, two-dimensional dunes: Implications for sediment transport and bedform stability", *Sedimentology,* vol. 42, no. 3, pp. 491-513.

Berg, J.H. 1987, "Bedform migration and bed-load transport in some rivers and tidal environments", *Sedimentology,* vol. 34, no. 4, pp. 681-698.

Best, J. 1992, "On the entrainment of sediment and initiation of bed defects: insights from recent developments within turbulent boundary layer research", *Sedimentology,* vol. 39, no. 5, pp. 797-811.

Best, J. 1993, "On the interactions between turbulent flow structure, sediment transport and bedform development: some considerations from recent experimental research", *Turbulence: Perspectives on Flow and sediment transport,* Wiley and Sons Ltd., Chichester, pp. 61-92.

Best, J. & Leeder, M. 1993, "Drag reduction in turbulent muddy seawater flows and some sedimentary consequences", *Sedimentology,* vol. 40, no. 6, pp. 1129-1137.

Best, J. 2005, "The fluid dynamics of river dunes: A review and some future research directions", *Journal of Geophysical Research: Earth Surface,* vol. 110, no. F4.

Bijker, E.W. 1967, "Some considerations about scales for coastal models with movable bed", *Delft Hydraulics Laboratory Publication 50*.

Black, K., Tolhurst, T., Paterson, D. & Hagerthey, S. 2002, "Working with natural cohesive sediments", *Journal of Hydraulic Engineering,* vol. 128, no. 1, pp. 2-8.

Block, M.E. 1994, *Wave generated flow over sand ripples and the resulting entrainment and suspension of sediment,* PhD edn, University of Wales, UK.

Blom, A., Ribberink, J.S. & de Vriend, H.J. 2003, "Vertical sorting in bed forms: Flume experiments with a natural and a trimodal sediment mixture", *Water Resources Research,* vol. 39, no. 2.

Boesch, D.F. 2002, "Challenges and opportunities for science in reducing nutrient over-enrichment of coastal ecosystems", *Estuaries and Coasts,* vol. 25, no. 4, pp. 886-900.

Bosman, J.J., van der Velden, Elsbeth TJM & Hulsbergen, C.H. 1987, "Sediment concentration measurement by transverse suction", *Coastal Engineering,* vol. 11, no. 4, pp. 353-370.

Boyes, S. & Elliott, M. 2006, "Organic matter and nutrient inputs to the Humber Estuary, England", *Marine pollution bulletin,* vol. 53, no. 1, pp. 136-143.

Brevik, I. & Bjørn, A. 1979, "Flume experiment on waves and currents. I. Rippled bed", *Coastal Engineering,* vol. 3, pp. 149-177.

Bridge, J.S. 1981, "Bed shear stress over subaqueous dunes, and the transition to upper-stage plane beds", *Sedimentology,* vol. 28, no. 1, pp. 33-36.

Bridge, J.S. 2009, *Rivers and floodplains: forms, processes, and sedimentary record,* John Wiley & Sons.

Bridge, J.S. & Best, J.L. 1988, "Flow, sediment transport and bedform dynamics over the transition from dunes to upper-stage plane beds: implications for the formation of planar laminae", *Sedimentology,* vol. 35, no. 5, pp. 753-763.

Carstens, M., Neilson, F. & Altinbilek, H. 1969, "Bed forms generated in the labora-tory under an oscillatory flow: analytical and ex-perimental study: US Coastal Eng", *Res.Ctr.Tech.Mem,* vol. 29, no. 39, pp. 208-222.

Chang, Y.S. & Hanes, D.M. 2004, "Suspended sediment and hydrodynamics above mildly sloped long wave ripples", *Journal of Geophysical Research: Oceans,* vol. 109, no. C7.

Christoffersen, J.B. & Jonsson, I.G. 1985, "Bed friction and dissipation in a combined current and wave motion", *Ocean Engineering,* vol. 12, no. 5, pp. 387-423.

Cizeau, P., Makse, H.A. & Stanley, H.E. 1999, "Mechanisms of granular spontaneous stratification and segregation in two-dimensional silos", *Physical Review E,* vol. 59.

Clifton, H.E. 1987, "Wave-formed sedimentary structures—a conceptual model", *Beach and Nearshore Sedimentation*, vol. 24.

Clifton, H.E. & Dingler, J.R. 1984, "Wave-formed structures and paleoenvironmental reconstruction", *Marine Geology,* vol. 60, no. 1-4, pp. 165-198.

Collins, M. 1990, "The behaviour of cohesive and non-cohesive sediments", *Proc. Int. Seminar Environment. Asp. Dredging Act. Port Autonome de Nantes Saint-Nazaire, Nantes*, pp. 15.

Coumou, D. & Rahmstorf, S. 2012, "A decade of weather extremes", *Nature climate change,* vol. 2, no. 7, pp. 491-496.

Crossland, C.J., Baird, D., Ducrotoy, J., Lindeboom, H., Buddemeier, R.W., Dennison, W.C., Maxwell, B.A., Smith, S.V. & Swaney, D.P. 2005, "The coastal zone—a domain of global interactions" in *Coastal Fluxes in the Anthropocene* Springer, , pp. 1-37.

Davidson, N., Laffoley, D.d., Doody, J., Way, L., Gordon, J., Key, R.e., Drake, C., Pienkowski, M., Mitchell, R. & Duff, K. 1991, "Nature conservation and estuaries in Great Britain", *Nature Conservancy Council, Peterborough*, pp. 1-76.

Davies, A., Soulsby, R. & King, H. 1988, "A numerical model of the combined wave and current bottom boundary layer", *Journal of Geophysical Research: Oceans,* vol. 93, no. C1, pp. 491-508.

Davies, A. & Thorne, P. 2005, "Modeling and measurement of sediment transport by waves in the vortex ripple regime", *Journal of Geophysical Research: Oceans,* vol. 110, no. C5.

Davies, A. & Villaret, C. 1997, "Oscillatory flow over rippled beds: Boundary layer structure and wave-induced Eulerian drift", *INTERNATIONAL SERIES ON ADVANCES IN FLUID MECHANICS,* vol. 10, pp. 215-254.

DETR, 2002. “Transport Statistics: Maritime Statistics: United Kingdom”. *Provisional Ports Statistics for the United Kingdom:2001 Data Statistical release*.

Doucette, J. & O'DONOGHUE, T. 2006, "Response of sand ripples to change in oscillatory flow", *Sedimentology,* vol. 53, no. 3, pp. 581-596.

Downing, A., Thorne, P.D. & Vincent, C.E. 1995, "Backscattering from a suspension in the near field of a piston transducer", *The Journal of the Acoustical Society of America,* vol. 97, no. 3, pp. 1614-1620.

Downing, J. 2006, "Twenty-five years with OBS sensors: The good, the bad, and the ugly", *Continental Shelf Research,* vol. 26, no. 17, pp. 2299-2318.

Du Toit, C. & Sleath, J. 1981, "Velocity measurements close to rippled beds in oscillatory flow", *Journal of Fluid Mechanics,* vol. 112, pp. 71-96.

Dubois, M., Gilles, K., Hamilton, J., Roberts, P. & Smith, F. 1956, "Phenol sulphuric acid method for carbohydrate determination", *Ann.Chem,* vol. 28, pp. 350-359.

Dugan, P.J., Barlow, C., Agostinho, A.A., Baran, E., Cada, G.F., Chen, D., Cowx, I.G., Ferguson, J.W., Jutagate, T. & Mallen-Cooper, M. 2010, "Fish migration, dams, and loss of ecosystem services in the Mekong basin", *AMBIO: A Journal of the Human Environment,* vol. 39, no. 4, pp. 344-348.

Dumas, S., Arnott, R. & Southard, J.B. 2005, "Experiments on oscillatory-flow and combined-flow bed forms: implications for interpreting parts of the shallow-marine sedimentary record", *Journal of Sedimentary research,* vol. 75, no. 3, pp. 501-513.

Dyer, K. 1986, "Coastal and estuarine sediment dynamics", John Wiley, New York, 342 pp.

Earnshaw, H., Bruce, T., Greated, C. & Easson, W. 1995, "PIV Measurements of Oscillatory Flow Over a Rippled Bed." in *Coastal Engineering 1994*, pp. 1975-1982.

Edwards, A. & Winn, P. 2006, "The Humber Estuary, Eastern England: Strategic planning of flood defences and habitats", *Marine pollution bulletin,* vol. 53, no. 1, pp. 165-174.

Fairweather P.G. and Quinn G.P., 1993. "Seascape ecology: the importance of linkages". In: Battershill C.B., Schiel D.R., Jones G.P., Cresse R.G., MacDiarmid A.B. (eds), Proceeding of the second international temperate reef symposium, January 7-10, 1992, Auckland, NIWA Marine, Wellington, p77-83.

Faraci, C. & Foti, E. 2002, "Geometry, migration and evolution of small-scale bedforms generated by regular and irregular waves", *Coastal Engineering,* vol. 47, no. 1, pp. 35-52.

FARO Technologies, 2013. FARO Laser Scanner Focus3D X 330 Manual, FARO Technologies Inc., Lake Mary, Florida.

Fredsøe, J. 1984, "Turbulent boundary layer in wave-current motion", *Journal of Hydraulic Engineering,* vol. 110, no. 8, pp. 1103-1120.

Fredsøe, J., Andersen, K.H. & Sumer, B.M. 1999, "Wave plus current over a ripple-covered bed", *Coastal Engineering,* vol. 38, no. 4, pp. 177-221.

Frostick, L.E. & McCave, I.N. 1979, "Seasonal shifts of sediment within an estuary mediated by algal growth", *Estuarine and Coastal Marine Science,* vol. 9, no. 5, pp. 569-576.

Gillott, J. 1987, "Clay in engineering geology: Developments in geotechnical Engineering", Elsevier Science, Amsterdam.

Glenn, S.M. & Grant, W.D. 1987, "A suspended sediment stratification correction for combined wave and current flows", *Journal of Geophysical Research: Oceans,* vol. 92, no. C8, pp. 8244-8264.

Goring, D.G. & Nikora, V.I. 2002, "Despiking acoustic Doppler velocimeter data", *Journal of Hydraulic Engineering,* vol. 128, no. 1, pp. 117-126.

Goswami, B.N., Venugopal, V., Sengupta, D., Madhusoodanan, M.S. & Xavier, P.K. 2006, "Increasing trend of extreme rain events over India in a warming environment", *Science (New York, N.Y.),* vol. 314, no. 5804, pp. 1442-1445.

Grabowski, R.C., Droppo, I.G. & Wharton, G. 2011, "Erodibility of cohesive sediment: the importance of sediment properties", *Earth-Science Reviews,* vol. 105, no. 3, pp. 101-120.

Grant, W.D. & Madsen, O.S. 1979, "Combined wave and current interaction with a rough bottom", *Journal of Geophysical Research: Oceans,* vol. 84, no. C4, pp. 1797-1808.

Grant, W.D. & Madsen, O.S. 1982, "Movable bed roughness in unsteady oscillatory flow", *Journal of Geophysical Research: Oceans,* vol. 87, no. C1, pp. 469-481.

Grant, W.D. & Madsen, O.S. 1986, "The continental-shelf bottom boundary layer", *Annual Review of Fluid Mechanics,* vol. 18, no. 1, pp. 265-305.

Grasmeijer, B. & Kleinhans, M. 2004, "Observed and predicted bed forms and their effect on suspended sand concentrations", *Coastal Engineering,* vol. 51, no. 5, pp. 351-371.

Grass, A. 1981, *Sediment transport by waves and currents,* University College, London, Dept. of Civil Engineering.

Gray, M. 1995, "The coastal fisheries of England and Wales, Part III: A review of their status 1992-1994", *Fisheries Research Technical Report,* no. 100*,* Ministry of Agriculture, Fisheries & Food, Directorate of Fisheries Research*,* Lowestoft.

Green, M.O. & Black, K.P. 1999, "Suspended-sediment reference concentration under waves: field observations and critical analysis of two predictive models", *Coastal Engineering,* vol. 38, no. 3, pp. 115-141.

Green, M., Vincent, C.E., McCave, I., Dickson, R., Rees, J. & Pearsons, N. 1995, "Storm sediment transport: observations from the British North Sea shelf", *Continental Shelf Research,* vol. 15, no. 8, pp. 889-912.

Grissinger, E., Little, W. & Murphey, J. 1981, "Erodibility of streambank materials of low cohesion", *Transactions of the ASAE,* vol. 24, no. 3, pp. 624-0630.

Grotzinger, J.P., Arvidson, R., Bell, J., Calvin, W., Clark, B., Fike, D., Golombek, M., Greeley, R., Haldemann, A. & Herkenhoff, K. 2005, "Stratigraphy and sedimentology of a dry to wet eolian depositional system, Burns formation, Meridiani Planum, Mars", *Earth and Planetary Science Letters,* vol. 240, no. 1, pp. 11-72.

Gust, G. 1976, "Observations on turbulent-drag reduction in a dilute suspension of clay in sea-water", *Journal of Fluid Mechanics,* vol. 75, no. 1, pp. 29-47.

Gust, G. & Walger, E. 1976, "The influence of suspended cohesive sediments on boundary-layer structure and erosive activity of turbulent seawater flow", *Marine Geology,* vol. 22, no. 3, pp. 189-206.

Guy, H.P., Simons, D.B. & Richardson, E.V. 1966, *Summary of alluvial channel data from flume experiments, 1956-61,* US Government Printing Office.

Hammond, T. & Collins, M. 1979, "On the threshold of transport of sand-sized sediment under the combined influence of unidirectional and oscillatory flow", *Sedimentology,* vol. 26, no. 6, pp. 795-812.

Hanes, D.M., Alymov, V., Chang, Y.S. & Jette, C. 2001, "Wave-formed sand ripples at Duck, North Carolina", *Journal of Geophysical Research: Oceans,* vol. 106, no. C10, pp. 22575-22592.

Hansen, D.V. & Rattray, M. 1966, "New dimensions in estuary classification", *Limnology and Oceanography,* vol. 11, no. 3, pp. 319-326.

Hardisty, J. & Rouse, H. 1996, "The Humber Observatory: monitoring, modelling and management for the coastal environment", *Journal of Coastal Research,* vol. 12, pp. 683-690.

Hardy, R.J., Lane, S.N., Ferguson, R.I. & Parsons, D.R. 2007, "Emergence of coherent flow structures over a gravel surface: A numerical experiment", *Water Resources Research,* vol. 43, no. 3.

Harms, J. 1969, "Hydraulic significance of some sand ripples", *Geological Society of America Bulletin,* vol. 80, no. 3, pp. 363-396.

Harms, J. 1979, "Primary sedimentary structures", *Annual Review of Earth and Planetary Sciences,* vol. 7, no. 1, pp. 227-248.

Hay, A.E. & Wilson, D.J. 1994, "Rotary sidescan images of nearshore bedform evolution during a storm", *Marine Geology,* vol. 119, no. 1-2, pp. 57-65.

Healy, T., Wang, Y. & Healy, J. 2002, *Muddy coasts of the world: processes, deposits and function,* Gulf Professional Publishing.

Horikawa, K. & Mizutani, S. 1993, "Oscillatory Flow Behavior in the Vicinity of Ripple Models" in *Coastal Engineering 1992*, pp. 2122-2135.

Horowitz, A.J. 1991, *Primer on sediment-trace element chemistry,* Lewis Publishers.

Horowitz, A.J. 2008, "Determining annual suspended sediment and sediment-associated trace element and nutrient fluxes", *Science of the Total Environment,* vol. 400, no. 1, pp. 315-343.

Hussain, Abul Khair Muhammad Fazle & Reynolds, W.C. 1970, "The mechanics of an organized wave in turbulent shear flow", *Journal of Fluid Mechanics,* vol. 41, no. 2, pp. 241-258.

IECS, 1987. *The Humber Estuary Environmental Background*. The Institute of Estuarine and Coastal Studies, University of Hull, Hull, UK.

Ikeda, S., Horikawa, K., Nakamura, H. & Noguchi, K. 1991, "Oscillatory boundary layer over a sand ripple model", *Coastal Eng in Japan,* vol. 32, pp. 15-29.

Inman, D.L. 1957, "Wave-generated ripples in nearshore sands*", U.S. Army Corps Engineers Beach Erosion Board Tech.* vol. 100, pp. 42.

Inmann, D. & Bowen, A. 1963, "Flume experiments on sand transport by waves and current", *Proc.8th ICCE,* Mexico City , pp. 137-150.

Jacobs, W., Le Hir, P., Van Kesteren, W. & Cann, P. 2011, "Erosion threshold of sand–mud mixtures", *Continental Shelf Research,* vol. 31, no. 10, pp. S14-S25.

Jarvie, H.P., Neal, C. & Robson, A.J. 1997, "The geography of the Humber catchment", *Science of the Total Environment,* vol. 194, pp. 87-99.

Jarvie, H.P., Neal, C., Tappin, A.D., Burton, J., Harrow, M., Hill, L. & Neal, M. 2000, "The water quality of the River Trent: from the lower non-tidal reaches to the freshwater tidal zone", *Science of the total environment,* vol. 251, pp. 335-367.

Jensen, B., Sumer, B. & Fredsøe, J. 1989, "Turbulent oscillatory boundary layers at high Reynolds numbers", *Journal of Fluid Mechanics,* vol. 206, pp. 265-297.

Jonsson, I.G. 1980, "A new approach to oscillatory rough turbulent boundary layers", *Ocean Engineering,* vol. 7, no. 1, pp. 109-152.

Jonsson, I.G. & Carlsen, N.A. 1976, "Experimental and theoretical investigations in an oscillatory turbulent boundary layer", *Journal of Hydraulic Research,* vol. 14, no. 1, pp. 45-60.

Jopling, A.V. & Forbes, D.L. 1979, "Flume study of silt transportation and deposition", *Geografiska Annaler.Series A.Physical Geography*, Vol. 61, pp. 67-85.

Jordan, T.E., Correll, D.L. & Weller, D.E. 1997, "Effects of agriculture on discharges of nutrients from coastal plain watersheds of Chesapeake Bay", *Journal of environmental quality,* vol. 26, no. 3, pp. 836-848.

Jørgensen, B.B. & Boetius, A. 2007, "Feast and famine--microbial life in the deep-sea bed", *Nature reviews.Microbiology,* vol. 5, no. 10, pp. 770.

Kalf, P. 2013, *Winnowing: Sub-surface entrainment of particles*, Master Dissertation edn, Delft University of Technology, Delft, Netherland.

Kemp, P. & Simons, R. 1982, "The interaction between waves and a turbulent current: waves propagating with the current", *Journal of Fluid Mechanics,* vol. 116, pp. 227-250.

Klaassen, G. 1990, "Sediment transport in armoured rivers during floods- a literature survey"*, Research Report Q790, Delft Hydraulics*.

Kleinhans, M. 2004, "Sorting in grain flows at the lee side of dunes", *Earth-Science Reviews,* vol. 65, no. 1, pp. 75-102.

Kleinhans, M. 2005, "Phase diagrams of bed states in steady, unsteady, oscillatory and mixed flows", in: Van Rijn, L.C.; Soulsby, R.L.; Hoekstra, P.; Davies, A. (Eds.), *Sandpit project*, Aqua Publication, Amsterdam, Netehrlands, pp. Q1-Q16.

Komar, P.D. 1974, "Oscillatory ripple marks and the evaluation of ancient wave conditions and environments", *Journal of Sedimentary Research,* vol. 44, no. 1.

Krone, R.B. 1963, "A study of rheologic properties of estuarial sediments"*, U.S. Army Corps Engineers,* Tidal Hydraul, Vicksburg, no.7.

Kummu, M. & Varis, O. 2007, "Sediment-related impacts due to upstream reservoir trapping, the Lower Mekong River", *Geomorphology,* vol. 85, no. 3, pp. 275-293.

Lamb, M.P., D'Asaro, E. & Parsons, J.D. 2004, "Turbulent structure of high-density suspensions formed under waves", *Journal of Geophysical Research: Oceans,* vol. 109, no. C12.

Lamb, M.P., Grotzinger, J.P., Southard, J.B. & Tosca, N.J. 2012, "Were aqueous ripples on Mars formed by flowing brines", *Sedimentary geology of Mars: SEPM (Society for Sedimentary Geology) Special Publication,* vol. 102, pp. 139-150.

Lamb, M.P. & Parsons, J.D. 2005, "High-density suspensions formed under waves", *Journal of Sedimentary Research,* vol. 75, no. 3, pp. 386-397.

Lapotre, M.G., Lamb, M.P. & McElroy, B. 2017, "What sets the size of current ripples?", *Geology,* vol. 45, no. 3, pp. 243-246.

Le Hir, P., Cann, P., Waeles, B., Jestin, H. & Bassoullet, P. 2008, "Erodibility of natural sediments: experiments on sand/mud mixtures from laboratory and field erosion tests", *Proceedings in Marine Science,* vol. 9, pp. 137-153.

Le Hir, P., Cayocca, F. & Waeles, B. 2011, "Dynamics of sand and mud mixtures: a multiprocess-based modelling strategy", *Continental Shelf Research,* vol. 31, no. 10, pp. S135-S149.

Lee, T. & Hanes, D. 1996, "Comparison of field observations of the vertical distribution of suspended sand and its prediction by models", *Journal of Geophysical Research: Oceans,* vol. 101, no. C2, pp. 3561-3572.

Leeder, M. 1983, "On the interactions between turbulent flow, sediment transport and bedform mechanics in channelized flows", *Modern and ancient fluvial systems,* vol. 6, pp. 5-18.

Leeder, M. 2011, *Sedimentology and sedimentary basins from turbulence to tectonics,* 2nd edn, Wiley-Backwell, Noida.

Li, M.Z. 2000, "Boundary layer dynamics and drag reduction in flows of high cohesive sediment suspensions", *Sedimentology,* vol. 47, no. 1, pp. 71-86.

Li, M. & O'CONNOR, B.A. 2007, "Numerical study of sediment transport above rippled beds under the action of combined waves and currents", *Sedimentology,* vol. 54, no. 6, pp. 1345-1363.

Liang, H., Lamb, M.P. & Parsons, J.D. 2007, "Formation of a sandy near-bed transport layer from a fine-grained bed under oscillatory flow", *Journal of Geophysical Research: Oceans,* vol. 112, no. C2.

Libicki, C., Bedford, K.W. & Lynch, J.F. 1989, "The interpretation and evaluation of a 3-MHz acoustic backscatter device for measuring benthic boundary layer sediment dynamics", *The Journal of the Acoustical Society of America,* vol. 85, no. 4, pp. 1501-1511.

Lindholm, R.C. 1987, "Mineral identification using X-ray diffraction" in *A Practical Approach to Sedimentology* Springer, Allen & Unwin, London, pp. 124-153.

Longuet, M.S. 1953, "Mass transport in water waves", *Philosophical Transactions of the Royal Society of London A: Mathematical, Physical and Engineering Sciences,* vol. 245, no. 903, pp. 535-581.

Lofquist, K.E. 1978, “Sand ripple growth in an oscillatory-flow water tunnel”, *U.S. Army Corps Engineers, Coastal Engineering Research*, Vol. 78-5, pp. 101.

Lowe, D.R. 1988, "Suspended-load fallout rate as an independent variable in the analysis of current structures", *Sedimentology,* vol. 35, no. 5, pp. 765-776.

Lundkvist, M., Grue, M., Friend, P. & Flindt, M. 2007, "The relative contributions of physical and microbiological factors to cohesive sediment stability", *Continental Shelf Research,* vol. 27, no. 8, pp. 1143-1152.

Maddux, T.B., Cowen, E.A., Foster, D.L., Haller, M.C. & Stanton, T.P. 2006, "The Cross-shore sediment transport experiment (CROSSTEX)", *COASTAL ENGINEERING CONFERENCE*ASCE AMERICAN SOCIETY OF CIVIL ENGINEERS, , pp. 2547.

Marieu, V., Bonneton, P., Foster, D. & Ardhuin, F. 2008, "Modeling of vortex ripple morphodynamics", *Journal of Geophysical Research: Oceans,* vol. 113, no. C9.

Mark, C.F. 2009, *A semi-analytical model for form drag of river bedforms,* University of Twente.

Mathisen, P.P. & Madsen, O.S. 1996, "Waves and currents over a fixed rippled bed: 1. Bottom roughness experienced by waves in the presence and absence of currents", *Journal of Geophysical Research: Oceans,* vol. 101, no. C7, pp. 16533-16542.

McCrone, A.W. 1963, "Paleontology and biostratigraphy of the Red Eagle cyclothem (Lower Permian) in Kansas.", *Kansas Geology Survey Bulletins,* vol. 164, pp. 114.

McLean, S. & Smith, J.D. 1986, "A model for flow over two-dimensional bed forms", *Journal of Hydraulic Engineering,* vol. 112, no. 4, pp. 300-317.

McLean, S., Wolfe, S. & Nelson, J. 1999, "Predicting boundary shear stress and sediment transport over bed forms", *Journal of Hydraulic Engineering,* vol. 125, no. 7, pp. 725-736.

McLean, S.R. 1990, "The stability of ripples and dunes", *Earth-Science Reviews,* vol. 29, no. 1-4, pp. 131-144.

McLean, S.R. & Smith, J.D. 1979, "Turbulence measurements in the boundary layer over a sand wave field", *Journal of Geophysical Research: Oceans,* vol. 84, no. C12, pp. 7791-7808.

McLelland, S.J. & Nicholas, A.P. 2000, "A new method for evaluating errors in high-frequency ADV measurements", *Hydrological Processes,* vol. 14, no. 2, pp. 351-366.

Meehl, G.A. & Tebaldi, C. 2004, "More intense, more frequent, and longer lasting heat waves in the 21st century", *Science (New York, N.Y.),* vol. 305, no. 5686, pp. 994-997.

Meehl, G.A., Washington, W.M., Collins, W.D., Arblaster, J.M., Hu, A., Buja, L.E., Strand, W.G. & Teng, H. 2005, "How much more global warming and sea level rise?", *Science (New York, N.Y.),* vol. 307, no. 5716, pp. 1769-1772.

Mehta, A. & Dyer, K. 1990, "Cohesive sediment transport in estuarine and coastal waters", *The sea,* vol. 9, no. Part B, pp. 815-839.

Meinshausen, M., Meinshausen, N., Hare, W., Raper, S.C., Frieler, K., Knutti, R., Frame, D.J. & Allen, M.R. 2009, "Greenhouse-gas emission targets for limiting global warming to 2 C", *Nature,* vol. 458, no. 7242, pp. 1158-1162.

Mie, G. 1908, "Beiträge zur Optik trüber Medien, speziell kolloidaler Metallösungen", *Annalen der physik,* vol. 330, no. 3, pp. 377-445.

Miller, M.C. & Komar, P.D. 1980, "Oscillation sand ripples generated by laboratory apparatus", *Journal of Sedimentary Research,* vol. 50, no. 1.

Mitchener, H. & Torfs, H. 1996, "Erosion of mud/sand mixtures", *Coastal Engineering,* vol. 29, no. 1-2, pp. 1-25.

Mogridge, G., Davies, M. & Willis, D. 1994, "Geometry prediction for wave-generated bedforms", *Coastal Engineering,* vol. 22, no. 3-4, pp. 255-286.

Mortimer, R., Krom, M., Watson, P., Frickers, P., Davey, J. & Clifton, R. 1999, "Sediment–water exchange of nutrients in the intertidal zone of the Humber Estuary, UK", *Marine pollution bulletin,* vol. 37, no. 3, pp. 261-279.

Myrhaug, D. 1989, "A rational approach to wave friction coefficients for rough, smooth and transitional turbulent flow", *Coastal Engineering,* vol. 13, no. 1, pp. 11-21.

Myrhaug, D. & Slaattelid, O.H. 1990, "A rational approach to wave-current friction coefficients for rough, smooth and transitional turbulent flow", *Coastal Engineering,* vol. 14, no. 3, pp. 265-293.

Myrow, P.M. & Southard, J.B. 1991, "Combined-flow model for vertical stratification sequences in shallow marine storm-deposited beds", *Journal of Sedimentary Research,* vol. 61, no. 2.

Nakato, T., Kennedy, J.F., Glover, J.R. & Locher, F.A. 1977, "Wave entrainment of sediment from rippled beds", *Journal of the Waterway, Port, Coastal and Ocean Division,* vol. 103, no. 1, pp. 83-99.

Nalluri, C. & Alvarez, E. 1992, "The influence of cohesion on sediment behaviour", *Water science and technology,* vol. 25, no. 8, pp. 151-164.

Nelson, J.M., Shreve, R.L., McLean, S.R. & Drake, T.G. 1995, "Role of near-bed turbulence structure in bed load transport and bed form mechanics", *Water Resources Research,* vol. 31, no. 8, pp. 2071-2086.

Nelson, J.M. & Smith, J.D. 1989, "Mechanics of flow over ripples and dunes", *Journal of Geophysical Research: Oceans,* vol. 94, no. C6, pp. 8146-8162.

Nelson, T.R., Voulgaris, G. & Traykovski, P. 2013, "Predicting wave-induced ripple equilibrium geometry", *Journal of Geophysical Research: Oceans,* vol. 118, no. 6, pp. 3202-3220.

Nicholls, R.J. & Cazenave, A. 2010, "Sea-level rise and its impact on coastal zones", *Science (New York, N.Y.),* vol. 328, no. 5985, pp. 1517-1520.

Nield, J.M., King, J. & Jacobs, B. 2014, "Detecting surface moisture in aeolian environments using terrestrial laser scanning", Aeolian Research, vol. 12, pp. 9-17.

Nielsen, P. 1981, "Dynamics and geometry of wave-generated ripples", *Journal of Geophysical Research: Oceans,* vol. 86, no. C7, pp. 6467-6472.

Nielsen, P. 1986, "Suspended sediment concentrations under waves", *Coastal Engineering,* vol. 10, no. 1, pp. 23-31.

Nielsen, P. 2002, "Shear stress and sediment transport calculations for swash zone modelling", *Coastal Engineering,* vol. 45, no. 1, pp. 53-60.

NRA. 1993, The water quality of the Humber Estuary 1989–1990.

O'donoghue, T., Doucette, J., van der Werf, Jebbe J & Ribberink, J.S. 2006, "The dimensions of sand ripples in full-scale oscillatory flows", *Coastal Engineering,* vol. 53, no. 12, pp. 997-1012.

O'Donoghue, T. & Clubb, G.S. 2001, "Sand ripples generated by regular oscillatory flow", *Coastal Engineering,* vol. 44, no. 2, pp. 101-115.

O'Hara Murray, R., Thorne, P. & Hodgson, D. 2011, "Intrawave observations of sediment entrainment processes above sand ripples under irregular waves", *Journal of Geophysical Research: Oceans,* vol. 116, no. C1.

Ojha, S.P. & Mazumder, B. 2010, "Turbulence characteristics of flow over a series of 2-D bed forms in the presence of surface waves", *Journal of Geophysical Research: Earth Surface,* vol. 115, no. F4.

Panagiotopoulos, I., Voulgaris, G. & Collins, M. 1997, "The influence of clay on the threshold of movement of fine sandy beds", *Coastal Engineering,* vol. 32, no. 1, pp. 19-43.

Papanicolaou, A., Diplas, P., Dancey, C. & Balakrishnan, M. 2001, "Surface roughness effects in near-bed turbulence: Implications to sediment entrainment", *Journal of Engineering Mechanics,* vol. 127, no. 3, pp. 211-218.

Paterson, D., Tolhurst, T., Kelly, J., Honeywill, C., De Deckere, E., Huet, V., Shayler, S., Black, K., De Brouwer, J. & Davidson, I. 2000, "Variations in sediment properties, Skeffling mudflat, Humber Estuary, UK", *Continental Shelf Research,* vol. 20, no. 10, pp. 1373-1396.

Pedocchi, F. & Garcia, M. 2009a, "Ripple morphology under oscillatory flow: 1. Prediction", *Journal of Geophysical Research: Oceans,* vol. 114, no. C12.

Pedocchi, F. & Garcia, M. 2009b, "Friction coefficient for oscillatory flow: the rough–smooth turbulent transition", *Journal of Hydraulic Research,* vol. 47, no. 4, pp. 438-444.

Perillo, M. 2013, *Flow, sediment transport and bedforms under combined flows,* PhD edn, University of Illinois, Urbana, USA.

Perillo, M.M., Best, J.L. & Garcia, M.H. 2014a, "A new phase diagram for combined-flow bedforms", *Journal of Sedimentary Research,* vol. 84, no. 4, pp. 301-313.

Perillo, M.M., Best, J.L., Yokokawa, M., Sekiguchi, T., Takagawa, T. & Garcia, M.H. 2014b, "A unified model for bedform development and equilibrium under unidirectional, oscillatory and combined-flows", *Sedimentology,* vol. 61, no. 7, pp. 2063-2085.

Pye, K. 1994, “Sediment transport and depositional processes”, *Basin Research*, Vol. 6, no. 2-3, pp. 179-180.

Ranasoma, K.M. & Sleath, J. 1993, "Velocity measurements close to rippled beds" in *Coastal Engineering 1992*, pp. 2383-2396.

Ranasoma, K.I.M. 1993, *Measurements in combined oscillatory and steady flow over rippled beds.* PhD edn, University of Cambridge, Cambridge, UK.

Raudkivi, A. 1963, "Study of sediment ripple formation", *Journal of the Hydraulics Division,* vol. 89, no. 6, pp. 15-34.

Ravisangar, V., Sturm, T. & Amirtharajah, A. 2005, "Influence of sediment structure on erosional strength and density of kaolinite sediment beds", *Journal of Hydraulic Engineering,* vol. 131, no. 5, pp. 356-365.

Reineck, H. & Singh, I.B. 2012, *Depositional sedimentary environments: with reference to terrigenous clastics,* Springer Science & Business Media.

Ribberink, J.S. & Al-Salem, A.A. 1995, "Sheet flow and suspension of sand in oscillatory boundary layers", *Coastal Engineering,* vol. 25, no. 3-4, pp. 205-225.

Richard Whitehouse 2000, *Dynamics of Estuarine Muds: A Manual for Practical Applications,* Thomas Telford.

Righetti, M. & Lucarelli, C. 2007, "May the Shields theory be extended to cohesive and adhesive benthic sediments?", *Journal of Geophysical Research: Oceans,* vol. 112, no. C5.

Rosenzweig, C., Iglesias, A., Yang, X., Epstein, P.R. & Chivian, E. 2001, "Climate change and extreme weather events; implications for food production, plant diseases, and pests", *Global change & human health,* vol. 2, no. 2, pp. 90-104.

Ross, D.A. 2012, *Opportunities and uses of the ocean,* Springer Science & Business Media.

Sandbach, S., Lane, S., Hardy, R., Amsler, M., Ashworth, P., Best, J., Nicholas, A., Orfeo, O., Parsons, D. & Reesink, A. 2012, "Application of a roughness-length representation to parameterize energy loss in 3-D numerical simulations of large rivers", *Water Resources Research,* vol. 48, no. 12.

Sato, S. 1987, *Oscillatory boundary layer flow and sand movement over ripples*, PhD edn, University of Tokyo, Japan.

Sato, S., Mimura, N. & Watanabe, A. 1984, "Oscillatory boundary layer flow over rippled beds", *19th Coastal Eng. Congress*Houston, USA, 1984.

Sato, S., Mimura, N. & Watanabe, A. 1985, "Oscillatory boundary layer flow over rippled beds" in *Coastal Engineering 1984*, pp. 2293-2309.

Sawamoto, M. 1991, "The structure of oscillatory turbulent boundary layer over rough bed", *Coastal Eng.in Japan, JSCE,* vol. 34, no. 1, pp. 1-14.

Schindler, R.J., Parsons, D.R., Ye, L., Hope, J.A., Baas, J.H., Peakall, J., Manning, A.J., Aspden, R.J., Malarkey, J. & Simmons, S. 2015, "Sticky stuff: Redefining bedform prediction in modern and ancient environments", *Geology,* vol. 43, no. 5, pp. 399-402.

Schretlen, J.J., Ribberink, J.S. & O'Donoghue, T. 2009, "Sand transport under full-scale surface waves" in *Proceedings of Coastal Dynamics 2009: Impacts of Human*

Activities on Dynamic Coastal Processes (With CD-ROM) World Scientific, Tokyo, pp. 1-13.

Schwartz, R.K. 1982, "Bedform and stratification characteristics of some modern small-scale washover sand bodies", *Sedimentology,* vol. 29, no. 6, pp. 835-849.

Sekiguchi, T. & Yokokawa, M. 2008, "Effect of wave period on combined-flow bedforms: a flume experiment", *Proceedings of Third International Workshop on Marine and River Dune Dynamics*, pp. 281.

Sheng, Y.P. & Villaret, C. 1989, "Modeling the effect of suspended sediment stratification on bottom exchange processes", *Journal of Geophysical Research: Oceans,* vol. 94, no. C10, pp. 14429-14444.

Siakeu, J., Oguchi, T., Aoki, T., Esaki, Y. & Jarvie, H.P. 2004, "Change in riverine suspended sediment concentration in central Japan in response to late 20th century human activities", *Catena,* vol. 55, no. 2, pp. 231-254.

Simons, D.B. & Richardson, E.V. 1961, "Forms of bed roughness in alluvial channel", *Journal of the Hydraulics Division,* vol. 87, no. 3, pp. 87-105.

Sleath, J. 1987, "Turbulent oscillatory flow over rough beds", *Journal of Fluid Mechanics,* vol. 182, pp. 369-409.

Sleath, J.F. 1991, "Velocities and shear stresses in wave-current flows", *Journal of Geophysical Research: Oceans,* vol. 96, no. C8, pp. 15237-15244.

Son, H. & Andre, T. 1991, "A numerical model of the rough turbulent boundary layer in combined wave and current interaction" in *Coastal Engineering 1990*, pp. 853-866.

Soulsby, R. 1987, "Calculating bottom orbital velocity beneath waves", *Coastal Engineering,* vol. 11, no. 4, pp. 371-380.

Soulsby, R. 1997, *Dynamics of marine sands: a manual for practical applications,* Thomas Telford.

Soulsby, R. & Davies, A. 1995, "Bed shear-stresses due to combined waves and currents" in *Advances in coastal morphodynamics* Delft Hydraulics Delft, , pp. 4-23.

Soulsby, R., Hamm, L., Klopman, G., Myrhaug, D., Simons, R. & Thomas, G. 1993, "Wave-current interaction within and outside the bottom boundary layer", *Coastal Engineering,* vol. 21, no. 1-3, pp. 41-69.

Soulsby, R.L. & Whitehouse, R.J. 2005, "Prediction of ripple properties in shelf seas-Mark 2 predictor for time evolution", *HR Wallinford Report TR*, pp.154.

Southard, J. & Harms, J. 1972, "Sequence of bedform and stratification in silts, based on flume experiments", *AAPG Bulletin,* vol. 56, no. 3, pp. 654-655.

Southard, J.B. 1991, "Experimental determination of bed-form stability", *Annual Review of Earth and Planetary Sciences,* vol. 19, no. 1, pp. 423-455.

Southard, J.B. & Boguchwal, L.A. 1990, "Bed configurations in steady unidirectional water flows. Part 2. Synthesis of flume data", *Journal of Sedimentary Research,* vol. 60, no. 5.

Southard, J.B., Lambie, J.M., Federico, D.C., Pile, H.T. & Weidman, C.R. 1990, "Experiments on bed configurations in fine sands under bidirectional purely oscillatory flow, and the origin of hummocky cross-stratification", *Journal of Sedimentary Research,* vol. 60, no. 1.

Styles, R. & Glenn, S.M. 2002, "Modeling bottom roughness in the presence of wave-generated ripples", *Journal of Geophysical Research: Oceans,* vol. 107, no. C8.

Sutherland, I.W. 1998, "Novel and established applications of microbial polysaccharides", *Trends in biotechnology,* vol. 16, no. 1, pp. 41-46.

Swart, D.H. 1974, *Offshore sediment transport and equilibrium beach profiles,* PhD edn, Delft University of Technology, Delft, Netherland.

Syvitski, J.P., Vorosmarty, C.J., Kettner, A.J. & Green, P. 2005, "Impact of humans on the flux of terrestrial sediment to the global coastal ocean", *Science (New York, N.Y.),* vol. 308, no. 5720, pp. 376-380.

Tanner, W.F. 1967, "Ripple mark indices and their uses", *Sedimentology,* vol. 9, no. 2, pp. 89-104.

Thorne, P.D. & Hanes, D.M. 2002, "A review of acoustic measurement of small-scale sediment processes", *Continental Shelf Research,* vol. 22, no. 4, pp. 603-632.

Thorne, P.D., Williams, J.J. & Davies, A.G. 2002, "Suspended sediments under waves measured in a large-scale flume facility", *Journal of Geophysical Research: Oceans,* vol. 107, no. C8.

Tolhurst, T., Gust, G. & Paterson, D. 2002, "The influence of an extracellular polymeric substance (EPS) on cohesive sediment stability", *Proceedings in Marine Science,* vol. 5, pp. 409-425.

Torfs, H., Huygens, M. & Tito, L. 1994, "Influence of the cross-section on the erosion criteria for partly cohesive sediments", *Water Science and Technology,* vol. 29, no. 1-2, pp. 103-111.

Traykovski, P. 2007, "Observations of wave orbital scale ripples and a nonequilibrium time-dependent model", *Journal of Geophysical Research: Oceans,* vol. 112, no. C6.

Tunstall, E.B. & Inman, D.L. 1975, "Vortex generation by oscillatory flow over rippled surfaces", *Journal of Geophysical Research,* vol. 80, no. 24, pp. 3475-3484.

Tyler, A., Svab, E., Preston, T., Présing, M. & Kovács, W. 2006, "Remote sensing of the water quality of shallow lakes: A mixture modelling approach to quantifying phytoplankton in water characterized by high-suspended sediment", *International Journal of Remote Sensing,* vol. 27, no. 8, pp. 1521-1537.

Uncles, R., Howland, R., Easton, A., Griffiths, M., Harris, C., King, R., Morris, A., Plummer, D. & Woodward, E. 1998, "Concentrations of dissolved nutrients in the tidal Yorkshire Ouse River and Humber Estuary", *Science of the total environment,* vol. 210, pp. 377-388.

Uncles, R., Stephens, J. & Harris, C. 2006, "Runoff and tidal influences on the estuarine turbidity maximum of a highly turbid system: the upper Humber and Ouse Estuary, UK", *Marine Geology,* vol. 235, no. 1, pp. 213-228.

Uncles, R., Stephens, J. & Smith, R. 2002, "The dependence of estuarine turbidity on tidal intrusion length, tidal range and residence time", *Continental Shelf Research,* vol. 22, no. 11, pp. 1835-1856.

Underwood, G.J. & Paterson, D.M. 1993, "Seasonal changes in diatom biomass, sediment stability and biogenic stabilization in the Severn Estuary", *Journal of the Marine Biological Association of the United Kingdom,* vol. 73, no. 4, pp. 871-887.

Valeport Limited, 2004, *MIDAS DWR & WTR Wave Recorders operational manual*, Valeport Limited, Totnes, UK.

Van den Berg, J. & Van Gelder, A. 2009, "A new bedform stability diagram, with emphasis on the transition of ripples to plane bed in flows over fine sand and silt", *Alluvial Sedimentation (Special Publication 17 of the IAS),* vol. 66, pp. 11.

Van der Mark, C., Blom, A. & Hulscher, S.J. 2008, "Quantification of variability in bedform geometry", *Journal of Geophysical Research: Earth Surface,* vol. 113, no. F3.

Van der Werf, Jebbe J, Doucette, J., O'Donoghue, T. & Ribberink, J.S. 2007, "Detailed measurements of velocities and suspended sand concentrations over full-scale ripples in regular oscillatory flow", *Journal of Geophysical Research: Earth Surface,* vol. 112, no. F2.

Van Kampen, H. & Nap, E. 1988, "Sediment concentrations and transport in case of irregular non-breaking waves with a current, Part C and D", *Rep., Delft University of Technology, Delft, The Netherlands,* .

Van Ledden, M., Van Kesteren, W. & Winterwerp, J. 2004, "A conceptual framework for the erosion behaviour of sand–mud mixtures", *Continental Shelf Research,* vol. 24, no. 1, pp. 1-11.

Van Olphen, H. 1977, *An introduction to clay colloid chemistry: for clay technologists, geologists, and soil scientists,* 2nd Edn , Jon Wiley and Sons, London.

Van Rijn, L.C. 1984, "Sediment transport, part I: bed load transport", *Journal of Hydraulic Engineering,* vol. 110, no. 10, pp. 1431-1456.

Van Rijn, L.C. 1993, *Principles of sediment transport in rivers, estuaries and coastal seas,* Aqua publications, Amsterdam, Netherland.

Van Rijn, L.C. 2007, "Unified view of sediment transport by currents and waves. I: Initiation of motion, bed roughness, and bed-load transport", *Journal of Hydraulic Engineering,* vol. 133, no. 6, pp. 649-667.

Vanoni, V.A. & Hwang, L. 1967, "Relation between bed forms and friction in streams", *Journal of the Hydraulics Division*, Vol. 93, pp. 121-144.

Venditti, J.G., Church, M.A. & Bennett, S.J. 2005, "Bed form initiation from a flat sand bed", *Journal of Geophysical Research: Earth Surface,* vol. 110, no. F1.

Villaret, C. & Perrier, G. 1992, *Transport of fine sand by combined waves and current: An experimental study,* Report No. E4202R.

Vincent, C.E., Hanes, D.M. & Bowen, A.J. 1991, "Acoustic measurements of suspended sand on the shoreface and the control of concentration by bed roughness", *Marine Geology,* vol. 96, no. 1-2, pp. 1-18.

Vongvisessomjai, S. 1984, "Oscillatory ripple geometry", *Journal of Hydraulic Engineering,* vol. 110, no. 3, pp. 247-266.

Voropayev, S., McEachern, G., Boyer, D. & Fernando, H. 1999, "Dynamics of sand ripples and burial/scouring of cobbles in oscillatory flow", *Applied Ocean Research,* vol. 21, no. 5, pp. 249-261.

Voulgaris, G. & Trowbridge, J.H. 1998, "Evaluation of the acoustic Doppler velocimeter (ADV) for turbulence measurements", *Journal of Atmospheric and Oceanic Technology,* vol. 15, no. 1, pp. 272-289.

Walling, D. & Fang, D. 2003, "Recent trends in the suspended sediment loads of the world's rivers", *Global and Planetary Change,* vol. 39, no. 1, pp. 111-126.

Wang, Z.Y., Larsen, P., Nestmann, F. & Dittrich, A. 1998, "Resistance and drag reduction of flows of clay suspensions", *Journal of Hydraulic Engineering,* vol. 124, no. 1, pp. 41-49.

Whitehouse, R., Soulsby, R., Roberts, W. & Mitchener, H. 2000, *Dynamics of estuarine muds*, Thomas Telford, London.

Wiberg, P.L. & Harris, C.K. 1994, "Ripple geometry in wave-dominated environments", *Journal of Geophysical Research: Oceans,* vol. 99, no. C1, pp. 775-789.

Wikramanayake, P.N. & Madsen, O.S. 1994, *Calculation of movable bed friction factors*, Technical Report, Massachusetts Institute of Technology, Cambridge, pp. 105.

Wilcock, P.R. & Southard, J.B. 1989, "Bed load transport of mixed size sediment: fractional transport rates, bed forms, and the development of a coarse bed surface layer", *Water Resources Research,* vol. 25, no. 7, pp. 1629-1641.

Williams, J., Bell, P., Thorne, P., Metje, N. & Coates, L. 2004, "Measurement and prediction of wave-generated suborbital ripples", *Journal of Geophysical Research: Oceans,* vol. 109, no. C2.

Williams, J., Bell, P., Thorne, P., Trouw, K., Hardcastle, P. & Humphery, J. 2000, "Observed and predicted vertical suspended sediment concentration profiles and bedforms in oscillatory-only flow", *Journal of Coastal Research,* Vol. 16, no. 3, pp. 698-708.

Willis, J. C. 1988, “Partial armouring of sand beds by gravel”, in *Mechanics of alluvial channels*, edited by Mahmood K.; Haque M.I.; Choudri A.M., Water Resource Publication, Littleton, Colorado, pp. 356–368.

Winterwerp, J. 2001, "Stratification effects by cohesive and noncohesive sediment", *Journal of Geophysical Research: Oceans,* vol. 106, no. C10, pp. 22559-22574.

Winterwerp, J.C. & Van Kesteren, W.G. 2004, *Introduction to the physics of cohesive sediment dynamics in the marine environment,* Elsevier.

Wotton, R.S. 2004, "The utiquity and many roles of exopolymers (EPS) in aquatic systems", *Scientia marina,* vol. 68, no. S1, pp. 13-21.

Xu, K. & Milliman, J.D. 2009, "Seasonal variations of sediment discharge from the Yangtze River before and after impoundment of the Three Gorges Dam", *Geomorphology,* vol. 104, no. 3, pp. 276-283.

Yalin, M.S. 1985, "On the determination of ripple geometry", *Journal of Hydraulic Engineering,* vol. 111, no. 8, pp. 1148-1155.

Yang, S., Milliman, J., Li, P. & Xu, K. 2011, "50,000 dams later: erosion of the Yangtze River and its delta", *Global and Planetary Change,* vol. 75, no. 1, pp. 14-20.

Ye, L. 2016, *Morphodynamcis and suspended sediment transport in cohesive substrates*, PhD edn, University of Hull, Hull, UK.

Yokokawa, M. 1995, "Combined-flow ripples: genetic experiments and applications for geologic records", *九州大学理学部紀要,* vol. 29, pp. 1-38.

Zanke, U. 2003, "On the influence of turbulence on the initiation of sediment motion", *International Journal of Sediment Research,* vol. 18, no. 1, pp. 17-31.